Hybrid Composite Sensors for Improved Visual Inspection of Impact Damage

by

Ali Tabatabaeian

James Watt School of Engineering

College of Science and Engineering

University of Glasgow

Submitted in fulfilment of the requirements for the degree of Doctor of Philosophy in Aerospace Engineering

May 2024

Abstract

Advanced visual inspection techniques are essential for ensuring the structural integrity and reliability of laminated fibre reinforced polymer (FRP) composite structures. Given the ever-increasing applications of FRP composites in various industries such as aerospace, wind turbine, and automotive, the demand for accurate, efficient, and non-destructive methods to monitor their health becomes paramount. Traditional inspection methods often fall short in detecting defects or damage in composite structures, which can compromise their performance and safety over time. A prime example of this is barely visible impact damage (BVID) caused by out-of-plane loadings such as indentation and low-velocity impact that can considerably reduce the residual strength. Therefore, developing advanced visual inspection techniques is essential for early detection, localisation, and characterisation of defects, thereby enabling proactive maintenance and extending the lifespan of composite structures.

The work in this thesis explores the viability of using hybrid composite sensors for detecting BVID in laminated FRP composite structures. Drawing inspiration from the colour-changing mechanisms found in nature, hybrid composite sensors composed of thin-ply glass and carbon layers are designed and attached to the surface of the laminated FRP composites exposed to out-of-pane loadings. A comprehensive experimental characterisation, including quasi-static indentation and low-velocity impact tests alongside non-destructive evaluations such as ultrasonic C-scan and visual inspection, is conducted to assess the sensor's efficacy in detecting BVID. After this, a complementary numerical and theoretical study is conducted to optimise the sensor's design through a parametric study, enabling the evaluation of key design parameters to tailor the sensor for specific applications. This numerical model can serve as a cost-effective and reliable tool for fast parametric design studies. The effectiveness of the sensor is further examined, particularly in automated visual inspection, when employing deep learning-assisted techniques. These deep learning models use images captured from the surfaces of both damaged and intact composites, enabling assessment of the sensors' potential in enhancing damage pattern recognition and classification. Ultimately, the proposed sensing technology is implemented on curved FRP composite panels, serving as a real-life case study representative of composite gas cylinders. The findings of this research offer insights into the design, characterisation, and application of bio-inspired hybrid composite sensors, thereby enhancing visual inspection capabilities for detecting BVID in composite structures.

Acknowledgment

Firstly, I would like to thank my supervisors, Dr. Mohammad Fotouhi and Dr. Philip Harrison, for trusting me and for their continued support throughout my academic research. Their professional guidance and knowledge were essential, and I am thankful for all the stimulating conversations and meetings we had together. They provided a platform for me to grow and develop critical and scientific thinking.

I would like to express my thanks to my colleagues and friends whom I have worked alongside during my time at the University of Glasgow, Dr. Sakineh Fotouhi and Sixin Liu, and technical staff at Materials Laboratory, Charlie Patterson and Iain Wood.

Another monumental thank you to my colleagues and friends who helped me during my visit to TU Delft, Ali Ghaderiaram, and Dr. Reza Mohammadi. I would also like to thank my colleagues from Radboud University, Professor Elena Marchiori and Bruno Jerkovic, for their help with the deep learning aspects of this work.

Last but not least, a huge thank you to my family – my wonderful parents and siblings, and my beloved wife. Your belief in me has meant the world. Your support has given me the courage to aim high and achieve great things. I dedicate this thesis to my amazing mother, who has been by my side since day one, cheering me on every step of the way.

Author’s declaration

“I declare that, except where explicit reference is made to the contribution of others, this dissertation is the result of my own work and has not been submitted for any other degree at the University of Glasgow or any other institution.”

Ali Tabatabaeian, May 2024

List of Publications

- **A. Tabatabaeian**, S. Liu, P. Harrison, E. Schlanegn, M. Fotouhi, 'A review on self-reporting mechanochromic composites: An emerging technology for structural health monitoring' – *Composites Part A: Applied Science and Manufacturing, 2022, https://doi.org/10.1016/j.compositesa.2022.107236*.

- **A. Tabatabaeian**, B. Jerkovic, P. Harrison, E. Marchiori, M. Fotouhi, 'Barely visible impact damage detection in composite structures using deep learning networks with varying complexities' – *Composites Part B: Engineering, 2023, https://doi.org/10.1016/j.compositesb.2023.110907.*

- **A. Tabatabaeian**, R. Mohammadi, P. Harrison, M. Fotouhi, 'Characterisation and application of bio-inspired hybrid composite sensors for detecting barely visible damage under out-of-plane loadings' – *Sensors, 2024, https://doi.org/10.3390/s24165170.*

- **A. Tabatabaeian**, S. Fotouhi, M. Fotouhi, 'Visual inspection of impact damage in composite materials' – *Non-destructive Testing of Impact Damage in Fiber-reinforced Polymer Composites, 2024, https://doi.org/10.1016/B978-0-443-14120-1.00002-9.*

- **A. Tabatabaeian**, S. Fotouhi, P. Harrison, M. Fotouhi, 'On the optimal design of smart composite sensors for impact damage detection' – *The 20th European Conference on Composite Materials (ECCM20), 2022, Switzerland.*

- **A. Tabatabaeian**, B. Jerkovic, E. Marchiori, M. Fotouhi, 'Data-driven structural health monitoring in laminated composite structures: Characterisation of impact damage' – *The 6th Brazilian Conference on Composite Materials (BCCM6), 2022, Brazil.*

- **A. Tabatabaeian**, B. Campbell, P. Harrison, M. Fotouhi 'Low velocity impact behaviour of mechanochromic sandwich composites' – *17th International Conference on Advances in Experimental Mechanics, 2023, Glasgow, UK.*

Contents

List of Figures

List of Tables

List of Abbreviations

Fibre Reinforced Polymer (FRP)

Carbon Fibre Reinforced Polymer (CFRP)

Barely Visible Impact Damage (BVID)

Non-Destructive Testing (NDT)

Structural Health Monitoring (SHM)

Visible Impact Damage (VID)

Non-Destructive Evaluation (NDE)

Unmanned Aerial Vehicle (UAV)

Artificial Intelligence (AI)

Remote Visual Inspection (RVI)

Artificial Neural Network (ANN)

Convolutional Neural Network (CNN)

Finite Element Analysis (FEA)

Continuum Damage Mechanics (CDM)

Cohesive Zone Method (CZM)

Region of Interest (ROI)

Reference (Ref)

In-plane Scaling (Is)

Ply-block Scaling (Ps)

Sub-laminate Scaling (Ss)

Deep Learning (DL)

Machine Learning (ML)

Binary Cross Entropy (BCE)

Categorical Cross Entropy (CCE)

Multi-Layer Perceptron (MLP)

Fully Connected (FC)

Rectified Linear Unit (ReLU)

Residual Network (ResNet)

True Positives (TP)

True Negatives (TN)

False Positives (FP)

False Negatives (FN)

Chapter 1

Introduction

1.1. Background

Fibre reinforced polymer (FRP) composites represent a class of advanced materials that offer excellent mechanical properties compared to their metallic counterparts. An FRP composite system consists of two main phases, including a polymeric matrix, such as thermoset or thermoplastic polymers, and a reinforcing fibre phase, such as carbon or glass fibres. Because of the heterogeneous nature of composites, the mechanical properties in different directions within a component can be tailored as desired. Their superior properties, such as high strength-to-weight and stiffness-to-weight ratio, advanced fatigue performance, and corrosion resistance, enable them to satisfy the increasing demands of the aerospace, automotive, and wind turbine industries, civil engineering, and sporting goods [1]. With continuous advancements in manufacturing techniques and material science, FRP composites continue to redefine the limits of structural performance, sustainability, and innovation in modern engineering applications. In the aerospace sector, for instance, a key driving factor for using FRP composites is their potential for substantial weight reduction. This has led to an increase in the use of advanced composites in overall structural weight, from 3% to more than 50%, in just under 30 years (see Fig. 1-1) [2]. The global transition of aircraft with composite architecture is estimated to contribute 15%–20% of industry CO_2 reduction targets by 2050 [3]. Therefore, advanced carbon fibre reinforced polymer (CFRP) composites are anticipated to play a significant role in the primary structure of the next-generation commercial aircraft.

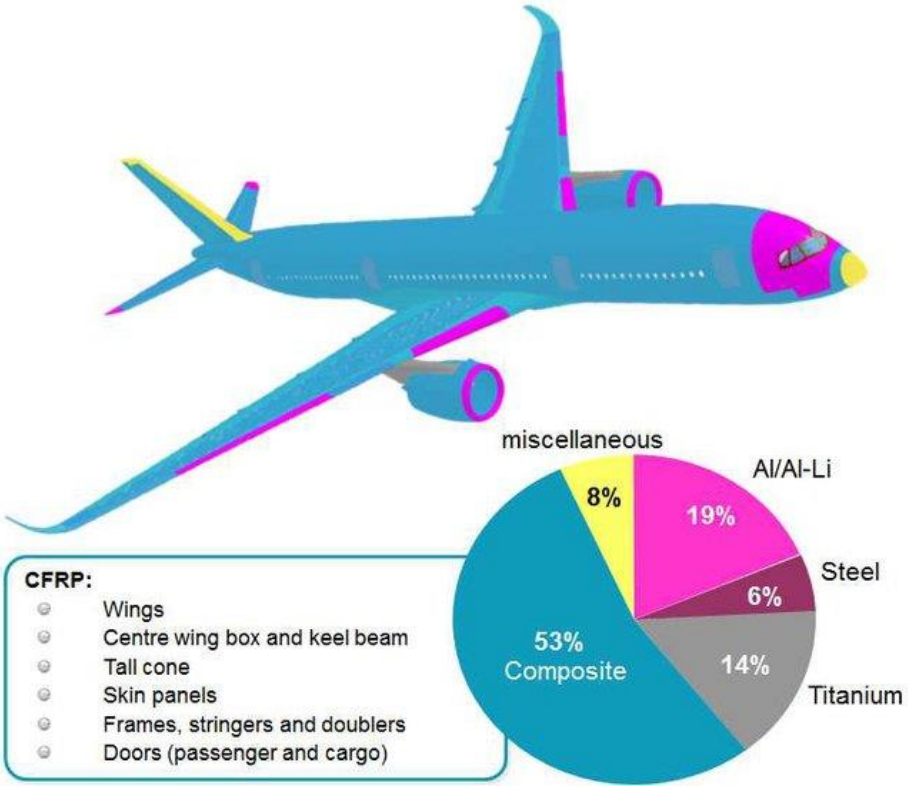

Fig. 1.1: Materials used in a modern aircraft, the Airbus A350 XWB [3]

In practical applications, a primary concern is that FRP composites are prone to delamination damage during both the manufacturing stage and service life, which is most likely to be induced by foreign object impact [4]. In aerospace sector, for instance, transverse impact and other forms of out-of-plane loading, such as dropping tools during manufacture, bird strike, small runway debris kicked up from tyres to airframe during taking-off and landing, hail impact during flight and even from vehicles during ground handling, may cause significant and highly complex internal damage to laminated composites. In some cases, this is likely to result in a complete loss of structural integrity. Delamination influences both the matrix and fibre regions. Nevertheless, due to a lower strength in the matrix region, it is more susceptible to impact loading. Moreover, due to lower mechanical properties at the interlaminar regions, delamination may occur at a relatively lower stress level compared to that in the direction of reinforcement. In the case of metallic materials, impact damage can be readily identified as a result of the plastic deformation process, and the damage might not significantly affect the residual properties and structural integrity. But delamination can hinder the scope of composite applications as sudden failure and poor residual load-bearing capacity cannot be tolerated. Therefore, for composite materials, it is of great importance to consider a proper safety margin

since a sudden failure or collapse may have consequences such as the loss of human life and significant financial costs.

1.2. Scope and Objectives

As explained above, in composite materials, the gradual accumulation of barely visible impact damage (BVID) can ultimately result in catastrophic failure, often occurring without any visual warning signal [5]. Accordingly, structures that have passed visual inspection might still fail at considerably lower load levels than expected. To mitigate this risk, conventional practices in composite design and manufacture emphasise increased safety margins and conservative design envelopes. This comes with substantial expense and consumes significant time and energy. Therefore, it is essential to develop new methods to monitor and detect damage at early stages before final failure occurs. This can prevent any sudden, catastrophic failure and also signal the requirement for additional non-destructive testing (NDT), facilitating timely repairs or maintenance interventions as needed. For this purpose, different structural health monitoring (SHM) methods have been developed. Acoustic emission is mainly used as an early warning for damage detection and propagation before it reaches a critical status, but it has significant drawbacks due to noise and can be difficult to interpret signals [6]. Fibre optic sensors are also a popular choice and widely used in SHM. Especially for laminated composite materials that are prone to impact-induced failure, these lightweight sensors can be used at different locations. Nevertheless, they require lots of cabling, are fragile, and tend to break fairly easily. They can also cause stress concentrations when incorporated in composite laminates [5]. Visual inspection is the most common technique to detect cracks or surface dents in composites, accounting for over 80% of inspections performed on large transport category aircraft [7]. However, the effectiveness of visual inspection heavily depends on the operator's skills, and there is an increasing need to cover large areas of structure that are usually not easy to access, increasing the cost, errors and health and safety risks. For instance, visual inspection of large aircraft may require up to 40,000 man-hours [7]. Moreover, the most common visual inspection practices include access by lift platforms for airplanes, and rope access for wind turbine blades, making the inspection highly demanding. BVID often occurs in environments where there are debris and other contaminants present on the surface, making it difficult to achieve a clean inspection. Hence, visual inspection is not reliable enough to identify BVID with much accuracy. This necessitates the development of improved and more efficient means of damage detection. Consequently, this investigation aims to fulfil this need by introducing bio-inspired

hybrid composites with enhanced damage visualisation, to improve the reliability of impact damage detection.

The primary objectives of this research are as follows:

- Design, manufacture and analysis of hybrid composite sensors to improve visual inspection of damage induced by transverse loads such as impact and indentation.
- Understand the influence of adding such sensors on a laminate's mechanical properties.
- Study the design parameters of the sensor to achieve an optimal sensor design.
- Investigate potential applications of the sensor in automated visual inspection, using deep learning models.
- Present a case study to showcase the application of the sensor.

Self-reporting hybrid composites feature a sensing layer on both impacted and non-impacted surfaces. The sensing layer enables improved visual inspection and detection of BVID that is likely to be left undetected in conventional CFRP structures. This is achieved by controlling the damage sequence in the sensor and substrate, promoting a specific failure mechanism in the sensor. A side benefit of the sensor might be enhancing impact damage tolerance through energy absorption mechanisms. This self-sensing approach would present a lightweight and completely wireless SHM tool, eliminating the requirement for any data acquisition or evaluation systems. Therefore, it could provide a cost-effective and straightforward visual solution for inspecting BVID. The successful design of self-reporting hybrid composites with improved visibility of impact damage can help exploit the true potential of the composite material by using less conservative design envelopes with smaller safety margins and, ultimately, it would result in reduced manufacturing time and cost, as well as a safer operation in service due to increased confidence in structural design and damage monitoring.

1.3. Thesis Outline

The work carried out to fulfil the main objectives of the PhD thesis is divided into the following chapters:

Chapter 1 provides a brief overview of composite materials and their growing applications in different industries, with a particular focus on their key role within the aerospace sector. Moreover, this chapter underscores the challenges related to impact damage monitoring and outlines the objectives, motivations and structure of the PhD thesis.

Chapter 2 presents a comprehensive literature review on visual inspection of impact damage in composite structures. It also explores how bio-inspired design principles could contribute to achieving enhanced impact damage tolerance and visual inspection capabilities.

Chapter 3 details the procedures and methodologies employed to design, manufacture, and analyse hybrid composite sensors. It covers experimental quasi-static indentation and low-velocity impact tests, as well as NDT methods such as ultrasonic C-scan and visual inspection. Additionally, a new analytical formulation for calculating the delamination threshold load is introduced. This is followed by the development of finite element models to simulate out-of-plane loading behaviour and numerically investigate sensor design parameters.

Chapter 4 presents the results of the experimental, numerical, and analytical studies introduced in Chapter Three and includes a detailed discussion and analysis aimed at achieving an optimal sensor design.

Chapter 5 employs four deep learning models with varying levels of complexity to investigate the effectiveness of hybrid sensors in enhancing automated visual inspection. It compares and discusses the accuracy and training time of these models for detecting BVID, in both conventional and sensor-integrated CFRP composites.

Chapter 6 demonstrates the feasibility of using hybrid sensors to visualise BVID in curved composite panels, selected to represent real-life applications. This involves the design and manufacture of curved composite panels, followed by indentation and impact testing.

Chapter 7 summarises the important conclusions and potential future work that could complement the research presented in this investigation.

Chapter 2

Literature Review

2.1. Introduction

Fibre reinforced polymeric composite materials are widely used in various industries such as civil, aerospace, biomedical, wind turbine, automotive, etc., where they are exposed to harsh environmental conditions, such as temperature fluctuations, humidity, strong winds, corrosion, etc. Static or dynamic overloading conditions such as impact strikes and fatigue are reported as primary causes of damage in glass and carbon fibre reinforced polymer composites [5]. For instance, low-velocity impact can happen due to bird strikes or dropping a tool during composite structure repair or assembly. This may not induce any visual damage on the surface while causing multiple internal delamination at the ply level. Such internal impact-induced damage, often referred as BVID, might lead to severe structural damage and unexpected failure. In this case, different structural health monitoring techniques have been developed, among which bio-inspired composites that can visualise damage are the focus of this investigation. This chapter discusses the key concepts and presents a comprehensive literature review on visual inspection of impact damage in composite structures. A diagram illustrating the information presented in this chapter is presented in Fig. 2-1. Each chapter in this thesis also includes separate references that are relevant to the specific topic being discussed.

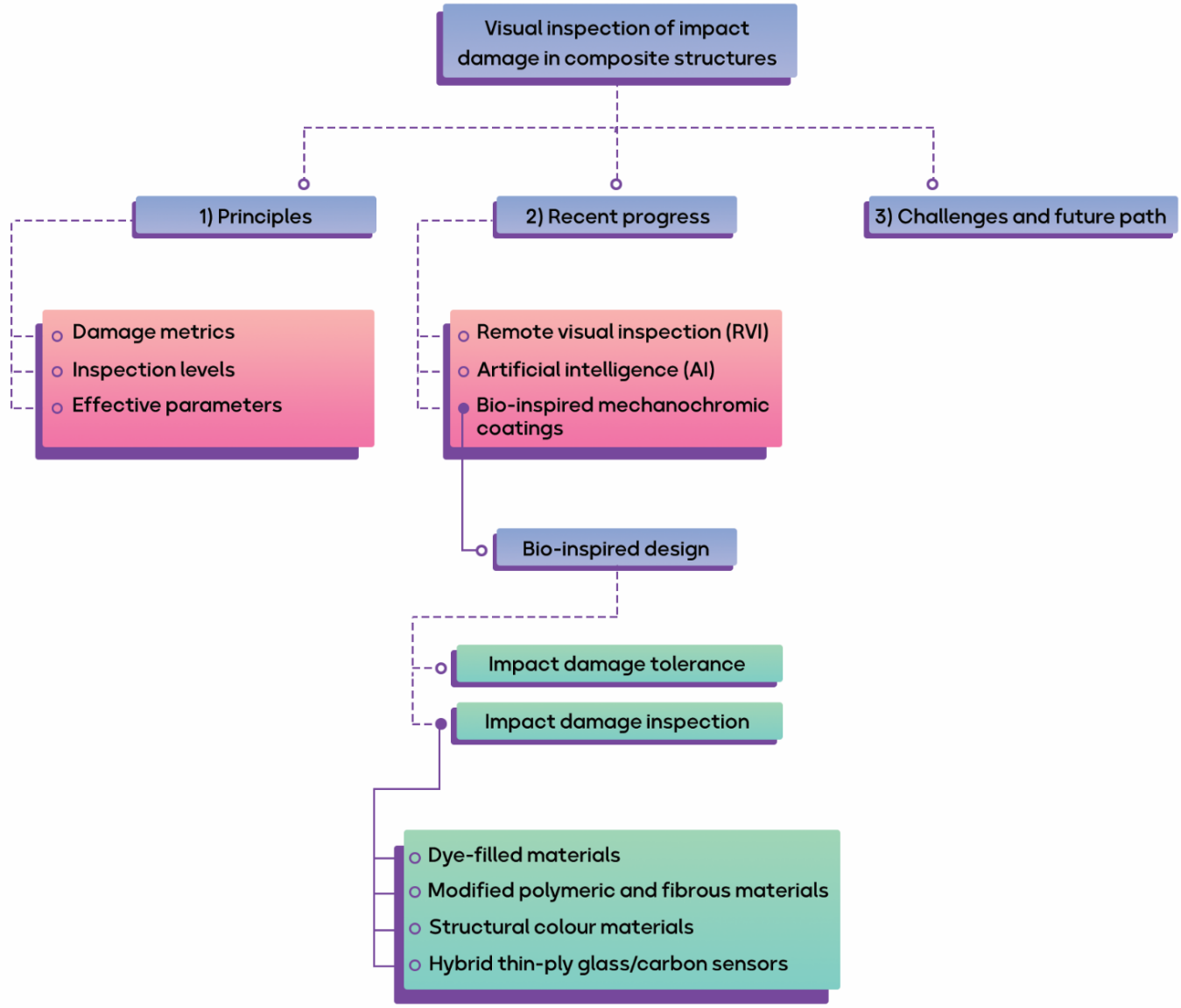

Fig. 2-1: The main concepts and information presented in Chapter Two

2.2. Visual Inspection of Impact Damage in Composite Structures

Recent decades have seen a growing use of composite materials in various industries such as automotive, sports, civil, and wind turbines, as well as aerospace structural components, due to the crucial importance of mass reduction. Despite several advantages that composites can offer over metallic structures, there are still challenges that should be addressed. Among their drawbacks, for instance, is their fragility and complex response to out-of-plane impact. Hence, composite damage inspection practices should be standardised. In structural engineering, damage tolerance refers to assessing a damaged structure's ability to withstand loads before failing catastrophically. This has also been defined by European certification JAR 25.571 [8] as: "the damage tolerance evaluation of a structure is intended to ensure that should serious

fatigue, corrosion or accidental damage occur within the operational life of the airplane, the remaining structure can withstand reasonable loads without failure or excessive structural deformation until the damage is detected". There are two factors contributing to a composite material's impact damage tolerance:

a) The impact-induced residual strength loss of the structure: The loss of strength can be as low as 50-75% of the structure's undamaged strength.

b) Impact detectability: Even though impact damage is often visible on the non-impacted side of a composite structure before being visible on the impacted side, in practice, "detectable impact damage" refers to detectable damage on the impacted side, as the visual inspection of the non-impacted side is often not straightforward, for example inside the wing, or the fuselage, in aircraft systems [9].

A well-established method to evaluate impact damage tolerance in aerospace composite structures is the visual inspection of the permanent indentation left on the impacted side of a composite after the impact event. This can be used in assessing the residual compressive strength and the level of damage, to determine whether it is visible impact damage (VID) or BVID. Visual inspection can be defined, according to the Federal Aviation Administration (FAA) advisory circular AC 43-204 [10], as follows: "Visual inspection is the process of using the eye, alone or in conjunction with various aids, as the sensing mechanism from which judgment may be made about the condition of a unit to be inspected". It is a fast and inexpensive method for SHM of engineering systems, especially those with indentations or cracks on the surface. This process not only relies on the human eye but also includes sensory and cognitive factors to enhance the accuracy of the tests and improve the visibility of the structure. For example, the angle and intensity of the light, or illumination, can be a critical factor in achieving high-quality visual inspection results. Test equipment may include but is not limited to borescopes, cameras, digital video magnifiers, video borescopes, and digital image correlation facilities for improving detailed inspections [11,12] (see Fig. 2-2).

Fig. 2-2: Examples of direct (in the centre) and assisted visual inspection [13–15]

2.2.1. Principles

In addition to the permanent indentation, impact loading can cause other types of damage in composite structures. These can vary from micro-scale damage, such as matrix cracks, to macro-scale delamination and fibre breakage. In laminated composites, matrix cracks and delamination are often the dominant damage types affecting the residual compressive strength and impact damage tolerance. Therefore, critically identifying and categorising different impact-induced damage types is of great interest in developing meaningful relations between the internal invisible damage, the surface visible damage and the structure's remaining residual strength. Transverse loading causes matrix cracking in a ply in the form of shear cracks and transverse cracks running parallel to the fibre direction. These are the initial damage modes, taking place at an early stage of impact and static indentation due to the relatively weak mechanical properties of the resin. Cracks in the matrix do not significantly affect the laminate's residual mechanical properties. Nevertheless, if this type of damage accumulates over time, it can cause more serious problems, such as delamination of adjacent plies. Contrary to other matrix-dominated damage modes such as delamination, matrix cracks cannot be detected by instrumented impact testing or conventional non-destructive evaluation (NDE)

techniques such as ultrasonic inspection [4,16]. Delamination occurs due to high interlaminar shear and normal stresses exceeding the strength of the laminate interface, especially at areas of discontinuities such as holes and free edges or because of thermal loading during the curing process. This is more likely to happen between plies with dissimilar fibre orientations [17,18]. Other impact-induced damage types are fibre breakage due to high tensile stress at the non-impacted side or compressive fibre failure at the impacted side of the structure. These failure modes occur after matrix cracks and delamination and are easier to detect by visual inspection. At this stage, a large amount of energy is absorbed through fibre failure mechanisms, which significantly reduces the load-bearing capability of the composite structure [19,20]. The next section will explain how these damage types can be connected to permanent indentation, which is believed to be a practical damage metric for visual inspection of impact damage in composite materials. The relation between these damage types and the permanent indentation is shown in Fig. 2-3(a).

2.2.1.1. Damage Metrics

Permanent indentation is considered the most practical damage metric for visual inspection of impact damage. However, this is defined differently by various organisations [21]. For example, based on the Airbus damage definition, "BVID is the minimum impact damage surely detectable by scheduled inspection. BVID corresponds to a probability of detection of 90% with an interval of confidence of 95%. Two values for the BVID criterion are typically established depending on the visual inspection type: Detailed and general visual inspection. Dent depth is the damage metric for transverse impact. For an edge impact, where internal cracks and delamination become visible, the damage metric is the dent depth and/or the crack length" [22]. Boeing, however, defines BVID as "small damages which may not be found during heavy maintenance general visual inspections using typical lighting conditions from five feet (1524mm). The damage metric is typically a dent depth of 0.01 to 0.02 inches (0.254mm - 0.508mm). Dent depth relaxation must be accounted for" [23]. According to the inspector's experience [24,25], it is possible to say with 95% confidence that a dent depth of 0.2 to 0.23 mm is detectable at a 2-meter distance. Chen et al. [26] used the dent depth and diameter to optimise the inspection intervals to maintain high structural reliability and minimise maintenance costs. According to general guidelines, permanent indentations between 0.3mm and 0.5mm can indicate BVID, whereas permanent indentations of 2mm or perforations of 20mm indicate minor VID. Also, perforation with a diameter of 50mm can be related to large VID [9,27,28]. Fig. 2-3 shows the evolution of impact damage and different visual

inspection levels in relation to the permanent indentation size and impact energy level. At the first stage, the dent size is so small, and damage happens in the form of matrix cracks. As impact energy increases, damage appears in the form of delamination, and dent size becomes larger. In the second stage, all three damage types can occur, and visual inspection becomes easier due to a larger dent size (dent depth and diameter). The fibre breakage in this stage can help achieve better inspection results. However, this can have a detrimental effect on the residual strength after impact, where the complex interaction of different damage types during an impact event necessitates detailed studies of damage mechanics during and after impact [9]. To date, no damage metric can replace permanent indentation for visual inspection purposes. Ideally, such alternative damage metrics would be easy to implement and fast to assess with only a few tools. New SHM technologies could be a promising alternative to visual inspection of dent depth, especially in the future aircraft industry. Recent progress in visual inspection of impact damage will be discussed in section 2.2.2.

2.2.1.2. Visual Inspection Levels

Visual inspection of impact damage can be categorised into four main levels (see Fig. 2-3(a)). The standard visual inspection aids are a flashlight, mirror and magnification glass. For special inspection tasks, further inspection aids may be required [29,30]. A *walk-around inspection* is a general check conducted from ground level to detect discrepancies and assess general condition and safety. This inspection is conducted daily and is expected to detect large visual impact damages such as fibre breakage. *General visual inspection* is made of an exterior with selected hatches and openings open or an interior, when called for, to detect damage, failure or irregularity. This inspection level is expected to detect minor visual impact damage and may require suitable lighting conditions, surface cleaning and equipment such as a mirror. A *Detailed visual inspection* is an intensive visual evaluation of a specific area, system or assembly to detect damage, failure or irregularity. This inspection level is expected to detect the BVID and may require surface preparation and elaborate access procedures. A *detailed visual inspection* is an intensive evaluation of a specific item, installation or assembly to detect damage, failure or irregularity. This inspection level may require intricate disassembly and cleaning as well as specialised techniques and equipment.

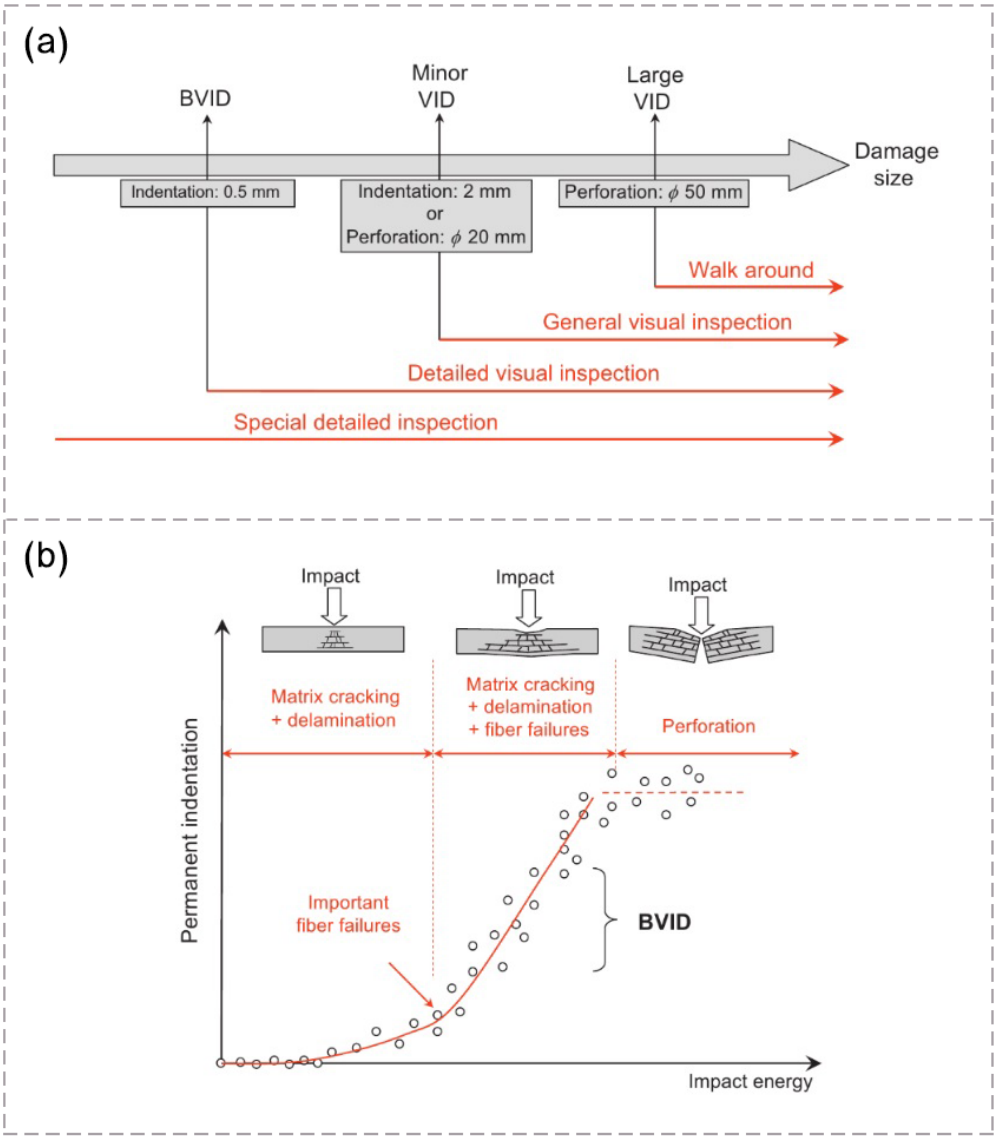

Fig. 2-3: Damage size in different (a) inspection levels and (b) impact energies [9]

2.2.1.3. Effective Parameters

An early study by Megaw [31] suggests that the four influential parameters affecting the visual inspection are the inspector's visual acuity, the workplace lighting conditions, the time available for inspection and the provision of feedback or knowledge of results to the inspector. In a study by Erhart et al. [32], the visual detectability of 0.05-inch (1.27mm) deep dents was investigated by considering different parameters. A list of the variables identified for further research in aircraft industries was provided accordingly. Comprehensive European Aviation Safety Agency research characterised the influence of parameters mentioned in previous

research in detail [30]. A list of effective parameters and critical findings for each parameter is presented below (see Fig. 2-4).

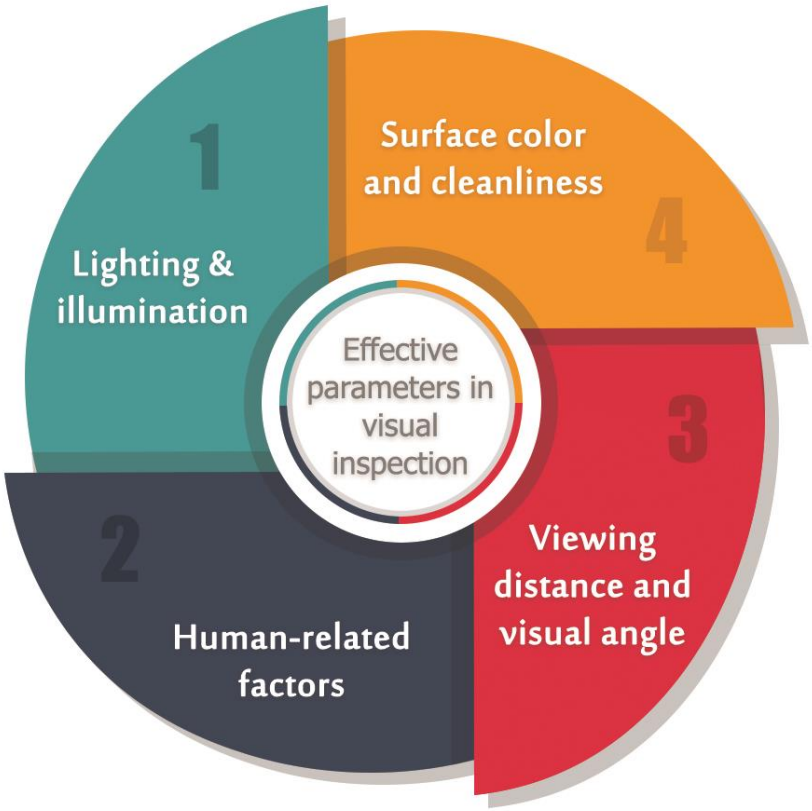

Fig. 2-4: Effective parameters for visual inspection of impact damage in composite materials

Lighting and Illumination: Visual inspection relies heavily on light, as the human eye sees nothing but light patterns. A report by the European Aviation Safety Agency [30] suggests that illumination can significantly influence damage visibility in composite structures. Visual inspection of a damaged structure may require different lighting conditions, as each damage type needs a specific lighting setup. Light brightness is a crucial factor in test environments since excessive light within the field of view leads to an unpleasant sensation called glare that interferes with a clear view for the inspector [11].

Human-Related Factors: Person-related factors can also be influential in visual damage inspection. For example, human eyesight, characterised by its colour vision capability and visual acuity, can affect visual inspection quality to a great extent. Colours and patterns around

the test structure can substantially influence the inspector's attitude during the inspection. For example, high contrast on the inspected pattern can cause eye fatigue and subsequently decrease inspection quality [11]. Adding high-resolution cameras to endoscopes and fibrescopes and projecting the inspection images on projection monitors are viable methods to reduce eye fatigue caused by the prolonged use of these devices. Also, psychological factors such as tension may play a great role in the inspector's performance. The results of [30] showed a clear trend for persons with greater experience in composite structures and visual inspection to find more damage on the same panel. That research also revealed that the age and gender of the inspector could influence the probability of damage detection to a low extent.

Viewing Distance and Visual Angle: Based on the viewing distance and viewing angle, visual inspection methods can be categorised into two main groups: direct and remote-based inspections. In direct visual inspection, the distance between the eye and the structure should not exceed a radius of 610mm, and the angle should not be less than 30°. The influence of the inspection angle is insignificant compared to other inspection parameters [30]. However, some studies suggest that an angle of 45° can be slightly worse for inspection ability than an inspection angle of 65°.

Surface Colour and Cleanliness: Cleanliness can help achieve a better visual inspection. However, compared to other parameters, the influence of cleanliness is not significant. Literature suggests that there is no clear indication of whether colour influences the detectability of damage. However, the subjective impression of the influence of colour on damage detectability shows a clear advantage for the colour red. Eight of the fifteen inspectors in a survey found the red panel easier to inspect, and six gave the colour as the reason. Only one inspector found the blue panel easier to inspect [30].

2.2.2. Recent Progress

Various indirect visual inspection equipment, including video cameras, endoscopes, borescopes and unmanned aerial vehicles (UAV), has been developed to inspect hard-to-reach composite structures. Recent advances in artificial intelligence (AI) systems have significantly decreased inspection costs and increased inspection accuracy. Using bio-inspired smart coatings to enhance the visual inspection of impact damage has also shown great potential. Moreover, the development of computer systems and digital storage technology has improved the documentation of inspection records. These inspection systems are still being developed to

address all related challenges. The following sections present the recent progress in visual inspection of impact damage, particularly in three primary areas.

2.2.2.1. Remote Visual Inspection (RVI)

Detecting BVID in composite structures like aircraft and wind turbine blades is crucial. However, the current manual process is expensive and labour-intensive [33,34]. Visual inspection heavily relies on the operator's skills, and there is a growing need to cover large areas that are typically difficult to access, thereby increasing costs, errors and health and safety risks [35,36]. For instance, over 80 percent of inspections on large transport category aircraft are conducted visually, and visual inspections for such aircraft can take up to 40,000 hours [37]. The prevailing visual inspection methods involve lift platforms for airplanes and rope access for wind turbine blades. Therefore, there has been a shift towards remote visual inspection (RVI) systems that utilise automated computer vision inspection with a combination of fixed and moving cameras and deterministic image processing algorithms to detect BVID [38]. RVI, also known as enhanced visual inspection [39], presents a promising alternative to traditional visual inspection methods as it addresses safety concerns, reduces time and costs, and enhances detection accuracy. With the integration of machine learning, RVI has made significant advancements in detecting and characterising impact damage in composite structures. The field of RVI has seen notable progress, ranging from simple bore scopes and endoscopes to video scopes, thanks to the development of miniature cameras and optical lenses that provide access to even small-bore locations like heat exchangers, drain headers, and stacks [40,41]. Deterministic advancements in computer vision are further complemented by machine learning techniques, enabling reliable processing of large numbers of images [42] and facilitating decision-making processes. However, these optical techniques and instruments are typically heavy, require substantial power, and need stable positioning for seconds to achieve the necessary in-depth resolution of approximately 0.1mm, with a typical in-plane size resolution of 15mm-20mm [43]. The use of the automated UAV-based RVI systems can significantly reduce health and safety risks and cost as little as 20% of manual visual inspections, as reported by Mainblades [37], a company conducting inspection tasks for KLM Royal Dutch Airlines and other asset owners. This cost reduction is achieved by improving accessibility, facilitating immediate identification and assessment of damage, and providing high-quality images and videos for documentation and processing, as depicted in Fig. 2-5. The software utilised in these systems includes a dent-and-buckle feature, which allows for

recording and reviewing all structural damages on the exterior of the aircraft, pinpointing the exact location of damage and anomalies.

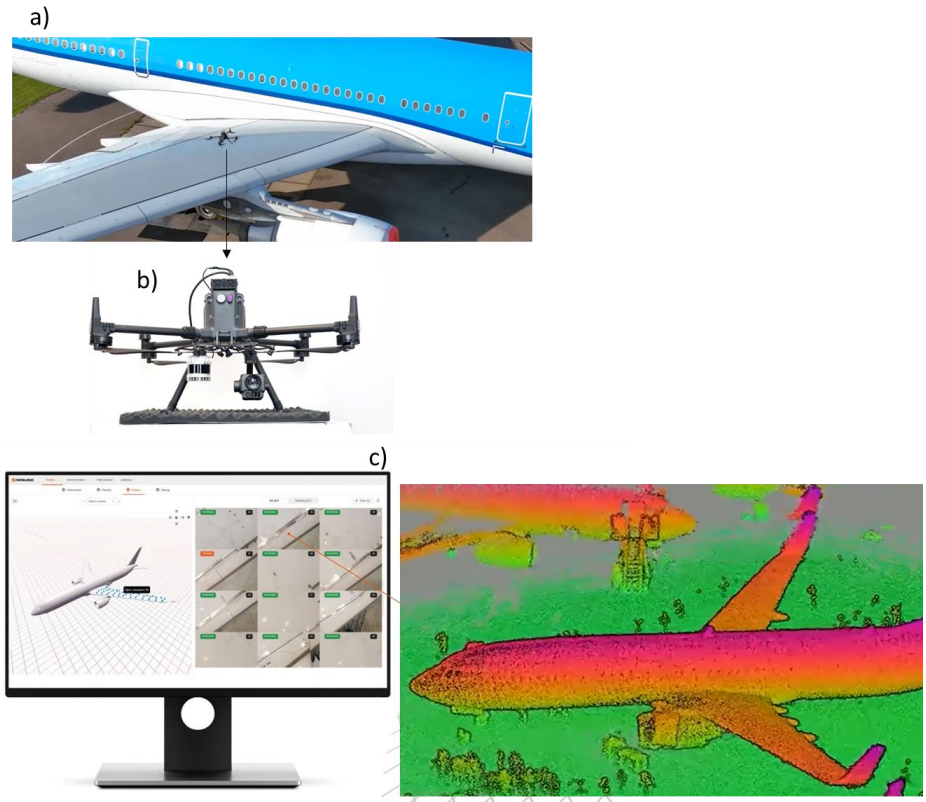

Fig. 2-5: a) An image of the aircraft inspection by Mainblades, b) UAV, c) the software, and scanned surface of the aircraft [44].

The current state-of-the-art approaches for RVI have limitations in measurement resolution, making them unreliable for measurements below 1mm [45]. These limitations arise from insufficient sharpness, exposure, high background noise, reliance on isolated frames, and a predetermined visual trajectory for material state classification [46]. Moreover, specific components like rivets cannot be detected [47]. While state-of-the-art drone-based development utilising on-board laser line scanners offers a better in-depth resolution of 0.3mm at a distance of 1.5m, it is still insufficient for detecting the smallest BVID [48]. Consequently, there is a need for further research and development efforts to optimise inspection processes and enhance the capabilities of RVI.

2.2.2.2. Artificial Intelligence (AI)

Impact damage is traditionally assessed through manual feature parameter extraction, which can be time-consuming and inaccurate. This has opened an avenue for new AI-based impact damage detection methods, such as vibration-based, acoustic-based and image-based

techniques, to be applied to complex impact-related problems [49,50]. The AI algorithm is trained and validated using a dataset and then tested on an unseen dataset. These learning algorithms are divided into different types, each of which can solve a specific problem. An excellent feature of an AI-based inspection method is its adaptability, meaning that it can be tested and modified several times to achieve an accurate and efficient damage pattern recognition function. Moreover, some AI-based algorithms can benefit from few-shot learning and transfer learning methods [51]. The former is a machine learning technique that uses a pre-trained model to accelerate the training of a new model on a related task, by reusing features learned from other tasks. However, these networks often have many layers with many trainable parameters that need to be estimated only from the data, which can become a problem in scenarios without access to big datasets [52]. Few-shot learning is a subfield of machine learning that deals with the problem of learning from a limited amount of labelled data. Therefore, thanks to these approaches, machine learning algorithms can work well with a small set of available data, and convey complex and qualitative empirical knowledge that is difficult to describe with mathematical formulas or conventional visual inspection practices. Unsupervised and supervised algorithms can be trained to perform different tasks such as damage detection, localisation, classification, and severity estimation. However, unsupervised learning is mostly used for damage detection and supervised learning for all mentioned tasks [53]. As reported in [54], artificial neural networks (ANNs) are the most popular machine learning algorithms for damage evaluation applications. In the case of BVID visual inspection, where dealing with an image-based dataset, a more complex family of neural networks, such as convolutional neural networks (CNNs), might be needed [42,55–57]. Recent examples of AI-based research in visual inspection of impact damage in composite materials are presented below.

Fotouhi et al. [58] collected a diverse image dataset of both microscale damage (matrix cracking) and macroscale damage (impact and erosion damage) from the literature to train a CNN and explore the possibility of automating the visual recognition of damage. Particularly, they used a pre-trained AlexNet for accomplishing three different tasks, including identifying damage type (impact, erosion or un-damaged), damage severity (low-energy impact or high-energy impact), and damage location (impacted side or non-impacted side). The network could identify the macro-scale damage type with a validation accuracy of 93%. The damage severity was identified on images of the impacted and non-impacted sides with a validation accuracy of 96% and 87%, respectively. The third task achieved a validation accuracy of 78% for low-

energy impact and 73% for high-energy impact datasets. These outcomes suggested that CNNs, in conjunction with transfer learning approaches, have great potential for automating the visual inspection of impact-induced damage in composite materials. The authors also suggested developing high-quality datasets for different damage types in composite structures to correlate the damage extent to the residual lifetime of the structure in the next stages.

Hasebe et al. [28] used three machine learning models, namely 'ridge regression', 'logistic regression', and 'random forest', on a dataset extracted from low-velocity impact tests on CFRP composites. The aim was to study the possibility of inferring BVID information from the surface damage profiles. The low-velocity impact tests were conducted on 246 specimens under three impact factors. The first factor was stacking sequence, where two different classes, cross-ply and quasi-isotropic, were considered. The second factor was the impactor shape with six different classes, and the third was the impact energy with several classes. A total of 104 impact conditions were created accordingly. After analysing the surface and C-scan images and dent measurements, the input data for machine learning models were prepared, and three impact factors, impactor shape, delamination area, and delamination length, were estimated, accordingly. The results showed that dent depth was the most effective feature for impactor shape prediction. It was also observed that the models could infer approximately 80% of results correctly using dent depth and indentation volume. As for further research, they suggested directly using the surface profiles as features without reducing raw data (surface profile) to human-designed features (depth, volume, etc.). Also, they suggested studying whether machine learning models are effective even if the target contains paint or other features that may be found in real structures but not in laboratory-level research. In another study, they developed a multi-task learning algorithm based on decision trees. The new algorithm was effective when the problem involved multiple objective variables related to each other or when it was challenging to collect numerous datasets. Furthermore, in addition to improving the prediction accuracy of objective variables, this model could be used to find the features that contribute to the model by investigating the model detail [59]. The work presented in Chapter Five is closely related to this section.

2.2.2.3. Bio-inspired Mechanochromic Coatings

BVID can pose different risks to structural integrity, as discussed previously. A recent development is bio-inspired mechanochromic coatings, which minimise these risks, reduce inspection time, and provide live information on the condition of a material. In response to

external stimuli such as impact strikes, these mechanochromic materials produce optical signals (changes in transparency, fluorescence and colour), giving users a direct and eye-detectable indication of damage [60]. Many technology applications are possible with these self-reporting coatings, including SHM in the aeronautics, automotive and construction industries, and as sensors to inspect mechanical events such as impact [61,62]. The next section introduces bio-inspired composites and discusses how they can improve impact damage tolerance and visual inspection.

2.3. Bio-Inspired Design

Taking lessons from nature to solve problems in synthetic systems has motivated extensive bio-inspired research in areas as diverse as robotics sensing, optics and architecture [63]. Over the past decades, nature has also been a source of inspiration for developing advanced materials. Despite the evident success of adopting a bio-inspired approach in material design for creating more efficient composite structures with improved mechanical performance, there remain unexplored and challenging opportunities in nature. These opportunities have the potential to initiate a new era of high-performance FRP composites. Specifically, regarding damage mechanisms, bio-inspired design can contribute in two key ways: firstly, by enhancing damage tolerance and secondly, by improving damage inspection capabilities.

2.3.1. How Bio-Inspired Design Can Improve Impact Damage Tolerance?

Research on natural composites has shown a variety of toughening mechanisms that can make a step-change in mechanical performance if applied artificially in the manufacture of bio-inspired composites. Two primary categories of toughening mechanisms are *intrinsic toughening* (resistance to crack growth initiation), which takes place at the crack tip, and *extrinsic toughening* (or shielding), that occurs in the wake of the crack tip and slows down the crack propagation [64]. These mechanisms can act at multiple length-scales, further enhancing the properties of natural composites by enabling energy dissipation at multiple levels. For example, the presence of different materials arranged in alternating patterns within a laminated structure (like hard and soft constituents) helps enhance its ability to withstand damage and increases its overall strength compared to structures made of uniform materials [65,66]. An exemplification of this is the deep-sea glass sponge Monorhaphis Chuni, which features a slender beam-like structure, highly subjected to bending loads. The sponge has a cylindrical laminated structure with layers of hard silica (bio-glass) alternated with layers of soft proteins. The laminated or inhomogeneous nature of the microstructure results in higher resistance to

crack initiation and the occurrence of crack arrest mechanisms, where the latter leads to multiple crack nucleation and sub-critical damage diffusion. In contrast to monolithic silica, the inhomogeneous microstructure significantly improves strength (by 45%) and a ten-fold increase in toughness [67,68]. The presence of both soft and hard materials within a structure leads to a repeating pattern of changes in its elastic properties and, consequently, a periodic variation of crack driving force that decreases in regions with lower elastic moduli. This decrease in crack driving force causes a crack arrest mechanism that enables crack re-nucleation in the surrounding material. In fibre reinforced structures, such a periodic change in elastic properties and hence crack driving force can be achieved by periodically changing the fibre orientation, such as in plywood structures [69,70]. Intrinsic and extrinsic toughening mechanisms introduce significant sub-critical control through diffusion. This prompts stable, greatly dissipative damage processes that safeguard the structure from catastrophic failure, yielding exceptional damage tolerance.

The toughening mechanisms in biological nacre-like structures present a remarkable opportunity to address the inherent brittleness and resulting poor damage tolerance of high-performance FRP composites, particularly CFRP composites. Many studies have explored the use of nacre-like microstructures to achieve pseudo-ductility in CFRPs, aiming to prevent catastrophic failure [71–74]. These studies have mainly focused on replicating the failure mechanisms observed in natural nacre structures, such as crack deflection and damage diffusion, to promote a stable and diffuse failure process, contrary to the highly localised and unstable failure in a conventional CFRP structure. Czel et al. [72] introduced discontinuities along the load-carrying fibres of unidirectional carbon/glass laminates to achieve a gradual failure response.

The excellent fracture behaviour and toughness of bone make it a promising type of structure that can serve as a model for advanced composites. Tang et al. [75–77] conducted combined analytical/experimental studies on the effect of hierarchical patterns on the tensile performance of a self-reinforced polypropylene/carbon fibre polypropylene hybrid composite featuring a single layer of carbon fibre polypropylene sandwiched between two polypropylene tapes. Their results indicated that a ‘pseudo-ductile’ tensile behaviour characterised by stable damage growth could be achieved using tailored hierarchical structures. Mencattelli et al. [78] established a multi-tailored material design framework centred around hierarchical patterns of discontinuities. These patterns were designed to increase damage diffusion (energy dissipation capability) and enhance the impact damage tolerance of a self-reinforced polypropylene/carbon

fibre polypropylene cross-ply structure. It was observed that the locally-tailored regions of the structure create high-energy dissipation paths through which the structure can safely dissipate large amounts of energy without catastrophic failure. Moreover, stabilised damage could propagate at sub-critical levels, enabling the structure to sustain high loads while maintaining its structural integrity. This led to a 90% increase in the energy dissipation capability of the structure compared to a non-engineered baseline structure. In addition, tailored discontinuity patterns were effectively designed to facilitate damage diffusion under impact, delaying the penetration occurrence and augmenting energy dissipation at sub-critical levels compared to the non-engineered structure.

A recurring design that is found both in the animal and plant kingdoms is the helicoidal structure (Bouligand structure), i.e., a multi-layer structure where adjacent layers rotate along a helical screw. Examples of such structures have been found in different plant tissues, algae, fish and insects [79]. Sub-critical damage mechanisms which prevent delamination and fibre failure present a great potential to mitigate the susceptibility of high-performance FRP composites to through-the-thickness loads such as impact. Remarkable improvements in terms of pull-out energy [80], interlaminar fracture toughness [81], residual strength [81,82] and impact resistance [82] can be seen in helicoidal bio-inspired composites, depending on the rotation (pitch) angle between adjacent plies. Grunenfelder et al. [82], Shang et al. [83] and Liu et al. [84] studied the impact performance of bio-inspired helicoidal carbon/epoxy prepreg-composites, compared to cross-ply, quasi-isotropic and unidirectional composites. Even though angles of 7.8◦, 16.3◦, 25.7◦, as well as 10◦ and 18◦, were used for the artificial composites, which exceed the angles found in the mantis shrimp, small-angle-laminates have shown improved residual strength and reduced impact damage [82]. The spiralling of the crack through the thickness of the laminate induced by the helical structure resulted in reduced fibre failure and larger delamination areas [83]. The crack front was thereby spread in-plane and dissipated more energy than quasi-isotropic or unidirectional composites, resulting in a higher toughness [82].

2.3.2. How Bio-Inspired Design Can Improve Impact Damage Inspection?

In recent years, SHM has gradually become a multidisciplinary field of research that seeks novel strategies to improve the lifetime and maintenance of engineering systems. Inspired by the colour-changing abilities of biological skins, the exploration of novel mechanochromic materials has become one of the popular and important research

directions, enhancing the competitive advantages over other smart devices. These bio-inspired mechanochromic materials could generate optical variations (transparency, fluorescence and colour) in response to external stimuli, such as force, providing a direct and eye-detectable visual presentation of environmental variation to the users. This technology has the potential to outperform conventional SHM methods in several ways; firstly, it is wireless and does not need any data acquisition system; secondly, it is light-weight and environmentally friendly; thirdly, it can be applied for online inspection during the system's operation, as opposed to most methods that can only be implemented for post-process inspection, and last but not least, mechanochromic composites can be designed to be both self-reporting and self-healing, which can significantly enhance the durability of the engineering structures [5,60].

Based on their origins, colours can be categorised into the following main groups: (1) *chemical-based* and (2) *physical-based* colours. Chemical-based colours stem from the selective absorption and reflection of specific wavelengths of electromagnetic radiation. Pigments and dyes are prime examples of chemical-based colours. The colour-changing process can occur by incorporating dye-filled materials such as micro-capsules or hollow fibres ruptured upon mechanical excitation (see Fig. 2-6(a)). Alternatively, the polymer or fibre can become 'smart' by adding functional groups that are sensitive to mechanical stimuli (mechanophores). For example, optical changes can be achieved using luminogens that show an aggregation-induced emission (see Fig. 2-6(b)). Physical-based colours are connected to both the shape and refractive index of the material and not to its chemical properties. In fact, physical-based colours originate from how light is scattered and diffracted by random or periodic structures. Fascinating biological-world examples of this group are the colour of peacock feathers and butterfly wings. A prime example of physical-based colours are structural colour materials which vary in line with structural dimensions and refractive indices, so that a single set of materials can produce various colours (see Fig. 2-6(c)). Another interesting colour-changing design are thin-ply composite sensors, where hybrids comprised of fibres with different strain-to-failure ratios are utilised, for example, a carbon layer and a translucent glass layer. The changes in light absorption at the interfacial glass/carbon damaged area can generate a clear visual cue by which damage, such as BVID, can be detected as an early warning to avoid catastrophic structural failure due to hidden damage (see Fig. 2-6(d)). This method is the focus of this investigation and will be discussed in detail in the following chapters. These four methods are discussed in more detail in the following.

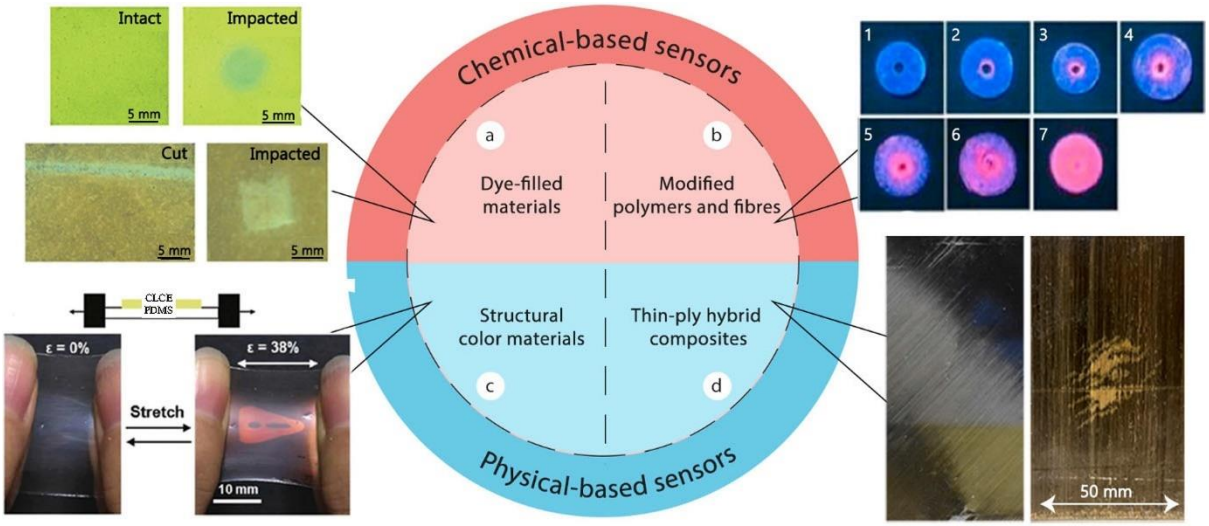

Fig. 2-6: Examples of different bio-inspired mechanochromic approaches for inspection of damage: (a) characterisation of impact damage and cuts in polymer composites prepared with microcapsules, (b) colour-changing process in composites under compression, increasing from left to right, indicating the fluorescent activation, (c) a mechanochromic film which reveals and conceals a pattern by stretching and releasing, working based on the structural colour principle, (d) comparison of the visual damage detection in a structure with (right) and without (left) hybrid composite sensors under the same impact energy [5].

Dye-Filled Materials: Mechanochromism based on dye-filled materials is the first approach in chemical sensors in which a dye-containing agent such as microcapsules is embedded into the desired system, and when experiencing strain, it is ruptured and releases its cargo. One strength of this method is its easy implementation. Double-walled capsules are a new and optimised encapsulation strategy in which one smaller capsule is contained within another larger capsule and shows greater promise for SHM compared to other encapsulation strategies. These coatings should be as thin as possible, which consequently requires efficient design of self-reporting micro-capsule-based materials. To this end, further research on the influence of the capsule material, capsule volume fraction, dispersion, and size and thickness of the shell, on the deformation and mechanical behaviour in different polymers, is needed. Research by Weder's group [85] reported two different methods for preparing micro-capsule-based self-reporting composites that relied on solvatochromic activation schemes. One mechanism was to embed fluorescent poly (urea–formaldehyde) microcapsules containing solutions of a solvatochromic cyanostilbene dye into the polymer matrix. When a composite is damaged, the dye solution is released from the microcapsules, diffuses into the matrix, and the solvent evaporates. Accordingly, the polarity around the dye molecules changes, resulting in a change

in the fluorescence colour. Another method was to blend the dye into a polymer matrix and load microcapsules with a solvent, where the solvent release could trigger the colour change. The applicability of encapsulated solvatochromic dyes was demonstrated through self-reporting the damage under impact loading. Both strategies could provide radiometric signals because the capsules that remain intact or dye molecules that are not exposed to the solvent could be seen as a built-in reference; therefore, a quantitative assessment of the damage inflicted on the material is a priori possible. For example, as showing in Fig. 2-9(b), the emission intensity can be correlated to the impact distance (impact energy). Despite the popular application of micro-capsules as primary dye-filled materials, hollow fibres can be advantageous for some applications, such as FRP composites, when incorporating the dye into a bulk structure. Fundamental and interesting works have been performed by Pang and Bond [86–90]. Developing the "bleeding composites" idea, they introduced a class of dual-function composites reporting damage by visual cues and subsequently healing it. Smart FRP composites equipped with hollow fibres were examined under flexural bending and low-velocity impact tests. Upon the fracture of the functionalised fibres, they released a healing agent into the damaged area. Also, given the fluorescent characteristics of the agent, visual inspection of the BVID could be carried out. Kling and Czigány [91] reported a more efficient dual-function system based on the application of very thin hollow fibres. The proposed SHM system could successfully visualise and heal the impact-induced damage with the help of a UV lamp. A challenge in using microcapsules and hollow fibers is that the healing/reporting liquid inside them can only be used for a limited time and will ultimately be used up. Therefore, the SHM via these materials is often a one-time process. Inspired by the transport in vascular biological systems, scientists have developed vascularised microchannel structured materials. These channels can be used to pump healing/reporting agents into the damaged regions. Unlike micro-capsules and hollow fibres, this design strategy can lead to continual healing of a damaged area. In pioneering works by White et al. [92,93], microchannels in a smart coating were filled with a solution of the monomer dicyclopentadiene to repeatedly heal the formation of the cracks. Nevertheless, the system was not self-reporting. Trask et al. [94,95] placed solder wire with a diameter of 0.25 or 0.5 mm between the composite plies to make the vascularised channels self-reporting. The solder wire was removed by heating the material after curing, leaving behind vascular channels. The resulting system could both monitor and heal the impact-induced damage thanks to a fluorescent dye incorporated into the healing solution.

Modified Polymeric and Fibrous Materials: The second mechanochromic approach in chemical sensors is based on modified polymeric and fibrous materials in which desired mechanophores are added to composites to functionalise them. Aggregation-induced emission- and Spiropyran-based composites are examples of mechanochromism by using functional additives. This method provides a reliable tool for analysing damage progression in FRP composites at the nanoscale. Nevertheless, there are still challenges, especially in processing and applying mechanochromic fluorescent molecules into a polymer matrix, that can be further improved in future studies. Another challenge is that these sensors are responsive to mechanical stimuli and temperature and light excitations, making strain monitoring difficult as the colour change can be due to a combination of mechanical and environmental parameters. Application-wise, this type of sensor has mostly been applied to polymeric structures rather than ceramic or metallic ones. Future studies in this field might involve designing and analysing mechanochromic functionalised polymers with sensitive and hierarchical responses to different types and levels of mechanical stimuli to be used in various engineering materials and systems. Brun's group [94] successfully detected BVID in CFRPs by applying a yellow fluorescent protein at the resin/fibre interface (see Fig. 2-7).

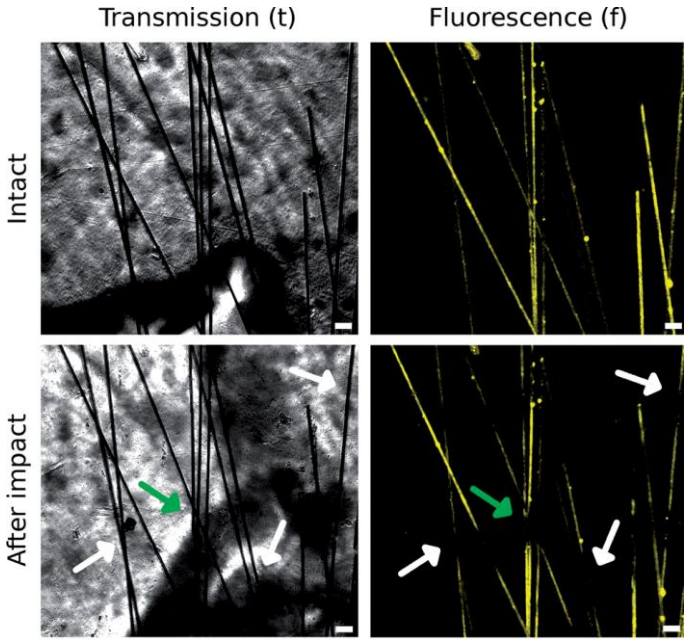

Fig. 2-7: Detection of BVID in CFRP composites by fluorescent proteins. The yellow fluorescent protein stops fluorescing after the occurrence of low-velocity impact damage [94]

The self-reporting of BVID in GFRPs has been studied by Shree et al. [95], who used Spiropyran as a functional self-reporting additive. Spiropyran mechanophores act through a reversible, mechanically-activated ring-opening reaction which converts the colourless and

nonfluorescent Spiropyran into the highly coloured and fluorescent merocyanine. It was observed that the GFRPs modified with Spiropyran could change their colour from yellow to purple due to periodic impact strikes. The number of impact strikes could also be related to the colour gradient (see Fig. 2-8). More recently, Magrini et al. reported the application of Spiropyran mechanophores to design and manufacture tough bio-inspired composites that can report damage. They established a correlation between the tensile deformation and emission intensity of the Spiropyran-modified polymer, leading to visualisation, quantification, and prediction of damage in the composite material before the onset of fracture [96].

Fig. 2-8: The self-reporting of BVID in GFRP/ Spiropyran composites under periodic impact strikes [95]

Such Spiropyran-containing materials offer good potential for microscale SHM applications. Nevertheless, it should be noted that initial high-performance or load-bearing properties of the desired materials are not influenced during the synthesis process. Additionally, some mechanophores can react to different stimuli such as mechanical, temperature- or light-related excitations [97]. In other research, tetraphenylethylene microcapsules were applied as a functional coating to improve the damage visibility of a CFRP composite. Fig. 2-9(a) demonstrates that impact-induced damage was clearly discernible under UV light [98]. Exploiting the concept of aggregation-induced excimer-formation of fluorescent dyes, Weder et al. [99] developed new microcapsules embedded in silicone rubber. The materials were tested under impact, tension and compression loadings. An advantage of excimer-forming chromophores is their mechanical response that provides a straightforward quantitative

assessment of the damage; thus, colour analysis can also be conducted to monitor the system's SHM performance (see Fig. 2-9(b)).

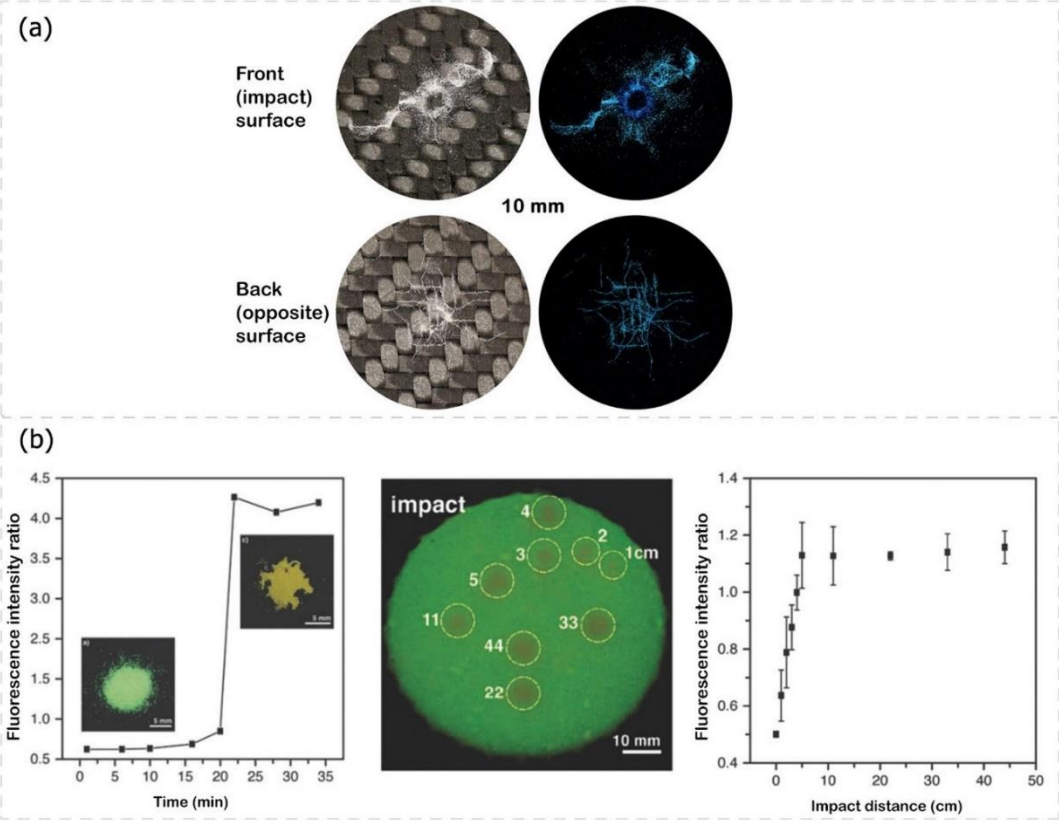

Fig. 2-9: a) Front face and back face images of micro-capsule-based CFRP panels under white and UV light after impact loading, b) SHM of polymer composites containing the excimer-forming dye: from left to right: the excimer:monomer ratio as function of solvent evaporation time after breaking the capsules, photographs recorded under UV illumination of microcapsules impacted by a missile from distances between 1 and 44 cm, the excimer:monomer emission intensities in the same sample recorded at 560 and 497 nm as function of the impact distance [5]

Structural Colour Materials: The colour-changing process in physical sensors, as opposed to the two previous methods, originates from the structural features of the materials. The first approach in physical-based sensors is based on following specific patterns at the nanoscale to manufacture structural colour materials in which the interaction of different wavelengths of light with the structure can produce diffraction and interference in various directions, leading to well-known iridescent colours. Structural colour materials vary according to structural dimension and refractive index; therefore, a single set of materials can produce various colours, making these materials more environmentally friendly than chemical-based colour sensors.

Butterfly and chameleon colourations are natural organisms exhibiting colourful patterning through structural colour materials. The colouration in structural colour materials comes from their structural features, so they represent an eco-friendly alternative to pigments and dyes [100]. Moreover, structural colour created with inorganic materials can tolerate higher temperatures than pigments. At high temperatures, structured colouration therefore appears to offer greater promise than pigmented colouration.

A photonic material with desired optical characteristics can be manufactured by tailoring the structure at the nanoscale, which would not be possible in bulk materials. Photonic crystals possess vivid structural colours, which arise from the selective Bragg diffraction of visible light by their periodic structures [101,102]. This can be explained by Bragg's and Snell's laws [103]:

$$\lambda = 2D(n_{eff}^2 - \cos^2\theta)^{1/2} \qquad (2\text{-}1)$$

where λ is the wavelength of the reflected light, n_{eff} is the average refractive index of the constituent photonic materials, D is the distance of the diffracting plane spacing, and θ is the Bragg angle of incidence of the light falling on the nanostructures (see Fig. 2-10(b)). This equation suggests different methods for tuning structural colour, for example, by changing D, n_{eff} or θ.

Despite remarkable achievements, current structural colour materials still do not represent a scalable and cost-effective manufacturing strategy that can mimic the complex features of natural creatures. Also, their SHM response is mostly angle-dependent, which may hinder the sensor's practical application. Nevertheless, more advanced mechanochromic photonic crystals are anticipated for SHM purposes with scalable manufacture, excellent colour perception and angle-independent colour displays. This research field would benefit from developing image analysis software for the real-time evaluation of membrane colour changes [100].

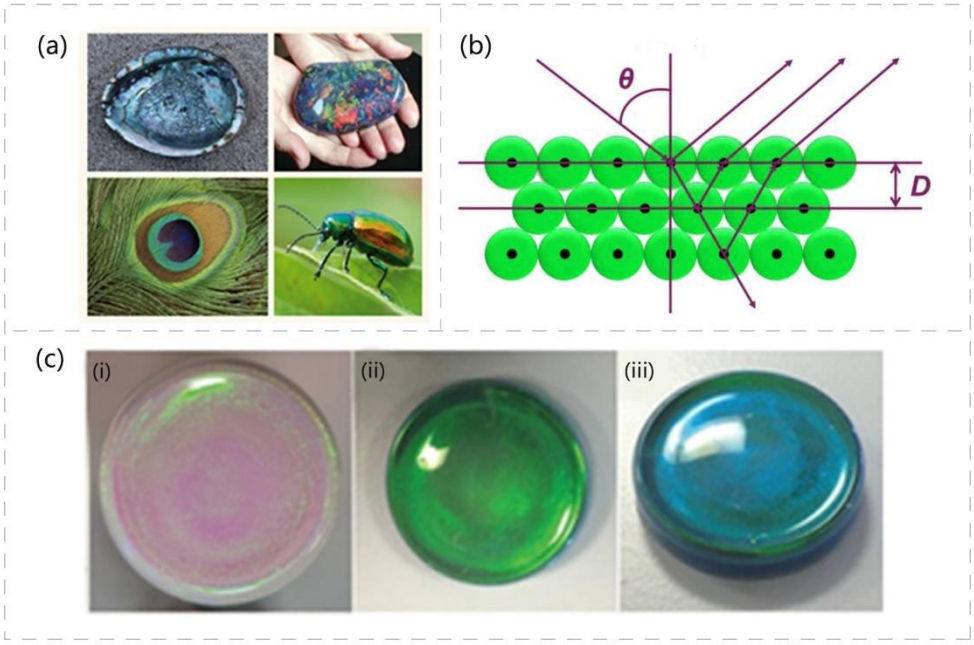

Fig. 2-10: a) Examples of natural structural colour: (clockwise from top left): mother-of-pearl, an opal, a beetle and a peacock feather [104], b) incident light with a wavelength predicted by a modified Bragg-Snell equation undergoes diffraction when propagating through a photonic crystal [103], c) colloidal photonic crystals: (i) top-view of a pristine photonic crystal; (ii) top-view of a graphene-based photonic crystal; (iii) the same graphene-based photonic crystal from a different viewing angle (which shows the angle-dependency of opal photonic crystal) [105]

Inspired by the colour-tuning behaviour of natural photonic crystals, scientists have developed artificial photonic crystals that can change their colour under different stimuli such as electricity, heat, light, and strain. Mechanical stimulus provides the most efficient colour change compared to other stimuli [106]. Photonic crystals have a broad application as mechanochromic sensors in SHM of engineering structures, and for this purpose, they should be attached to the substrate material. However, conventional photonic crystals are made of hard materials which are only elastic up to a few percent strain, and the stop-band shift with mechanical deformation is not large enough to enable optical detection by the naked eye. To address this, polymer-based photonic crystals are swollen with a low-molar solvent to form photonic gels with extreme elasticity [107]. However, gels rely on solvent-induced swelling which can cause challenges [106]. Much effort has been made to improve photonic gels, as the latter show high sensitivity to mechanical stimulation and can, therefore, act well as

mechanochromic sensors. For example, a plasticised photonic gel has proved to be responsive to various mechanical deformations, such as uniaxial tension and shear (see Fig. 2-11(a), (b), (c)). The mechanochromic response of a photonic gel under uniaxial compression loading was demonstrated in research by Chan et al. [108], where contact mechanical testing was conducted to characterise the applied compressive strain, stress and contact area. Given the spherical shape of the indenter, an axisymmetric strain field was developed within the contact area of the gel, which was captured by the local colour changes, see Fig. 2-11(d). Fig. 2-11(e) illustrates another SHM application of structural colour films. Here, a sensing layer made of a block copolymer and an ionic gel embedded in a polymer medium was sandwiched between ionic hydrogel electrodes, enabling complete visual monitoring of strain up to 100% [109].

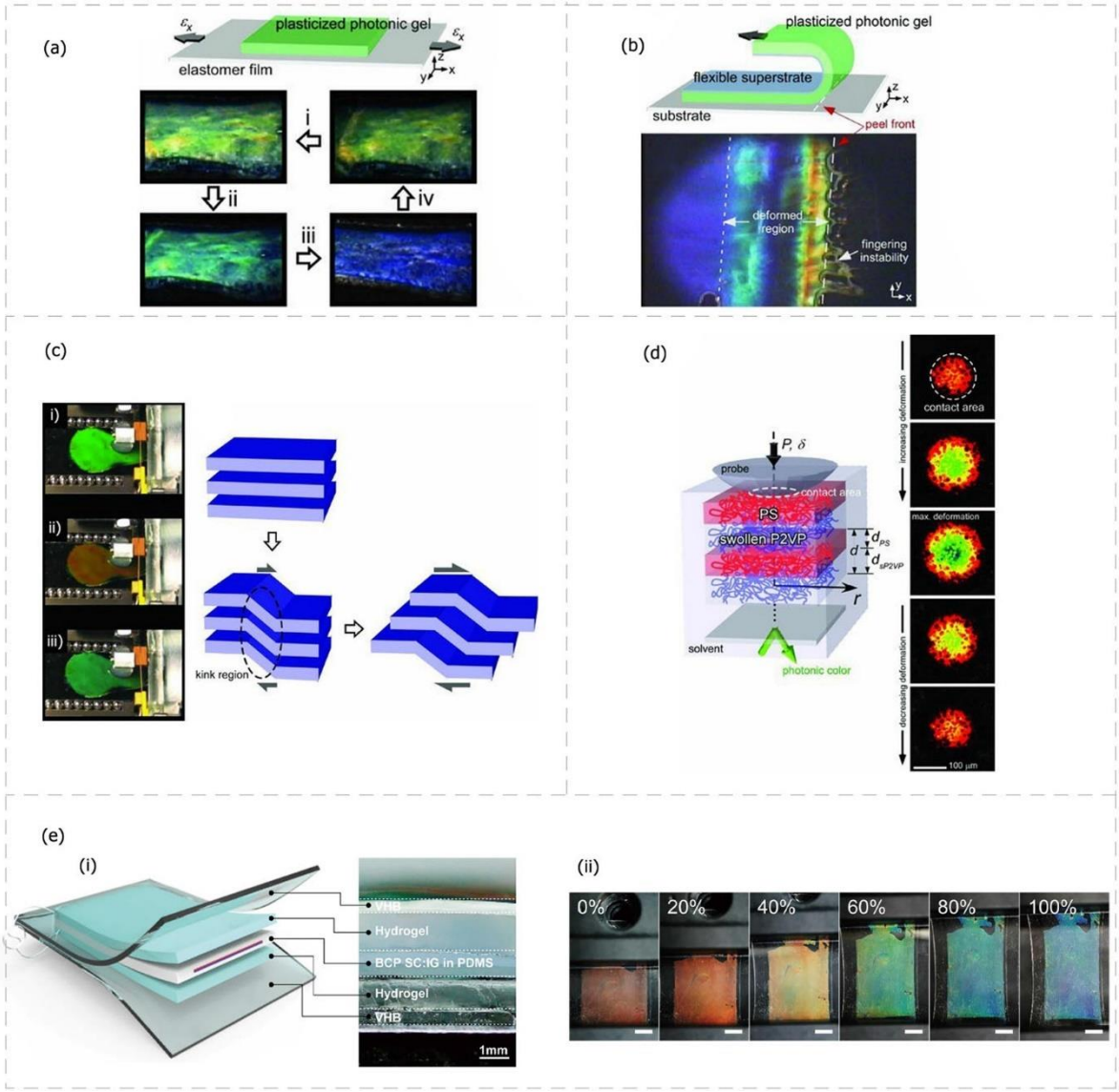

Fig. 2-11: Mechanochromism of photonic gels under different mechanical stimuli: a) uniaxial tension, b) peeling, c) shear, d) uniaxial compression [108], e) a strain sensor based on a block copolymer structural colour film [109]

Despite great progress in developing structural colour materials, they remain in the laboratory due to their complex nature, so their applications in the real world are limited. Furthermore, its application in impact-damage inspection has not been widespread to date. However, the mentioned examples suggest that structural colour materials, in the form of coated films, are promising as mechanochromic sensors to detect different types of damage in composite structures.

Hybrid Thin-Ply Glass/Carbon Sensors: The second physical-based mechanochromic method is related to the composite hybridisation concept. Strong potential for demonstrating pseudo-ductility while maintaining high performance in unidirectional composites was shown by Wisnom et al. [1,71,110,111] using emerging thin-ply prepregs to suppress delamination in interlayer hybrid configurations. The main focus of researchers investigating thin-ply composites was to explore the change in damage modes due to more dispersed lay-up designs [112–114]. Their main conclusion was that the onset of damage is delayed in thin-ply composites because premature matrix cracking and delamination can be suppressed due to the low-energy release rate of thin plies in static loading, but the final failure generally becomes more brittle. Thin-ply laminates also show less interlaminar but more fibre damage under impact [115]. When demonstrating pseudo-ductile behaviour in thin interlayer glass/carbon-epoxy hybrid composites, a pattern was observed by Czél and Wisnom [71] during the gradual failure of the specimens. The translucent nature of the constituent glass-epoxy layers made delamination detection possible to the naked eye. It was realised that this could be used to sense damage on the surface of a structure.

The manufacturing process of this method is simpler than the previously discussed strategies, and the so-called hybrid composite sensor can act as both a sensing and a repairing or reinforcing system. Also, these sensors can be designed to be direction-dependent. Glass/carbon hybrid sensors are simple and easy to implement, making them attractive for visual inspection. Since the research presented in this study is centrally concerned with this method, a more in-depth review of recent literature in this field is presented.

Thin-ply hybrid composite sensors are made using commercial prepregs, and the sensing mechanism is activated by fracture of the sensing layer. Different types of failure in a three-layer unidirectional hybrid laminates made from high- and low-strain-materials are shown in Fig. 2-12. Damage and failure mechanisms lead to a visual indication of strain overload, where delamination is suppressed, and several low-strain fractures occur, followed by stable localised pull-out, see Fig. 2-12(c). This is achieved by choosing appropriate material properties, relative low-strain-material to high-strain-material thicknesses, and absolute thickness of the low-strain-material [111].

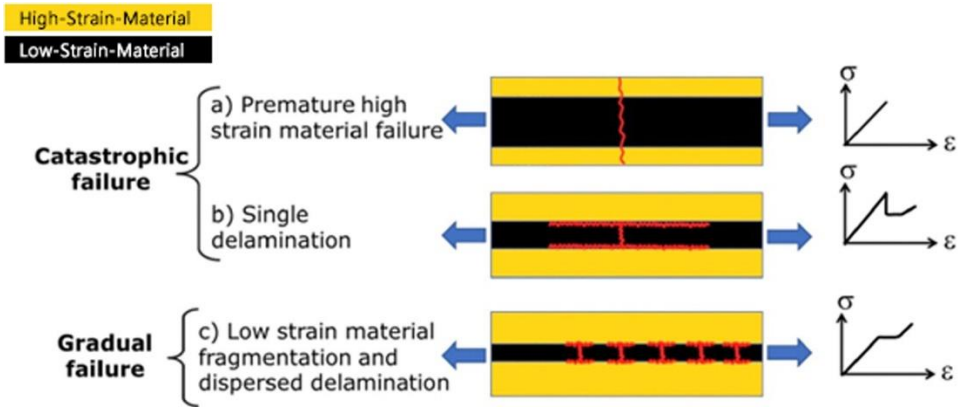

Fig. 2-12: Different failure mechanisms in a three-layer unidirectional hybrid composed of high-strain material and low-strain material (red lines indicate fracture) (a) single crack through the whole specimen, (b) single crack in the low-strain material followed by instantaneous delamination, and (c) multiple fractures and localised stable pull-out of the low-strain material [116]

Fig. 2-13 shows two different designs of the unidirectional hybrid composite sensors, where the visual change is achieved by a purpose-designed, thin interlayer of glass/carbon-epoxy hybrid composite loaded by a predefined strain value [116]. Light passes through the translucent glass layer and is absorbed by the intact carbon layer, creating a dark appearance. Fig. 2-13(a) shows the fragmentation of the low-strain material followed by gradual, dispersed delamination [117]. The incident light is reflected from the locally damaged glass/carbon interface around the carbon layer fractures, creating light stripes. Fig. 2-13(b) shows another type of failure in thicker carbon layers: a single fracture of the low-strain material is followed by sudden delamination [118]. Both can act as good overload indicators since it is easy to monitor the delamination through the translucent glass layer visually.

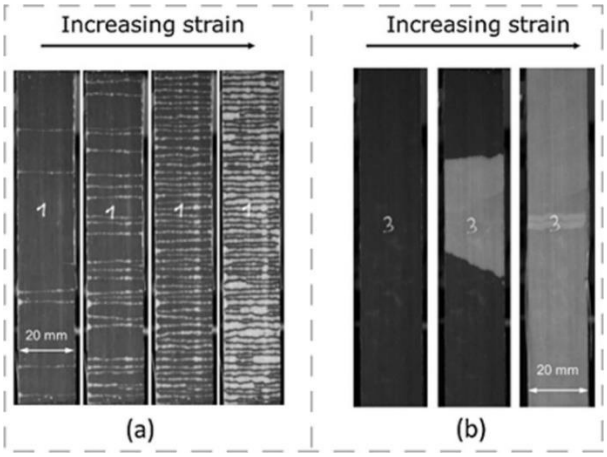

Fig. 2-13: Visual indication of damage in thin-ply glass/carbon hybrids: (a) carbon layer fragmentation followed by stable, dispersed delamination. (b) carbon layer fracture followed by sudden delamination [5]

Hybrid sensors can also be used for fatigue life monitoring, where an increase in the delamination area can be correlated to the number of cycles, as shown in Fig. 2-14 [117].

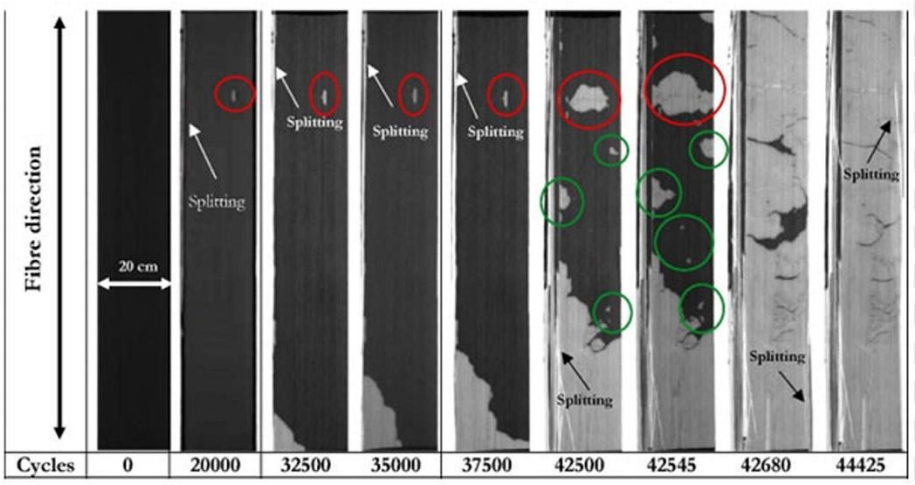

Fig. 2-14: Fatigue life monitoring in a unidirectional thin-ply glass/carbon hybrid composite at 90% stress level of the carbon fragmentation initiation [117]

Multidirectional pseudo-ductile thin-ply hybrid laminates with improved ductility and notch insensitivity have also been developed [116,119]. These multidirectional laminates showed damage mechanisms similar to those of the unidirectional laminates. However, they can monitor damage evolution, as the damage can be observed around the notches before any catastrophic failure occurs, as shown in Fig. 2-15.

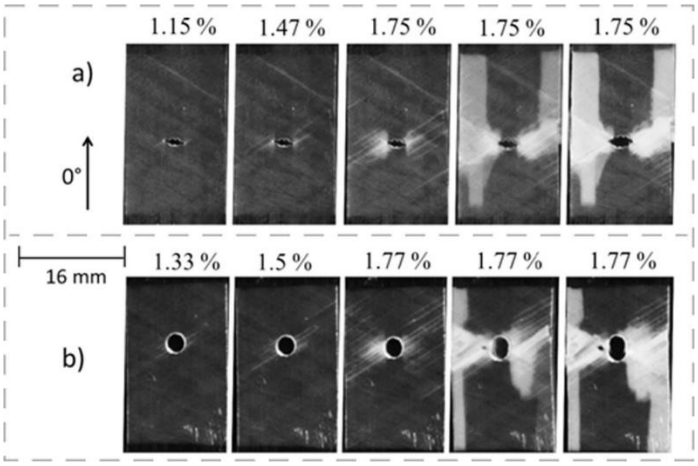

Fig. 2-15: Visual indication of damage in (a) sharp notched and (b) open-hole ± 60QI/Hexcel laminates at different strains in tensile test [116,119]

Typically, hybrid composite sensors are bonded directly onto the structures' surface or incorporated into the structure as a sensing layer. Combining different sensing materials activated at different strains can provide a more detailed picture of the overload. Also, the overload direction can be monitored by designing an array of sensors orientated in various directions. A sensor mounted on a component is anticipated to be subjected to the same strains as the material below. In this case, carbon and glass layers serve as the 'sensing' and 'outermost' layers. Unlike other mechanochromic systems reviewed in previous sections, the simplicity and practicality of glass/carbon hybrid sensors have led to their relatively rapid use in SHM [5]. For example, a set of short and long sensors made of single-ply XN80/EPOXY were applied on some commercially available CFRP bike handlebars, and both handlebar structures with and without sensors were tested under a three-point bending load. Fig. 2-16 shows the force-displacement response of the tested structures; here, the activation point for long sensors is between 1500 N and 2000 N. The graph also shows the load (1000 N) prescribed for testing Racing Bicycle handlebars according to the European Standard (EN14781) [120]. The results of this test suggested that sensors did not induce any noticeable increase in stiffness.

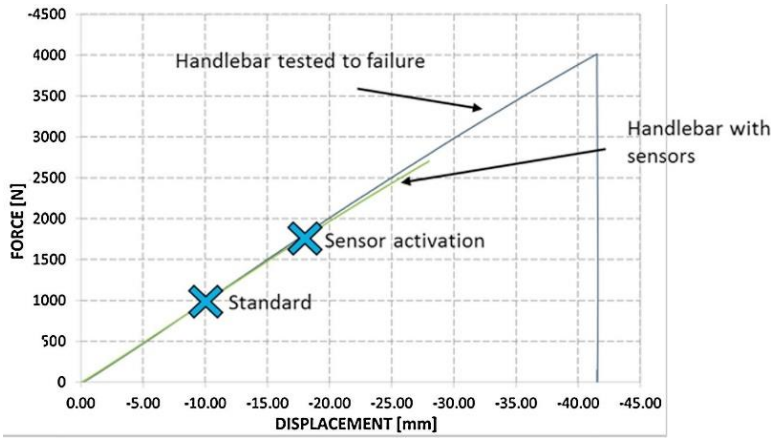

Fig. 2-16: Force-displacement response of the tested CFRP bike handlebars [120]

Fig. 2-17 illustrates a handlebar equipped with both short and long sensors. Here, the first fracture of the long sensor was observed at 1750 N. The self-reporting concept could be successfully achieved using long sensors, warning the user that a critical loading condition had occurred.

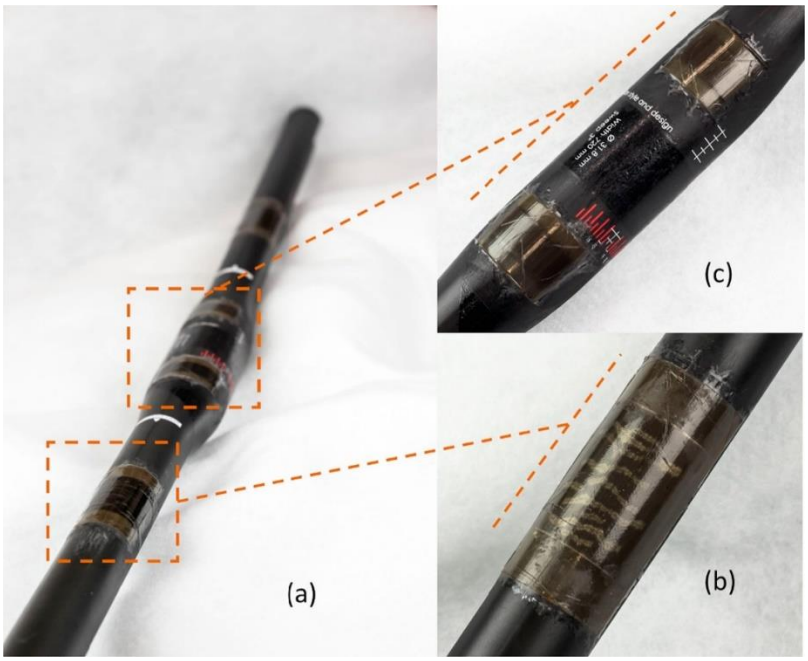

Fig. 2-17: Bike handlebar equipped with hybrid composite sensors. (a) MTB Racing flat handlebar, fitted with (b) long and (c) short sensors [120]

A bonded composite patch is used to repair cracks in aluminium panels used in aerospace structures. However, in the case of standard repair techniques, damage beneath the repair patch cannot be detected by simple visual inspection alone. Therefore, hybrid composite sensors can be used as a composite repair patch to self-report critical situations, e.g., an overload or crack

extension in the substrate. As discussed, these sensors are designed not to change the local strain distribution. Nevertheless, in the case of a repair patch, it is necessary to have enough stiffness so that the load in the substrate damaged area is reduced and carried instead by the patch. The practicality of the concept was investigated by applying a hybrid composite sensor on an aluminium panel with a 20mm initial crack length (see Fig. 2-18) [121].

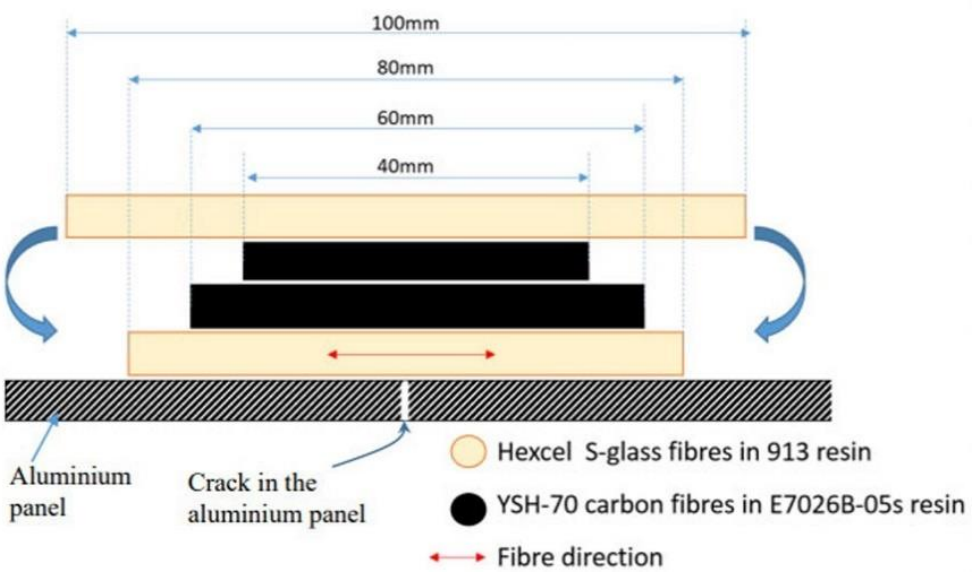

Fig. 2-18: Schematic of hybrid composite repair patch [121]

During the quasi-static tensile test, changes in appearance were evident above the threshold load in the repaired specimen (see Fig. 2-19). By overloading the specimen, crack propagation began beneath the repair patch. Fig. 2-19 shows a change of appearance due to delamination induced by fractured carbon at the centre of the specimen (above the crack), demonstrating the self-warning ability of the repair patch.

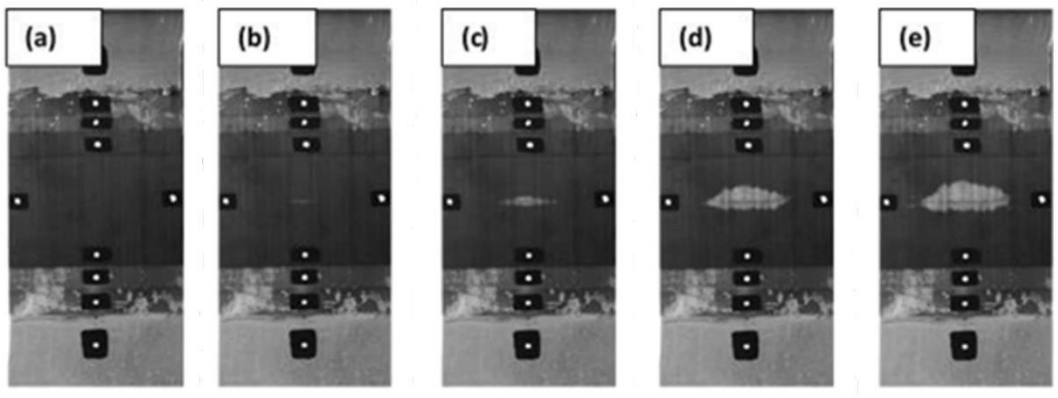

Fig. 2-19: Self-reporting hybrid composite sensors subjected to increasing loads: (a) 195 MPa; (b) 197 MPa; (c) 304 MPa; (d) 336 MPa; (e) 340 MPa (99 % failure load) [121]

A summary of all four mechanochromic strategies is provided in Table 2-1. It should be mentioned that the information provided for each method is relative to the other methods. For example, while there may be reports of reversible visual signals in dye-filled materials compared to other methods, it is fair to mention that mechanochromism based on dye-filled materials is not reversible.

Table 2-1: Summary of mechanochromic approaches

Mechanism	Colour origin	Functionalities	Specifications and challenges	Visual signal
Dye-filled materials	Chemical	Self-reporting Self-healing	**Specifications** - easy manufacturing - macro-scale SHM **Challenges** - leakage and diffusion of the encapsulated core - shelf-life and optimal capsule size and volume fraction	- requires UV light - not reversible - angle-independent - neither repeatable nor continual monitoring (encapsulated coatings) - repeatable and continual monitoring (vascular channels)
Modified polymers and fibres	Chemical	Self-reporting Self-healing	**Specifications** - better SHM by using functional materials such as Spiropyran-based additives - implementing AIE method by physical and chemical linking manufacturing strategies - nano, micro, and macro-scale SHM **Challenges** - challenging synthesis process - multi-responsiveness (excited by light, heat, force, etc.) - molecular diffusion and phase separation process (physical-linking strategy) - detailed SHM over desired structures' regions but complex manufacturing (chemical-linking strategy)	- requires UV light - reversible - angle-independent - repeatable and continual monitoring
Structural colour materials	Physical	Self-reporting Self-healing	**Specifications** - eco-friendly - high-temperature tolerance - manufacturing in the form of gels and hydrogels by adding solvents - better SHM by adding graphene or coloured platelets - micro and macro-scale SHM **Challenges** - complex manufacturing - scalability for large structures	- requires UV light - reversible - angle-dependent - repeatable and continual monitoring
Glass/carbon hybrid composites	Physical	Self-reporting Load carrying	**Specifications** - easy manufacturing - macro-scale SHM **Challenges** - limited strain monitoring range - thermal compatibility of sensing and substrate layers	- does not require UV light - not reversible - angle-independent - not repeatable but continual monitoring

2.4. Challenges and Future Path

Visual inspection offers several advantages over other NDE methods. For example, it does not require high-tech and expensive testing facilities or advanced testing setup, and its testing instruments are portable. Moreover, it is easy to train while providing fast inspection with reliable accuracy for surface damage. Nevertheless, there are some challenges in visual inspection of impact damage that can be addressed in future research. These challenges can be classified into three primary groups: accessibility, visibility, and human dependency [11,122].

Inspection of very large or geometrically complex structures in hazardous environmental conditions in real-life applications can be challenging because there should be access to critical parts of the structure to have a direct observation. For example, access to damaged areas in wind turbine blades through the small passages or openings can pose health and safety risks to the inspector. Also, the whole system should sometimes be shot down or disassembled for a thorough visual inspection of a specific area, causing downtime and expenses. A viable method to deal with access restrictions that limit the inspection view is to use remote visual inspection and optical aids tools such as UAV, magnifying devices, microscopes, borescopes, video scopes, and thermal imaging cameras. This equipment can improve inspection safety, efficiency, and accuracy in various industries, including manufacturing, aviation, energy, and healthcare, particularly in difficult or dangerous areas. Another concern is that using such technologies might be expensive. Therefore, an area for future work would be to develop remote visual inspection strategies and devices that are both cost-effective and reliable, allowing for visual inspection of hard-to-reach or hazardous areas without requiring direct access by an inspector.

Another major challenge of visual inspection, especially for impact damage detection, is damage visibility. The application of this method is mainly limited to the inspection of surface damage, and sub-surface damage cannot be monitored unless the structure has a transparent/translucent surface and the damage is large enough to be visually detected. Even in translucent materials such as glass fibres, in thick or painted sections, or where the surface layer has lost the resin due to environmental conditions, detecting and evaluating the severity of impact damage is complicated. In addition to the difficulties due to a small and barely visible damage pattern, surface illumination can also cause challenges in damage visibility. For example, shadows, glare, or uneven lighting conditions can obscure impact damage areas, making visual inspection difficult or impossible. In such cases, care should be taken to adjust

the light source at an angle that minimises glare, shadow or uneven lighting. Moreover, additional tools such as borescopes, magnifiers, or microscopes can be used to perform a more detailed and accurate visual inspection.

As discussed, permanent indentation or dent depth is a well-known impact damage metric. However, this cannot provide much information about the severity of the damage. Also, dent depth could be influenced by different parameters such as impactor shape and can decrease over time due to fatigue and humidity due to viscoelasticity. [25]. In some cases, the initial dent depth just after impact is three times greater than at the end of life. To make it even worse, the dent depth decrease over time can also vary in different materials [25]. Some papers in the literature report that higher energy impact damage from a larger diameter hemispherical object results in damage with a lower depth and greater delamination than lower energy impact damage from a smaller diameter object [123]. Therefore, BVID sizing tests should be carried out at end-of-life dent depth to use permanent indentation as a reliable damage metric. Also, visual inspection detection thresholds such as BVID must not be considered in terms of either dent depth or width alone. At the minimum, both the indentation width and depth are required to determine detectability thresholds. In general, for the most part, visual inspection can only detect visible impact damage, and BVID might be left undetected. A potential route for future studies might be developing smart coatings that can generate larger and more visible damage patterns. This can be achieved by managing the damage mechanisms on the surface layer through the proper design of the smart coating layer (bio-inspired self-reporting coatings) [5]. This will be studied in Chapters Three, Four and Six of this thesis.

Finally, a serious limitation of visual inspection stems from its dependency on an inspector, meaning that depending on the experience, age, gender, eyesight, mood, diligence, competence and fatigue of the inspector, results may vary significantly, leading to missing or wrongly identifying BVID. To mitigate such problems, new SHM methods can be developed by combining visual inspection with other NDE techniques, especially by automating the inspection process using machine learning algorithms. This can also help move from a qualitative to a quantitative and more accurate impact damage assessment. This will be studied in the fifth chapter of this thesis.

2.5. Summary

Visual inspection is a fundamental technique for ensuring the safety and reliability of composite structures, particularly in aerospace applications. It involves visually examining the surface of the composite structure for signs of impact or other forms of damage. Permanent indentation, delamination, cracks or other anomalies can indicate areas of concern. This chapter outlined the fundamental principles of visual inspection, encompassing aspects such as damage metrics, various inspection levels and their relationship with different types of impact-induced damage, alongside essential parameters for effective inspection. Subsequently, recent progress in this field was discussed, including remote visual inspection, AI-based inspection methods, and bio-inspired mechanochromic coatings (sensors) to enhance visual inspection capabilities. Furthermore, a brief overview of bio-inspired composites was presented, particularly focusing on their roles in improving impact damage tolerance and inspection techniques. The latter was further detailed into four types of bio-inspired mechanochromic approaches, with particular emphasis on the hybrid thin-ply glass/carbon composite sensors as the primary focus of this investigation.

Chapter 3

Design of Hybrid Glass/Carbon Sensors: Methodologies

3.1. Introduction

This chapter outlines the procedures and methodologies employed in the experimental testing, as well as the analytical and finite element analysis (FEA) aspects of this investigation. The experimental section involves conducting a series of quasi-static indentation and drop tower impact tests on composite specimens, both with and without attached hybrid sensors. A detailed assessment of damage evolution is performed using non-destructive techniques such as ultrasonic C-scan and visual inspection. In the analytical and FEA section, a new analytical formulation is developed to estimate the delamination threshold load, complemented by simplified finite element models, to provide an accurate and computationally efficient platform for designing and analysing hybrid composite sensors.

3.2. Design Principles of the Sensor

Wisnom and colleagues [1] reported that well-designed thin-ply hybrids can develop multiple fractures of the higher modulus/lower strain constituent. This characteristic enables them to evade catastrophic failure and unstable delamination, thanks to the low-energy release rate primarily influenced by the thickness of the stiffer component layer within the hybrid structure. For example, in thin-ply glass/ultra-high modulus carbon hybrids, the cracks and delamination in the carbon ply are visible to the naked eye due to the translucency of the glass/epoxy plies. This study's idea for designing hybrid sensors is based on a unique characteristic of the thin interlayer glass/carbon hybrid composites: a visible colour change occurs when subjected to strains surpassing a predefined threshold. As the sensor is applied onto the surface of the structure, it experiences similar strains as the underlying material. It comprises a carbon sensing layer and an outermost glass layer. As shown in Fig. 3-1, a *Reference* specimen (without a sensor) absorbs the light after being subjected to an impact load, indicating a dark appearance. In the *Sensor* specimen, on the other hand, after the impact, when the strain goes beyond the failure strain of the carbon sensing ply, the carbon ply develops multiple fractures, reflecting

the light from the damaged glass/carbon interface around the fractures in the carbon layer, making the damage visible.

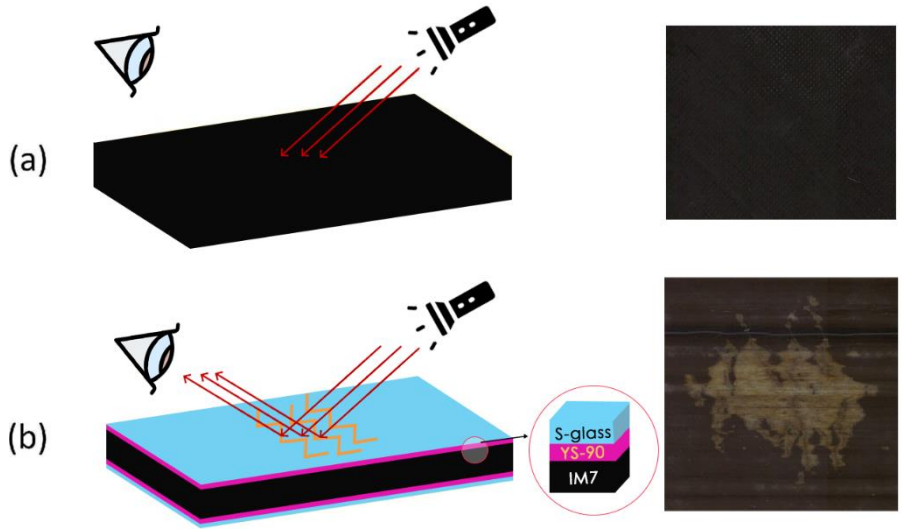

Fig. 3-1: Schematic of (a) a reference specimen and (b) a sensor-integrated specimen, showcasing the sensor's working principle and configuration (left). The images on the right show the post-low-velocity impact surface of the specimens, highlighting the mechanochromic function in the sensor-integrated sample [120]

Hybrid composite sensors can be designed considering different parameters that control the damage mechanisms, i.e. fibre fragmentation and/or delamination. These include the sensor material strain to failure, thickness, stacking sequence and critical energy for delamination initiation. For example, different values of the sensor-to-substrate stiffness ratio can be achieved by either changing the thickness of the layers or using different composite prepreg materials. Another critical design parameter is the failure strain of the carbon sensing layer that controls the sensor activation time and strain threshold. The design of hybrid sensors for monitoring impact damage, i.e., selection of the thickness, materials, and lay-up, can be done by calculating the critical load levels for the three failure mechanisms of mid-plane delamination, impacted face compressive fibre failure, and back-face tensile fibre failure in a laminate under low-velocity impact.

In a laminated composite structure composed of different orthotropic layers under flexural loading through the thickness, plies with different fibre orientation tend to deform differently due to the bending stiffness and bending-twisting coupling effect. Normal (i.e., normal to the plane of ply) and shear stresses are developed at the interface between plies with different orientations. As the flexural deformation increases, these interlaminar stresses increase and

exceed the critical values, causing delamination initiation. Despite shear and tensile matrix cracking, delamination leads to a high level of energy release rate, which can cause a sudden load drop in the load-displacement graph (see Fig. 4-2). The critical load for initiation of midplane delamination (F_d) can be calculated using equation (3-1) [124,125]:

$$F_d{}^2 = \frac{8\pi^2 E t^3 G_{IIC}}{9(1-\vartheta^2)} \tag{3-1}$$

where E, t, ϑ and G_{IIC} are bending modulus, thickness, Poisson ratio , and critical strain energy in mode II delamination, respectively. Therefore, the load associated with delamination initiation depends not only on the thickness ratio ($t^{1.5}$) but also on the critical energy release rate ($G_{IIC}{}^{0.5}$) and Young's modulus ($E^{0.5}$) of the laminate.

Generally, fibre failure occurs much later in the fracture process than matrix cracking and delamination, which is considered a sign of plate perforation. There are two types of fibre failure, which are the result of compressive and tensile loads. Compressive fibre failure occurs on the impacted side, where contact and compressive bending stresses dominate. On the impacted side, both normal stress and transverse shear stress may be responsible for the fibre failure. On the other hand, tensile fibre failure occurs on the back face of the laminate (opposite side of the impact), where the tensile bending stresses are high. Delamination is identified as the most critical damage mode in composites exposed to transverse impact. Since this study focuses on low-energy impact energies that cause BVID, delamination is of significant interest here. Moreover, the results of research by Hallet et al. [4,16] on quasi-isotropic composite laminates with similar materials, stacking sequence, and geometries to those of this study showed that under static indentation and low-velocity impact, delamination always occurs before both back-face tensile fibre failure and impacted side compressive fibre failure. In this case, delamination will be the baseline for designing hybrid composite sensors for this study. Therefore, the idea is to prevent mid-plane delamination damage as the first damage mode and instead trigger fibre failure in the low-strain sensor material (carbon sensing layer) as the first active mode.

The sensor can be integrated by either co-curing or retrofitting by bonding onto finished parts. Depending on the curing temperature of the sensor and substrate prepreg materials, the co-curing itself can also be done through either a one-step or a two-step curing procedure. By co-curing, the sensor acts as a structural sensing layer, while by retrofitting, it acts as a discrete sensor on the structure. It should be noted that the thickness of the sensing material must be

thin enough to exhibit failure with fragmentation and dispersed delamination. This was studied in detail in a work by Jalalvand et al [110], where a damage mode map was developed using numerical damage analysis of hybrid glass/carbon composites with different thicknesses of the carbon layer (see Fig. 3-2).

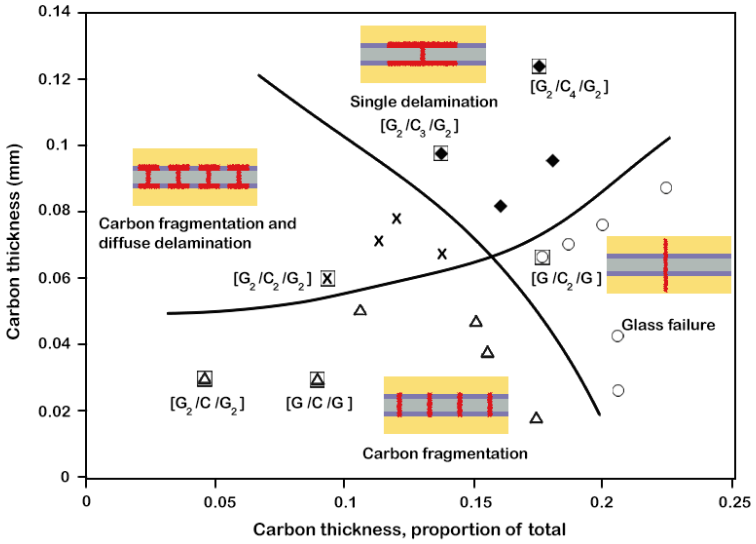

Fig. 3-2: Categorisation of different damage modes as a function of absolute and relative thickness of carbon layers [110]

3.3. Experiments

3.3.1. Materials and Manufacturing

Two main groups of composite specimens were manufactured, including reference (*Reference*) and sensor-integrated (*Sensor*) laminates. According to the prepreg type, each group was subdivided into two additional groups (see Fig. 3-3). The *Reference* laminate had a quasi-isotropic stacking sequence, $[45/0/90/-45]_{4s}$, made of either a unidirectional IM7 carbon/8552 epoxy or a unidirectional IM7 carbon/913 epoxy prepregs. The direction of unidirectional fibre orientation that runs parallel to the longer side of the plate is considered as 0°. Each sensor consisted of a single layer of YS-90A carbon prepregs placed between the core laminate and a single layer of S-glass/913 epoxy prepreg with a 90° orientation. Some *Sensor* samples featured a discontinuous carbon sensing layer, meaning that this layer had intentional cuts (represented in the rest of the chapter as *Sensor with cuts*). The motivation behind introducing these cuts was to facilitate delamination in the sensing layer to occur at a strain level lower than the strain to failure of the carbon layer, therefore ensuring that delamination is the initial mode of damage observed in the sensor. Moreover, to investigate the influence of the fibre orientation of the

sensing layer, different fibre directions were used in carbon sensing ply of *Sensor* samples. According to the ASTM D7136 standard test method, all samples were manufactured with dimensions of 100mm*150mm. For a better understanding of the sample classification, Fig. 3-3 summarises all the specimens manufactured for the tests in this chapter.

All composite specimens were fabricated using the conventional process of prepreg composite manufacturing. Following hand lay-up, a standard bagging method was applied on a flat aluminium tool plate. Additional silicone sheets were placed on top of the laminates to ensure a smooth top surface and an even pressure distribution in the autoclave. The laminates were cured in an autoclave at the recommended temperature and pressure cycle. After initial testing, it was found that the indentation test results were highly repeatable. Therefore, one sample for each indentation test and two for each impact test were manufactured.

For *Sensor* samples with IM7/913 prepreg, the sensor and the substrate were co-cured in a one-step process, while for *Sensor* samples with IM7/8552 prepreg, due to different curing temperatures, the substrate was manufactured first, followed by applying the sensor onto the substrate (both sides) and co-curing the entire structure under the curing temperature required for the sensor. These two manufacturing methods allowed for investigating the influence of different attachment methods on the properties and potential applications of the laminates. Specifically, the separate application of the sensor (the two-step curing process) could potentially broaden the range of applications for which these laminates could be used.

The curing cycle for the co-cured plates, consisting of the substrate laminate (IM7/913) and the hybrid sensor layers, was 60 minutes at 125 °C, with 0.7 MPa applied pressure. In the other group (IM7/8552), the substrate was initially cured at 110 °C for 60 minutes, followed by 180 °C for 120 minutes under a constant 0.7 MPa pressure. Then, on the next day, a second curing procedure for 60 minutes at 125 °C, with 0.7 MPa applied pressure, was conducted. These were used according to the recommended curing cycles for IM7/8552, IM7/913, and S-glass/913 prepregs [125,126]. Fig. 3-4 shows the manufacturing process followed in this study. After conducting low-velocity impact tests, some impacted samples were cut to examine the internal damage at the cross-section under the microscope.

Table 3-1: Cured ply properties of the prepregs [7,125,127]

Prepreg	Cured ply thickness (mm)	Strain to failure (%)	Tensile modulus (GPa)
IM7 carbon/8552 epoxy [125]	0.125	1.6	161
IM7 carbon/913 epoxy [127]	0.095	1.6	163.2
S glass/913 epoxy [127]	0.153	3.7	45.6
YS-90A carbon/epoxy [7]	0.070	0.5	520

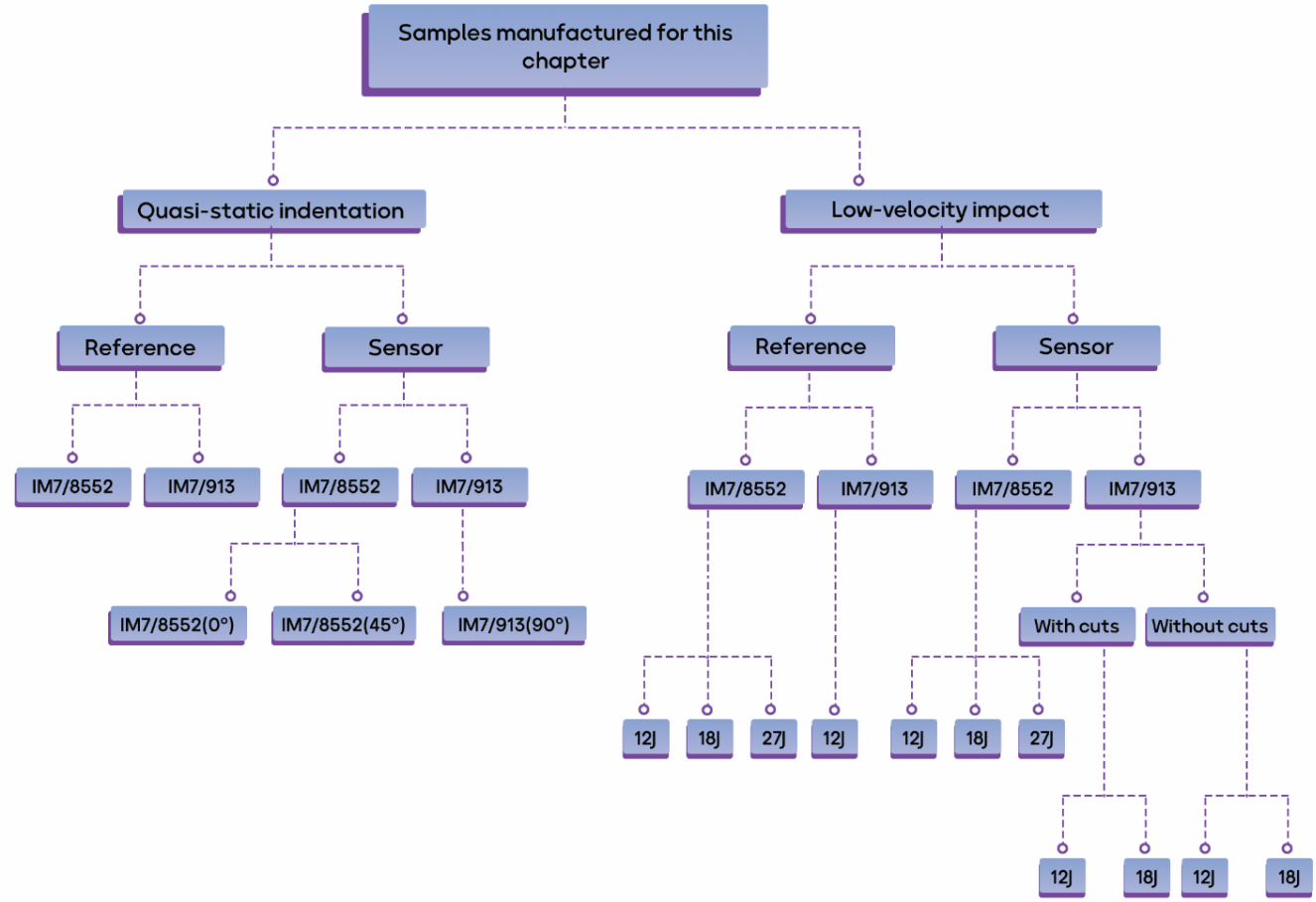

Fig. 3-3: Schematic overview of samples in Chapter Three. Sensor samples using IM7/913 prepreg underwent one-step curing, while those with IM7/8552 prepreg underwent a two-step curing process. The fibre orientation of the sensing layer in all samples manufactured for impact tests is 90°.

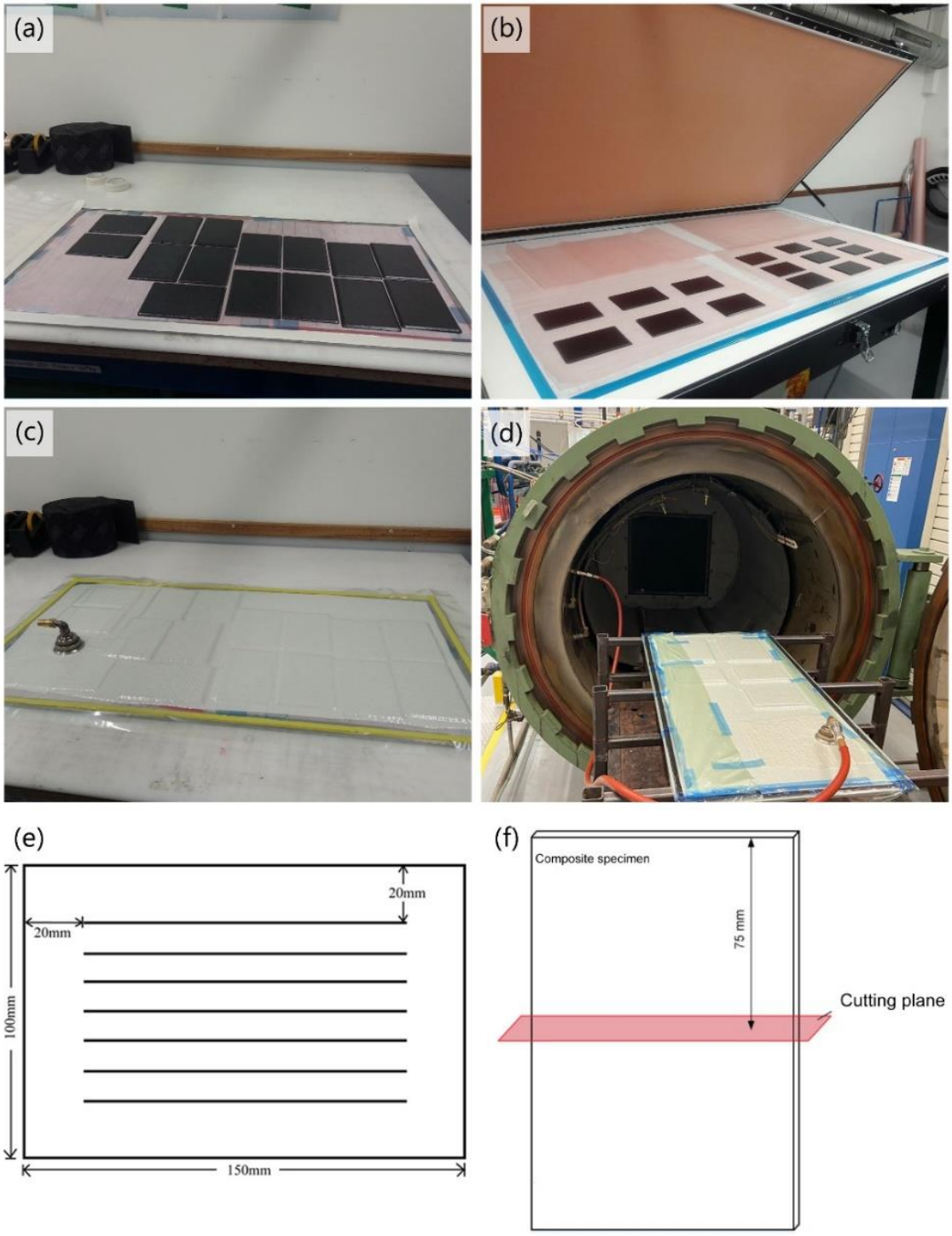

Fig. 3-4: Manufacturing process: a) cutting the prepregs into standard specimen size and stacking the layers, b) applying pressure after stacking every four layers to ensure there is no air or bubbles, c) completing the vacuum-bag lay-up, d) curing at autoclave under desired temperature and pressure, e) schematic of cuts in the carbon sensing layer, f) cutting plane for examining the cross-section of the impacted specimen

3.3.2. Quasi-Static Indentation

Quasi-static indentation testing can be used as an alternative for low-velocity impact testing for FRP composites; however, several factors affect how comparable the results are, for instance, the impact energy and stiffness of the laminate [128–130]. This section uses indentation testing to estimate the impact properties and the sensing layer activation energy. The information from the indentation testing was then used to determine suitable impact energy values for the drop weight impact testing. As the purpose of the sensing layer is to increase the visibility of BVID, the main objective for performing indentation tests is to determine the energy range at which BVID will occur. This range is defined as the energy range that cause internal damage in the form of delamination, but the damage on the surface is either invisible or barely visible from viewing distance of 40cm and viewing angle of 0°. Indentation tests were conducted at two laboratories. The IM7/913 samples were tested in the Materials Testing Laboratory at the University of Glasgow, and the IM7/8552 samples were tested in Delft Aerospace Structures and Materials Laboratory at Delft University of Technology. In both cases, a Zwick Roell material testing machine was used. The out-of-plane indentations were applied vertically on the front surfaces of the specimens at a constant indentation rate of 2 mm/min using a steel hemispherical indenter with a diameter of 16mm, in accordance with the ASTM D7136-07 standard for drop weight impact damage resistance on FRP composites, ensuring the indentation test results match drop weight impact testing as closely as possible. The dynamic and rate effects of the laminate were considered to be minimal at this loading rate [4].

The specimen was positioned centrally over a 75mm*125mm supporting window and was clamped in position, ensuring that the clamping base and the specimen were central to the indenter. Experiments were continued until a significant drop in force was observed, and the force did not continue to rise after the drop. This is the termination load drop, marked by an audible cracking sound. All tests (indentation and impact) were performed at room temperature. In the indentation test of IM7/913 samples, the specimen was clamped with four rubber-tipped toggle clamps. Video recordings were taken on all samples' front and back faces throughout the testing. As seen in Fig. 3-5(a), the sample was lit from behind to ensure that damage could be clearly seen (the test stand was raised to allow for recording from below). Care was taken to ensure the platform was completely stable, as any movement of the stand could have had an undesirable effect on the results. Audio time stamps within the video enabled synchronicity with experimental force results (readouts were announced as certain force values were met). In

the indentation test of IM7/8552 samples, the specimen was clamped on top-side with another aluminium plate as shown in Fig. 3-5(b), and a Nikon camera was placed beneath the supporting window to capture the initiation and propagation of the damage as well as sensor activation. The camera was set to take a photo every one second, collecting an image-based dataset during the whole test time.

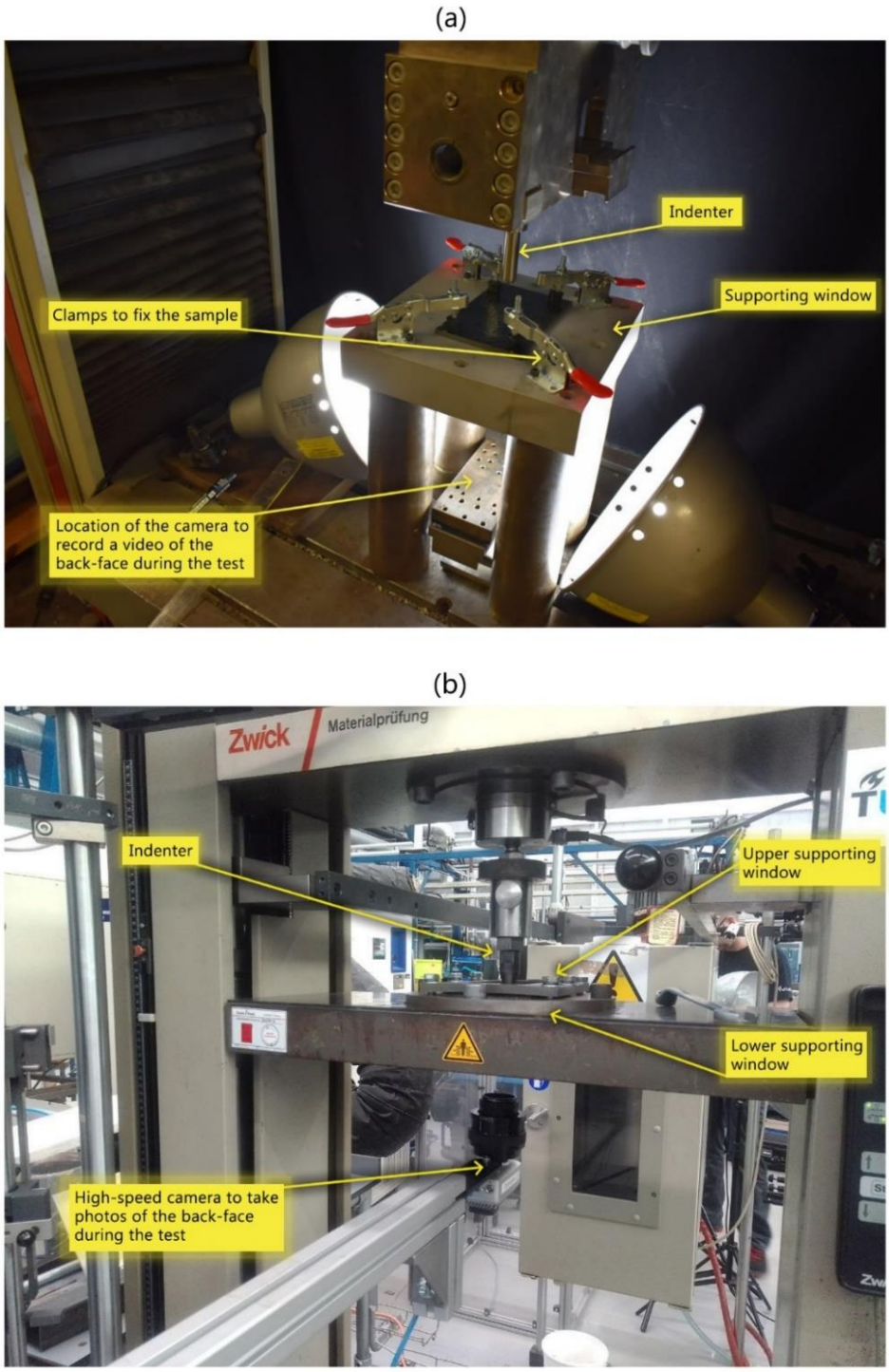

Fig. 3-5: Indentation test set-up: a) IM7/913 samples, b) IM7/8552 samples

3.3.3. Low-Velocity Impact

All impact tests were performed using the drop weight impact tower in the Materials Testing Laboratory at the University of Glasgow. This machine was custom designed as shown in Fig. 3-6(a). The drop weight impact testing apparatus consists of a freestanding tower with a height-adjustable release mechanism capable of performing drop tests of up to 100cm. Impact energy is adjusted by varying the drop height and adding steel weights to the drop sledge. The falling sledge is guided by rails on the drop tower to ensure the specimen is struck in the desired location. Between the sledge and the striking tup is a Kistler 9333 load cell, capable of recording impact forces of up to 50kN. The tup can be changed to provide a striking surface with appropriate dimensions and geometry to suit the test specifications. The final component is the specimen holder that holds the test samples in place during impact. This contains a window underneath the specimen to allow for deformation and four clamps to ensure the specimen does not move during testing. Note that this is the same supporting window used for indentation tests. The load cell is connected to a 5165A Kistler laboratory charge amplifier unit with data acquisition, which can be controlled and recorded through Kistler LabVIEW driver software running on a PC. Based on the indentation results, three impact energy levels were considered (12J, 18J, and 27J) and carried out according to the ASTM D7136 standard [4]. The drop mass was chosen to ensure the lowest drop energy of 12J would not require a drop height of less than 300mm, ensuring test standards were met. As a result, the drop mass was recorded to be 3.94kg, including all components on the dropping sledge. A low pass filter embedded within the data acquisition software was used to ensure the results had minimal noise. This was a Butterworth filter, and the cut-off frequency was set to 3000Hz. This frequency was chosen by performing multiple drop tests with different filter frequencies. The frequency was chosen so that the section of the curve indicating elastic rebound was smooth with minimal noise, yet the oscillatory areas resulting from specimen damage remained visible.

To determine the drop height for the desired impact energy, $E_{impactor}$, the gravitational potential energy equation was used (equation (3-2)), where m is the mass of the sledge, g is the gravitational acceleration, and h is the drop height measured from the specimen's top surface to the impactor's point of first contact. The energy lost due to friction was assumed to be negligible. Displacement was calculated using Newton's second law and the integral of the velocity:

$$E_{impactor} = mgh \tag{3-2}$$

$$a(t) = g - \frac{F(t)}{m} \tag{3-3}$$

$$v(t) = v_1 + \int_0^t a(t)dt \tag{3-4}$$

$$x(t) = \int_0^t v(t)dt \tag{3-5}$$

Due to potential variability in dynamic loading tests, all impact tests were conducted twice to ensure the reliability of the results. Post-impact specimens were labelled, and images were taken of both sides to enable visual inspection of the impacted and non-impacted surfaces. Plots of the impact energy vs. time were made to confirm a correct drop tower setup, and that post-processing had been carried out effectively, as shown in Fig. 3-6(b). The peak values on this plot represent the point when all the impact energy has been transferred into the test specimen. As seen below, the peak energy values closely match the impact energy the impact test set at. This confirms an effective setup and post-processing of the force-time results.

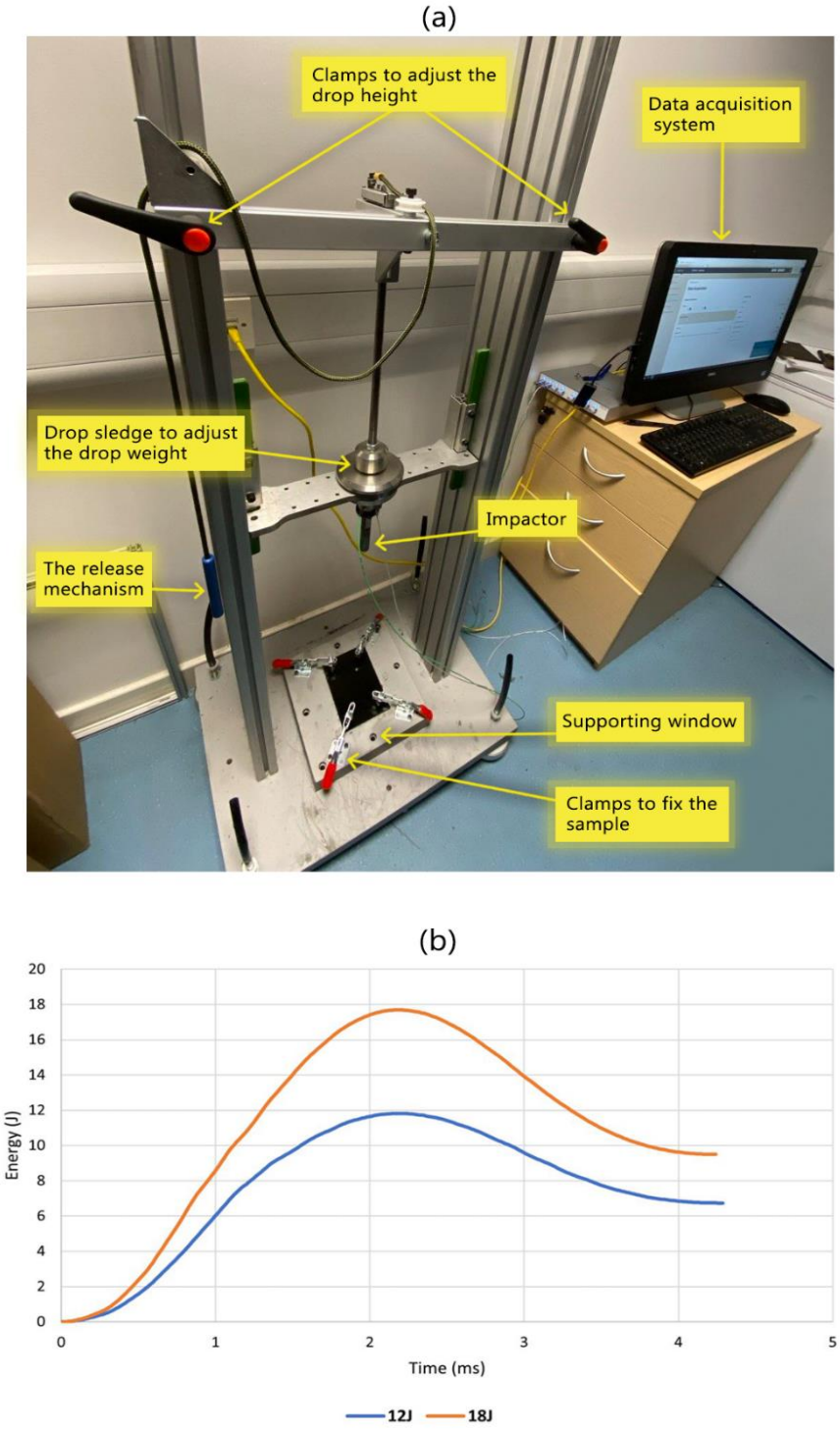

Fig. 3-6: Impact test setup: a) different parts of the custom-designed drop tower apparatus, b) calculated impact energy at 12J and 18J impact tests from force-time results. Peak values are seen to match the corresponding test energy, demonstrating an effective setup.

3.3.4. Visual Inspection, Ultrasonic C-Scan, and Image Processing

Santos et al. [131] used different ultrasonic C-scan approaches to evaluate CFRPs submitted to low-energy impacts to assess their effectiveness for detecting and characterising small defects. Ultrasonic C-scan images were produced by immersion pulse-echo (in amplitude and time-of-flight), immersion through-transmission, and air-coupling through-transmission. The results showed that all methods could detect defects and give acceptable information about their size and shape. However, if delamination over thickness is of interest, the images by time-of-flight should be used.

In the present research, two NDT methods were used to further analyse the damage after completing low-velocity impact tests. First, the impacted and non-impacted faces of all samples were scanned using a Canon C257i scanner (visual inspection). After that, all samples were C-scanned using a DolphiCam2 camera, see Fig. 3-7(a). It emits high-frequency sound waves into materials, capturing reflections and refractions caused by defects or interfaces. Sophisticated algorithms process the data to reconstruct images of the material's internal structure, aiding in defect detection and analysis. A coupling agent (gel) was used to enhance the transmission of ultrasound waves between the transducer and the specimen's surface, facilitating accurate imaging and defect detection. Finally, the damage area was measured and recorded from the image obtained.

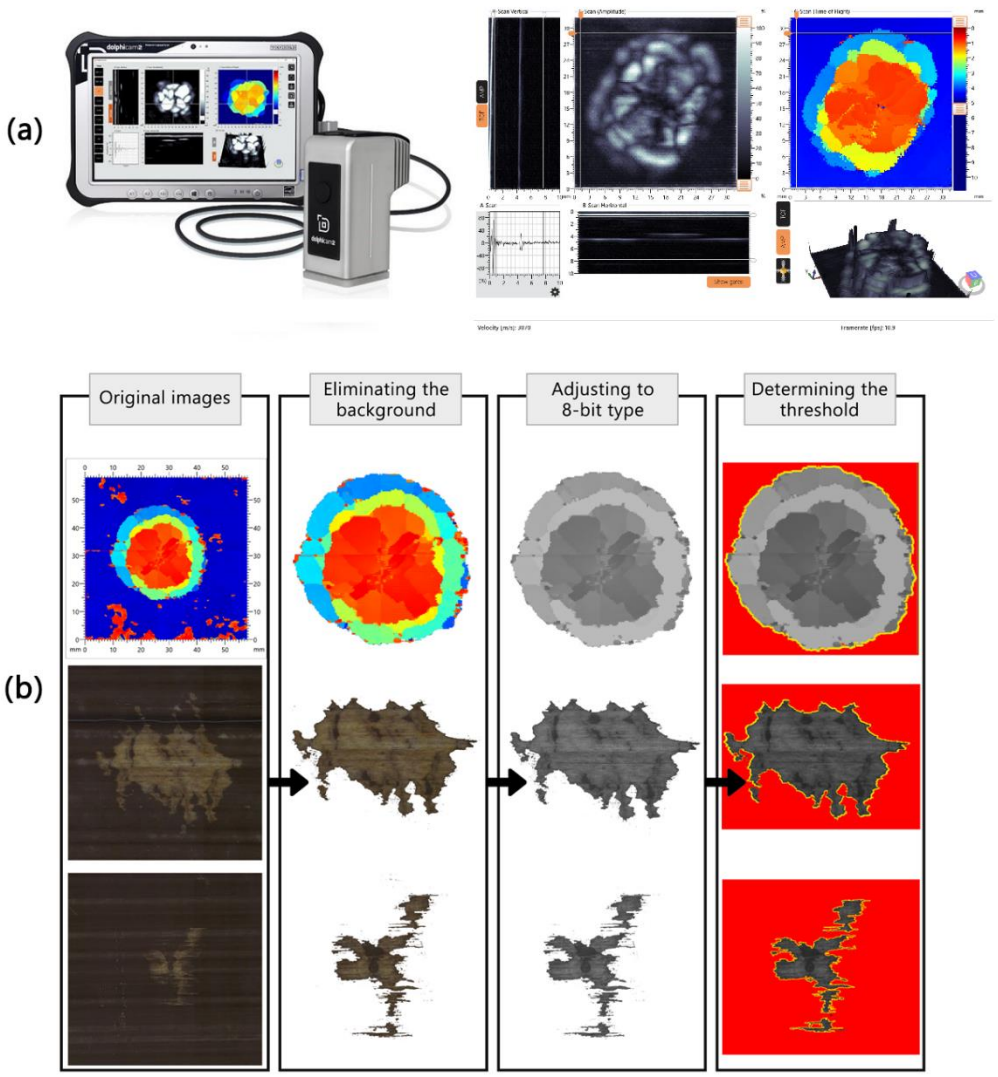

Fig. 3-7: a) Ultrasonic C-scan equipment [132], b) the image processing method to measure the C-scanned area and sensor activated areas

Following the collection of image-based data from the front face, back face, and C-scan of the samples impacted at various energies, image processing was performed using ImageJ software to measure the sensor-activated area on the surface as well as the C-scanned area. This analysis aimed to establish a correlation between surface and internal damage (see Fig. 4-18). The image processing procedure involved utilising Adobe Photoshop software to eliminate the background, followed by adjusting the image type to 8-bit using ImageJ software. Subsequently, the boundary of the area was determined, and the area was measured using the Region of Interest (ROI) manager toolbox. This process is illustrated in Fig. 3-7(b).

3.4. Analytical Solution and Finite Element Analysis

3.4.1. Steps of Development in Modelling Impact

Analysis of impact in laminated composite structures has been a topic of research since the early nineties [133]. Many models featuring different abstraction scales and applied methods have been developed for the last twenty years. Recent studies prove that achieving promising simulation results through meso-scale FEA is possible. Nevertheless, the simulation of impact is still challenging from the numerical point of view. Achieving a high level of accuracy in a reasonable computation time remains a challenge. For coupon simulations with state-of-the-art models, four days or more computation times are reported [134–136]. The impact analysis methods progressed from simple analytical models to high-fidelity finite element approaches. This can be generally categorised into five main steps, as shown in Fig. 3-8. It is evident that with increasing the predictive capabilities, the analysis effort is increasing as well. The main objective of impact analysis is damage prediction. While analytical or empirical models can provide information about the damage onset and its quantitative dimensions, numerical methods can predict the damage type and shape, depending on the modelling strategy, with a different degree of detail. Early analytical methods consider an impact system a multi-body system in which springs connect one or more masses [133]. Considering the plate deformation and local surface indentation, these models can capture an elastic impact response. These analytical methods can estimate the impact duration, maximum contact force, and impactor displacement [137,138]. A higher abstraction level in analytical methods is a plate model. This approach comprises more natural frequencies of the impact system [139]. Such plate models can capture the undamaged dynamic behaviour with higher accuracy than spring-mass methods [140]. The inclusion of material-specific non-linearities even extends this capability [141]. Spring-mass and plate models can be combined with an empirical or analytical prediction of damage threshold loads. Analytical estimations of the initiation and extent of damage build on such damage threshold load. The equations for damage threshold load are derived using fracture mechanics to predict the contact force that makes a delamination grow [4,137,142]. In addition to analytical methods, impact analysis can be conducted using FEA in many variations, including macro-, meso- and micro-models. FEA approaches can be categorised into three main groups, namely “Layered”, “Stacked Layer”, and “Ply-Splitting” models.

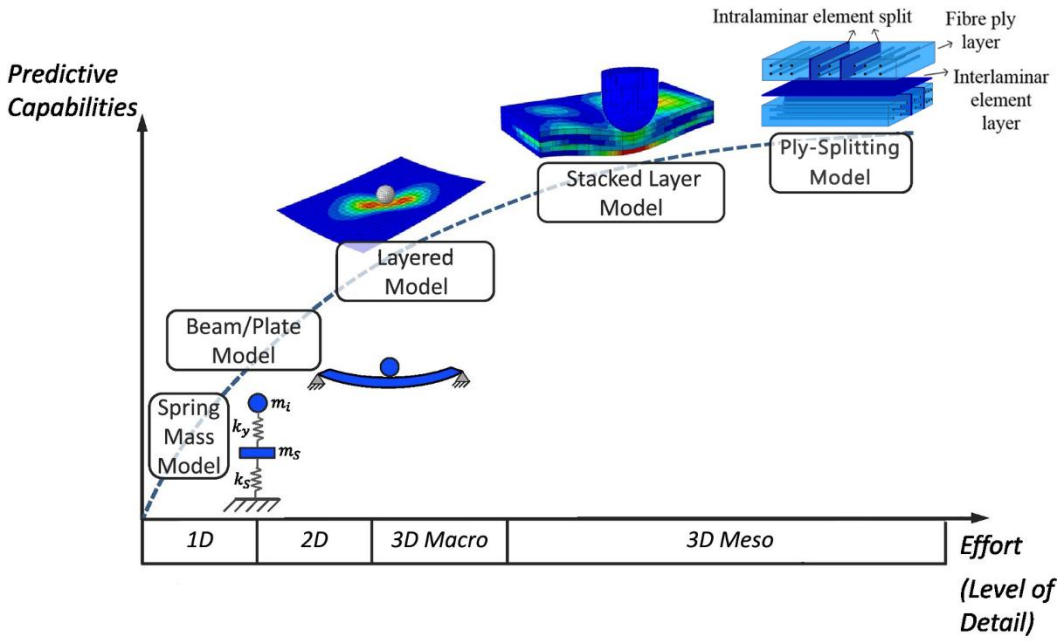

Fig. 3-8: Overview of impact analysis methods [143]

The *Layered* models belong to the macro-scale that can capture impact kinematics like a plate model. However, using such methods, one can evaluate the failure conditions on the ply-level and the corresponding stiffness degradation [144,145]. The main idea of a *Layered* model is to consider the entire composite structure as a single layer, then divide it into the desired number of plies with different materials and fibre orientations. This allows for avoiding introducing contact between different plies that significantly enhance the computational time and effort (see Fig. 3-9(a)). This modelling approach can be subdivided into shell-layered and solid-layered models, depending on the type of elements being used. In the former, ply failure is calculated at the plies' integration points, using the built-in Hashin's criterion from Abaqus, while in the latter, user material subroutines are required to apply the 3D Hashin's criterion. An important advantage of the *Layered* models is their efficiency, which allows for the application of impact simulation in the design process. On the one hand, the low number of empirical parameters and the applicability of coarse meshes are very convenient for quick FEA. On the other hand, the low numerical effort does not call for a high-performance processor, and it keeps the computing time low if, e.g., material and lay-up parameters must be extensively varied in the design process. Depending on the extent of degradation, the simulations can be as fast as a few seconds to a few minutes on a personal computer [146].

A *Stacked Layered* model is the first representative of the meso-scale. In the meso-scale models, the plies are equipped with a damage model based on Continuum Damage Mechanics (CDM), and the Cohesive Zone Method (CZM) is used at the interface. There is a wide range

of published meso-scale methods; the interface model, the ply model, element types, and meshing approaches are essential characteristics in which recent models differ [143]. A *Stacked Layered* model allows for using an interface model between plies to capture delamination damage. Similar to the *Layered* model, the *Stacked Layered* model can be subdivided into shell and solid models. In the shell model, linear, reduced-integrated shell elements with enhanced hourglass control represent each unidirectional layer (represented by S4R in Abaqus). Cohesive volume elements with eight nodes (COH3D8 in Abaqus) connect the layers. Tie constraints couple the cohesive layer to each neighbour ply. As Abaqus provides an appropriate CDM model for shell elements, this stacked-shell model can be fully realised through the onboard means of Abaqus. The damage model is based on the Hashin's failure condition and applies a bilinear degradation law. In the solid model, linear, reduced-integrated brick elements with enhanced hourglass control (C3D8R in Abaqus) represent each unidirectional layer. This is an extension of the stacked-shell model. The solid elements consider out-of-plane stresses and strains entirely. Moreover, the interface contact can be introduced using either cohesive contact (cohesive surface) or cohesive layers (cohesive elements). Controversial results on comparing these strategies were reported in the literature [16,136,147]. A suitable direct comparison of both methods is presented in [148,149]. A *Stacked Layered* modelling strategy requires more computational time and effort than a *Layered* model. Nevertheless, it can capture interlaminar damage (see Fig. 3-9(b)).

The *Ply-Splitting* model is an advanced variant of the stacked-solid model, where cohesive zones parallel to the fibre direction are placed within the ply, as demonstrated in Fig. 3-9(c) [150]. Highly accurate results can be achieved using this method. However, the computation effort is high, and numerical difficulties have been reported [136,143,151]. Recent improvements possibly provide a better solution accuracy but increase the computational effort rather than reduce it. Usually, user-defined material models are necessary for the CDM damage models. Especially if permanent indentation or non-linear shear behaviour shall be included, onboard materials of commercial finite element codes do not provide the required features.

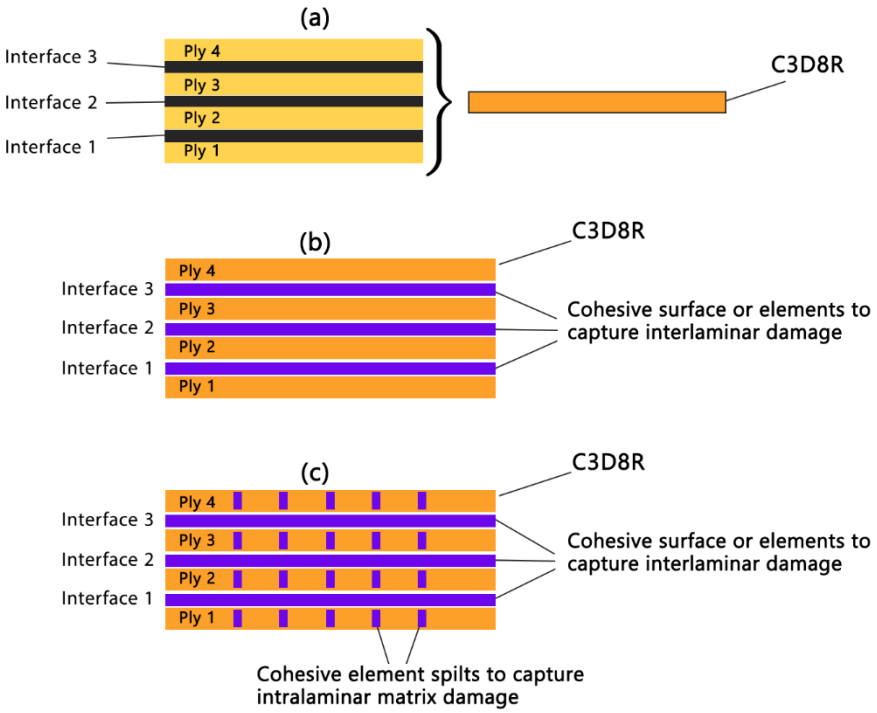

Fig. 3-9: Different FEA approaches: a) a *Layered* solid model, b) a *Stacked Layer* solid model, c) a *Ply-Splitting* model

Bogenfeld et al. [143] conducted a comparative study of all mentioned impact analysis methods. They concluded that for a quick estimation, applying a macro-scale model with layered-shell elements is preferred. In this case, contact modelling should be avoided, and implicit time integration is the right choice. To achieve better damage results, they recommend applying a meso-scale approach. The modelling and computation efforts are much higher than for a layered-shell model, but the impact process and its damage are captured physically plausible. Cohesive surfaces and finite solid elements were suggested for this approach. Moreover, they reported that in high-fidelity models, many material parameters, especially for fracture mechanics, must be determined experimentally. With the degree of detail, the number of required parameters also increases. Cohesive zone approaches, particularly, require additional parameters that depend on physical and numerical properties. Their definition itself is an object of research. This results in a further aspect for the best choice of a simulation method: the availability of material parameters. High-fidelity methods require a large set of parameters for elasticity, strength, and damage behaviour. Especially the latter is often not available. In that case, it was concluded that the application of a layered-shell model is preferred since the progressive damage behaviour is unlikely to be predicted correctly. If there

is also no strength data available, applying analytical analysis in combination with evaluating threshold forces can be a good alternative.

Given that this chapter aims to assess the sensor design parameters rather than conduct a high-fidelity impact analysis, a new analytical solution is presented to calculate the delamination threshold load. Then, two finite element *Layered* models are developed: one shell model and one solid model. After verifying both analytical and finite element models against experimental data, the proposed FEA models are used to study the influence of different sensor design parameters. Detailed explanations of these models are provided in the next section.

3.4.2. Important FEA Parameters

After conducting a brief literature review and initial parameter analysis, three key parameters were identified as potentially influential in the modelling of laminated composites under out-of-plane loading. The first parameter is the modelling strategy which includes a 3D shell modelling and a 3D solid modelling approach. The second influential parameter was the size and shape of the region of interest (ROI). Initial investigations compared two ROI shapes, circular and rectangular, and the results favoured the circular shape due to superior meshing, reduced computational time, and enhanced accuracy. Consequently, subsequent studies will focus on circular ROIs. Two sizes were selected for each laminate: D20 and D40. The selection rationale stems from experimental data in [4], wherein the delamination size immediately post-first load drop in load-displacement graphs from quasi-static indentation tests was measured. Notably, the projected delamination areas (assuming circular delamination instead of direct measurements) for 32-ply samples (similar to those manufactured in this chapter) were found to be 19.5mm. Thus, 20mm was chosen as the initial ROI size (represented by D20). Furthermore, to investigate the effect of the region of interest size on the accuracy, a second ROI size, twice the size of the former (40mm), was also utilised, which is referred to as D40 (see Fig. 3-10(b)). The third modelling-related parameter is the boundary conditions that features the inclusion or removal of four clamps used to fix the sample from the top side (see Fig. 3-10(c)). The mentioned parameters are presented in Table 3-2. More details regarding the modelling procedure are provided in the next section.

Table 3-2: FEA parameters and their levels

Parameters	Levels	
Modelling strategy	3D shell	3D solid
ROI size	D20	D40
Boundary conditions	No clamp	With clamps

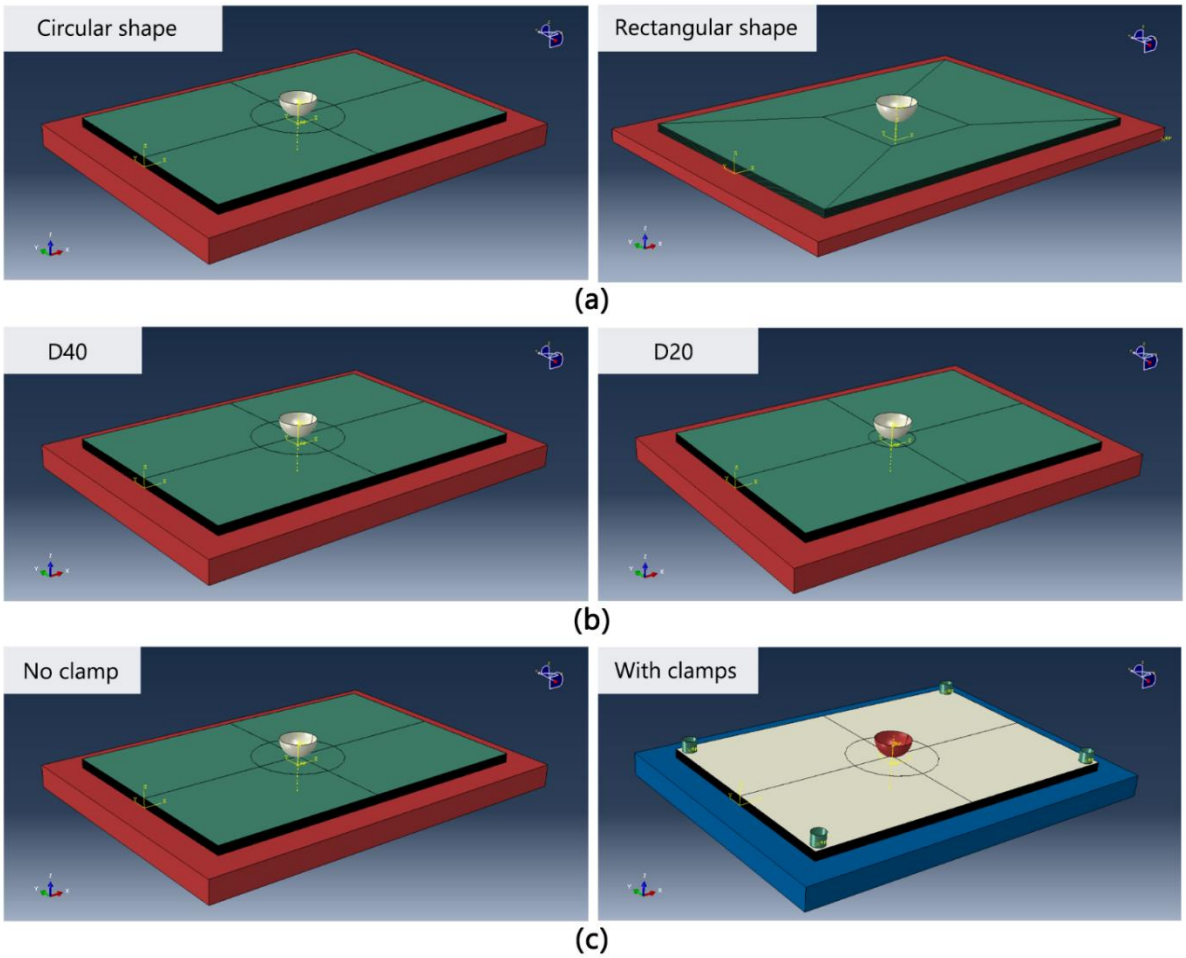

Fig. 3-10: Important finite element parameters: a) the shape of the region of interest, b) the size of the region of interest, c) boundary conditions

3.4.3. Modelling Approach

This section presents the problem formulation and solution procedure for the analytical method and the modelling procedure for the FEA, and the results of both methods are presented in the next chapter.

3.4.3.1. Analytical Solution for Determining Delamination Threshold Force

Determining threshold forces for the onset of delamination is crucial to assess the barely visible impact damage through analytical models. The associated formulas are based on analytical relations between the laminate characteristics and an out-of-plane loading. A combination with any impact model that predicts the contact force history is possible. Different analytical models to estimate the onset and propagation of delamination within a plate loaded by a central transverse load have been proposed in the literature [152–155]. One frequently cited equation for predicting delamination, which accounts for a circular isotropic plate with clamped boundaries under a central point load, derives from thin plate theory [4]. This equation can estimate the loading conditions necessary for the propagation of a single circular delamination situated at the middle of the plate or for (N-1) equally spaced circular delaminations throughout the plate thickness, thereby dividing the plate into N sub-laminates, considering both linear and geometric non-linear aspects. These models provide an initial assessment of how the behaviour of the plate relates to its dimensions. According to the linear model, delamination propagation occurs under a constant load F_d, influenced by the material and geometric properties of the plate as well as the number of circular delaminations. The general equation for (N-1) delaminations is as follows [152–154]:

$$F_d = \sqrt{\frac{8\pi^2 h^3 E G_{\mathrm{IIC}}}{3(N+1)(1-\upsilon^2)}} \tag{3-6}$$

Where h, E, G_{IIC}, and ϑ are the thickness, bending modulus, critical strain energy in mode II delamination, and Poisson's ratio, respectively. For singular delamination, when N equals 2, it provides the threshold load for delamination (see equation (3-1)).

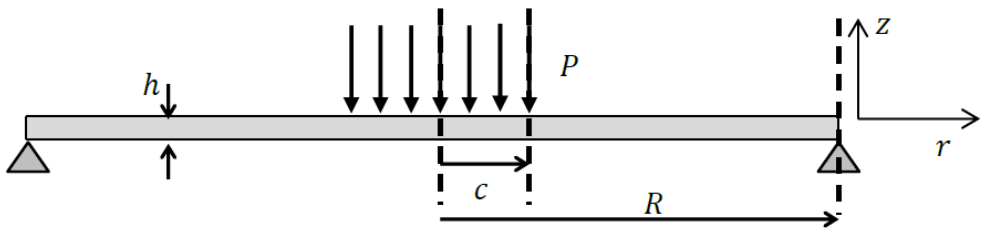

Fig. 3-11: A circular plate subjected to transverse uniform loading

Herein, the procedure for deriving a new equation for the delamination threshold load of a laminated composite plate under indentation is presented. The proposed model is based on the load-deflection relation of an orthotropic circular plate with a radius of R, which is subjected to a uniform load of P, as shown in Fig. 3-11, where both flexural and shear rigidity of the

laminate are taken into account. Lukasiewicz [155] showed that the deflection of such loaded plate, for $0 \leq r \leq c$, can be defined as:

$$u = \frac{FR^2}{16\pi D}\left[\left\{\frac{r^4}{4c^2} + r^2\left[\frac{(1-\vartheta_{rz})c^2-4}{2(1+\vartheta_{rz})} + 2\ln c + 8\epsilon\frac{1-\vartheta_{rz}}{1+\vartheta_{rz}} - 2(\eta-\epsilon)c^{-2}\right]\right.\right. \quad (3\text{-}7)$$
$$\left.\left. + \frac{4(3+\vartheta_{rz})-(7+3\vartheta_{rz})c^2}{4(1+\vartheta_{rz})} + c^2\ln c - 8\epsilon\frac{1-\vartheta_{rz}}{1+\vartheta_{rz}} + 2(\eta-\epsilon)(1-2\ln c)\right\}\right]$$

Here, u represents the plate deflection, ε is a coefficient expressing the effects of stress normal to the middle surface, and η is a coefficient expressing the effects of transverse shear. These are defined as follows [155]:

$$\epsilon = \frac{\upsilon_{rz}E_z h^2}{E_r l^2} \quad (3\text{-}8)$$

$$\eta = \frac{D}{k_3 G_z h l^2} \quad (3\text{-}9)$$

In these equations, υ_{rz} is Poisson's ratio, E, G, and D are elastic, transverse shear, and flexural (bending) modulus and k_3 is a constant coefficient [155]. Note that for the bending rigidity of the plate $D = \frac{Eh^3}{12(l-\vartheta^2)}$, l is an arbitrary characteristic length.

Considering $F = Ku$ and equation (3-7), the stiffness of the laminate can be defined as:

$$K = \frac{16\pi D}{R^2}\left[\left\{\frac{r^4}{4c^2} + r^2\left[\frac{(1-\vartheta_{rz})c^2-4}{2(1+\vartheta_{rz})} + 2\ln c + 8\epsilon\frac{1-\vartheta_{rz}}{1+\vartheta_{rz}} - 2(\eta-\epsilon)c^{-2}\right]\right.\right. \quad (3\text{-}10)$$
$$\left.\left. + \frac{4(3+\vartheta_{rz})-(7+3\vartheta_{rz})c^2}{4(1+\vartheta_{rz})} + c^2\ln c - 8\epsilon\frac{1-\vartheta_{rz}}{1+\vartheta_{rz}} + 2(\eta-\epsilon)(1-2\ln c)\right\}\right]^{-1}$$

The above equation can be rewritten as follows:

$$K = \frac{DJ}{R^2} \quad (3\text{-}11)$$

where J is defined as:

$$J = 16\pi\left[\left\{\frac{r^4}{4c^2} + r^2\left[\frac{(1-\vartheta_{rz})c^2-4}{2(1+\vartheta_{rz})} + 2\ln c + 8\epsilon\frac{1-\vartheta_{rz}}{1+\vartheta_{rz}} - 2(\eta-\epsilon)c^{-2}\right]\right.\right. \quad (3\text{-}12)$$
$$\left.\left. + \frac{4(3+\vartheta_{rz})-(7+3\vartheta_{rz})c^2}{4(1+\vartheta_{rz})} + c^2\ln c - 8\epsilon\frac{1-\vartheta_{rz}}{1+\vartheta_{rz}} + 2(\eta-\epsilon)(1-2\ln c)\right\}\right]^{-1}$$

The stiffness presented by equation (3-10) is for an undamaged plate, but in a damaged plate, it decreases due to delamination. Consider a laminate with n delamination of a radius. According to Fig. 3-12, the stiffness of the laminate can be derived as:

$$\frac{1}{K_{eq}} = \frac{R^2}{DJ} - \frac{a^2}{DJ} + \frac{a^2(n+1)^2}{DJ} \tag{3-13}$$

$$K_{eq} = \frac{DJ}{R^2 + a^2(n^2+2n)} \tag{3-14}$$

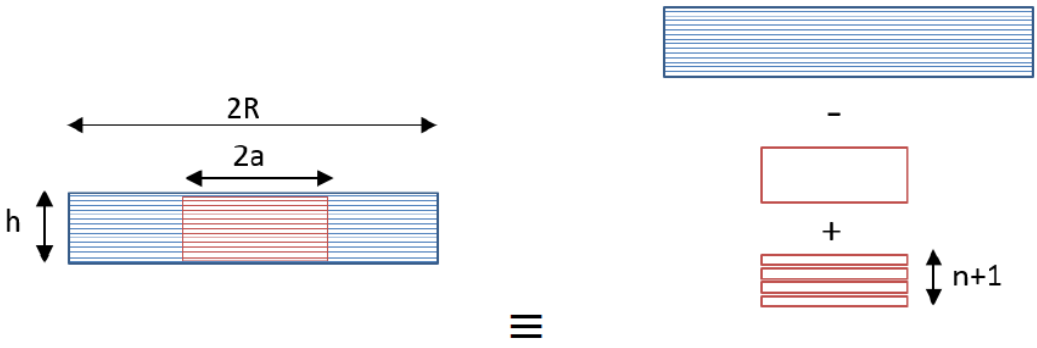

Fig. 3-12: Schematic diagram of a laminate with n delamination

As stated in [156], the load-displacement response of a laminate can be expressed in terms of the shear and bending (linear) stiffness, as well as the membrane stiffness of the plate. Therefore, considering $F = K_{eq}u + K_m u^3$, the total force is obtained as follows:

$$F_t = \frac{DJu}{R^2 + a^2(n^2+2n)} + K_m u^3 \tag{3-15}$$

where K_m is the membrane stiffness and can be defined as [156,157]:

$$K_m = \frac{h\pi E_r}{R^2(3+\vartheta_{rz})^4}\left[\frac{191}{648}(1+\vartheta_{rz})^4 + \frac{41}{27}(1+\vartheta_{rz})^3 + \frac{32}{9}(1+\vartheta_{rz})^2 + \frac{40}{9}(1+\vartheta_{rz}) + \frac{8}{3}\right] \tag{3-16}$$

The elastic energy of the plate can be calculated as:

$$U = \int F du = \frac{DJ}{2(R^2 + a^2(n^2+2n))}u^2 + \frac{1}{4}K_m u^4 \tag{3-17}$$

From linear elastic fracture mechanics, we know that the strain energy of a laminate can be derived as:

$$G = -\frac{1}{2\pi an}\frac{\partial U}{\partial a} \tag{3-18}$$

Substituting equation (3-17) in equation (3-18) and considering the fact that delamination will grow if the strain energy reaches the critical strain energy level ($G = G_{IIc}$), for one delamination ($n = 1$), the first load drop in the load-displacement curve can be derived as:

$$G_{IIc} = \frac{1}{2\pi}\frac{3DJ}{(R^2 + 3a^2)^2}u^2 \tag{3-19}$$

Considering the $F=K_{eq}u$ and substituting K_{eq} from the equation (3-14) the critical delamination force is obtained as:

$$F_d = \sqrt{\frac{2\pi G_{IIc} DJ}{3}} \tag{3-20}$$

While previous analytical solutions are restricted to laminate dimensions and flexural modulus, here, the effects of indenter radius, shear, and flexural modulus, as well as laminate dimensions on delamination threshold load, are taken into account simultaneously.

3.4.3.2. Finite Element Analysis

Two different FEA approaches are evaluated within Abaqus software to produce two distinct sets of results for comparison and the selection of the superior model. Both methodologies use a *Layered* modelling technique to avoid introducing contact between plies. The first model employs shell elements (referred to as the shell model), while the second model uses solid elements (referred to as the solid model). Both models simulate a 32-ply composite with a lay-up of $[45/0/90/-45]_{4s}$.

In the shell model, a rectangular ply was created, and, using the *Composite Lay-up* toolbox, 32 plies with identical material properties and individual thicknesses of 0.125mm, along with varying fibre orientations, were defined using 4-node doubly curved thin or thick shell, reduced integration, hourglass control, finite membrane strains elements (S4R). In the solid model, an initial layer made of 8-node linear brick, reduced integration, hourglass control (C3D8R) elements with a 4mm thickness was created and subsequently partitioned into 32 plies, each having a thickness of 0.125mm. Following this, identical material properties and diverse fibre orientations were assigned to each ply using *Solid Homogeneous Section*. This modelling

technique was identified as the most widely employed and straightforward approach for generating three-dimensional solid models of laminated composite materials. As the impact load is an out-of-plane indentation, the laminate experiences a significant bending load. Since the mesh of macro-scale models describes the laminate as a whole, the elements have to be capable of capturing this bending. Therefore, shell elements are preferred on macro-scale. In contrast, the single plies undergo only slight bending. Compression on the impact side or tension on the impact backside dominates the state of stress in each ply. Accordingly, solid elements can be applied. These capture the out-of-plane strain and stresses, which is advantageous for capturing the local surface indentation of the impactor. As the bending load can cause locking effects, reduced integrated elements are suitable in both macro and meso-scale models (S4R shell elements and C3D8R solid elements in Abaqus) [158]. The supporting window, hemispherical indenter, and four rubber-tipped clamps were represented as discrete rigid parts, sized identically to those used in the static indentation tests conducted previously in this chapter. A reference point was created for the supporting window, four clamps, and the indenter, positioned near the centre of gravity of each component. As for the interaction, a contact was defined between three pairs of parts, as follows: between the indenter and the topmost ply, between the four clamps and the topmost ply, and between the supporting window and the bottommost ply. The contact properties included tangential behaviour with a friction coefficient of 0.3 and normal behaviour with hard contact, which minimises the penetrations between the contact surfaces and does not allow the transfer of tensile stress across the mating surfaces [136]. The friction coefficient of 0.3 was chosen based on the literature review [16,136,159]. However, different values of friction coefficient were then tested, and no significant differences in the FEA results were observed. Regarding the boundary conditions, the reference point of the supporting window and all four clamps were assigned a fixed support boundary condition (referred to as *Encastre* in Abaqus). Additionally, the indenter was constrained to displace solely in the Z direction, while all other displacements and rotations were set to zero (at its reference point). A fine mesh with a sufficiently small size was employed in the circular region of interest where the indenter induces damage to the ply. A mesh sensitivity analysis was conducted for each model to ensure the selection of an appropriate mesh size. The mesh size gradually increased as it extended away from the damaged area towards the edges of the ply. History outputs, such as reaction forces and displacements were defined for the reference point of the indenter. The elastic orthotropic materials properties that were used for FEA are listed in Table 3-3.

Table 3-3: Mechanical properties of the materials used in the FEA [16,116,160]

Prepregs	Density (g/cm^3)	E_{11} (GPa)	E_{22} (GPa)	E_{33} (GPa)	ν_{12}	ν_{13}	ν_{23}	G_{12} (GPa)	G_{13} (GPa)	G_{23} (GPa)
IM7/8552	1.6	161	11.4	11.4	0.3	0.3	0.436	5.17	5.17	3.98
S-glass/913	1.9	45.6	15.4	15.4	0.3	0.3	0.45	4.34	4.34	3.6
YS-90A	2.19	520	5.6	5.6	0.26	0.26	0.4	5.1	5.1	3.5

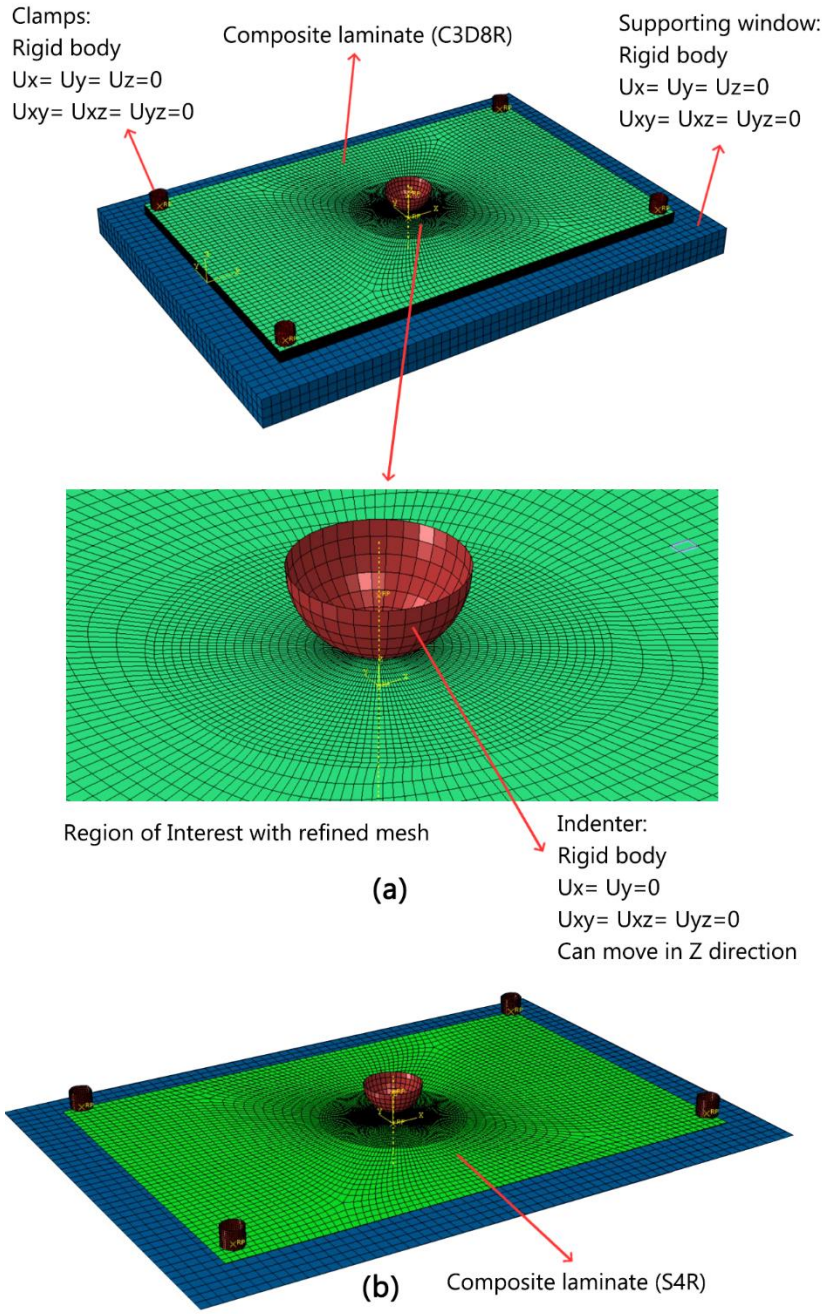

Fig. 3-13: Assembly model, mesh scheme, and boundary conditions for finite element (a) solid, and (b) shell models

3.5. The Choice of the FEA Model

This section investigates how the size of the region of interest affects the accuracy of the solid and shell models in determining the F_d, which is the force at displacement of 2mm. This displacement corresponds to the onset of delamination, as identified in experimental test results. Consequently, in this section, the force at a 2mm displacement is regarded as the delamination force, in alignment with the experimental results that will be discussed in the next chapter. Specifically, this section compares two ROI sizes denoted as D20 and D40. Moreover, the influence of the boundary conditions is studied, where a model with four clamps on the top side of the laminate is compared with another model without any constraint on the top side. Then the best model is selected to study the sensor design parameters in the next chapter, including the fibre orientation and thickness of the carbon sensing layer.

3.5.1. Solid Model

The results of the solid model are presented here. First, a mesh sensitivity study is performed to verify the appropriateness of the mesh size within the region of interest, followed by studying the effect of the size of the region of interest and the boundary conditions on the initial stiffness (before delamination onset) and the delamination critical load (F_d). Note that F_d is not calculated by the FEA; rather, it represents the force corresponding to the displacement at which delamination occurred in the experimental tests.

Fig. 3-14 illustrates the outcomes of the mesh sensitivity analysis, indicating that varying the mesh size (within the region of interest with a diameter of 40mm) from 0.375mm to 1mm has minimal impact on the results. Specifically, the observed variation in F_d within this range was lower than 2%. Therefore, a mesh size of 0.75mm is considered to be suitable here and will be used in the following analyses associated with the solid model. Table 3-4 shows a comparison of F_d from finite element models with two different sizes of region of interest (D20 and D40) and for two distinct mesh sizes. It is observed that for both D20 and D40, the model can predict the force associated with delamination well, with nearly 16% error compared to the experimental results. Moreover, the influence of the ROI size in this model was found to be negligible, as the force-displacement graphs for D20 and D40 were seen to overlap, with less than 2% difference between F_d given by D20 and D40 (see Table 3-4). Given that the D40 model slightly outperforms in both mesh sizes, the D40 model with a mesh size of 0.75mm is selected as the reference for the solid model.

The influence of boundary conditions on indentation response is demonstrated in Fig. 3-15. The model with clamps shows a slightly more rigid response. Particularly, the values of the forces associated with delamination for the “no clamp” and “with clamps” models were 6424N and 7091N, respectively. The influence of boundary conditions seems to be more noticeable than that of the ROI size.

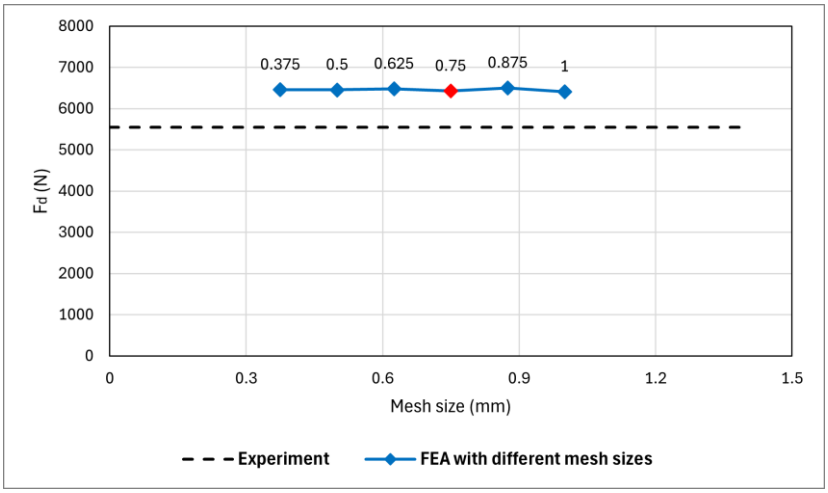

Fig. 3-14: Mesh sensitivity study for the solid model

Table 3-4: Comparison of forces at displacement of 2mm, obtained from FEA (solid model) with region of interests D20 and D40 for two mesh sizes, alongside experimental data.

Mesh size	Experiment	D20	D40	Difference between D20 and D40
0.5mm	5542N	6555N	6453N	1.5%
0.75mm		6494N	6424N	1%

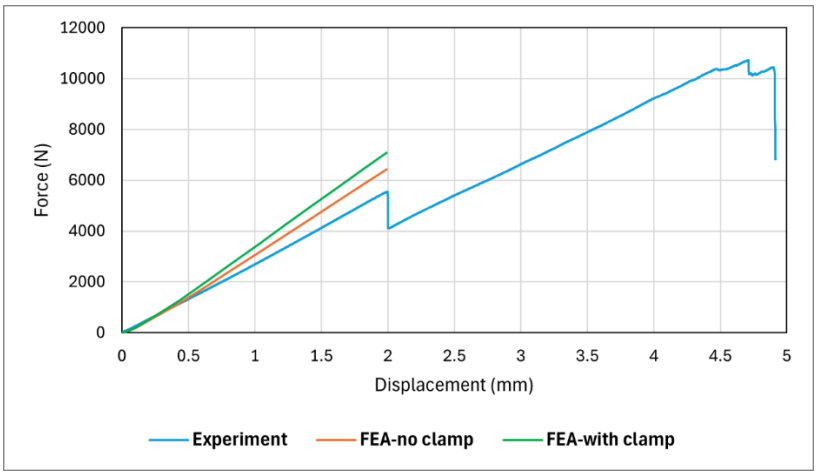

Fig. 3-15: Comparison of indentation response obtained from FEA (solid model) with different boundary conditions, alongside experimental data.

3.5.2. Shell Model

Similar to the solid model, a mesh sensitivity study is conducted for the shell model. While different mesh sizes (within the region of interest with a diameter of 40mm), ranging from 0.375mm to 1mm, appeared to not make a significant difference in F_d values (less than 3%), the mesh size of 0.75 was selected for this model, given its more consistent results compared to other values (see Fig. 3-16). The results of comparing D20 and D40 models for two mesh sizes are presented in Table 3-5. It is observed that the worst case out of four cases in this table can predict the force (at displacement of 2mm) with only 18% error compared to the experimental results. Moreover, the difference between D20 and D40 models is lower than 1%. However, the D40 model gives slightly more accurate results than the D20. Therefore, the D40 model with a mesh size of 0.75mm is selected as the reference for the shell model.

Fig. 3-17 shows a comparison of the indentation response for experimental tests and finite element models with and without the four clamps on the top side of the laminate. Overall, finite element models slightly overestimate the stiffness, and this is more significant for the model with clamps. Particularly, the force associated with delamination (F_d) for the models with and without clamps was 7076N and 6495N, respectively. The difference between these two models is less significant than the difference between similar models in the solid modelling approach.

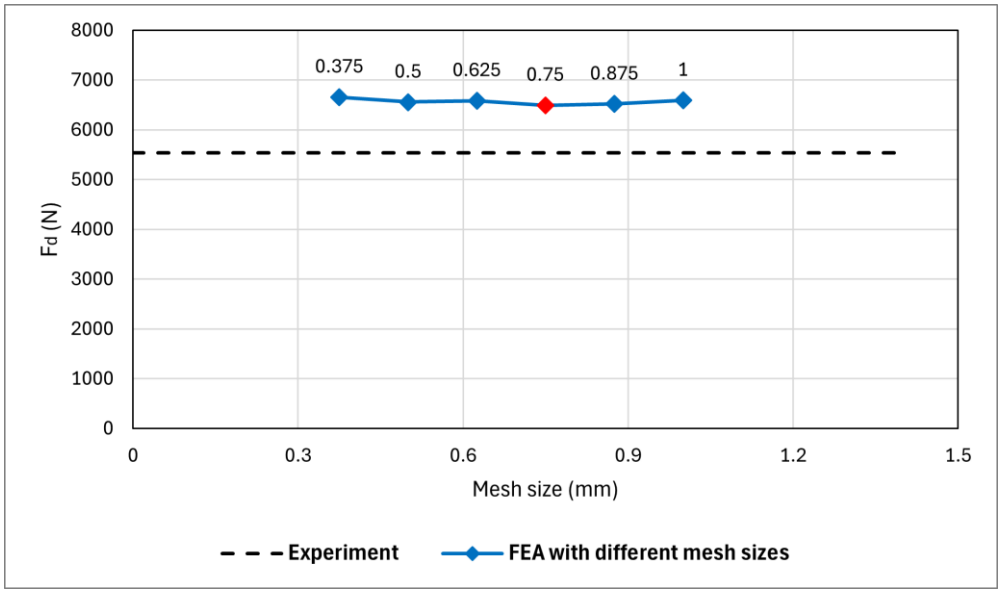

Fig. 3-16: Mesh sensitivity study for the shell model

Table 3-5: Comparison of forces at displacement of 2mm, obtained from FEA (shell model) with region of interests D20 and D40 for two mesh sizes, alongside experimental data.

Mesh size	Experiment	D20	D40	Difference between D20 and D40
0.5mm	5542N	6596N	6559N	0.5%
0.75mm		6496N	6495N	~0%

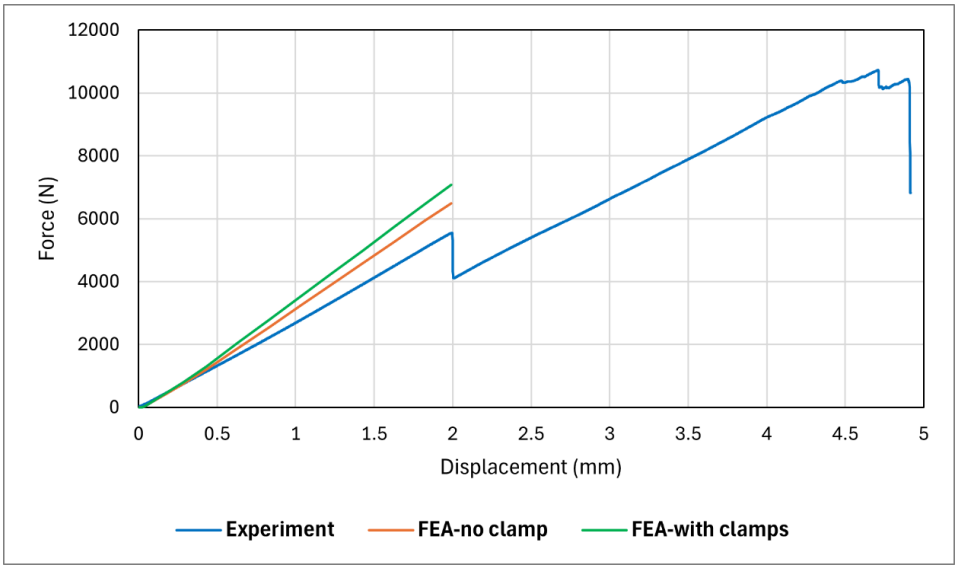

Fig. 3-17: Comparison of indentation response obtained from FEA (shell model) with different boundary conditions, alongside experimental data.

3.5.3. Discussion

A comparison of the solid and shell models with experimental results is shown in Fig. 3-18. Both FE models slightly overestimate the stiffness, as detailed in the previous section. Several factors may contribute to this, including assuming the indenter and clamps as rigid bodies or input material properties that may not precisely reflect those of the actual composite product [143,161,162]. A comparison between the shell and solid models should examine three key factors: accuracy, computational time, and modelling effort. As presented in Table 3-6, the shell model demonstrates superior computational efficiency compared to the solid model, with comparable accuracy. Furthermore, in terms of modelling effort, the shell model holds a clear advantage. Its simplicity facilitates easy revisions for parametric studies, such as adjusting sensor design parameters. Note that the error in Table 3-6 is calculated based on the difference between the F_d value given by each shell and solid model with that of the experiment. In all cases, the displacement equals to 2mm.

A comparison of D20 and D40 in the previous section suggests that the influence of the ROI size is negligible compared to other studied parameters. Nevertheless, the D40 model provided better outcomes with similar computational time. The influence of boundary conditions, particularly the inclusion or exclusion of four clamps on the top side, appears to be more notable. A review of the literature reveals varying modelling approaches regarding boundary conditions. Some studies substitute the supporting window with simply-support boundary conditions along the edges [163,164], which was initially tested in this study but led to a considerable underestimation of stiffness. Therefore, modelling the window and introducing contact is deemed a valid approach. Regarding the top side, while some papers neglect any constraints [16,159,162,165], others model four clamps and assign mass to them [166] or apply specific constraints on the edges of the laminate [115,136,147,149,163,164,167]. Additionally, some papers consider four clamps with fixed boundary conditions [143,161]. In this study, the clamps are defined as rigid and fully fixed using the Encastre feature in Abaqus.

The difference between the two models with different boundary conditions is more notable in higher force/energies. This is shown in Fig. 3-19, where the two models are compared for two different displacements, including 2mm and 5mm. Notably, the difference between the obtained force values for a displacement of 2mm is 666N, but for a displacement of 5mm, it goes up to 1878N, nearly three times higher than that of a 2mm displacement. This shows that the influence of boundary conditions becomes more significant as force/energy increases. This is because during an impact event, a significant amount of energy is dissipated through friction, i.e., the effect of the rubber-end clamps, and the higher energy, the greater the effect of boundary conditions. This is in line with the experimental results presented in Chapter Four (see section 4.2.2.2). Given that the finite element simulations of this study are limited to the linear elastic region (before the first load drop) (see Fig. 3-19(a)), the ‘no clamp’ model would be valid. Therefore, the shell model with an ROI size of D40 and boundary conditions of ‘no clamp’ is chosen to study the sensor design parameters in the next chapter.

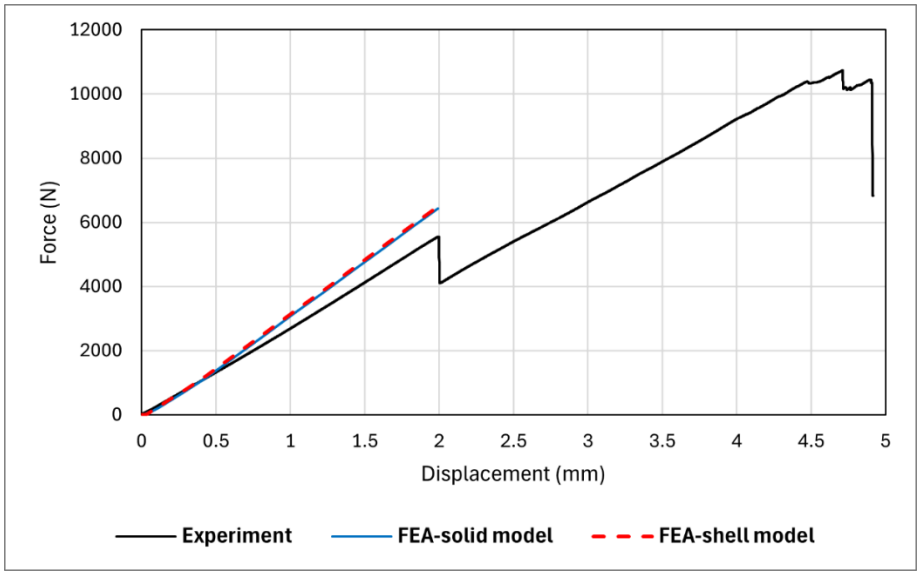

Fig. 3-18: Comparison of the shell and solid models with experimental results

Table 3-6: Comparison of computational time and accuracy between the solid and shell models

Modelling strategy	System time (s)	CPU time (s)	Error (%)
Solid	5330	127543	15.9
Shell	961	1516	17.1

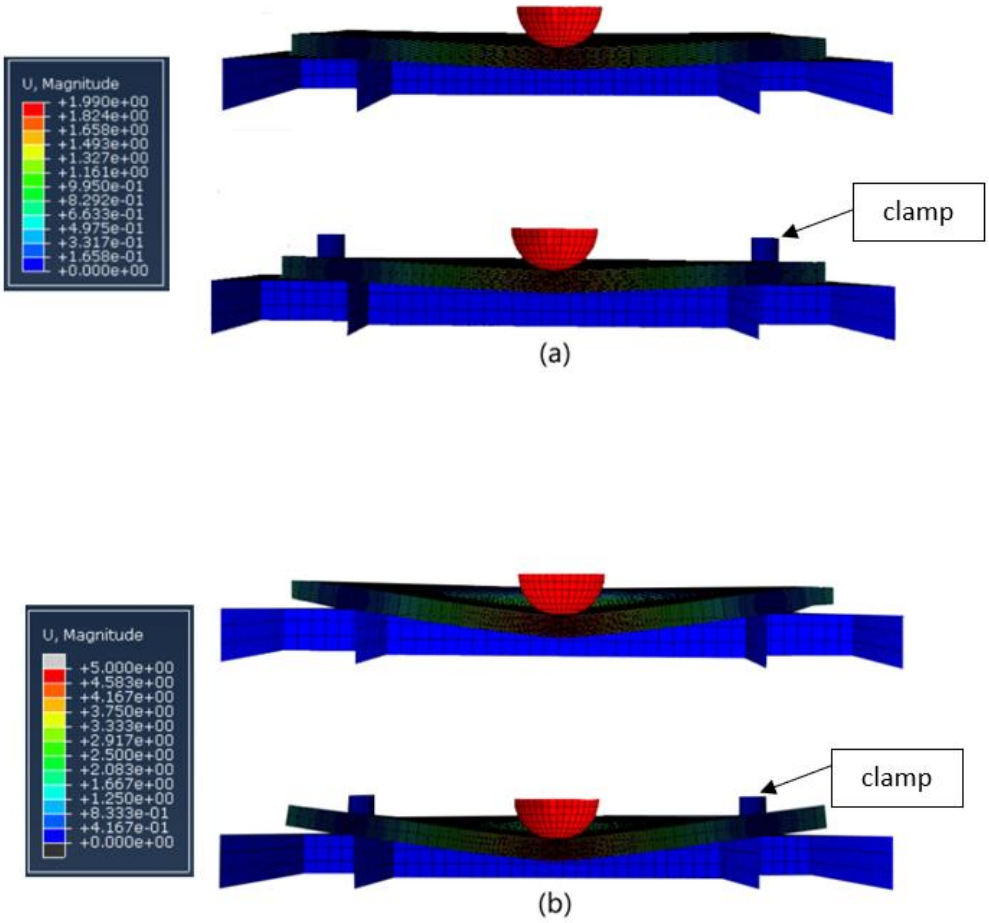

Fig. 3-19: Boundary conditions with and without clamps: a) deformation of 2mm, b) deformation of 5mm. Within the linear elastic region, when deformation is low, the effect of the clamps is negligible.

3.6. Summary

In this chapter, initially, the key principles for designing the sensor were outlined, followed by manufacturing two groups of composite specimens. Some samples from both groups were equipped with the sensor on both the front face (impacted side) and back face (not-impacted side), applying different sensor attachment methods. Both one-step and two-step curing methods provided excellent sensor adhesion to the substrate and achieved a high-quality surface finish. The design and performance of the sensor were further investigated using sensors with different fibre orientations and with discontinuities in the carbon sensing layer.

First, quasi-static indentation tests were conducted. Given its static nature, this test allowed for monitoring damage initiation and propagation and sensor activation during the test. This was achieved by taking images every second using a Nikon camera and recording videos from both the front face and back face. Moreover, indentation tests provided insight into the minimum

required energy to induce delamination damage, which was used to determine impact energies for the low-velocity impact tests. A drop tower impact test apparatus was then designed, manufactured, assembled, and set up to conduct low-velocity impact tests. After completing impact tests, destructive and non-destructive evaluation methods were applied to analyse the internal damage and compare it with the damage on the surface. The non-destructive methods included visual inspection and ultrasonic C-scan, and the destructive method was to cut the impacted samples and analyse the microscopy images of the cross-section to evaluate the internal damage.

Moreover, analytical and FEA methods were employed to investigate damage mechanisms within a laminated composite structure under static indentation, focusing on delamination in the substrate and fibre fracture in the sensor. The analytical solution derived a new equation for the delamination threshold load by examining the relationships between laminate characteristics and out-of-plane loading. This equation takes into account the radius of the indenter, as well as both shear and flexural modulus, in addition to laminate dimensions. Two FEA models, using shell and solid elements, were constructed and assessed against experimental data, with both demonstrating satisfactory performance. The models were analysed to determine the impact of two parameters: the size of the ROI and the boundary conditions. Analysis of both shell and solid models showed that the ROI size has a minimal effect on both computational time and accuracy. Regarding boundary conditions, the numerical findings indicated that boundary conditions become increasingly significant with higher levels of force or energy. For low-energy impacts (before delamination onset), it remains reasonable to leave the top side of the laminate unconstrained. Both the shell and solid models achieved comparable levels of accuracy, but the shell model required less computational time and effort. Consequently, it was chosen for the parametric sensor design analysis in the next chapter.

Chapter 4

Design of Hybrid Glass/Carbon Sensors: Results

4.1. Introduction

This chapter presents the findings from the experimental, analytical, and FEA studies detailed in the previous chapter. The experimental section is divided into two parts: The first part examines quasi-static indentation behaviour, providing reference data essential for designing low-velocity impact experiments. The second part assesses the sensor's performance in enhancing the detection of low-energy impact damage. A comparison of these two loading types is also provided. In the analytical and FEA section, a new analytical formulation and an optimised finite element model are developed and verified against experimental results. These tools are then applied to analyse the sensor design and its performance under quasi-static indentation loading.

4.2. Experimental Results

4.2.1. Quasi-Static Indentation

4.2.1.1. Global Behaviour

Fig. 4-1 shows the results of all *Reference* and *Sensor* samples tested under static indentation loading. It is seen that regardless of resin type (913 epoxy and 8552 epoxy), and sample configuration (*Reference* or *Sensor*), all curves follow the same general pattern (global behaviour), featuring a linear behaviour until a noticeable load drop, followed by a non-linear behaviour that reaches a second, more significant load drop, and then multiple smaller drops. This pattern has also been seen in static indentation testing of quasi-isotropic CFRPs by other researchers [4,7,125,147,168]. The graphs presented in this figure show the high repeatability and accuracy of both the test setup and the obtained results. Comparing the IM7/8552 and IM7/913 graphs, it is observed that both graphs follow the same trend, with slight differences at certain points. This may stem from differences in resin types and thickness of the two

prepregs. The results align with findings from indentation tests conducted on quasi-isotropic CFRP laminates in other studies [4,125,159], where similar testing setup were employed.

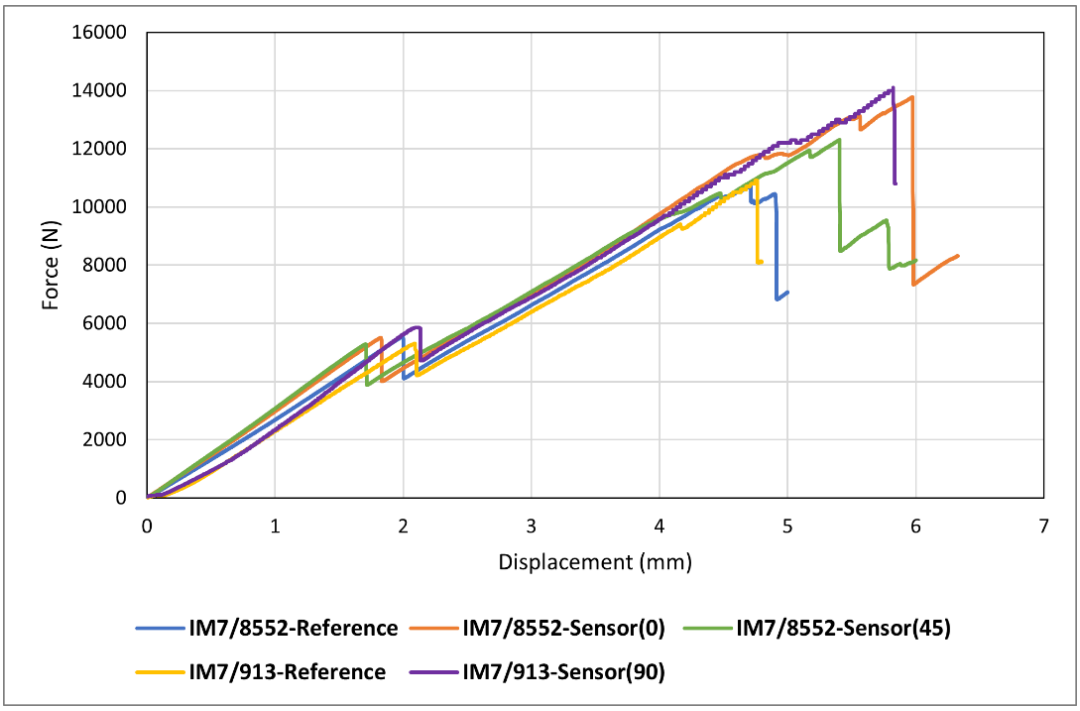

Fig. 4-1: Static indentation results of all tested samples

To further investigate global behaviour, the results of the first sample (IM7/8552-Reference) is chosen and shown in Fig. 4-2. Three primary stages are evident from this figure. The first stage starts from the beginning of the test until a load drop occurs at displacement and force of approximately 2mm and 6000N, respectively. This initial phase represents the elastic region, characterised by a linear load-displacement response. The primary damage mechanism in this stage is matrix cracking, with the load drop marking the onset of delamination [4,159]. This delamination onset was distinctly identifiable during testing by an audible sound. The associated critical load at this point is shown by $F_{d,}$ which is of great interest in this work. After the first load drop, a nearly linear response is seen until a second significant drop occurs at displacement and force of approximately 5mm and 10,000N, indicating more severe damage in the form of fibre failure. Alongside the load drop, this type of damage was identifiable by a distinct sound during testing. The minor load drops in the second stage, between the first and second significant load drops, are mainly associated with delamination propagation. Furthermore, the magnitude of the second load drop surpasses that of the first, indicating more severe damage to the specimen (see Table 4-1). Generally, damage in CFRPs is not visible until this point, and it only becomes visible on the surface after fibre failure happens. The third stage,

initiated after the second load drop, signifies that the sample has incurred significant damage and cannot withstand further loading. Consequently, multiple small drops occur until the sample undergoes complete failure. Given that the objective of this research is to develop sensors capable of enhancing visual inspection of BVID, the emphasis in this PhD thesis will be on the first two stages. Accordingly, all subsequent low-velocity impact tests are designed to induce damage within these two regions.

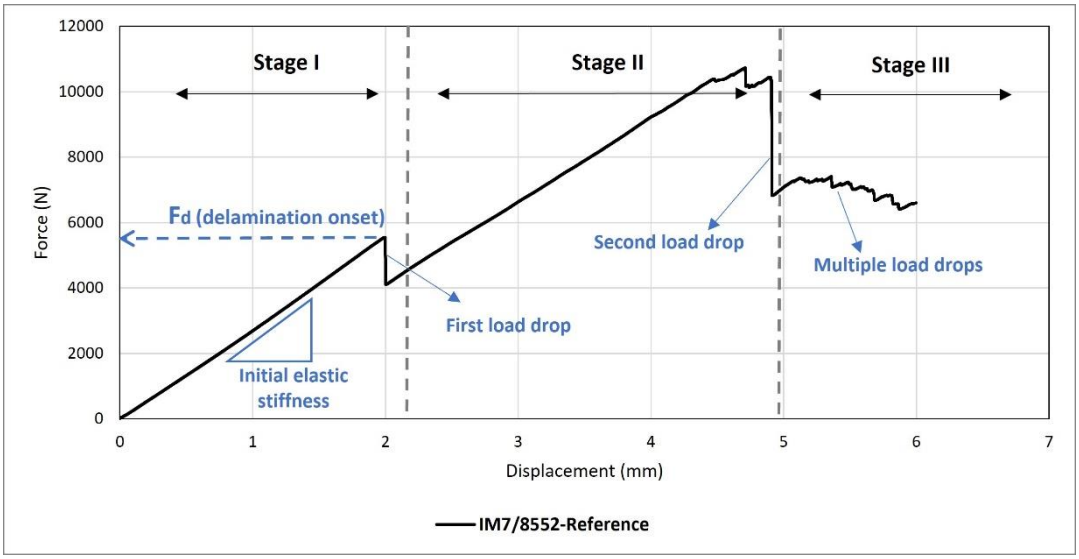

Fig. 4-2: Different stages of damage initiation and propagation in a laminated quasi-isotropic CFRP composite under quasi-static indentation

4.2.1.2. Influence of Adding Sensors on Indentation Properties

The sensor-to-substrate stiffness ratio is critical in designing bio-inspired mechanochromic hybrid composites [169]. Therefore, determining the extent to which the sensor affects the stiffness of the structure is crucial. Basic calculations can be conducted regarding the axial structural stiffness of both the sensor and substrate to assess the stiffness increase induced by the sensors. The most accurate results are typically achieved when employing low-structural stiffness sensors on high-structural stiffness substrates, as this minimises any substantial increase in substrate structural stiffness. In practice, the sensors must be made the thinnest and narrowest possible if the substrate has a relatively low structural stiffness [120]. In this case, the influence of adding sensors on the mechanical properties is experimentally studied here.

Fig. 4-3(a) shows the load-displacement curves for IM7/8552 samples, including a reference sample (IM7/8552-Reference) and two sensor-integrated samples with different fibre orientation in the carbon sensing layer (IM7/8552-Sensor(0) and IM7/8552-Sensor(45)), and

Fig. 4-3(b) shows the curves for IM7/913 samples, which are a reference sample (IM7/913-Reference) and a sensor-integrated sample (IM7/913-Sensor(90)). Qualitatively speaking, adding a sensor on each side of the laminate appears to have marginally increased the structural stiffness of both IM7/8552 and IM7/913 samples. The structural stiffness alteration attributed to the sensor addition is negligible within the elastic region before the initial load drop, becoming more discernible beyond this point. A comparison between IM7/8552-Sensor(0) and IM7/8552-Sensor(45) samples suggests a slightly higher structural stiffness in the latter. This could be attributed to the alignment of the fibre orientation in the sensing layer and its adjacent carbon layer on the substrate, both positioned at 45°, thereby contributing to the sample's increased structural stiffness. Another point highlighted by Fig. 4-3 is that adding sensors can slightly change the first load drop and second load drop thresholds, meaning that the onset of delamination and final fibre failure is slightly influenced by incorporating sensors, and it is specifically more significant for the second load drop. This is regardless of the sensor attachment method and fibre orientation of the sensing layer, as this trend can be observed in all graphs.

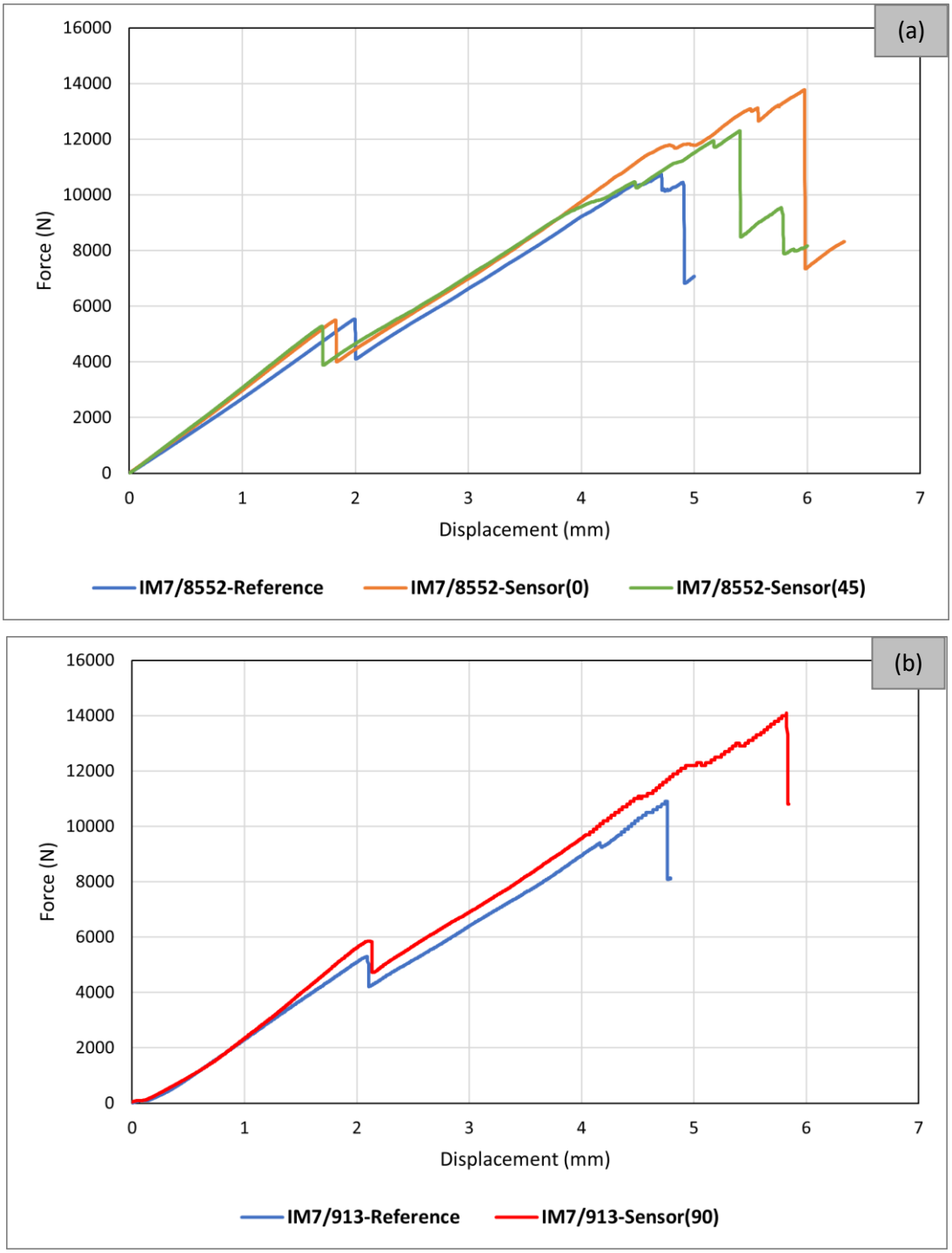

Fig. 4-3: Comparison of *Reference* and *Sensor* samples: a) IM7/8552, b) IM7/913

A summary of important information for a quantitative analysis that is obtained from indentation tests is presented in Table 4-1. The absorbed energy during an impact or indentation event at the first and second load drop can be attributed to the induced damage due to elastic and plastic deformations in the form of delamination and fibre failure, respectively. Therefore, comparing the absorbed energy of different samples can give interesting information about the damage mechanisms. Note that the absorbed energy at each displacement increment can be

easily calculated by multiplying the force and displacement values, then adding this result to the absorbed energy from the previous displacement increment. The results indicate that the energy absorption at the first load drop across all samples is relatively consistent. However, there is notable variability in the maximum energy absorption values (observed at the second load drop). For instance, adding sensors could increase the maximum absorbed energy by up to 56% and 27% for sensors with sensing layer fibre orientation of 0° and 45° in IM7/8552 samples, respectively, and by up to 62% for sensors with a sensing layer fibre orientation of 90° in IM7/913 samples. The higher energy absorption in IM7/8552-Sensor(0) compared to IM7/8552-Sensor(45) suggests more significant induced damage, characterised by increased deformation and energy dissipation.

Table 4-1: Summary of important information obtained from indentation tests

Sample	First load drop (delamination)				Second load drop (fibre failure)			
	Force (N)	Displacement (mm)	Energy absorbed (J)	Load drop ratio (%)	Force (N)	Displacement (mm)	Energy absorbed (J)	Load drop ratio (%)
IM7/8552-Reference	5542.28	1.99	5.43	25.85	10445.30	4.89	27.81	34.63
IM7/8552-Sensor(0)	5506.07	1.824	5.01	27.12	13780.18	5.97	43.37	46.73
IM7/8552-Sensor(45)	5284.29	1.70	4.498	26.47	12304.06	5.40	35.24	31.05
IM7/913-Reference	5300	2.09	5.16	20.56	10900	4.76	25.14	25.87
IM7/913-Sensor(90)	5850	2.12	5.69	19.31	14100	5.82	40.66	23.40

4.2.1.3. Sensor Activation and Visual Inspection

This section presents the visual inspection results, focusing on sensor activation and damage detection performance. Note that two methods were employed for inspection during the test: for IM7/8552 samples, a Nikon camera was synchronised with the test machine to capture images of the back face (non-impacted side) every second (see Fig. 4-4), while for IM7/913 samples, two cameras were utilised to record a video from either side of the sample throughout the test (see Fig. 4-5). As a result, Fig. 4-4(a), Fig. 4-4(b), and Fig. 4-4(c) exclusively display images of the back face, whereas Fig. 4-5(a) and Fig. 4-5(b) present screenshots extracted from the videos, showcasing images of both the front and back face at various stages of the test. For

the scale, images of the back face cover the whole sample size (100mm*150mm), and the diameter of the indenter in the images of the front face is 16mm.

As shown in Fig. 4-4(a), in IM7/8552-Reference sample, damage on the back face remains imperceptible until just before fibre failure occurs at the second load drop, around forces of approximately 10,000N. The initial point of visible damage is denoted by red colouring on the graph. This is where the structure has undergone significant damage and poses a very low residual structural integrity. However, across all three graphs associated with *Sensor* samples, it is evident that the sensor on the back face activates before the first load drop at forces below 5000N (highlighted by red colouring). This observation highlights the sensor's ability to detect damages as subtle as matrix cracks, given that its activation precedes the initial load drop, thereby rendering it a viable early-warning tool for BVID detection and avoiding delamination.

In Fig. 4-4(b), Fig. 4-4(c), and Fig. 4-5(b), the sensor on the back face activates before the first load drop, with the activated area expanding as the force increases. Upon analysing images captured during the indentation test of *Sensor* samples, it was observed that the visible damage pattern on the surface enlarges up to a certain point, that is where delamination has already happened, but fibre failure is yet to occur. However, beyond this point, the activated area exhibits minimal change despite increasing force. This suggests that in terms of detecting damage "levels" (rather than damage "existence"), the sensor is well-suited for identifying low-energy damage types such as matrix cracks and delamination. This is evidenced by the lack of significant alterations in the appearance of the samples (size and shape of damage pattern) beyond a certain force threshold. Nonetheless, the sensor can also be utilised for visualising and detecting higher-energy damage types. Furthermore, a comparison between Fig. 4-4(b) and Fig. 4-4(c) reveals sensor activation at a lower force for samples with a sensing layer orientation of 45°. This suggests that the activation force threshold could be influenced by altering the fibre direction of the sensing layer. This is further studied in the FEA section.

Fig. 4-5(a) illustrates that in the IM7/913-Reference sample, damage on the back face remained invisible even after fibre failure; however, it became visually detectable on the front face shortly before fibre failure, at forces around 9000N (highlighted in red). Conversely, with the incorporation of the sensor, damage in the IM7/913-Sensor(90) sample could be detected at forces as low as approximately 3000N and 6000N on the back face and front face, respectively (see Fig. 4-5(b)). Consequently, the sensor successfully visualised the BVID on both impacted and non-impacted surfaces. When subjected to out-of-plane loading, the damage on the back

face is tensile fibre failure because of the global bending effect, whereas the front face undergoes compressive fibre failure and local deformation due to local contact force. In thicker laminates, local damage tends to be predominant, whereas, in thinner laminates, such as those of this study, the global bending effect prevails, leading to more significant damage on the lower plies (back face). Consequently, initial failure in thin, flexible laminates typically occurs in the lower plies. Conversely, in thicker and stiffer laminates, initial failure occurs on the top surface due to contact stress [142,159]. This can explain an earlier sensor activation on the back face than the front face in the IM7/913-Sensor(90) sample. This was also observed in other studies on application of the hybrid sensor on CFRP and hybrid flax/carbon composites [170,171]. Note that the images showcased here were captured using a black-and-white camera available at the time of testing. For a more comprehensive interpretation of the images and to observe the colour changes induced by the sensor, please refer to the post-indentation images depicted in Fig. 4-7.

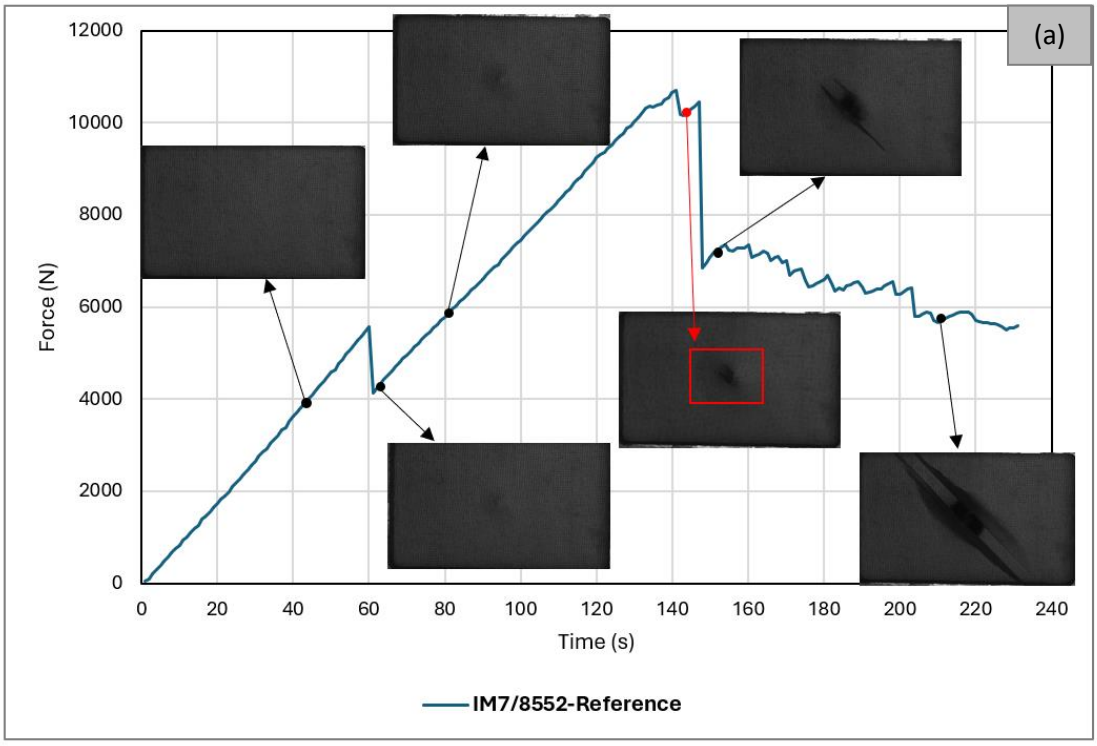

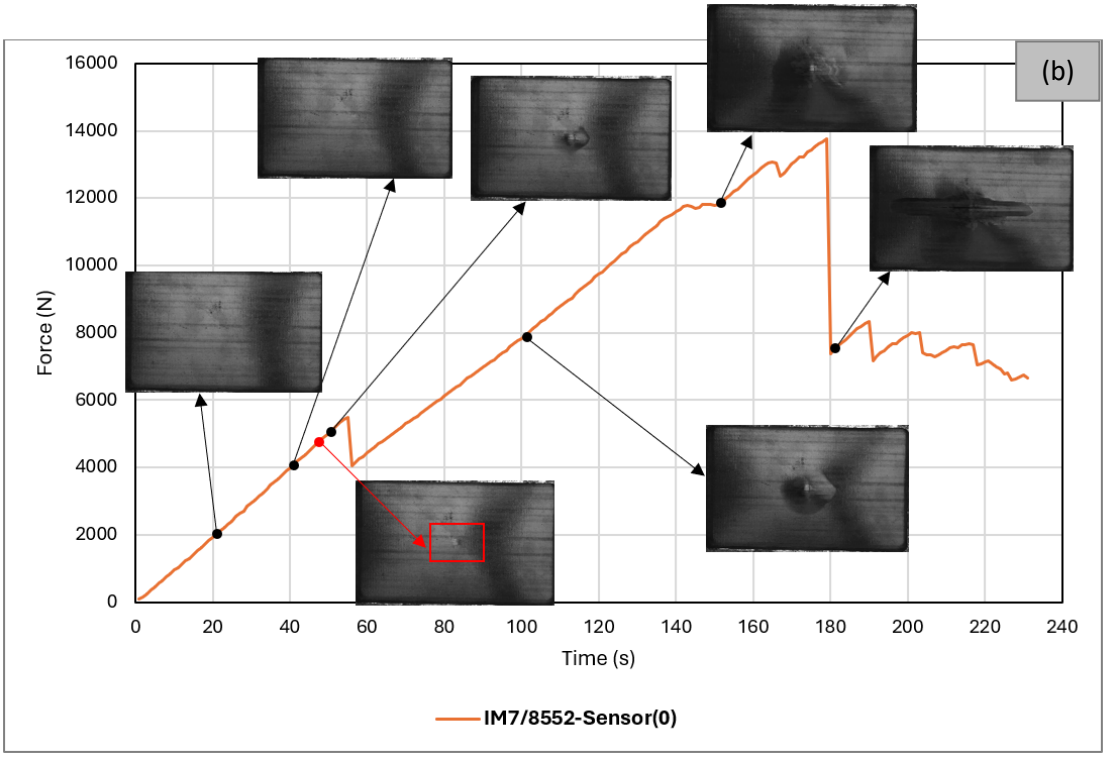

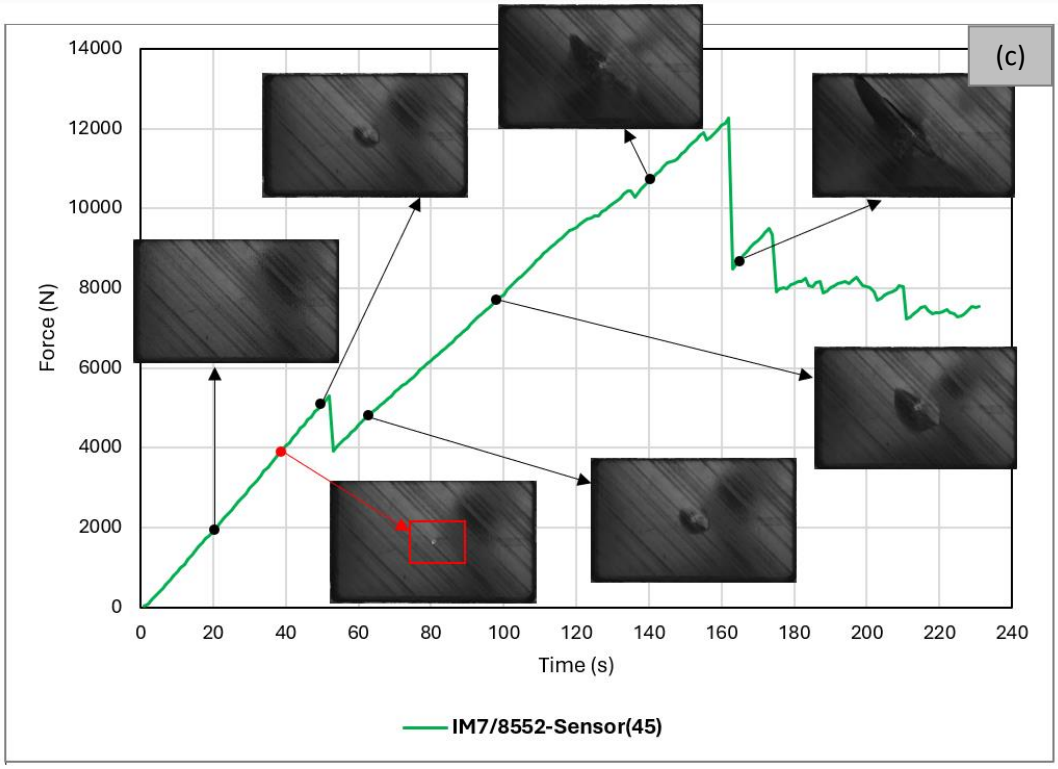

Fig. 4-4: Visual inspection and sensor activation during static indentation experiment: a) IM7/8552-Reference, b) IM7/8552-Sensor (0), c) IM7/8552-Sensor (45)

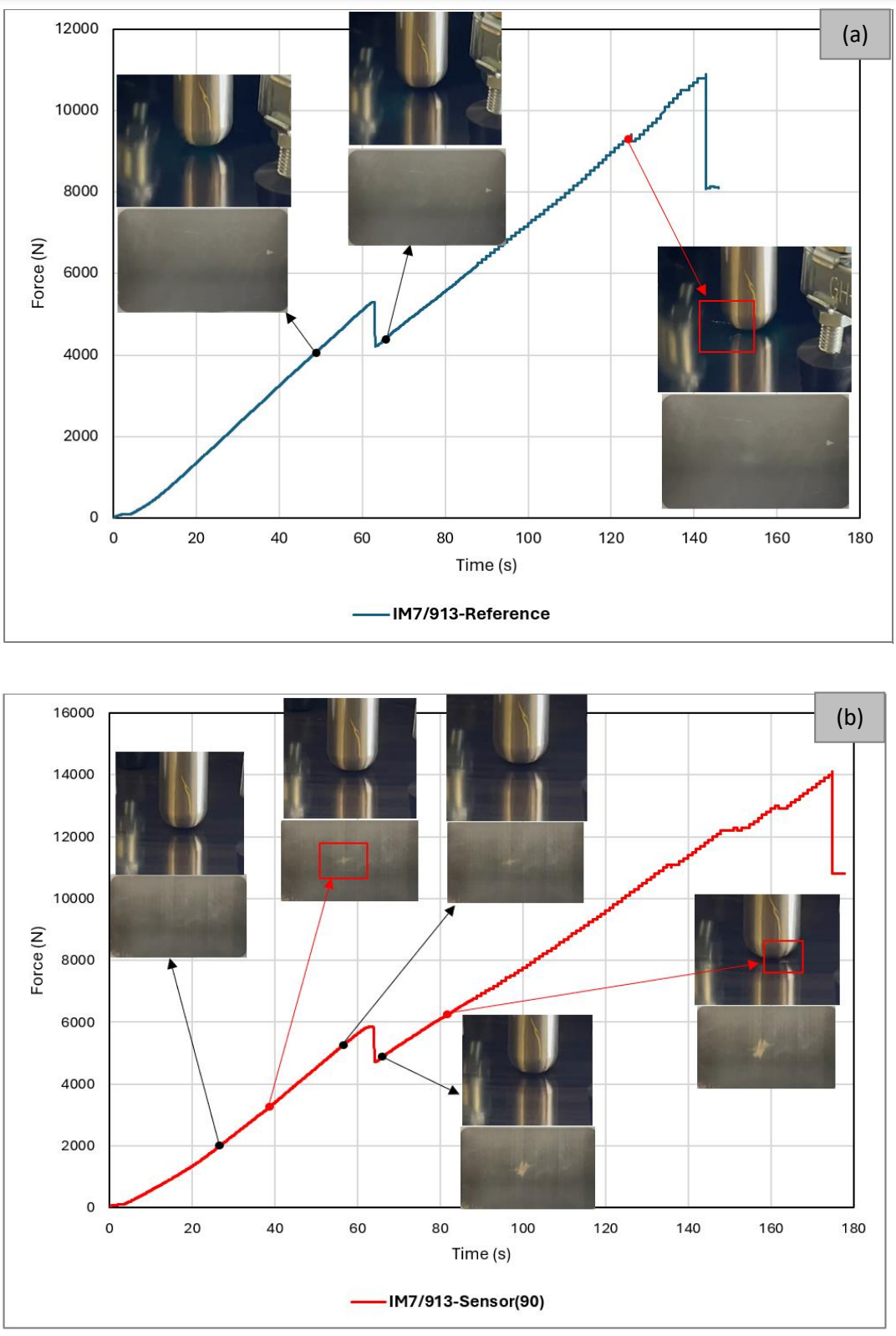

Fig. 4-5: Visual inspection and sensor activation during static indentation experiment: a) IM7/913-Reference, b) IM7/913-Sensor (90)

Fig. 4-6 represents a comparison of threshold energies for detecting damage across all tested samples, highlighting the performance of the sensor in visualising damage on the back face in IM7/8552 samples and on both the back face and front face in IM7/913 samples at very low energies. The threshold energies were determined as the point at which surface damage first became visible during testing. This damage appeared as a small dot indicating sensor activation for sensor samples, and as a visible dent or fibre failure for reference samples. Note that the energy thresholds for the front face and back face of the IM7/913-Sensor(90) sample in this figure allow for comparing the sensor activation time on either side. It is observed that while damage on the back face of IM7/8552-Reference sample is not visible until over 27J, it becomes visible in *Sensor* samples at energies as low as less than 5J. Moreover, interestingly, the damage on the back face of the IM7/913-Reference sample was not visually detectable even at termination time (which is the reason for the absence of data in the graph for the back face of IM7-Reference), while when adding a sensor, it could be detected before the delamination onset (at energies lower than 2J).

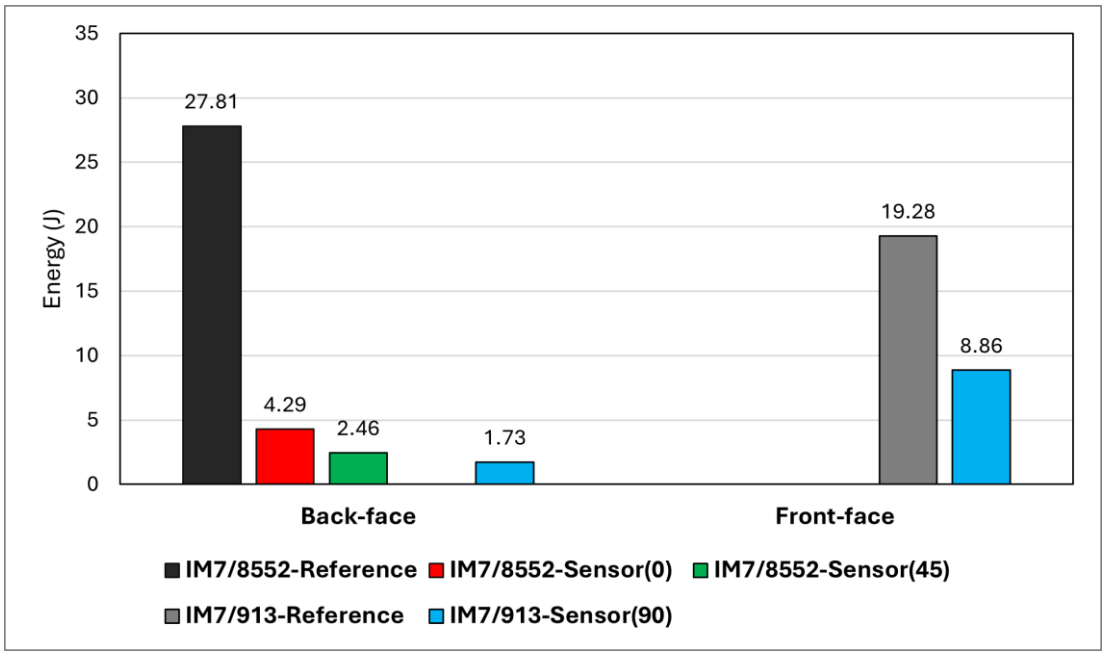

Fig. 4-6: Threshold energies for visually detectable damage.

The post-experiment inspection images are displayed in Fig. 4-7. Note that for IM7/913 samples, the tests were paused shortly after the second drop, whereas it continued for a relatively longer duration for IM7/8552 samples. Consequently, the varying damage patterns and sizes observed in these two groups do not necessarily indicate a difference in sensor performance. Moreover, the damage on the back face of the IM7/913-Reference was not visually detectable even at termination time, as shown by post-experiment visual inspection

images presented in Fig. 4-7(b). Note that Fig. 4-7(a) includes visual inspection images of an IM7/8552-Sensor(90) sample. This test was conducted initially, and its force-displacement graph was not included in the preceding sections. Its purpose here is to illustrate a comparison of visual damage patterns at various degrees.

Various modes of composite failure are observed in these specimens, stemming from indentation tests continuing until significant load drops are observed. In IM7/8552 samples (see Fig. 4-7(a)), noticeable damage is evident on the front face of the *Reference* sample. A recessed area is evident, where the indenter made contact with the specimen. Additionally, a series of small, stepped lines indicate cracks propagating in the upper carbon layer. On the back face, there is significant evidence of damage, particularly fibre failure at the centre of the image directly under the indenter, running parallel to the fibre direction. On the front face of *Sensor* samples, light-coloured patches parallel to the sensor fibre direction indicate sensor activation. On the back faces, the significant light patch directly under the contact area of the indenter demonstrates good sensor activation. Above and below the activated patches, the sensor activation appears striped; this indicates the strain due to the tension on the back face has exceeded the strain to failure of the carbon sensing layer. This result was seen when sensor-integrated specimens were tested in tension by Czél and Wisnom [71]. Overall, the visual damage pattern is larger on the back face than the front face. The IM7/913 samples demonstrate the same results (see Fig. 4-7(b)). However, there is a slightly different damage pattern in these samples. This is because of using a different peel ply in the manufacturing stage of these samples.

In summary, the findings of this section suggest that incorporating sensors can lead to notable improvements in visual inspection by revealing visible damage patterns on both the top and back surfaces. Additionally, it enhances the load-bearing capacity, offering flexibility in design to meet the specific requirements of each application. This adaptability can be achieved by adjusting sensor-related parameters, such as the fibre orientation of the sensing layer, to suit desired outcomes [172]. A more detailed collection of images captured during the indentation test of IM7/8552 samples, along with a link to access the videos recorded from both the top face and back face of IM7/913 samples, is included in Appendix A.

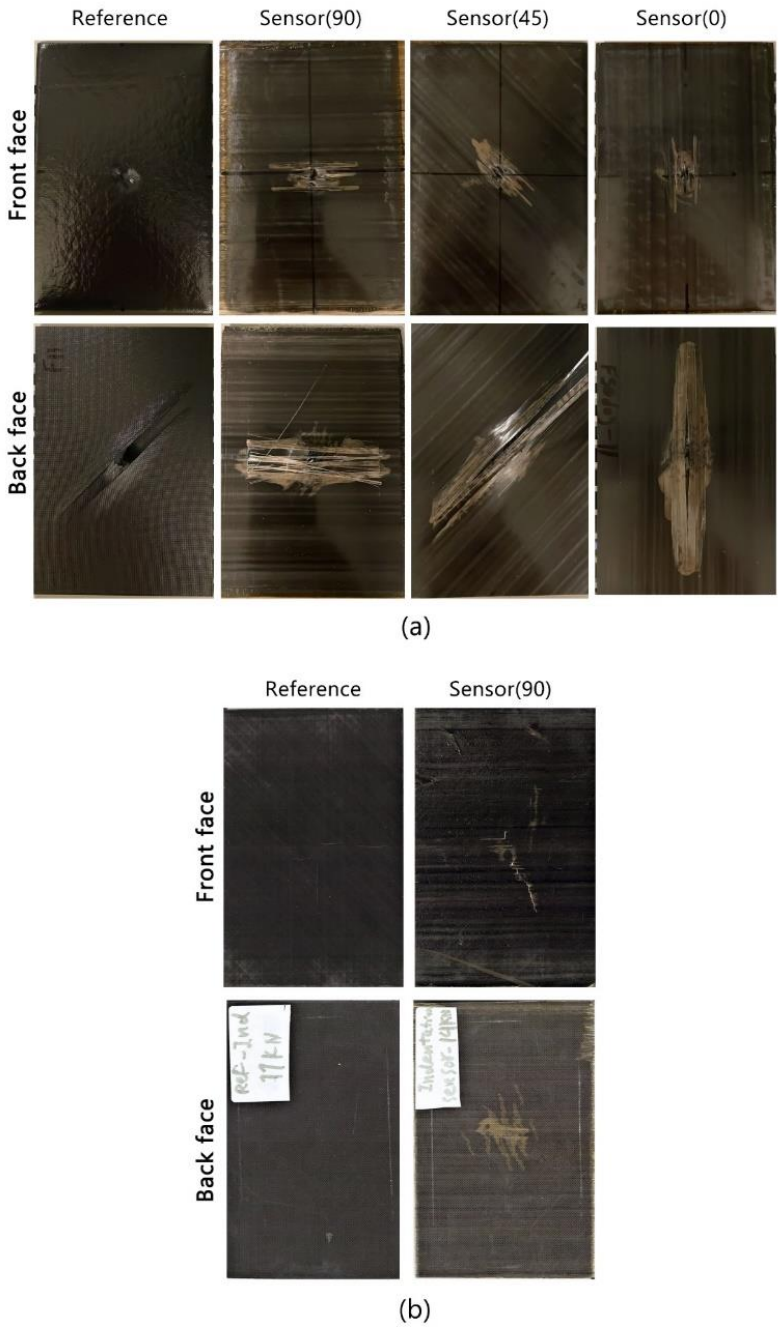

Fig. 4-7: Post-experiment visual inspection: a) IM7/8552 samples, b) IM7/913 samples.

A slightly different damage pattern in the samples shown in (a) and (b) is because of using a different peel ply in the manufacturing stage of these samples, and the fact that for (b), the test was interrupted at an earlier stage (immediately after fibre failure).

4.2.2. Low-Velocity Impact

4.2.2.1. Definition of BVID

Shah et al. [173] reviewed impact resistance and damage tolerance of FRP composites, summarising different damage scenarios with respect to permanent deflection (indentation) of the composite, including permanent indentation with rebounding of the impactor without perforation, with perforation and the penetration of the impactor (see Fig. 4-8(a)). As discussed in Chapter Two, BVID can be defined using various metrics or standards. In accordance with general guidelines, permanent indentations ranging from 0.3mm to 0.5mm suggest the presence of BVID, while indentations of 2mm or perforations of 20mm indicate minor visible impact damage. As indicated in [7], the impact energy required to induce BVID was estimated to be 40% higher than the critical energy level derived from the indentation test, owing to strain-rate sensitivity. Nevertheless, other studies have presented diverse correlations between the critical energy level in quasi-static indentation and low-velocity impact tests [18,128–130,159,174–179]. This will be studied in more detail in section 4.2.4 of this chapter. Based on indentation test results (Table 4-1), the required indentation energy to induce delamination was 5.69J. Therefore, the required impact energy for inducing delamination is estimated at 8.6J (around 50% higher). Hence, to guarantee the force is sufficient to induce delamination in impact tests, 12J was considered as the minimum impact energy in this chapter. Additionally, for investigating impact behaviour at higher energy levels, 18J and 27J were considered as the second and third impact energies for examination. Indentation results showed that for the IM7/8552-Reference sample, the energy required to induce fibre failure slightly exceeds 27J (see Table 4-1). Hence, this value was selected as the upper limit to study in this chapter. At these energies, samples undergo delamination; nonetheless, there is no perforation or penetration. This is indicated by a similar trend observed in the graphs obtained from the tests (see Fig. 4-9) to the situation ‘G’ depicted in Fig. 4-8(a). Furthermore, microscopy images of the cross-section of impacted samples confirm delamination occurring at the minimum considered impact energy (12J) (see Fig. 4-8(b)). For the scale, the image shows the central 5cm throughout the width. Nevertheless, surface damage is either invisible or barely visible on both impacted and non-impacted surfaces when viewed from a distance of 40cm at a viewing angle of 0°, thus classifying the damage as BVID. Moreover, the measured dent depth data from the Alicona 3D profilometer averaged around 0.5mm, showing minimal deviation across different groups. This confirms that for all samples, the dent depth aligns with the specified BVID range outlined in the aerospace sector [180].

Similar to indentation results, the impact test results are categorised into two sample groups: IM7/8552 and IM7/913. The former encompasses three impact energies (12J, 18J, and 27J) applied to two sets of samples, namely, the *Reference* and *Sensor* samples, with emphasis on the sensor performance across various impact energies. However, the latter involves two impact energies (12J and 18J) applied to three sample sets, *Reference*, *Sensor*, and *Sensor with cuts*, aiming to assess sensor performance with and without discontinuities (i.e., cuts) in the sensing layer. Every individual impact coupon test performed on IM7/8552 samples underwent two repetitions to verify repeatability. Given its stable repeatability at lower energy levels (12J and 18J), each test was subsequently conducted once for the lower energies on IM7/913 samples.

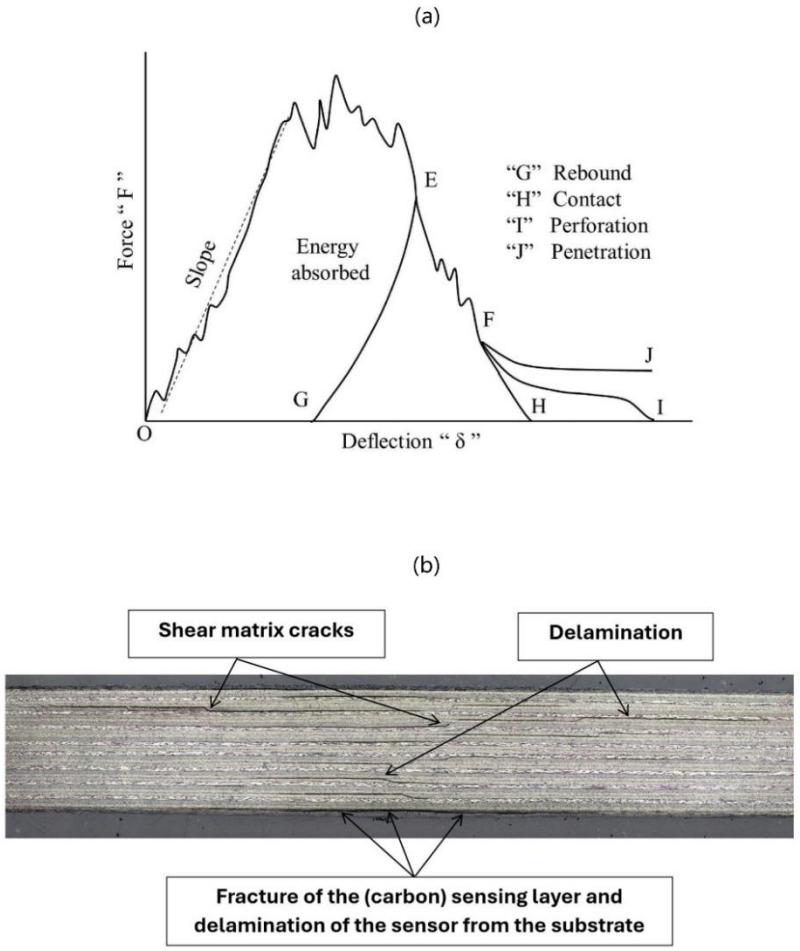

Fig. 4-8: a) Different damage scenarios with respect to permanent deflection (indentation) [173], b) The microscopy image depicts impact-induced damage at 12J, captured from the cross-section of the IM7/913-Sensor specimen, demonstrating internal damage mechanisms, such as shear matrix cracks and delamination. Additionally, the fracture of the carbon sensing layer and delamination of the sensor from the substrate are evident, both at the point of impact on the front and back faces.

4.2.2.2. Global Behaviour

The results of all impact tests on IM7/8552 samples are shown in Fig. 4-9. It indicates that at impact energies of 12J and 18J, both *Reference* and *Sensor* samples exhibit excellent repeatability, as evidenced by the close alignment of the graphs. However, some discrepancies arise at the impact energy of 27J, particularly noticeable when approaching the maximum force and displacement. Notably, this trend persists in both *Reference* and *Sensor* samples at the 27J energy level. This can be attributed to two potential factors. Firstly, the influence of boundary conditions may become more pronounced as the impact energy increases. This is because, in the impact tests conducted in this investigation variations in impact energy were achieved by altering the height from which the sample is dropped while maintaining a consistent weight. Consequently, at higher impact energies (27J), the sample undergoes a substantial increase in drop distance, intensifying the impact of boundary conditions on the dynamic response. This effect is notably more pronounced compared to lower energies (12J), where the distance between the impactor and the sample is minimal. This was also shown in the FEA section of Chapter Three (see section 3.5.3). Another factor contributing to the varying impact response at 27J energy could be related to the results obtained from the indentation tests. The energy required to induce fibre failure in the IM7/8552-Reference sample was measured at 27.81J, indicating that 27J serves as the threshold for failure occurrence. Therefore, upon examining the trends in the graphs in Fig. 4-9, it can be inferred that at 27J, one instance denotes the sample having undergone fibre failure, as evidenced by a distinct change in its curve pattern, particularly after reaching maximum force (see 27J-2 graphs in both Fig. 4-9(a) and Fig. 4-9(b)). However, in another instance, the sample sustained damages leading up to failure but did not reach failure, resulting in similar curve and drop patterns to lower energies (12J and 18J) across the entire displacement range (see 27J-1 graphs in both Fig. 4-9(a) and Fig. 4-9(b)). This is confirmed by visual inspection results that will be presented in section 4.2.2.5. In line with the research objective, which focuses on developing sensors for BVID, throughout the remainder of this chapter, the 27J-1 sample (the one without fibre failure) will represent the 27J energy in all graphs and tables, unless otherwise specified.

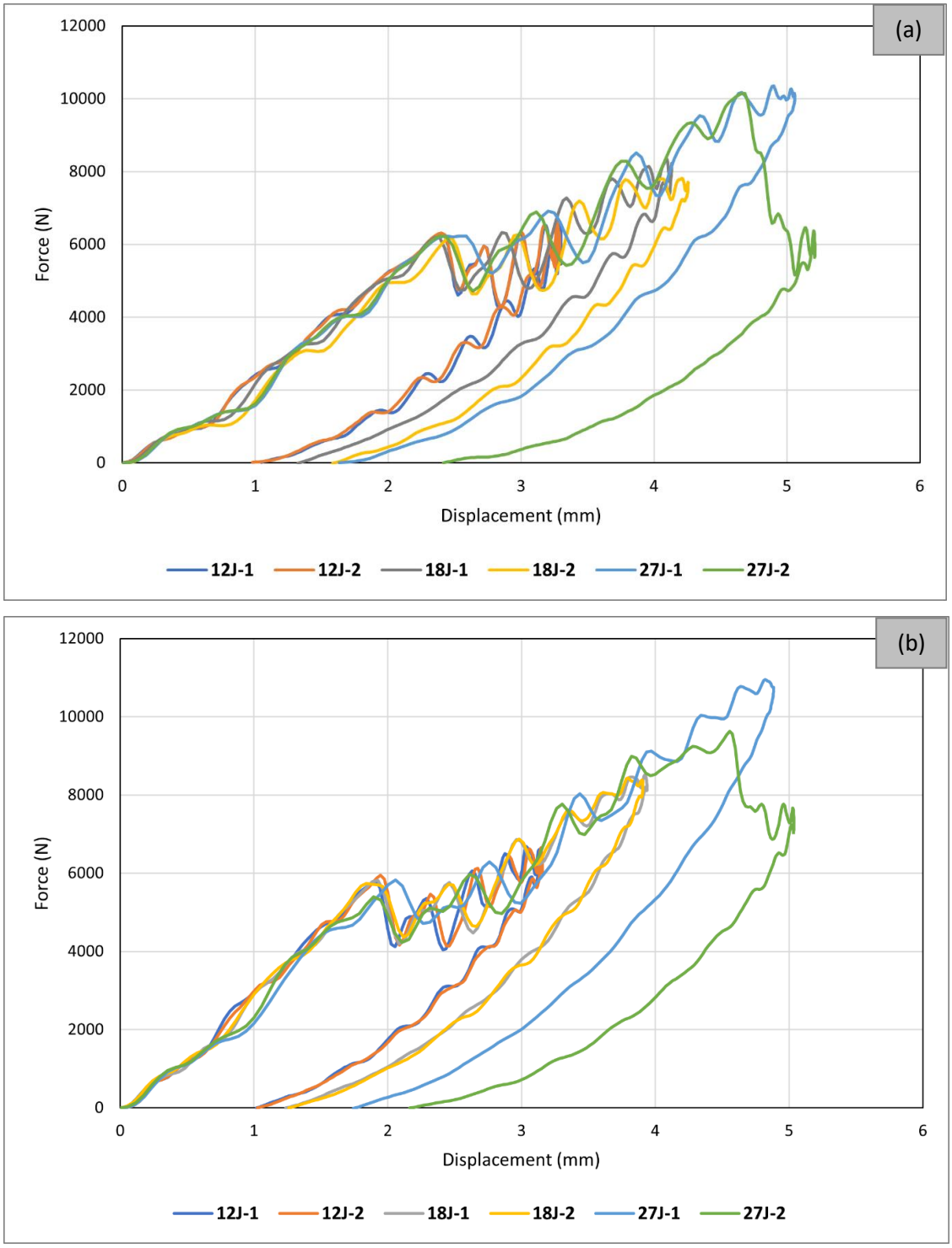

Fig. 4-9: Low-velocity impact test results of IM7/8552 samples: a) *Reference*, b) *Sensor*

To comprehensively analyse the global behaviour of a CFRP under the impact, the force-time, force-displacement, and absorbed energy-time graphs of the *Sensor* sample (18J-1) are depicted in Fig. 4-10. In Fig. 4-10(a), the force-time results, directly recorded and obtained from the data acquisition system during the impact test, are illustrated. The graph can be divided into two distinct phases. The first half commences with the initial contact between the

impactor and the specimen and extends until the velocity of the impactor reaches zero, indicating the point at which the impactor is about to rebound. Notably, a significant load drop associated with delamination is observable during this phase. A red graph corresponding to a hypothetical lower impact energy that does not cause any damage is also included, demonstrating no significant drop in load. The second half portrays the rebound process, concluding at the moment when the impactor completely separates from the sample. As damage is primarily incurred during the first half, multiple drops are evident in the graph, while the second half displays a smoother and less fluctuating trend. Fig. 4-10(b) illustrates the force-displacement history, calculated from the force-time results as detailed earlier in this chapter. The graph exhibits an initial almost linear response from 0 to nearly 6000N. Minor load drops in this region may be attributed to matrix cracking. Then, a sudden drop in load is observed, signifying the onset of delamination. Subsequently, intermittent minor drops occur until reaching a maximum force of slightly over 8000N. Following this, once the impactor has fully transferred its energy to the specimen, there occurs a redirection of elastic energy stored within the specimen back to the impactor, inducing a rebound phenomenon. This transition is graphically represented by a gradual reduction in both force and deformation. The plot of the unloading curve passes under the loading section of the plot; this encloses an area that corresponds to the total absorbed impact energy. This energy is absorbed through both the dynamic response of the specimen and through damage mechanisms. The change in gradient and the enclosed area indicate that damage has occurred for this impact energy. Nevertheless, the enclosed nature of the graph means that there is no penetration or structural failure [173], which supports findings from both indentation and visual inspection. Fig. 4-10(c) shows the energy-time history that can be divided into two parts: (a) elastic energy and (b) absorbed energy. The curve exhibits a progressive increase during loading, reaches a peak, decreases during unloading, and ultimately levels off at a constant value. The latter signifies the total energy permanently absorbed through damage mechanisms by the composite specimen at the end of the impact event. The peak of the curve corresponds to the respective impact energy (18J here). The force-time, force-displacement, and energy-time graphs for all tested samples are provided in Appendix B.

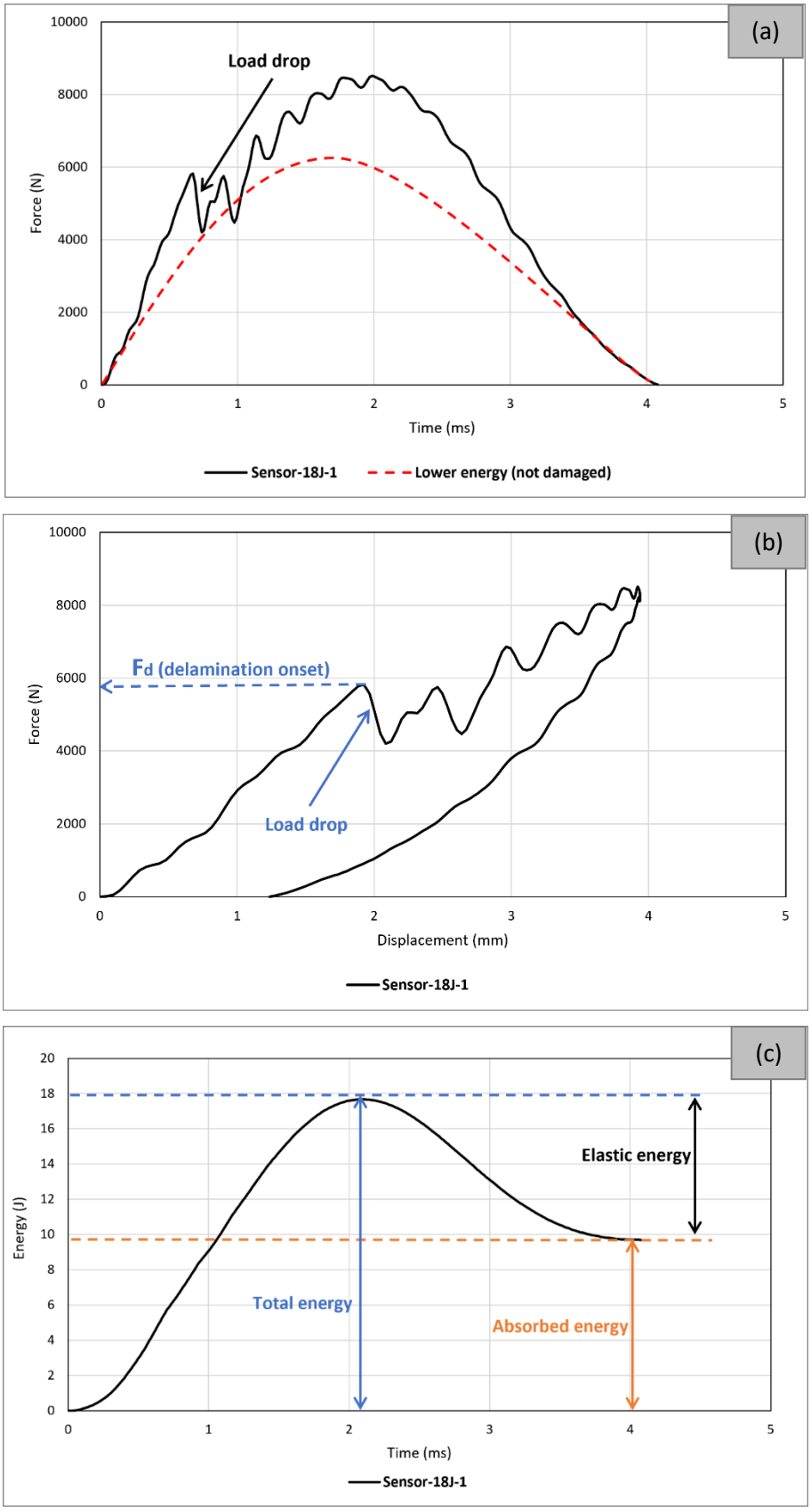

Fig. 4-10: Typical low-velocity impact test results: a) Force-Time, b) Force-Displacement, c) Energy-Time

4.2.2.3. Influence of Adding Sensors on Impact Properties

The assessment of composite materials' impact resistance typically involves examining aspects such as impact energy absorption, resistance to damage (specifically, the extent of damage following a non-penetrating impact), and tolerance to damage (residual properties after non-penetrating impact) [181]. This research focuses on energy absorption and resistance to damage. Accordingly, it is essential to understand the influence of sensor incorporation on the mechanical properties of the substrate structure and minimise this effect to achieve a reliable self-sensing system. Fig. 4-11 compares two groups of IM7/8552 samples, *Reference* and *Sensor*, at three different impact energies and important information obtained from the graph is presented in Table 4-2. The results demonstrate a higher maximum force at a relatively lower maximum displacement for *Sensor* samples compared to *Reference* ones, meaning that adding sensors slightly increased the rigidity and stiffness. Considering the maximum force, for example, the results suggest that adding sensors could increase the maximum force by approximately 1% at 12J energy, 2% at 18J energy, and 6% at 27J energy, indicating that the effect of adding sensors on impact behaviour appears to be more significant at higher impact energies. Overall, no significant difference can be seen between the two types of specimens, indicating the addition of sensors has little influence on the maximum force generated by the specimen, though it does slightly increase the energy absorption, suggesting the sensor may slightly enhance impact resistance in terms of the energy absorption capacity. The post-impact visual inspection revealed that these drop energies had activated the sensor, meaning that energy was absorbed by damage within the sensing layer, which could be a possible reason for the increased energy absorption in *Sensor* specimens. Overall, results suggest that within the BVID range, the sensor does not change mechanical properties significantly while improving the load-bearing capabilities (energy absorption) of the entire structure. A similar conclusion can be made when analysing IM7/913 samples (see Fig. 4-14). This aligns well with the indentation test results.

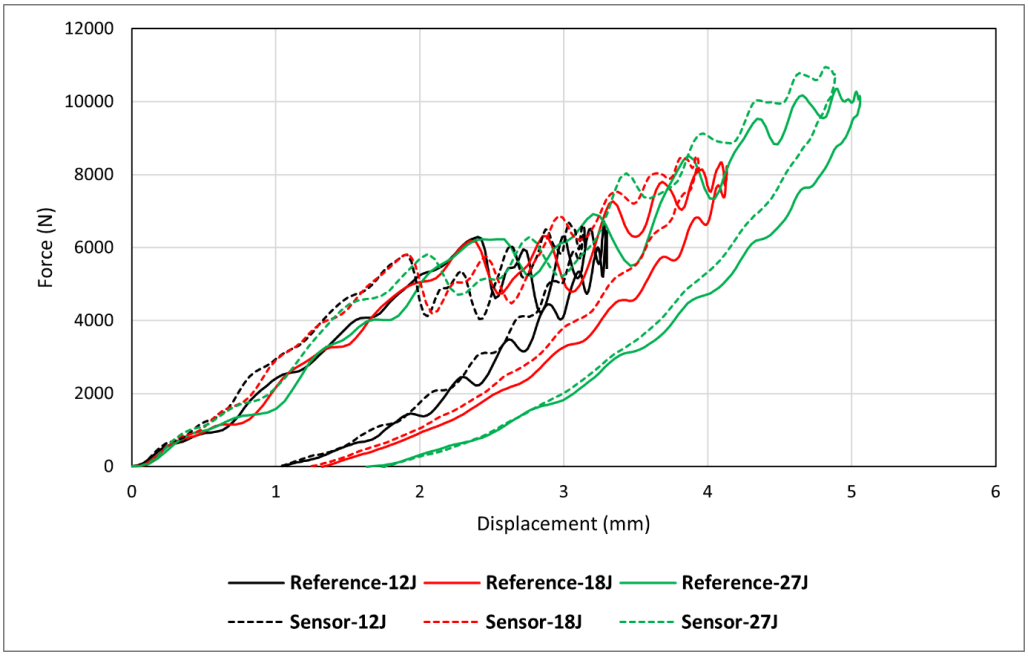

Fig. 4-11: Influence of adding sensors at different impact energies in IM7/8552 samples

Table 4-2: Summary of important information obtained from impact tests of IM7/8552 samples

	Maximum force (N)	Maximum displacement (mm)	Total energy (J)	Elastic energy (J)	Absorbed energy (J)
Reference-12J	6626.23	3.29	12	5.27	6.73
Reference-18J	8340.01	4.13	18	8.49	9.51
Reference-27J	10347.64	5.05	27	12.31	14.69
Sensor-12J	6686.51	3.14	12	5.10	6.90
Sensor-18J	8509.39	3.93	18	8.31	9.69
Sensor-27J	10949.49	4.88	27	11.98	15.02

4.2.2.4. Influence of Discontinuities in the Sensing Layer on Impact Properties

To expand the scope of impact testing on IM7/913 samples beyond the study of sensor integration influence, the effect of discontinuities (or cuts) in the carbon sensing layer of the sensor was also examined as another parameter of interest. Discontinuous composites provide an additional mechanism for generating extra strain by slip between ply fragments or fibres, producing a non-linear response that gives a warning before failure [1].

The suppression of delamination can be exploited in thin-ply unidirectional interlayer hybrid composites to make the pull-out of the broken low-strain material stable [71]. One issue with the thin ply hybrids is that the resulting carbon/glass volume ratio is relatively low if the thickness limit of around 85µm for that specific material combination is kept and standard thickness glass plies are used. In order to overcome this limitation, a unidirectional partially discontinuous architecture with a discontinuous carbon and continuous glass layers was proposed by Czel et al. [182]. Stable, progressive pseudo-ductile failure in tension with significant warning and margin before final failure was demonstrated with utilising the discontinuous hybrid architecture, and favourable stress–strain responses, with smooth transitions between the elastic and plateau strain regimes were achieved (see Fig. 4-12).

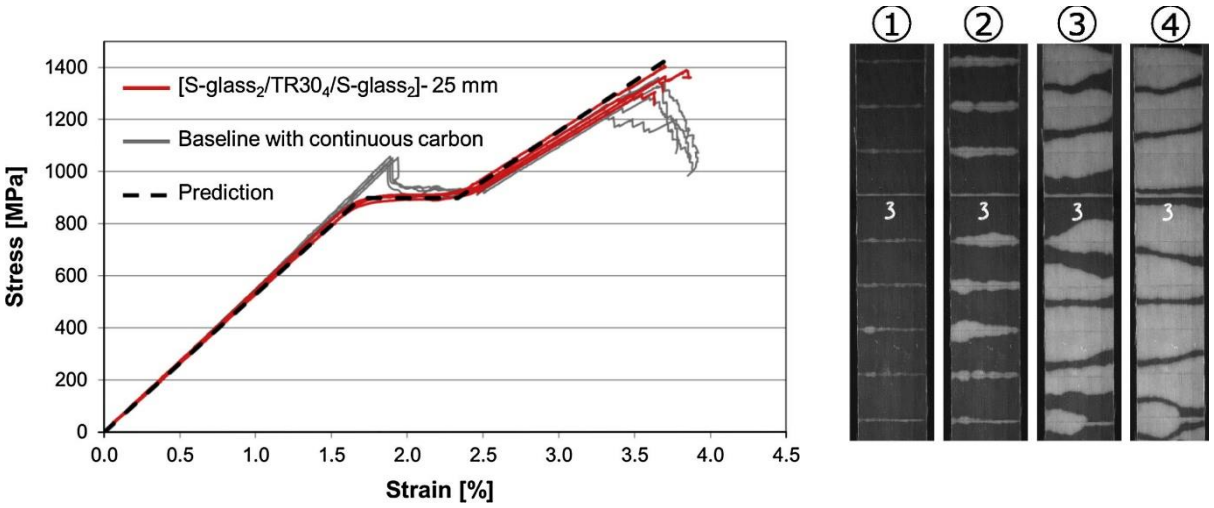

Fig. 4-12: Stress–strain curves of the specimens with continuous (baseline) and discontinuous architectures under tensile test with images showing different stages of damage process in the discontinuous specimen [182]

Discontinuous fibre composites allow intimate mixing of different fibres, which is very difficult to achieve with continuous fibres. Aligned fibre hybrid composites have demonstrated the largest potential for pseudo-ductility and other performance targets in discontinuous materials [1]. The design space can be greatly increased by combining different lengths as well as different types of fibres to optimise performance. Aligned discontinuous fibre composites provide a route to make use of recycled fibres, which are usually in a discontinuous, randomly-oriented form. This approach enables the creation of a high value product, contributing to the sustainability of composites. Recycled and virgin fibres can be combined to optimise mechanical properties. These discontinuous fibre composites can also show a ductile response during component manufacturing, allowing more complex geometries to be formed with less

defects. To the best of the author's knowledge, this approach has only been utilised under tensile loading and not under out-of-plane loading conditions. Hence, the introduction of discontinuities in the carbon sensing layer aims to explore the effect of cuts on the mechanical and sensing capabilities of the sensor-integrated composites. A collaborative project with a master's student was undertaken during the experimental phase of this investigation to comprehensively investigate the influence of introducing cuts in the sensing layer. Together, we designed and manufactured quasi-isotropic hybrid flax/carbon composites outfitted with hybrid thin-ply glass/carbon sensors, subjecting them to static indentation and low-velocity impact tests. Alongside participating in the manufacturing, testing, and result analysis, I co-supervised the student. The hybrid flax/carbon composite samples involved 16 plies of flax sandwiched between 2 carbon plies on each side, with lay-up arrangement of $[(0/90)^{C}(45/0/90/-45)_2^{F}]_s$ (see Fig. 4-13).

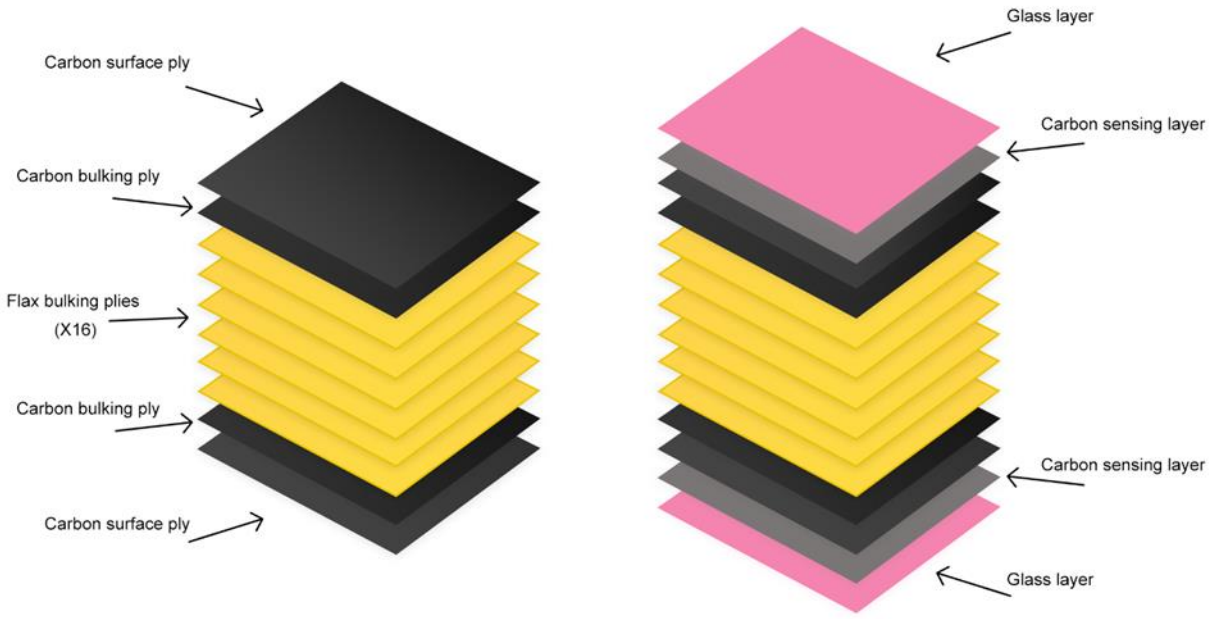

Fig. 4-13: Comparison of flax/carbon samples with and without hybrid glass/carbon sensors: left side depicts samples without hybrid sensors, while the right side shows samples with sensors integrated on both front and back faces. The sample on the left measures 5.6mm in thickness, while the one on the right measures 6mm.

In this chapter, for brevity, only a selection of force-displacement graphs and post-experiment visual inspection results are provided (see Fig. 4-15). Note that the manufacturing and testing procedures for the hybrid flax/carbon samples were similar to those utilised in this study. Essential details from that project are outlined in Table 4-3.

Table 4-3: Mechanical properties of the prepregs used in flax/carbon project [171,183]

Prepreg	Cured ply thickness (mm)	Strain to failure (%)	Tensile Modulus (GPa)
XC130 carbon/epoxy	0.25	1.5	55.2
EPC300 flax/epoxy	0.28	-	30.4
S-Glass/R913 glass/epoxy	0.15	3.7	45.6
YS-80 carbon/epoxy	0.05	0.5	785

The graphs depicted in Fig. 4-14 illustrate that the *Sensor with cuts* samples exhibits similar impact behaviour to *Sensor* samples, with only a slight reduction in overall stiffness. Specifically, the graph for *Sensor with cuts* sample falls between the curves of the *Reference* and *Sensor* samples (for 12J). This indicates that while the addition of cuts decreases rigidity compared to *Sensor* samples, it remains higher than that of the *Reference* samples. This trend is evident in the force-displacement graphs of both indentation and impact tests for the hybrid flax/carbon samples, as shown in Fig. 4-15. Furthermore, a comparison of maximum force, maximum displacement, and absorbed energy values presented in Table 4-4 supports this observation. A lower energy absorption in *Sensor with cuts* sample than the *Sensor* sample is because in the former, the sensing layer is already partially fractured, so less energy than an intact sensor is required to completely fracture it. Therefore, it can be concluded that, in terms of mechanical properties under out-of-plane loading, introducing cuts does not induce a significant change. If achieving mechanical behaviour closer to that of structures without sensors is desired, utilising a sensor with a discontinuous carbon sensing layer would be advantageous. Additionally, the indentation results of the hybrid flax/carbon composite project suggest that introducing cuts can activate the sensor at a lower force threshold. This implies that the sensor activation threshold can be controlled through the introduction of cuts. This is because once a crack initiates at a cut, it can propagate more readily through the material, leading to faster failure.

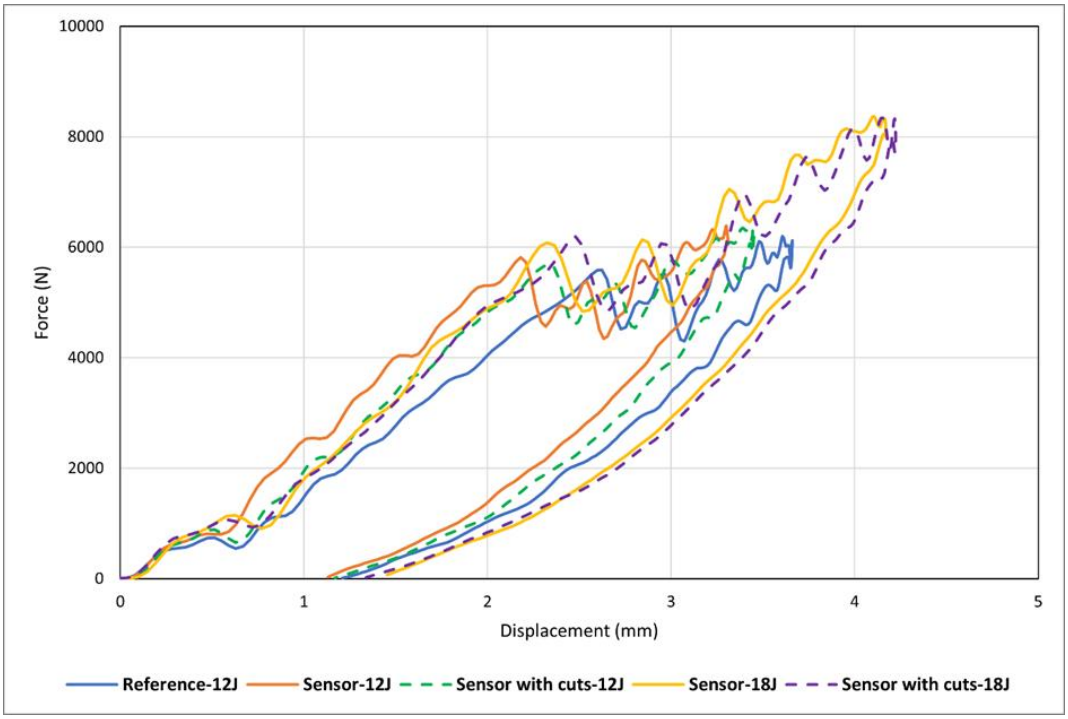

Fig. 4-14: Low-velocity impact test results of IM7/913 samples, highlighting the influence of discontinuities in the sensing layer on the impact properties at different energies

Table 4-4: Summary of important information obtained from impact tests of IM7/913 samples

	Maximum force (N)	Maximum displacement (mm)	Total energy (J)	Elastic energy (J)	Absorbed energy (J)
Reference-12J	6201.17	3.66	12	5.66	6.34
Sensor-12J	6384.93	3.31	12	5.20	6.80
Sensor with cuts-12J	6350.27	3.45	12	5.29	6.71
Sensor-18J	8367.37	4.16	18	8.46	9.54
Sensor with cuts-18J	8342.74	4.22	18	8.50	9.50

Looking at the visual inspection results for hybrid flax/carbon samples under both indentation and impact conditions (see Fig. 4-15), as well as for IM7/913 samples under impact (see Fig. 4-19), it becomes evident that introducing cuts can significantly enhance the visibility of damage. In both Fig. 4-15(a) and Fig. 4-15(b), a more pronounced visual damage pattern is observed for samples with cuts compared to those without cuts, under similar indentation termination force and impact energy, respectively. While this holds true for both the front face

and back face, the efficacy of cuts appears to be more pronounced on the back face, where the primary damage mode is tensile fibre failure. For the scale, images in Fig. 4-15(a) covers the entire width of the sample (100mm). A more detailed analysis of the visual inspection results is presented in the next section.

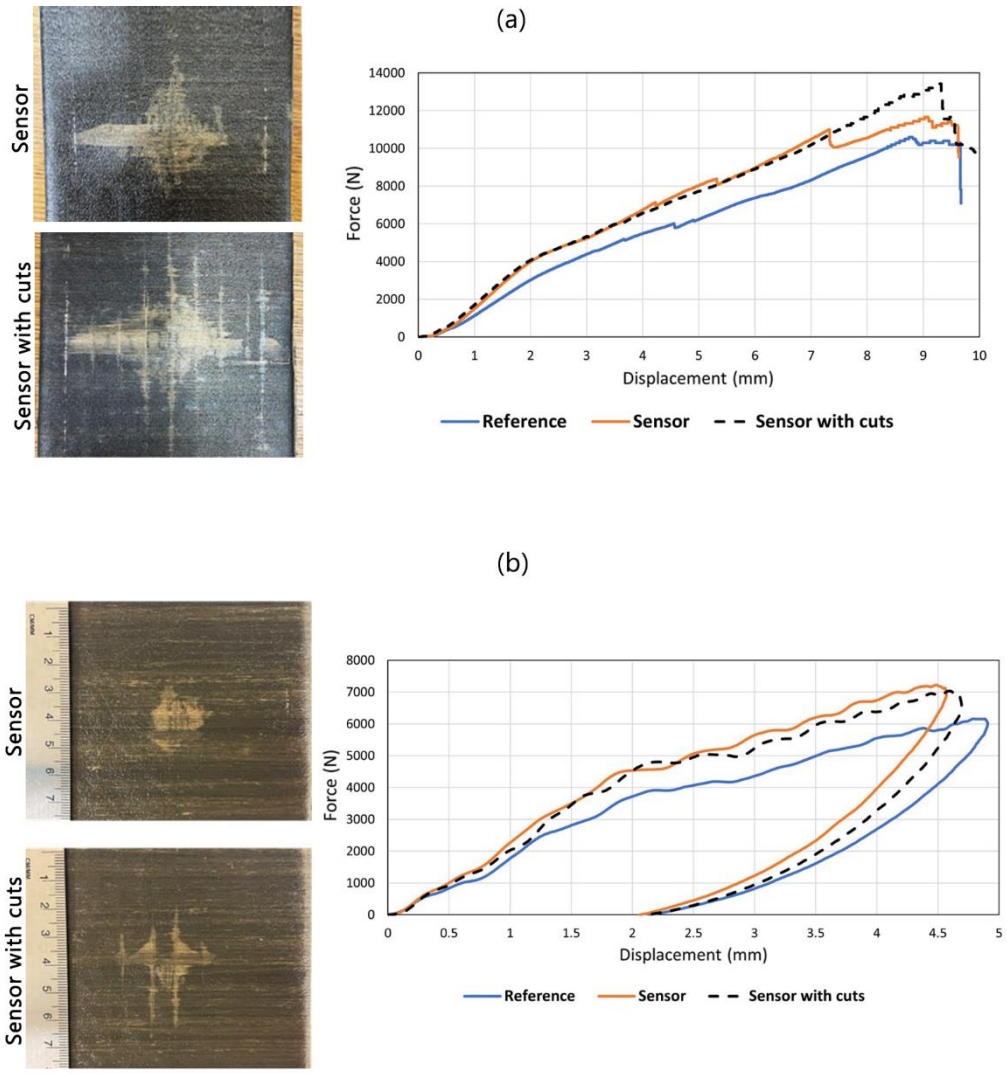

Fig. 4-15: The influence of sensing layer discontinuities on mechanical properties and visual damage inspection in hybrid flax/carbon composites: a) indentation, b) impact [171,183]

A comparison of the absorbed energy between the *Reference* and *Sensor* samples at different impact energies is depicted in Fig. 4-16. The results signify that across both IM7/8552 and IM7/913 groups and all impact energy levels, *Sensor* samples constantly absorb slightly higher energy than *Reference* ones. This can be seen as a side benefit of the sensor, enhancing impact damage tolerance through energy absorption mechanisms. Moreover, it is seen that the energy

absorption of the *Sensor with cuts* samples is between those of the *Sensor* and *Reference* samples.

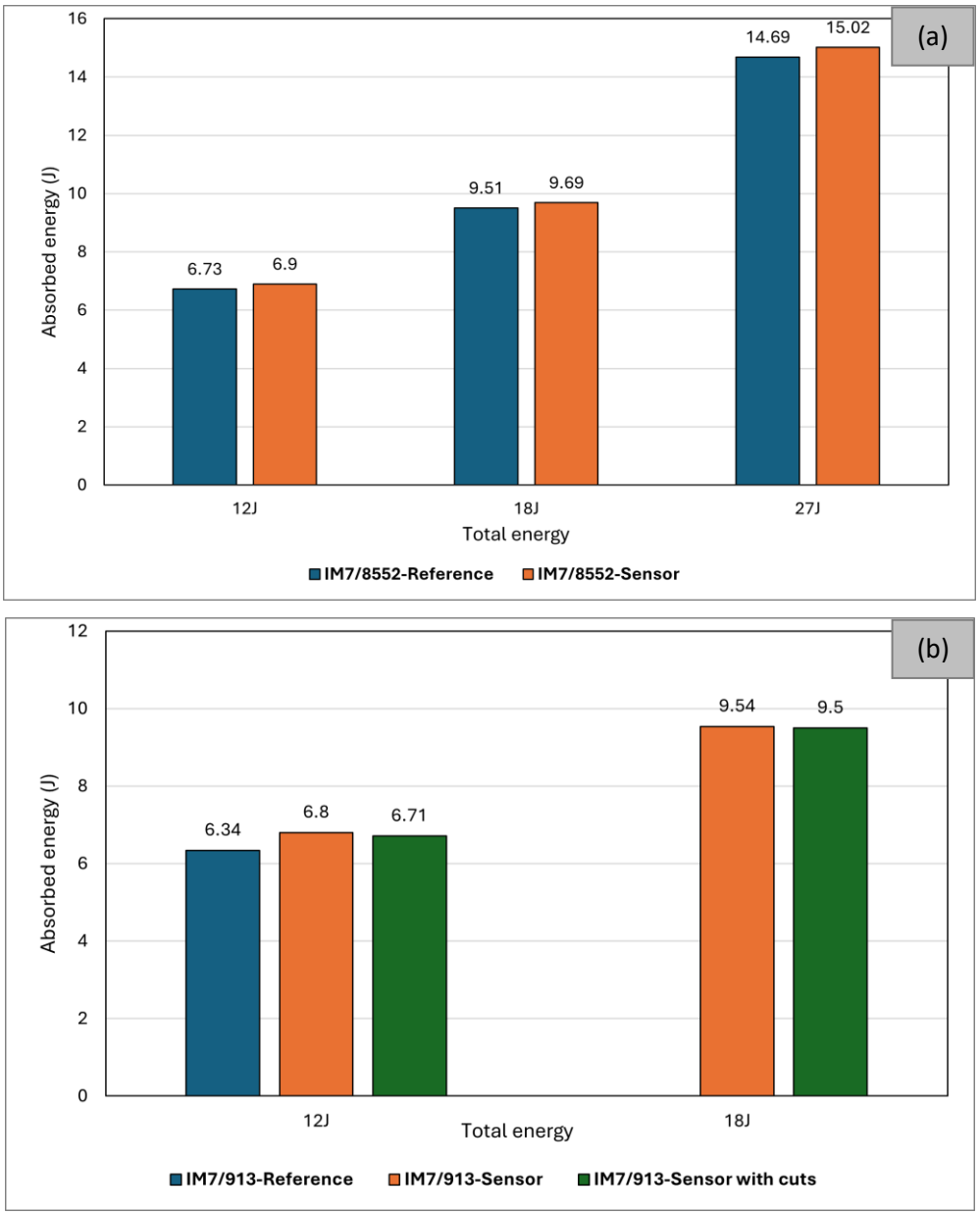

Fig. 4-16: Comparison of the absorbed energy in all samples at various impact energies: a) IM7/8552 samples, b) IM7/913 samples

4.2.2.5. Ultrasonic C-scan and Visual Inspection

No visible signs of impact damage on the back face are apparent in any of the three energies investigated in the *Reference* samples within the IM7/8552 group. However, upon closer scrutiny of the 27J sample, a subtle indentation is discernible in the region directly affected by the impactor on the front face, suggesting internal damage within the specimen, indicative of

BVID. This becomes more apparent upon physical examination. Ultrasonic examination, on the other hand, reveals evidence of internal delamination damage across all three energy levels, with the extent of damage increasing proportionally with energy input (see Fig. 4-17(a)). In contrast to the *Reference* samples, the visual inspection results of the *Sensor* samples clearly reveal damage on both the top and back faces. This indicates that the sensor was triggered at all three energy levels, with the visual damage proportionately increasing as energy levels rise. Notably, the visual damage pattern on the back face differs from that on the front face due to different damage modes. On the back face, a discernible light patch suggests sensor activation due to tensile strain from the impact loading. Within this region, a darker speckled area indicates fibre fracture within the sensing layer, while a larger, lighter area signifies delamination of the glass layer from the carbon sensing layer. The front face displays less pronounced sensor activation, though it still exhibits a discernible activated area. With increased energy, the activated area expands more prominently in a direction perpendicular to the fibre direction. Additionally, short white lines surrounding the impacted area, aligned parallel to the sensor fibre direction, indicate matrix damage within the sensing layer. This is particularly noticeable in the case of 27J energy (see Fig. 4-17(b)). For the scale, all images in this figure cover a dimension of 50mm*50mm.

Fig. 4-18 compares the size of the visual damage area on the surface and the size of the C-scanned damage area for the *Sensor* samples at the three impact energies. It is evident that as the impact energy increases, both the C-scanned and sensor-activated areas on the surface also increase. However, there is an exception with the activated area on the front face of the 18J sample. Note that the values on the vertical axis of this graph represent the activated area size, which is smaller for the front face at 18J compared to 12J due to its inconsistent elongated length but relatively shorter width, unlike the 12J sample, which covers a consistently smaller area. Nevertheless, the visible damage in the 18J sample is still more significant than in the 12J sample. Overall, this graph suggests that the activated damaged area on the surface can serve as an estimate of the severity of internal damage.

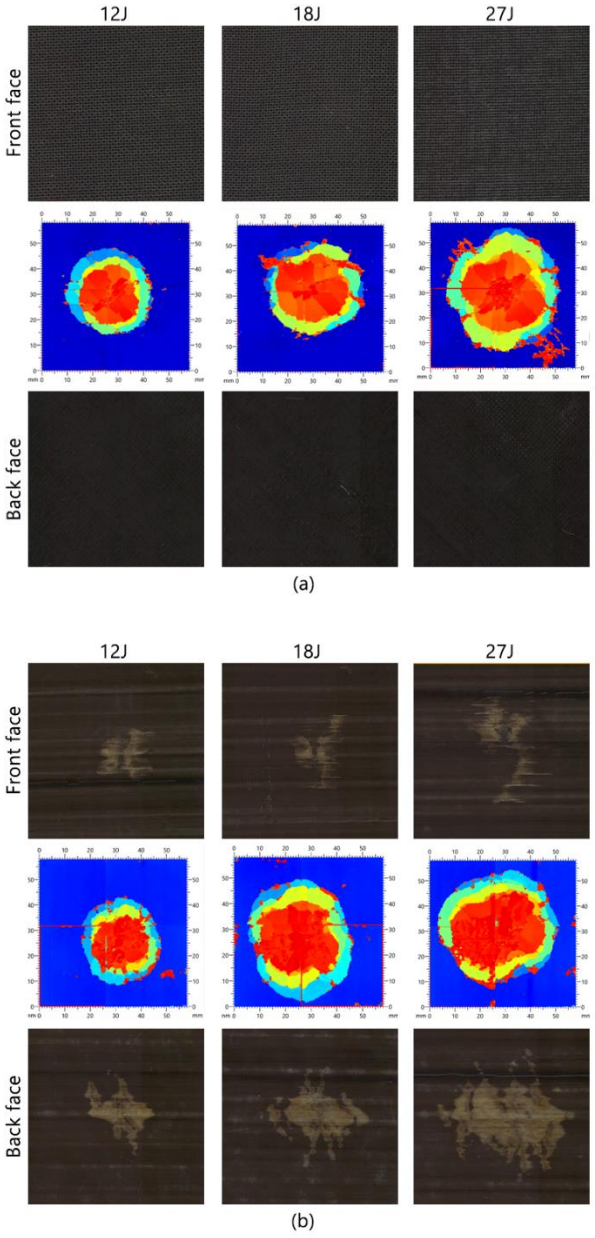

Fig. 4-17: Ultrasonic C-scan and visual inspection results of IM7/8552 samples, a) Reference, b) Sensor

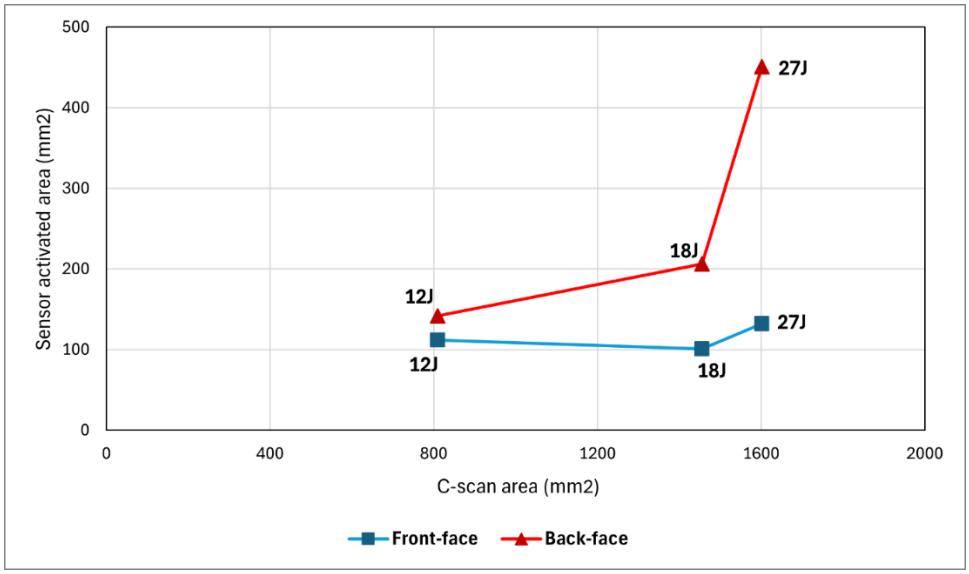

Fig. 4-18: Comparison of the surface visible damage area and C-scan damage area for IM7/8552 samples at three impact energies

The findings from the IM7/913 samples align closely with those obtained from the IM7/8552 samples, underscoring the sensor's efficacy in detecting damage that is not visible in *Reference* samples (see Fig. 4-19). For the scale, all images in this figure cover the entire surface of the specimens. In Fig. 4-19, the back face of the *Sensor with cuts* samples exhibits sensor activation in a pattern similar to that of the *Sensor* specimens. Notably, light-coloured lines perpendicular to the fibre orientation indicate activation surrounding the cuts in the sensing layer. The front faces of the *Sensor* and the *Sensor with cuts* specimens display similar appearances. The effect of the discontinuities is revealed by the lighter lines running around the slits in the sensing layer, underscoring the efficacy of introducing such discontinuities for enhanced inspection. Interestingly, this effect appears more pronounced on the surface opposite the impacted area. Moreover, it proves more effective at higher energies, as a comparison between the *Sensor* and *Sensor with cuts* samples at 18J reveals a more significant difference compared to the comparison at 12J. Overall, the results suggest that adding discontinuities does not significantly alter the mechanical response. However, it enables the adjustment of the sensor activation force threshold and markedly improves visual inspection. This underscores the effectiveness of the proposed discontinuous architecture in damage inspection under out-of-plane loading conditions.

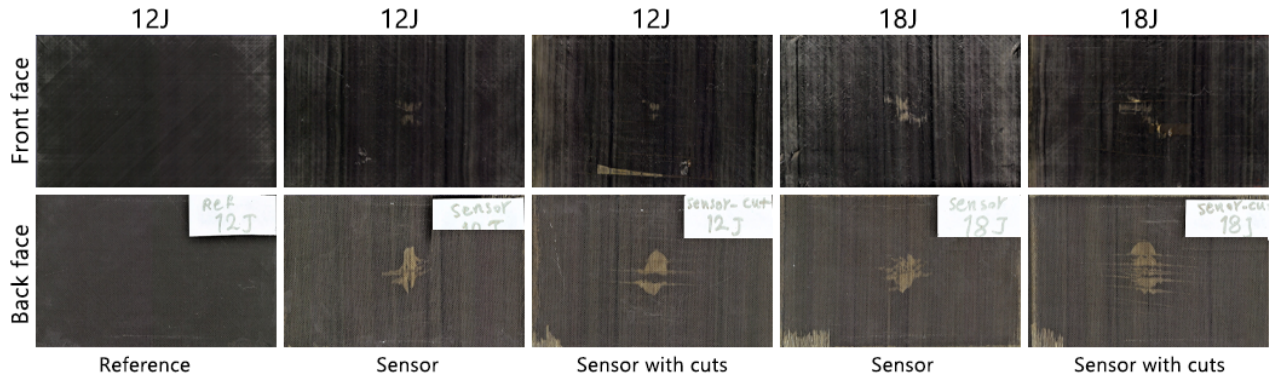

Fig. 4-19: Visual inspection results of IM7/913 samples

4.2.3. Comparison of Sensor Attachment Methods

A brief study was conducted to assess the efficacy of the two bonding methods. It was concluded that both one-step curing and two-step curing methods provide excellent sensor adhesion to the substrate and achieve a high-quality surface finish, as evidenced by all sensors displaying the anticipated striped pattern without premature debonding. However, a notable difference emerged in the final thickness of the sensor. In the case of the one-step method (IM7/913 samples), the thickness of the *Sensor* samples increased by 0.4mm compared to the *Reference* samples. However, with the two-step curing method (IM7/8552 samples), the thickness only increased by 0.16mm when comparing *Reference* and *Sensor* samples. A similar trend was observed when comparing the mass of the structures in IM7/913 and IM7/8552 samples. In IM7/913 samples, the mass increased from 77g in the *Reference* to 89g in the *Sensor* samples, while in IM7/8552 samples, it only increased from 95g in the *Reference* to 102g in the *Sensor* samples. This suggests that the two-step curing method appears to provide a higher level of integrity, resulting in a smaller difference in the total thickness and mass of the structure when incorporating sensors.

4.2.4. Comparison of Low-Velocity Impact and Quasi-Static Indentation

Given the dynamic nature and short duration of low-velocity impact tests, analysing the progression and development of degradation mechanisms within a structure during such tests proves challenging and can mainly occur post-test completion. Consequently, researchers have redirected their attention to the static indentation test, which has demonstrated similar overall behaviour and resulting damage states compared to low-velocity impact tests [18,128–130,159,174–179]. The static indentation test offers the advantage of pausing the test at different stages, allowing for the observation of damage evolution. Nonetheless, it is crucial to

thoroughly examine the similarities and disparities between these two tests to gain a deeper understanding of their correlation and the potential for substituting a low-velocity impact test with a quasi-static indentation test. Fig. 4-20(a) compares force-displacement curves for the indentation and impact tests of this research. Note that the curve labelled "27J" in Fig. 4-20(a) corresponds to the "27J-2" curve depicted in Fig. 4-9(a). This choice was made because the "27J-2" sample experienced fibre failure, enabling a comparison of fibre failure in both indentation and impact tests. Different parameters can be considered to compare the quasi-static indentation and low-velocity impact tests, such as the dent depth, the initial stiffness (before the first load drop), the percentage of the first load drop, critical delamination load (at first load drop), the delamination size, and the fibre failure load (or its equivalent absorbed energy). Abi Abdellah et al. [18] reported that during low-velocity impact tests, the total energy exceeded that of static tests for the same impactor displacement. However, the absorbed energy remained consistent between static and dynamic scenarios, indicating an equivalence in terms of damage under comparable displacement conditions. This finding was supported by observations made through X-ray analysis, microscopic examination, and the evolution of crack lengths. Sun and Hallett [16] conducted both tests on quasi-isotropic composites with ply-block scaling and sub-laminate scaling configurations (the latter is similar to specimens used in this investigation). Some indentation tests were paused at different stages of damage progression, and X-Ray CT scanning and ultrasonic C-scan tests were conducted to compare the delamination patterns with matrix cracks in neighbouring plies in both tests. The overall damage morphologies showed remarkable similarities regarding individual delamination shapes, the number of major matrix cracks, interactions between matrix cracks and delamination, bottom transverse crack length, and delamination-free zone size. Given the high similarities between the two loading scenarios at both interlaminar and ply levels, they inferred that the interaction mechanism between matrix cracks and delamination is governed by the plate response under transverse loading, regardless of the loading rate employed during testing. The permanent indentation depth resulting from the quasi-static indentation test was larger than that from the impact test for equivalent energy absorption levels. Furthermore, it was noted that, for a specified delamination area, the indentation depth is greater in indentation tests than in impact tests. This could be attributed to the significantly longer duration of transverse loading in static tests compared to impact tests, resulting in less energy dissipation through other mechanisms. Similar results about the comparison of the permanent indentation between the two tests were reported in [176].

Herein, a comparison of the critical delamination load, the initial stiffness, and fibre failure load obtained from the test results of this investigation are provided (see Fig. 4-20(a)). This comparison is also extended to the test results reported by Fotouhi et al. [7], as depicted in Fig. 4-20(b). The inconsistency in critical delamination loads between indentation and impact tests is readily apparent, with the critical loads in static indentation tests consistently lower than those in impact tests. Additionally, the critical load for impact tests under various energy levels appears to align closely, all approximately 6300N, whereas the equivalent static load is nearly 5500N (see Fig. 4-20(a)). The critical indentation and impact loads shown by Fig. 4-20(b) are 4900N and 6900N, respectively. These align with findings reported in [16,18,174]. Sun and Hallett [16] also observed a similar trend, reporting an average increase of nearly 30% in the ply-block scaling and samples and 40% in the sub-laminate scaling samples for dynamic critical load compared to static critical load. Hence, it can be concluded that the increase in critical load under dynamic loading is independent of impact energy, sub-laminate scaling (ply-block), and laminate overall thickness for a given material system. Moreover, there appears to be variation in the percentage of load drop. However, due to significant vibrations and the dynamic effects of the plate during the loss of stiffness, the level of load drop in impact cases directly taken from force plots may not be entirely accurate.

Both Fig. 4-20(a) and Fig. 4-20(b) demonstrate a high level of similarity in the initial stiffness of the load-displacement curves obtained from the static and dynamic tests. This observation indicates that both displacement and force measurements obtained from static indentation and impact tests are precise. Therefore, the higher dynamic critical load observed in impact tests may not be due to misinterpretation or measurement errors. The disparity is believed to reflect the influence of loading rate on alterations in material intrinsic properties. Consequently, the increase of the critical load in the impact test is more likely a consequence of the strain rate dependence of the Mode II critical strain energy release rate.

The critical load corresponding to fibre failure (second significant drop) in the indentation test closely mirrors that of impact tests in both Fig. 4-20(a) and Fig. 4-20(b). In Fig. 4-20(a), this load drop for both indentation and impact tests occurs at a force and displacement of approximately 10,000N and 5mm, respectively, while in Fig. 4-20(b), these values are 12,000N and 6mm, respectively. The calculated absorbed energy values from the area under the force-displacement curve of the indentation tests for both figures were slightly higher than 27J. Thus, an impact energy of 27J or higher was anticipated to result in fibre failure. Notably, the impact energy of 27J in Fig. 4-20(a) has caused this damage, indicated by a recognisable drop, while

in Fig. 4-20(b), the impact energy of 64J has led to fibre failure and perforation, evidenced by a force-displacement graph similar to scenario "I" in Fig. 4-8(a). When examining the trends of second load drops, it is apparent that the values associated with these drops consistently align between the indentation and impact tests. This observation suggests that forces linked to fibre failure also appears to exhibit similarities between the two tests. Overall, the comparative study presented in this section, along with the findings from the literature, confirm that static indentation properly represents the barely visible damage induced in impact tests of quasi-isotropic laminates, offering a controlled, reliable, and repeatable loading setup, as well as stable damage growth [16,130,174].

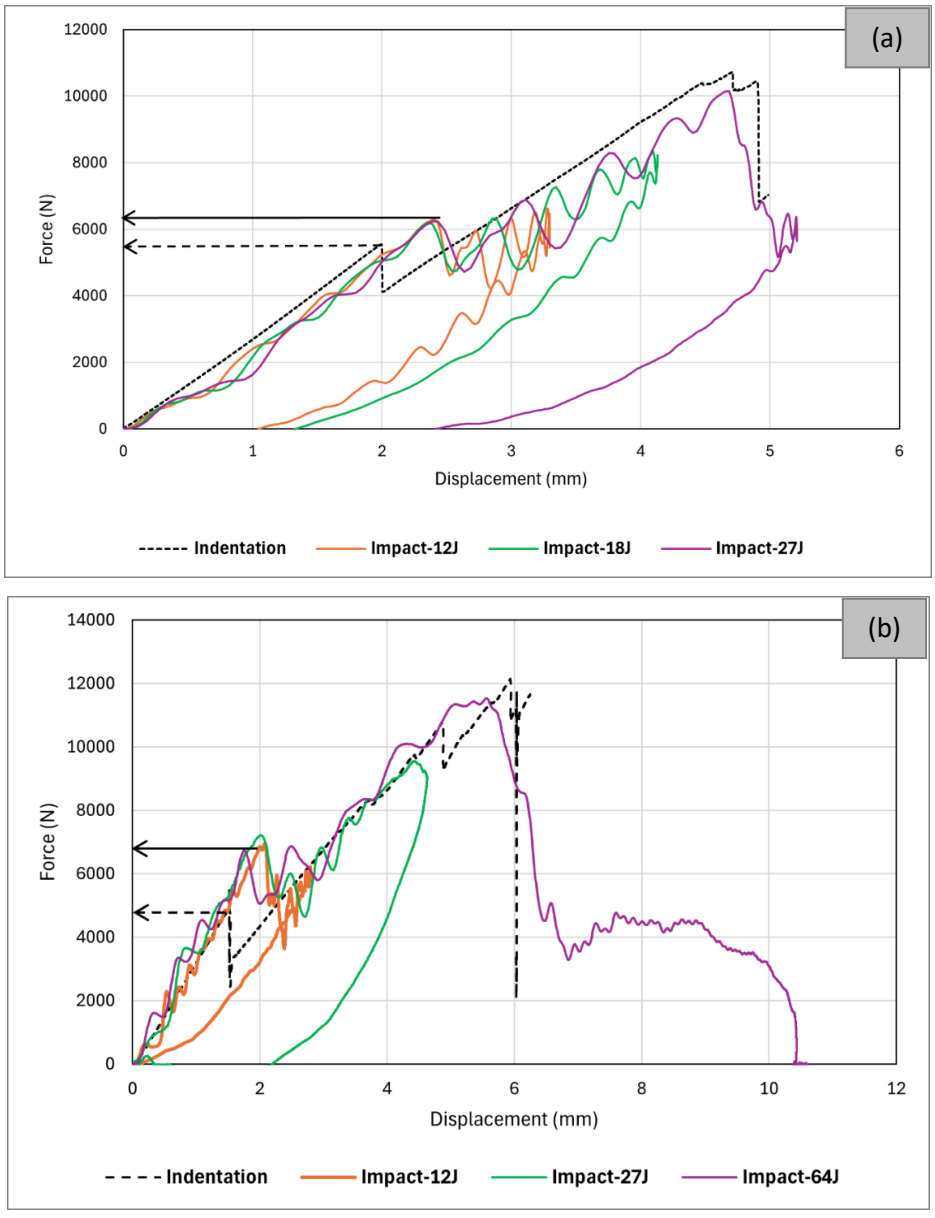

Fig. 4-20: Comparison of indentation and impact response: a) IM7/8552 samples of this research (*Reference* samples), b) T800/MTM49-3 samples of work by Fotouhi et al. [7]

4.3. Analytical Results: Delamination Threshold Force

The testing results of this thesis solely include data from the 32-ply laminates. Abisset et al. [4] presented a detailed experimental result for four different laminate configurations, named Reference (Ref), in-plane scaling (Is), ply-block scaling (Ps), and sub-laminate scaling (Ss), under indentation test. These four laminates were manufactured using Hexcel IM7/8552 unidirectional prepregs with 0.125 mm nominal cured ply thickness and a stacking sequence of $[45_m/0_m/90_m/-45_m]_{ns}$. Table 4-5 shows characteristics of the tested specimens. Note the Ss laminate is similar to the 32-ply laminates of this thesis. Hence, experimental outcomes from reference [4] will serve as reference points for verifying the analytical model, and FEA results are compared to and verified against the experimental results of this investigation.

Table 4-5: Configuration of the test specimens in reference [4]

Specimen	m	n	h (mm)	In-plane dimensions (mm)	Indenter diameter (mm)
Ref	1	2	2	75*50	8
Is	1	2	2	150*100	16
Ps	2	2	4	150*100	16
Ss	1	4	4	150*100	16

Abisset et al. [4] reported the first load drop and its associated displacement for four test specimens, as mentioned earlier, based on both experimental and analytical investigations. This data is used to verify the model, and the results are compared in Table 4-6.

Table 4-6: Comparison of the analytical and experimental results

Specimen	u (mm)	F_d (KN) **Experiment** [4]	F_d (KN) **Analytical** [4]	F_d (KN) **Analytical (proposed model)**
Ref	1	1.28	1.61	1.42
Is	2.8	1.7	1.61	1.73
Ps	1.5	3.96	4.55	3.77
Ss	1.7	4.73	5.05	4.22

The results of the proposed analytical model are in good agreement with the experimental results. The model outperforms the analytical model presented in [4] for three specimen configurations Ref, Is, and Ps, and its accuracy is only less than 4% lower than the one in [4] for the Ss sample. The proposed model considers the effects of laminate dimensions, indenter

size, and shear, and flexural modulus, providing an accurate prediction of delamination threshold load. Therefore, it can be used as a practical tool for estimating delamination onset in laminated composites.

4.4. FEA Results: Sensor Design

This section outlines the FEA results for two sensor design parameters, including different fibre directions and thicknesses of the carbon sensing layer. In FRP laminated composites, the mechanical behaviour can be influenced by the alignment of the fibres. Therefore, fibre direction can be employed as a design parameter to engineer the sensor performance and activation threshold load. Fig. 4-21 presents a comparison of the indentation response between the *Reference* sample and *Sensor* samples across four different fibre directions. The results show that integrating a sensor with fibre direction of 0° led to an increase of approximately 1000N in force at a 2mm displacement. The graph illustrates that as the fibre direction increases from 0° to 90°, there is a corresponding rise in structural stiffness. Hence, sensors with a smaller fibre orientation would result in a comparatively lesser alteration in structural stiffness.

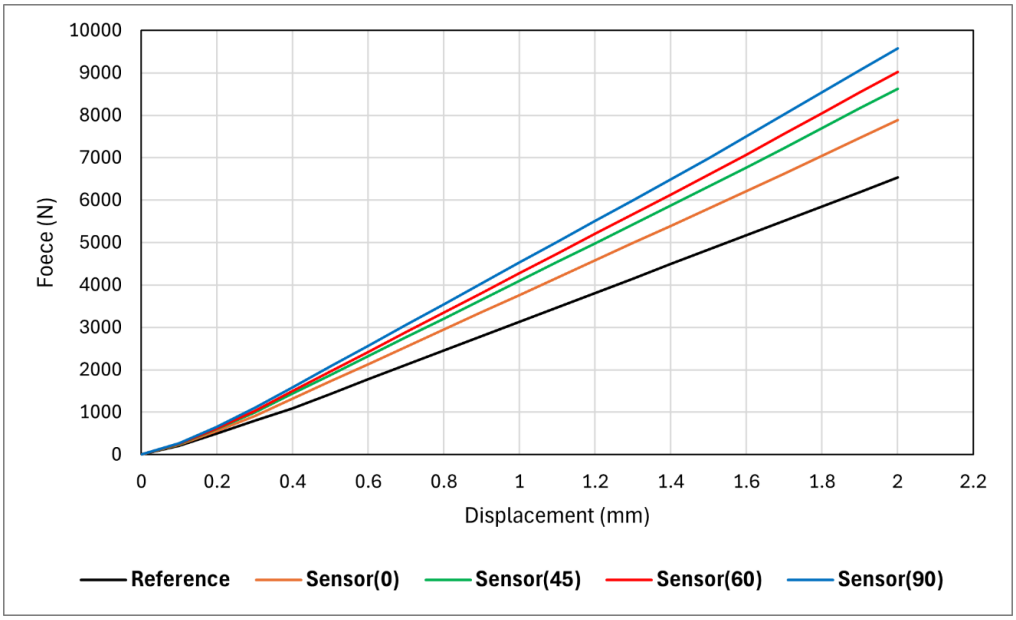

Fig. 4-21: The influence of the fibre orientation on indentation response

Hybrid glass/carbon sensors can be designed in different ways, depending on the competition between different damage modes occurring in the sensor, such as fibre fracture of the carbon sensing layer or delamination of the carbon and glass layers. In the former, the strain to failure of the sensing layer serves as the design criterion for the sensor, while in the latter, the critical strain energy (G_{IIc}) is the design parameter criterion. In this section, fibre fracture is regarded

as the triggering parameter for the sensor. Thus, a comparison of the strain distribution in the sensing layer across different displacements (test stages) with the strain to failure of the prepreg utilised as the sensing layer would indicate the sensor activation threshold. This is shown in Fig. 4-22, where the sensor activation threshold obtained from FEA is compared with that of experimental tests from the previous section. An increment before and after the sensor activation is highlighted in black colour. The results demonstrate that FEA and test outcomes concur on the sensor activation occurring at displacements of approximately 1.3mm and 1.4mm, showing the validity and practicality of the FEA method in providing a fast and reliable estimate of the sensor activation threshold. This analysis is for the sensor applied on the back face, where the dominant damage mode is tensile fibre failure; therefore, the strains obtained from FEA are compared with the tensile strain to failure, which is 0.5%. Note that this analysis is for a sensor with a carbon ply fibre direction of 0°. A comparison of the sensor activation threshold energy for all four studied fibre directions is presented in Fig. 4-23. This figure demonstrates that the energy threshold for activating the sensor decreases as the fibre direction of the sensing layer increases.

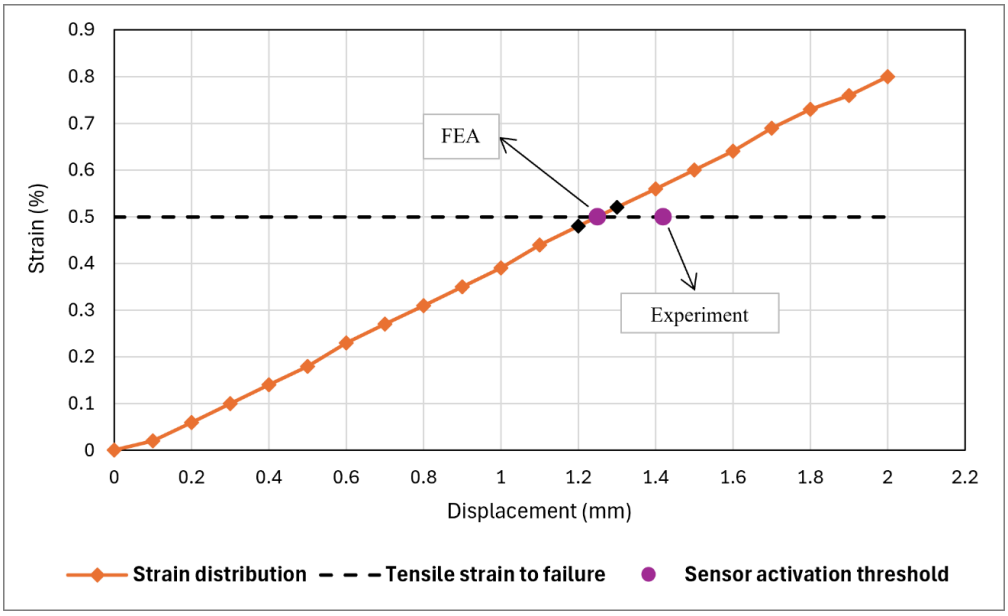

Fig. 4-22: Strain levels at the sensing layer with fibre direction of 0° at different displacement increments and the comparison of the sensor activation threshold obtained from the experiment and FEA

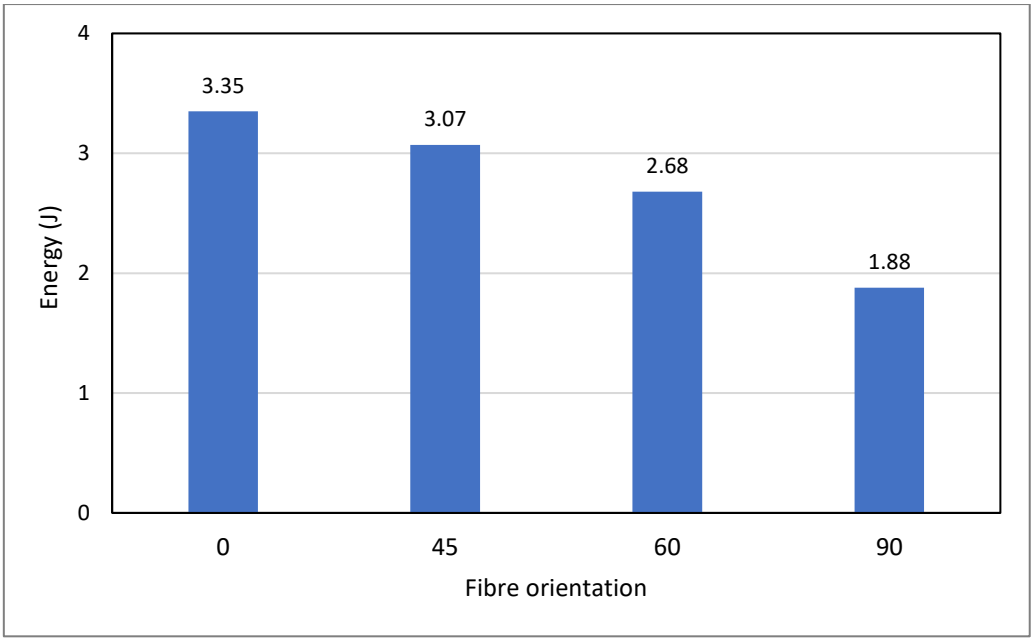

Fig. 4-23: Sensor activation threshold energy for different fibre directions of the sensing layer

The carbon layer thickness affects the structural stiffness and strain energy release rate and, consequently, the fracture and the delamination growth of the sensing layer in a hybrid sensor. Here, three distinct carbon thickness options for the hybrid sensor design are studied, including 0.07mm, 0.1mm, and 0.14mm, where the latter represents using two carbon layers in the sensor. Fig. 4-24 illustrates the variations in the strain response across three different carbon layer thicknesses. It is seen that for a given displacement, the strain value increases with the decrease of the thickness. Moreover, it is known that increasing the thickness would result in a higher structural stiffness. Therefore, a higher energy threshold for activating sensor in thicker laminates is anticipated. This is shown in Fig. 4-25, where energy thresholds are compared for the three thicknesses. The results suggest that if activating the sensor at higher energy levels is desirable, this can be achieved by increasing the number of carbon layers. Note that this is valid when the design criterion is fibre fracture of the sensing layer. However, this might still help with delamination damage criterion, as the interface angle change between the carbon and glass can control the delamination initiation threshold as well.

The results presented in this section can help achieve an optimal design of hybrid glass/carbon sensors by engineering parameters such as the fibre orientation and thickness of the carbon sensing layer.

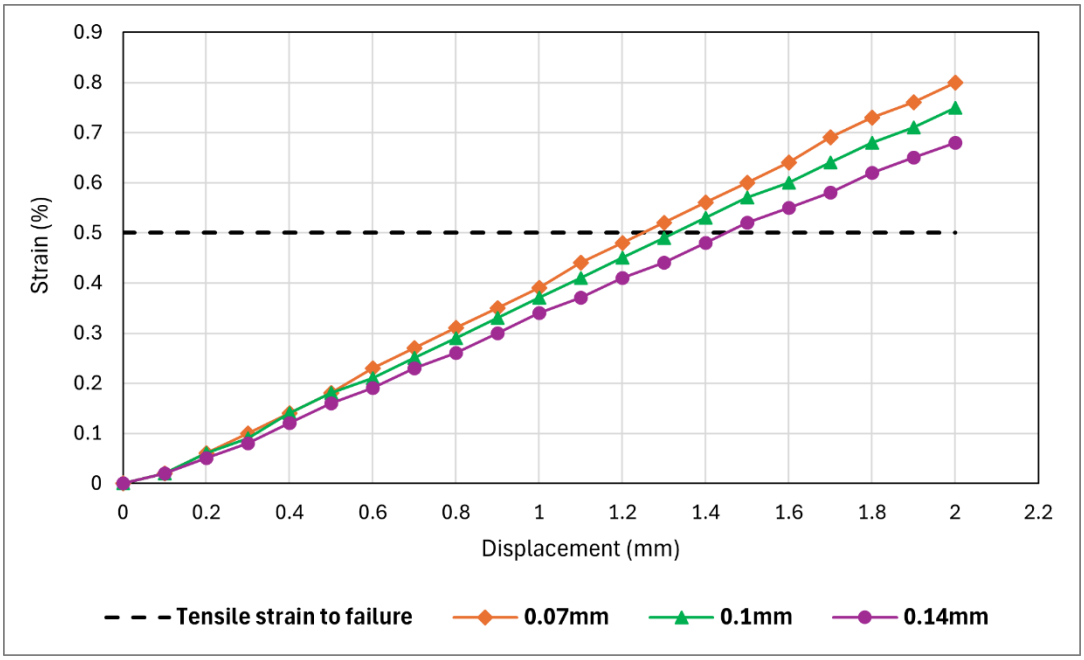

Fig. 4-24: The influence of the sensing layer thickness on strain distribution

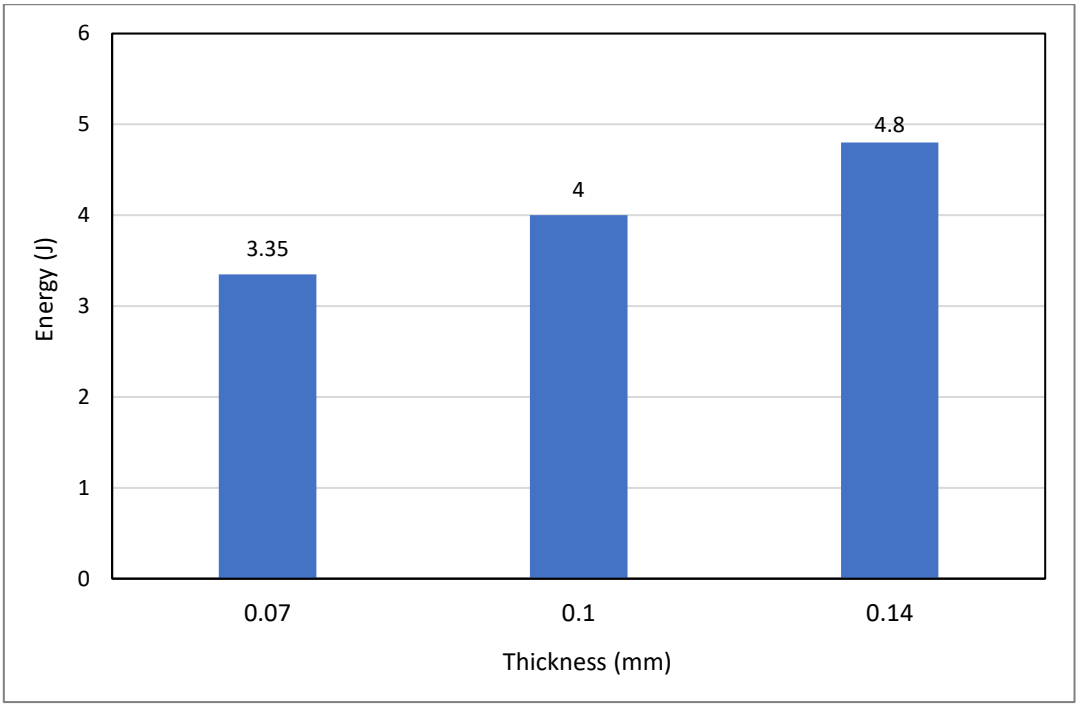

Fig. 4-25: Sensor activation threshold energy for different thicknesses of the sensing layer

4.5. Summary

This chapter presented the results of experimental, analytical and numerical studies for designing the sensor. Both indentation and impact test results showed that adding sensors on the two sides of a composite sample does not significantly change its mechanical properties. A slight increase in absorbed energy was observed in the *Sensor* samples compared to the *Reference* samples. The changes in the fibre direction and introducing discontinuities in the carbon sensing ply affect the out-of-plane loading response, indicating that the effect of adding sensors on mechanical properties can be managed by adjusting these parameters through an appropriate design.

Visual inspection results demonstrated the effectiveness of the sensor in visualising damage under both static indentation and impact loadings. The analysis of indentation test results highlighted a few points:

The sensor on the back face activates before the first load drop, which is considerably earlier than the activation on the front face. This can stem from different damage mechanisms on each side which were discussed in this chapter. Moreover, applying the sensor could decrease the threshold energy for visually detectable damage on the back face from nearly 27J in a *Reference* sample to less than 5J in *Sensor* samples. On the front face, the threshold energy decreased from nearly 20J in a *Reference* sample to nearly 9J in a *Sensor* sample. Furthermore, changing the fibre orientation of the sensing layer influences the sensor activation threshold load though it does not influence the shape or size of the visual damage pattern. On the other hand, introducing discontinuities can change both the sensor activation threshold load and the shape and size of the visual damage pattern on the surface. The samples with discontinuous sensing layer exhibited an improved damage visualisation under a similar indentation force and impact energy to sensor samples without discontinuities.

C-scan and microscopy images confirmed that impacted samples at all studied energies had undergone delamination damage. Nevertheless, in *Reference* samples, the damage was barely visible on the front face of 27J samples and not visible on the front face and back face of all other samples. In *Sensor* samples, however, the impact-induced damage could be detected at energies as low as 12J, with the size of the activated area increasing in-line with the impact energy. Different sensor-activated patterns and sizes on the back face and front face of the *Sensor* samples signified different damage modes on each side, with the back face showing a larger activated area at all energies. Moreover, while introducing discontinuities in the sensing

layer improved the visual inspection on both sides, it was particularly effective on the back face. Comparing the C-scan and visual inspection images at different impact energies provided a correlation between the size of the internal damage and surface visible damage.

A comparison was conducted between the results of the indentation and impact tests to evaluate their degree of similarity as potential substitutes. It was observed that despite a lower delamination threshold energy in the indentation test compared with the impact test, the static indentation effectively captures the barely visible damage induced in impact tests of quasi-isotropic CFRP laminates.

The new analytical formulation for determining the delamination critical force provided an accurate estimate of the delamination onset across various lay-up configurations when compared to experimental data. In the FEA section, two design parameters, the fibre orientation and the thickness of the sensing layer, were evaluated. The results indicated that a smaller fibre orientation (within the range of $0° - 90°$) and greater thickness of the sensing layer lead to a higher activation threshold energy. The analytical and FEA models presented in this chapter can act as a fast and inexpensive estimate for designing the sensor.

Chapter 5

Visual Inspection of Impact Damage using Hybrid Glass/Carbon Sensors and Deep Learning

5.1. Introduction

Visual inspection is one of the most common non-destructive testing methods that offers a fast evaluation of surface damage in aerospace composite structures. However, it is highly dependent on human-related factors and may not detect barely visible impact damage. In this chapter, low-velocity impact tests with different energy levels are conducted on two groups of composite panels, namely 'reference' and 'sensor-integrated' samples. Then, the results of impact tests, together with C-scan and visual inspection images, are analysed to define the BVID range and create an original image dataset. Next, four different deep learning models[1] are trained, validated, and tested to capture the BVID only from the images of the impacted and non-impacted surfaces. The results show that all four networks can learn and detect BVID quite well, and the sensor-integrated samples reduce the training time and improve the accuracy of deep learning models. ResNet outperforms other networks with the highest accuracy of 96.2% and 98.36% on the back-face of reference and sensor-integrated samples, respectively. The proposed damage recognition method can act as a fast, inexpensive, and accurate structural health monitoring tool for composite structures in real-life applications.

5.2. Application of Deep Learning in Damage Detection

Deep learning-based techniques for detecting impact damage in composite materials can be broadly categorised into the following primary types: (i) image-based, (ii) vibration-based, and

[1] Deep learning algorithms were developed in collaboration with Professor Elena Marchiori's research group from Radboud University.

(iii) acoustic-based techniques. Image-based methods utilise computer vision algorithms to scrutinise images of the surface of composite panels both before and after an impact event. This technique detects any changes in surface topography, such as cracks and fibre breakage. Vibration-based methods, on the other hand, focus on measuring and analysing the vibrational response of the composite structure to detect any changes in mechanical properties, including stiffness and damping, caused by impact damage. Acoustic-based techniques involve using acoustic sensors to detect changes in the acoustic emission signals generated by impact damage. Several studies have explored the application of AI-based methods for detecting impact-induced damage in polymer composite materials [27,28,59,184–187]. In addition to impact damage detection, AI-based techniques can be applied for damage classification, damage quantification, and remaining useful life prediction [188]. For example, Zargar and Yuan [185] demonstrated the possibility of using a Deep Learning (DL) model to characterise impact damage by analysing the evolution of impact-generated propagating waves. The DL model used there was not merely data-driven, but the physics of the wave propagation phenomenon was embedded into the model's architecture to make it a physics-inspired DL model. Wei et al. [186] used infrared thermography data of impacted CFRP composites to train two different DL models. Both models could identify impact damage and predict the damaged location with an F1-score of 92.74% on mid-wave infrared data and an F1-score of 87.39% on long-wave infrared data. Hasebe et al. [28] applied three Machine Learning (ML) models on a dataset extracted from low-velocity impact tests on composites with particular attention to three influential factors, namely stacking sequence, impactor shape, and impact energy. Their results indicated that local volume, the gradient of the dent surface, and the pure dent depth could be used for characterising internal damage in CFRP laminates.

It is seen that in all similar research works, collecting a dataset needs advanced knowledge and measurement facilities such as Pulsed Thermography equipment [184], 3D measurement systems for evaluating impact dent depth [28,59], or signal processing to convert impact signals into input image data [187]. In addition, these methods may not be widely feasible. For example, when measuring the dent depth, the relaxation in dent depth over time is often neglected [28]. Moreover, the dent depth of impact-induced damage depends on impactor size and cannot be determined based on visual observation alone [189]. In the case of using thermal images as input data, there is a challenge of light reflection and not enough emissivity, as most composite structures have a reflective surface [190]. Accordingly, the method cannot be widely used to collect thermal image datasets of various composite materials and structures. As for

further research, the authors of [28] suggested developing new SHM methods to directly use the surface profiles as features without a reduction in raw data (surface profile) to human-designed features (depth, volume, etc.). Also, they suggested studying whether AI models are effective even if the target contains paint or other features which may be found in real structures, but not in laboratory-level research. This is a source of inspiration for this chapter, to use only surface images as inputs to the AI system. An improvement of this work over other research in the literature is the successful implementation of four different DL models, from a simple two-layer Convolutional Neural Network (CNN) to an advanced CNN composed of a Residual Network (ResNet) and a Prototypical network, to predict the BVID only from very simple surface images. The data collection procedure in this chapter is very simple, and there is potential to add a remote photography system to make the SHM process fully autonomous. In addition, the idea of applying AI while adding self-reporting hybrid glass/carbon coatings [5] on the surface is explored and shows how this sensing technology can improve the autonomous recognition of BVID using DL models. A detailed description of different DL models used in this chapter is presented in section 5.3.2. Fig. 5-1 shows the procedure followed in this chapter.

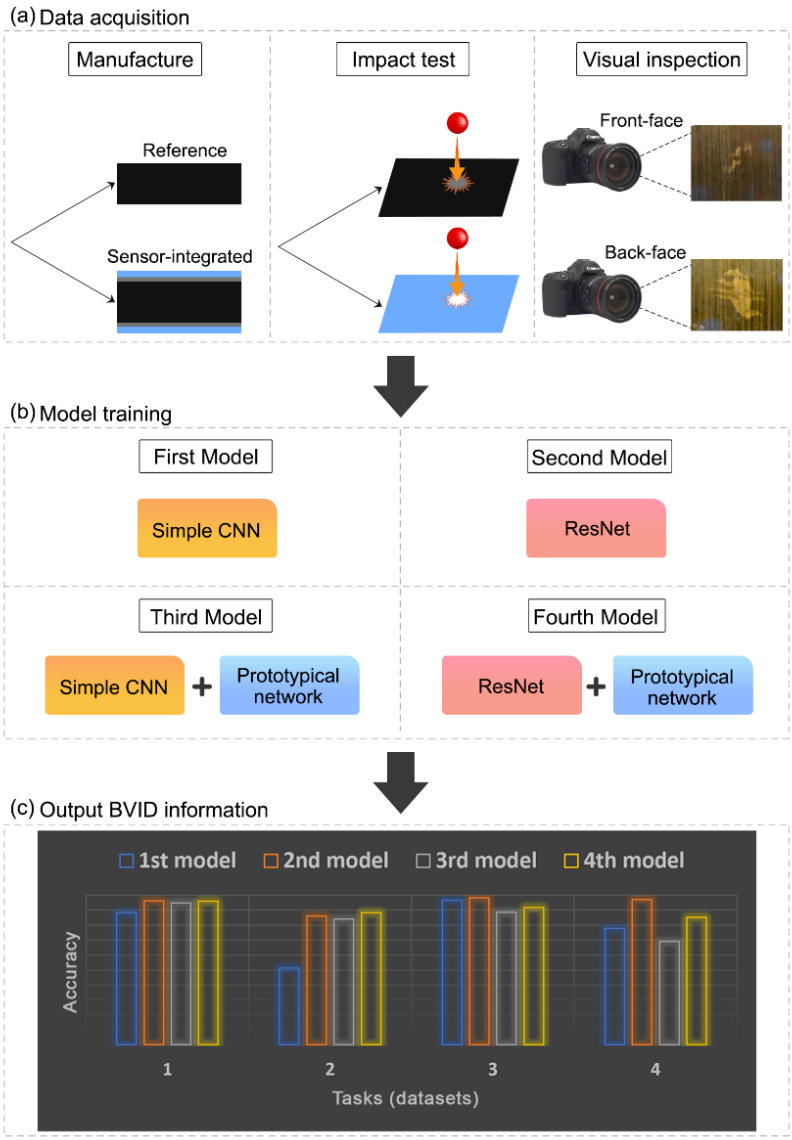

Fig. 5-1: The procedure followed in this chapter:

a) data acquisition, b) model training, c) output BVID information, including accuracy, F-1 score, precision, recall and training time of each of the four DL models (shown with different colours) for four different tasks

5.3. Methodology

5.3.1. Experiments

Given the close similarity between the experimental procedures outlined in this chapter and Chapter Three, including manufacturing of samples, indentation and impact tests and non-destructive evaluation methods, only a concise description is presented here to maintain brevity. Two groups of samples were manufactured, including CFRP composites without a sensor (reference) and CFRP composites with a sensor (sensor-integrated). In the former, 32

plies of T800 carbon prepregs were laid up with the $[45/0/90/-45]_{4s}$ configuration. In the latter, a sensor composed of a layer of YS-90 carbon and a layer of S-glass/913 epoxy (both with ply degree of 90°) was added on each side of the panel, where the 32-ply substrate and sensors on two sides were co-cured according to supplier's instructions [7].

Quasi-static indentation tests were first used to understand the behaviour of the investigated samples and to choose appropriate energy levels for the impact tests, as described in Chapter Three. This is because quasi-static indentation and low-velocity impact tests can provide comparable results according to prior research [128,129,175]. Low-velocity impact tests with different energy levels, from 3J to 128J, were then carried out according to the ASTM D7136 standard.

After completing impact tests, two NDE methods, including C-scan and visual inspection were conducted. In the first approach, a10 MHz transducer was used to scan the samples in a water tank. The damage area was measured in the software and the results were recorded [7]. In the second approach, a Nikon camera was used to take images of the front face and back face of all samples. Multiple images of each sample with viewing angle of 0° and viewing distance of 40cm were taken. Effort was made to set a lighting level intense enough to achieve quality images while avoiding reflections as much as possible. Accordingly, a detailed internal (C-scan) and surface (visual inspection) damage dataset was collected.

5.3.2. An Overview of Deep Learning Algorithms

The field of AI, specifically ML and computer vision, offers a way to detect defects in materials in seconds [54,191]. Regardless of the task at hand, certain parts of a ML algorithm's pipeline are almost always prevalent. The general idea is that data-driven algorithms are not completely hard-coded by the programmer, but rather learn from the data itself. In this way, ML algorithms can be tailored to specific tasks. A ML algorithm is defined by a hypothesis, a loss-function and an optimisation procedure. A hypothesis is a function that receives data as input and outputs a prediction. It is parametrised by its trainable parameters and hyperparameters. The data automatically determines the former, while the ML engineer pre-sets the latter. The loss function is a function that outputs the error made by the model while using the output of the hypothesis as input. In the case of classifying whether an image contains damage or not, since it is a binary classification, the common approach is to use a Binary Cross Entropy (BCE) loss function. This measures the difference between the classification predicted by the model's hypothesis and the true classification of the datapoint. Another popular loss function used for

classification is a Categorical Cross Entropy (CCE). This is a more generic form of the BCE, meaning that a datapoint can be classified into more than just damaged or undamaged [192,193]. An optimisation procedure is an algorithm that defines how the trainable parameters of the ML model are iteratively changed to improve its accuracy, which is achieved by minimising the error of the model's prediction tasks. These errors are defined by the loss function. When it comes to the construction of the dataset, the data is split into three parts: the training set, the validation set and the testing set. The training set is used to determine the trainable parameters of the model via an optimisation process. The validation set determines the model's hyperparameters by trying out different values. Finally, the testing set estimates the model's performance on unseen data.

ML can be used to automate damage detection in composite materials. However, more complicated ML architectures are required when the dataset is a collection of images. A ML architecture that mimics the workings of the human brain is known as an Artificial Neural Network (ANN). The simplest neural network is a Multi-Layer Perceptron (MLP). It contains multiple functions where the output of a function is used as an input to the next one. These functions are called the layers of the model. The simplest layers of a MLP are Fully Connected (FC) layers [194]. When using a neural network with multiple layers as an ML hypothesis, it falls into the realm of DL. Rautela et al. [195] applied two ML and one DL algorithms in three benchmark experimental datasets to develop a SHM tool for delamination prediction in composite structures. It was clarified that the DL approach could generate better reconstructions with lower mean squared error and provide higher accuracy on all the datasets compared to ML models. When dealing with an image-based dataset, a more complex family of neural networks, such as Convolutional Neural Networks (CNNs) might be needed [55,57]. CNNs differ from other neural network architectures because of their convolutional layers [196]. There might be some layers of a CNN which do not have any trainable parameters. Prime examples of this are max pooling and average pooling layers [197,198].

ResNet is a deep neural network architecture that was introduced in 2015 to address the problem of vanishing gradients in very deep CNNs [199]. ResNet allows for the training of much deeper networks with hundreds of layers by introducing shortcut connections between the layers, which skip over certain layers and allow the network to learn residual functions. The residual connections enable the network to better propagate gradients through the entire network, leading to improved performance and faster training time than simpler CNNs [184]. Another advantage of using a well-known architecture, such as ResNet, is that it is possible to

start the training with the values of its weights learned from a different task or dataset. For example, ImageNet [200] is a large-scale image database containing over 14 million images, widely used for training and evaluating computer vision models. In this chapter, ResNet weights trained on the ImageNet dataset were used as the initial starting values before the network was trained on the dataset. This approach is known as transfer learning [201]. Another subfield of ML is few-shot learning that deals with the problem of learning from a limited amount of labelled data [202]. In traditional supervised DL, a large amount of labelled data is required to train a model that can accurately classify new (unseen) data. However, in few-shot learning, the goal is to learn from a small number of labelled examples. Few-shot learning can be combined with metric learning to learn from small datasets. Metric learning is another subfield of ML that focuses on learning a vector representation of an image, known as embedding, in the feature space [203]. The few-shot learning and metric learning can be combined in Prototypical networks. Prototypical networks are a type of neural network architecture commonly used in few-shot learning tasks. They are designed to learn a feature space in which examples from the same class are closer to each other than to examples from other classes. The dataset splitting here is more complex than in standard supervised ML. Firstly, the dataset is split into meta-train and meta-test sets. Then, each of these sets is divided into shot-images and query-images. This approach is effective in few-shot learning tasks, where only a few labelled examples are available for each class [204].

A binary classification contains four entries: True Positives (TP), True Negatives (TN), False Positives (FP) and False Negatives (FN). In the case of damage detection, these terms can be defined as follows:

TP: The number of images that the network has correctly identified as containing damage

TN: The number of correctly identified images without damage

FP: The number of images without damage that are incorrectly identified as containing damage

FN: The number of images containing damage that are incorrectly identified as images without damage

Table 5-1: Confusion matrix

Truth \ Predicted	**Defect**	**No defect**
Defect	TP	FN
No defect	FP	TN

In addition to the confusion matrix, other common metrics to evaluate the model's performance are precision, recall, F-1 score, and accuracy. Also, measuring a model's training time can be important. The equations below show the definition of the evaluation metrics.

$$Precision = \frac{TP}{TP + FP} \tag{5-1}$$

$$Recall = \frac{TP}{TP + FN} \tag{5-2}$$

$$Accuracy = \frac{TP + TN}{TP + TN + FP + FN} \tag{5-3}$$

$$F_1 = 2\frac{precision * recall}{precision + recall} = \frac{2 * TP}{2 * TP + FP + FN} \tag{5-4}$$

In this chapter, four different supervised networks are used as follows:

- Model one is a simple two-layer CNN
- Model two is a ResNet with 18 trainable layers pretrained on ImageNet dataset
- Model three is a Prototypical network, a more complex CNN that can use other simpler CNNs as a base. In the third model, the simple two-layer CNN from the first approach was used as a base for the Prototypical network.
- In the fourth model, the ResNet from the second approach was used as a base for the Prototypical network (pretrained on ImageNet dataset).

Also, to pre-process the data, instead of using raw pixels, the mean and standard deviation of each of the three RGB channels[2] of an input image were calculated and the raw image data were standardised before starting any of these pipelines. Note that the mean and the standard deviation for standardisation were only calculated on the training set, and this information was saved and fixed for test data. The reason to choose these four networks is that the first model is a simple CNN that is commonly used for image-based dataset. Then, ResNet-18 is used as the second model. This is a powerful deep neural network that has shown a promising performance in the field of computer vision and image recognition and can presumably capture complex data [52]. Given the small size of dataset in this research, a pretrained version of ResNet is used. Another type of DL models which work well with small dataset is a Prototypical network. This class of DL models uses few-shot learning, enabling an efficient generalisation of unseen data based on only a small number of samples. Therefore, it is used in

[2] Red-Green-Blue (RGB) channels. That is how images are stored in the computer.

the third and fourth models of this study. All models have been implemented in Python programming language (version 3.9) using a popular library, PyTorch, for implementation and experimentation with artificial neural networks. This was a collaborative work between the MMRG at University of Glasgow and Institute of Computing and Information Sciences at Radboud University, and DL models were developed in collaboration with Professor Elena Marchiori's research group.

5.3.2.1. Description of the First Supervised Network

The first network used a simple CNN with only two convolutional layers. Both convolutional layers output 64 feature maps, have 3x3 kernels, and are followed by: batch normalisation[3] layers, Rectified Linear Unit (ReLU) activation functions [205], and max pooling layers with a 3x3 kernel. The output of the CNN is flattened and used as an input to the MLP with FL layers. MLP also consists of two layers, where the first layer outputs a 512-dimensional representation, and the second layer takes that and outputs a one-dimensional representation of the image. This value is then passed on to the Sigmoid layer to get a value between 0 and 1, which classifies an image in one of the two classes. Finally, the outputted value is rounded up to either 0 or 1 to receive the final classification of the network (see Fig. 5-2). Furthermore, Adam is used as an optimiser [184,206], and BCE function is used as a loss function.

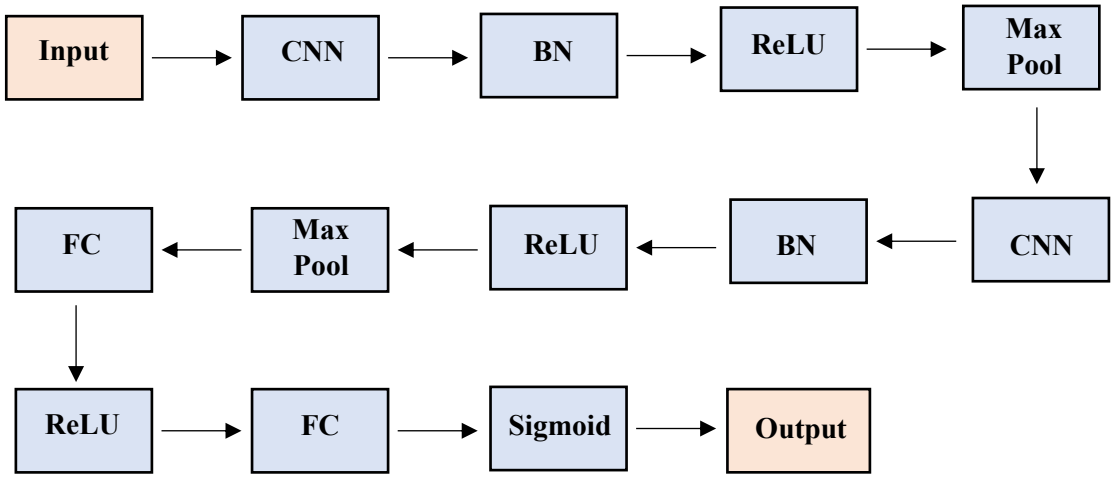

Fig. 5-2: A simple flowchart of the first network's architecture

5.3.2.2. Description of the Second Supervised Network

The second network used a pre-trained ResNet architecture with 18 trainable layers. Even though there are available pre-trained ResNet architectures with more layers, because of the

[3] Batch Normalisation is written as (BN) in Fig. 5-2.

small size of dataset in this chapter, a bigger architecture was not used to avoid overfitting the data. ResNet 18 (available from PyTorch [207]) was pre-trained on more than a million images from the ImageNet database. However, its last FC layer was replaced with a new one that outputs only one number. After that, a Sigmoid activation function was added to turn it between 0 and 1, so that it could be used as a probability of the input image either being damaged or not. Furthermore, Adam was used as an optimiser, and the BCE as a loss function.

5.3.2.3. Description of the Third and Fourth Supervised Networks

The third and fourth models used a Prototypical network, which works very differently from the first two approaches. During the meta-training phase, a random batch is sampled from a subset of meta-training images. The meta-training subset contains 30% of the total number of images in the dataset. The base network used in the Prototypical networks outputs a 32-dimensional embedding. Any desirable network can be used as a base network to embed the image into this latent space with 32-dimensional representations. The 32-dimensional output is not a representation of a binary classification label, but it captures the semantical representation of an image in a high-dimensional latent space (which is used for binary classification later in the pipeline). To that note, 50% of the embeddings are used for training (shot-images) and 50% for testing (query-images). Since this is a supervised approach, the labels of the shot-images are known, and they are used to calculate the mean for each label, resulting in two 32-dimensional embeddings, one for each label (labels are ‘damaged’ and ‘undamaged’). These are known as the prototypes of labels. Then, the distances from each query-image to each prototype are calculated. The query image takes the label of its closest prototype (in this latent space), which is how prototypical networks perform classification. The Euclidian distance is used to calculate the means, similar to [204]. Prototypical networks allow the use of any desirable CNN to encode the image into the 32-dimensional latent space. However, this network does not output the classification prediction of the image, but instead, its 32-dimensional embedding in the latent metric space, where the distances are calculated. This approach was used on the networks that had been used in the first and second models. They both have the same setup as the first two approaches, but this time instead of outputting a one-dimensional number, they output a 32-dimensional vector.

5.4. Results and Discussion

5.4.1. Low-Velocity Impact and NDE

The results of low-velocity impact tests are shown in Fig. 5-3. As seen in Fig. 5-3(a), except for 3J and 6J, a significant load drop can be seen in all energy levels associated with delamination initiation. Low energy levels (3J and 6J) do not cause any damage to the samples; therefore, there is no load drop for these energies. A considerable load drop occurred in 96J and 128J due to fibre failure. In these impact energies, there is a significant residual deflection. Energy absorption in composite structures under impact can cause various damage mechanisms. Therefore, damage mechanisms can be characterised by analysing energy absorption. As shown in Fig. 5-3(b), there is a significant change in the absorbed energy-time response of specimens, where energy absorption for impact energies lower than 64J is almost half of those higher than 64J. This is in line with the results of Fig. 5-3(a), suggesting that a specific range of energy from 8J to 64J is of great importance as the damage mechanism in this energy range is delamination, which causes BVID. Fig. 5-3(c) shows a comparison of impact response in reference and sensor-integrated samples for two impact energies within the BVID range (12J and 36J). The results suggest that adding the hybrid glass/carbon sensor does not significantly change the mechanical properties (impact response), as in both 12J and 36J, the same trend is followed for reference and sensor-integrated samples.

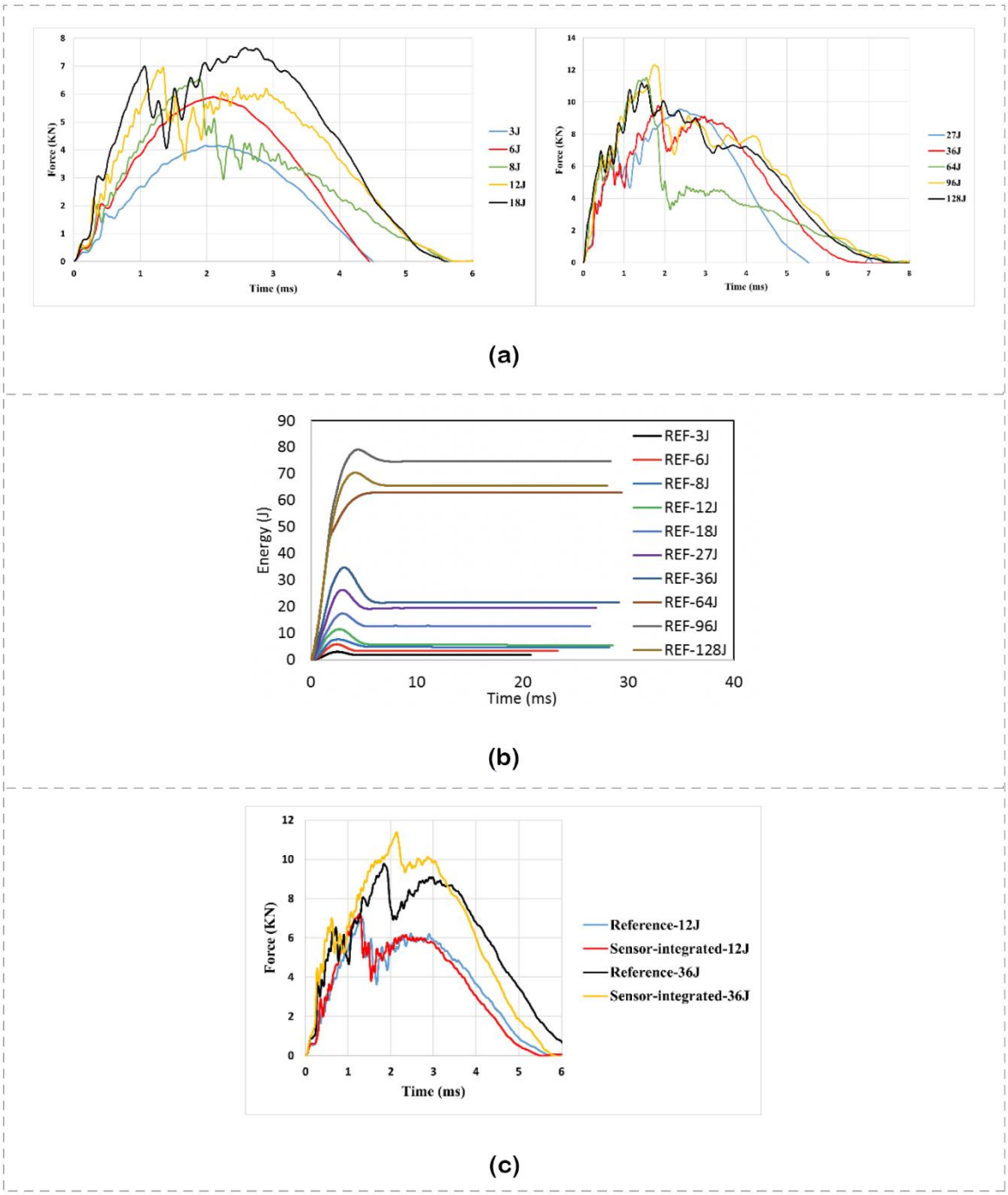

Fig. 5-3: Low velocity impact test results: a) Force-time response of reference samples (without a sensor) under different impact energies from 3J to 128J, b) Absorbed energy-time response of reference samples (without a sensor) under different impact energies from 3J to 128J, c) comparison of the impact response in reference and sensor-integrated samples at impact energies of 12J and 36J

Fig. 5-4 shows the C-scan, front face, and back face images of the reference samples. The C-scan images show no internal damage associated with 6J impact energy, and delamination starts

from 8J. It is also indicated that damage size varies in line with impact energy. Images of the front face and back face of samples clarify that damage is visible only at the energy levels of 96J and 128J, barely visible at 12J-64J, and invisible at 8J. These images suggest that the back face may allow for better damage visibility than the front face, particularly for higher energy levels such as 64J, 96J, and 128J. Fig. 5-5 demonstrates C-scan, front face, and back face images of sensor-integrated samples. Similar to the reference samples, there is no damage in 6J impact energy. However, a significant improvement in visual inspection of damage is achieved when adding sensors. The hybrid glass/carbon sensor allows the visually detecting of the damage caused by low energies such as 8J. A comparison of Fig. 5-4 and Fig. 5-5 suggests that this sensing technology can work well and improve visual inspection, particularly for BVID, ranging from 8J-64J.

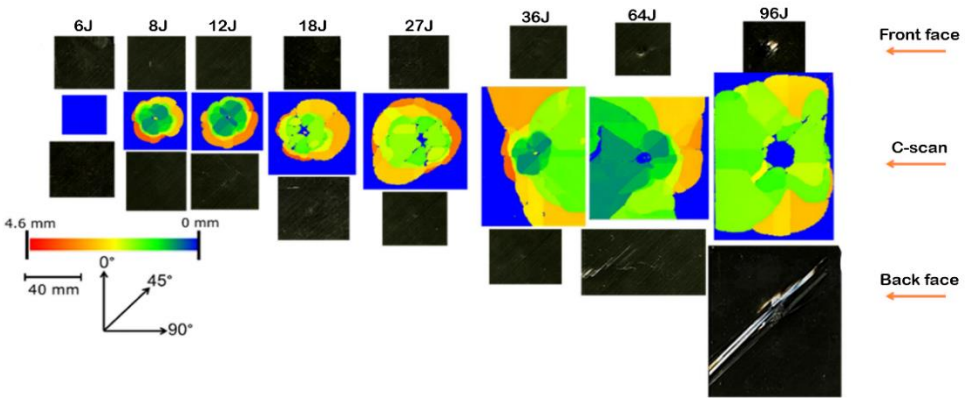

Fig. 5-4: Front-face, back-face, and C-scan images of reference samples at different impact energies [7]

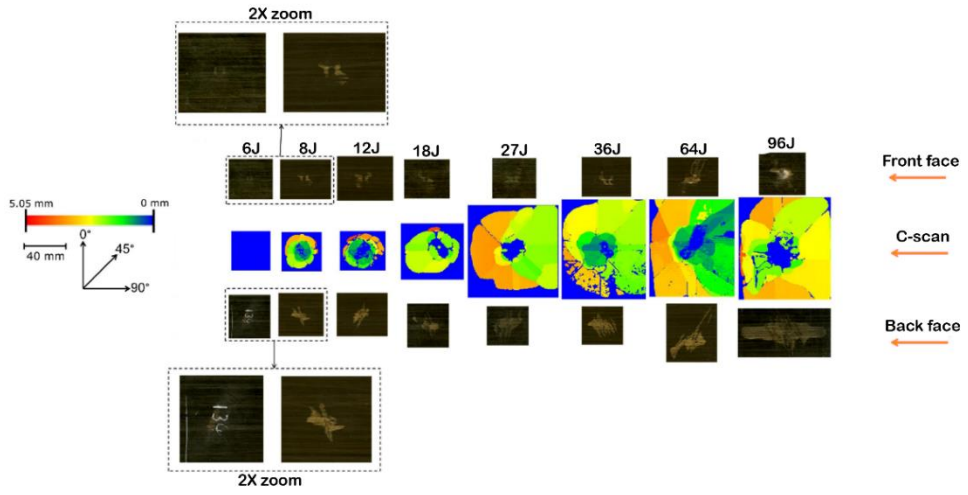

Fig. 5-5: Front-face, back-face, and C-scan images of sensor-integrated samples at different impact energies [7]

BVID can be defined based on different metrics or standards. In this research, after conducting quasi-static indentation tests, impact tests were conducted at different energies, ranging from 3J to 128J, to generate a complete dataset of different impact-induced damage modes such as matrix cracks, delamination, fibre failure and perforation. The C-scan results revealed that the internal damage happens from 8J. However, visual inspection results suggested that damage (permanent indentation) is (barely) visible from 12J. Moreover, it was observed that impact energies higher than 64J can cause fibre failure, which was beyond the BVID (the damage was not an indentation but a significant fibre fracture). This was also confirmed by load-displacement curves obtained from the impact tests. Therefore, this range (12J-64J) was considered as the BVID range and images of samples impacted at 12J, 18J, 27J, 36J, and 64J were used as an input for training the models.

Table 5-2 represents the classification of the dataset. After experimental investigations, it was concluded that the best way to train and test the CNNs is to classify the dataset into four main groups (or tasks), as shown in Table 5-2. In task 1, the model is trained and tested to recognise BVID using images of the back face of reference samples. In task 2, the model uses images of the front face of reference samples. Similarly, tasks 3 and 4 deal with images of the back face and front face of sensor-integrated samples, respectively. Therefore, a model can output one of the two possible classes (damaged or undamaged) in each task.

Table 5-2: Classification of the dataset

Task number	Type of composite panel	Damage location	Damage range
1	Reference	Back-face	Within the BVID range
2	Reference	Front-face	Within the BVID range
3	Sensor-integrated	Back-face	Within the BVID range
4	Sensor-integrated	Front-face	Within the BVID range

5.4.2. First DL Model (ConvNet)

The results of the first model are presented in Tables 5-3, 5-4, 5-5 and Fig. 5-6. All evaluation parameters show that it is easier for the model to detect the damage on back face than front face, regardless of whether using a sensor or not. For example, the accuracy of damage

prediction on back face is 37% higher than on the front face in reference samples. This could be due to different visible or barely visible damage patterns developed during the impact event on the two sides. This difference in sensor-integrated samples is only 19%, proving the effectiveness of adding a sensor in generating recognisable damage patterns on both sides. The beneficial effect of adding a sensor can also be seen through comparing the accuracy in back faces of reference and sensor-integrated samples (tasks 1 and 3), and front faces, similarly (tasks 2 and 4), where there has been an increase in damage prediction accuracy of 8% and 26% on back face and front face, respectively. Here, the higher improvement percentage achieved on the front face is because when there is no sensor (reference samples), and the damage is within the BVID range, the damage pattern on the front face is very difficult to detect. That explains the lowest accuracy of 51.25% (task 2) among all four different tasks. However, adding a sensor generates a significantly easier-to-detect damage pattern. The highest accuracy is achieved in task 3 (96.72%), where the damage is studied on the back face of sensor-integrated samples. Note that here, only images of samples damaged within the BVID energy range are used, and different results may be achieved if images of higher impact energies are used as input to the model. Table 5-5 suggests that the network's training time for the two sides of the same samples is almost the same, while it is significantly faster in sensor-integrated ones. Therefore, adding a sensor can improve the damage detection process in terms of accuracy and time, when using this network.

Table 5-3: Evaluation metrics for four different tasks (1st model)

NAME	**Values per dataset**			
Task	1	2	3	4
Accuracy	88.46%	51.25%	96.72%	77.94%
Precision	90.90%	78.26%	100%	86.84%
Recall	88.89%	55.38%	93.93%	76.74%
F-1	89.88%	64.86%	96.87%	81.48%

Table 5-4: Confusion matrix for four different tasks (1st model)

Predicted \ Truth	Defect	No defect
Defect	39	5
No defect	4	30

Task: 1

Predicted \ Truth	Defect	No defect
Defect	36	29
No defect	10	5

Task: 2

Predicted \ Truth	Defect	No defect
Defect	31	2
No defect	0	28

Task: 3

Predicted \ Truth	Defect	No defect
Defect	33	10
No defect	5	20

Task: 4

Table 5-5: Average training time of each task (1st model)

Task	1	2	3	4
Average Train Time	54m 12s	40m 55s	16m 56s	13m 18s

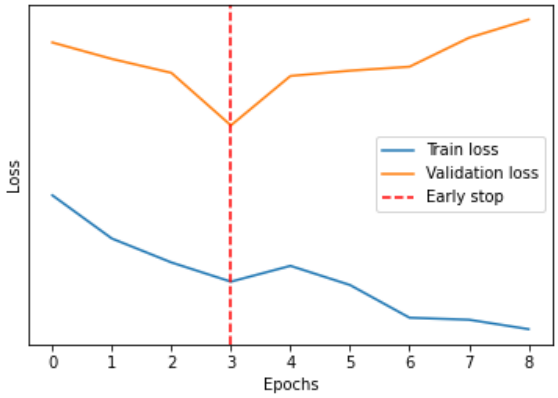

Fig. 5-6: Example of train and validation losses of the 1st model (task 1)

5.4.3. Second DL Model (ResNet)

Tables 5-6, 5-7 and 5-8 and Fig. 5-7 show the results of the second model. Similar to the first model, all metrics confirm that the model can learn and predict damage on the back face easier than front face. However, the difference between the two sides is less significant than that of the first model. For example, the difference between the accuracy of the front face and back face in reference and sensor-integrated samples is only 10% (tasks 1 and 2) and 1% (tasks 3 and 4), respectively. This model has the highest and lowest accuracy of 98.36% (task 3) and 86.25% (task 2). This aligns with the visual observation results, as damage on the back face of sensor-integrated samples is the most visible, and on the front face of reference samples is the least visible. The results also suggest that adding a sensor can improve this model's accuracy, which is more considerable on the front face (comparing tasks 2 and 4). The results presented

in Table 5-8 indicate that the difference between the training time for the back face and front face of reference samples is considerably higher than that of sensor-integrated ones. Also, overall, the training time for both sides of the sensor-integrated samples is lower than for reference samples, proving the effectiveness of adding a sensor on the second model's performance.

Table 5-6: Evaluation metrics for four different tasks (2nd model)

NAME	**Values per dataset**			
Tasks	1	2	3	4
Accuracy	96.2%	86.25%	98.36%	97.05%
Precision	100%	91.3%	100%	97.37%
Recall	93.62%	85.71%	96.88%	97.37%
F-1	96.7%	88.42%	98.42%	97.37%

Table 5-7: Confusion matrix for four different tasks (2nd model)

Predicted \ Truth	Defect	No defect
Defect	44	3
No defect	0	31

Task: 1

Predicted \ Truth	Defect	No defect
Defect	42	7
No defect	4	27

Task: 2

Predicted \ Truth	Defect	No defect
Defect	31	1
No defect	0	29

Task: 3

Predicted \ Truth	Defect	No defect
Defect	37	1
No defect	1	29

Task: 4

Table 5-8: Average training time of each task (2nd model)

Task	1	2	3	4
Train Time	1h 2m 2s	42m 7s	17m 10s	13m 5s

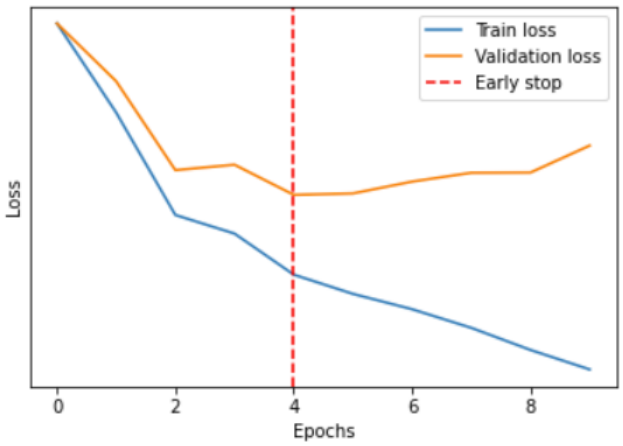

Fig. 5-7: Example of train and validation losses of the 2nd model (task 1)

5.4.4. Third DL Model (ProtoNet + Convnet)

The results of the third model are presented in Tables 5-9, 5-10, 5-11 and Fig. 5-8. It is seen that when comparing the evaluation metrics values of the front face and back face, the same trend as the two previous models is followed here, meaning that the model can predict the damage on back face better than the front face. Overall, the network has a better performance compared to the first model, which suggests that using the first model as a base for a Prototypical network, for this analysis, is a good choice. This is more notable when comparing the training time of the first and third models, where the third network offers a higher accuracy (or other evaluation metrics), while requiring the same training time. This model has the best and worst prediction performance in task 1 and task 4, respectively. An interesting result here is that the model's performance deteriorates when adding a sensor, as opposed to the two previous models. This might be explained by the different working principles of a Prototypical network compared to a simpler CNN. Adding a sensor can improve the visibility of damage by causing a clear colour change and a nice damage pattern. However, when adding a sensor, the difference between the damage patterns of a sample impacted at 12J and 64J is much higher than those of 12J and 64J in the case of a reference sample (without any sensor). Given that the dataset includes images of all samples damaged within the BVID range, in sensor-integrated samples, a more different damage pattern between various images can adversely influence the network's performance, thus, achieving a slightly lower accuracy, precision, or recall. Even though adding the sensor makes the damage on the images easier to predict, this shows how AI works differently from the human brain, and sometimes a task that is easier for humans is harder for an AI. It should be noted that the sensor can still be beneficial when looking at the training time of different tasks (Table 5-11). Therefore, using the third model for the sensor-

integrated dataset may still be advantageous, particularly if images of only specific impact energy are used as input.

Table 5-9: Evaluation metrics for four different tasks (3rd model)

NAME	**Values per dataset**			
Task	1	2	3	4
Accuracy	94.87%	84%	88.52%	69.12%
Precision	100 %	81.25%	93.55%	78.95%
Recall	91.67%	72.22%	85.29%	69.77%
F-1	95.65%	76.47%	89.22%	74.11%

Table 5-10: Confusion matrix for four different tasks (3rd model)

Predicted \ Truth	Defect	No defect
Defect	44	4
No defect	0	30

Task: 1

Predicted \ Truth	Defect	No defect
Defect	13	5
No defect	3	29

Task: 2

Predicted \ Truth	Defect	No defect
Defect	29	5
No defect	2	25

Task: 3

Predicted \ Truth	Defect	No defect
Defect	30	13
No defect	8	17

Task: 4

Table 5-11: Average training time of each task (3rd model)

Task	1	2	3	4
Train Time	53m 32s	36m 20s	20m 54s	16m 3s

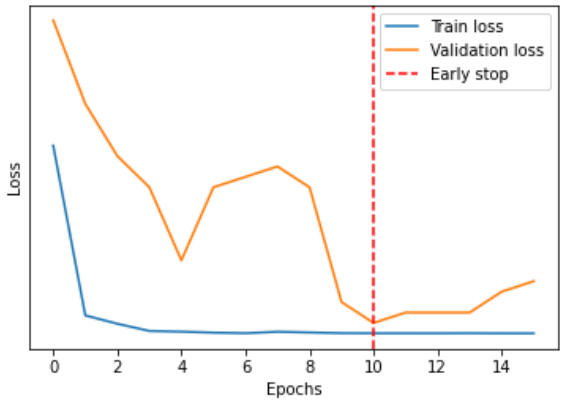

Fig. 5-8: Example of train and validation losses of the 3rd model (task 1)

5.4.5. Fourth DL Model (ProtoNet + ResNet)

This section presents the results of the fourth model in Tables 5-12, 5-13, 5-14 and Fig. 5-9. Like all previous models, here, detection and prediction of damage on the back face is a more straightforward task than the front face. This model shows the best and worst performance in task 1 and task 4, respectively. As this model employs a Prototypical network in its architecture, its performance is more similar to the third model, than the first two. This is particularly true when comparing the results of reference and sensor-integrated samples (tasks 1&3 and 2&4), where a slight accuracy reduction can be seen in the latter. The reason for this poorer performance was discussed in the previous section. However, here, the performance deterioration due to adding a sensor is less considerable compared to the third model, suggesting that the ResNet can act better as a base for the Prototypical network compared to the first simpler CNN. With an exception for task 4, the results of the training time (Table 5-14) also indicate the efficiency of the fourth model for different damage prediction tasks. Given the complex architecture of this model, it might be more beneficial when dealing with more challenging damage detection tasks, for example, composite structures without a sensor with lower impact damage energies.

Table 5-12: Evaluation metrics for four different tasks (4th model)

NAME	**Values per dataset**			
Task	1	2	3	4
Accuracy	96.15%	88.24%	91.8%	85.29%
Precision	100%	94.12%	96.77%	92.1%
Recall	93.6%	84.2%	88.24%	83.3%
F-1	96.69%	88.88%	92.3%	87.48%

Table 5-13: Confusion matrix for four different tasks (4th model)

Predicted \ Truth	Defect	No defect
Defect	44	3
No defect	0	31

Task: 1

Predicted \ Truth	Defect	No defect
Defect	32	6
No defect	2	28

Task: 2

Predicted \ Truth	Defect	No defect
Defect	30	4
No defect	1	26

Task: 3

Predicted \ Truth	Defect	No defect
Defect	35	7
No defect	3	23

Task: 4

Table 5-14: Average training time of each task (4th model)

Task	1	2	3	4
Train Time	55m 33s	37m 59s	23m 2s	39m 45s

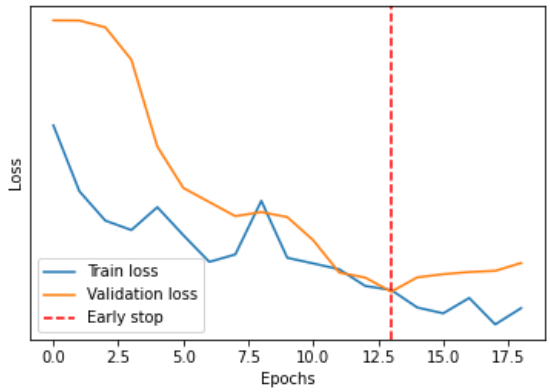

Fig. 5-9: Example of train and validation losses of the 4th model (task 1)

5.4.6. Comparison and Discussion

Herein, two important evaluation metrics, accuracy (Fig. 5-10) and training time (Table 5-15), are chosen to compare and analyse the results of the four models. The reason for selecting accuracy is that it considers both TF and TN (all correct predictions) when considering the whole dataset (not just a part). Therefore, in the case of damage detection, this criterion may allow for a better understanding of the system's performance. Moreover, training time can be an important parameter, as in some real-life or controlled laboratory monitoring scenarios, the structure's health should be assessed rapidly. For example, short-term monitoring might take only a few hours [208]. Furthermore, it may be necessary to apply the NDE part by part in very large composite structures through different steps, highlighting the necessity of developing a fast damage recognition tool. Accordingly, in real-world applications, longer training times can make it harder to deploy the model since it can impact its scalability and practicality. Therefore, finding the optimal training time that balances accuracy and efficiency is crucial in developing effective DL models.

A comparison of all results suggests that the first convolutional network achieves the lowest score while the ResNet or combining a Prototypical network with a ResNet achieves the highest scores. This is as expected because the first convolutional network is the simplest one, whereas the fourth one was adapted for the case of a 'few-shot' classification. Prototypical networks are a good choice for a small dataset and a simple task (such as a binary classification on this dataset). Comparison of the outcomes of the first and third models, as well as those of the

second and fourth models, shows a great improvement in damage recognition accuracy both on front-face and back-face due to applying a Prototypical network. It is seen that both in the second model (when ResNet is used as a classification model) and in the fourth model (when ResNet is used as a base model for the Prototypical network), the ResNet performs better than a simpler convolutional network. This is because of the better architecture of the ResNet (by using the residual connections) and the fact that it has been pre-trained. Using pre-trained models that have been trained on other datasets can improve their performance because the network does not start learning from scratch. Instead, it starts learning with the set of parameters where the last learning converged. Also, a deeper network such as ResNet offers a higher capacity to understand and analyse the image.

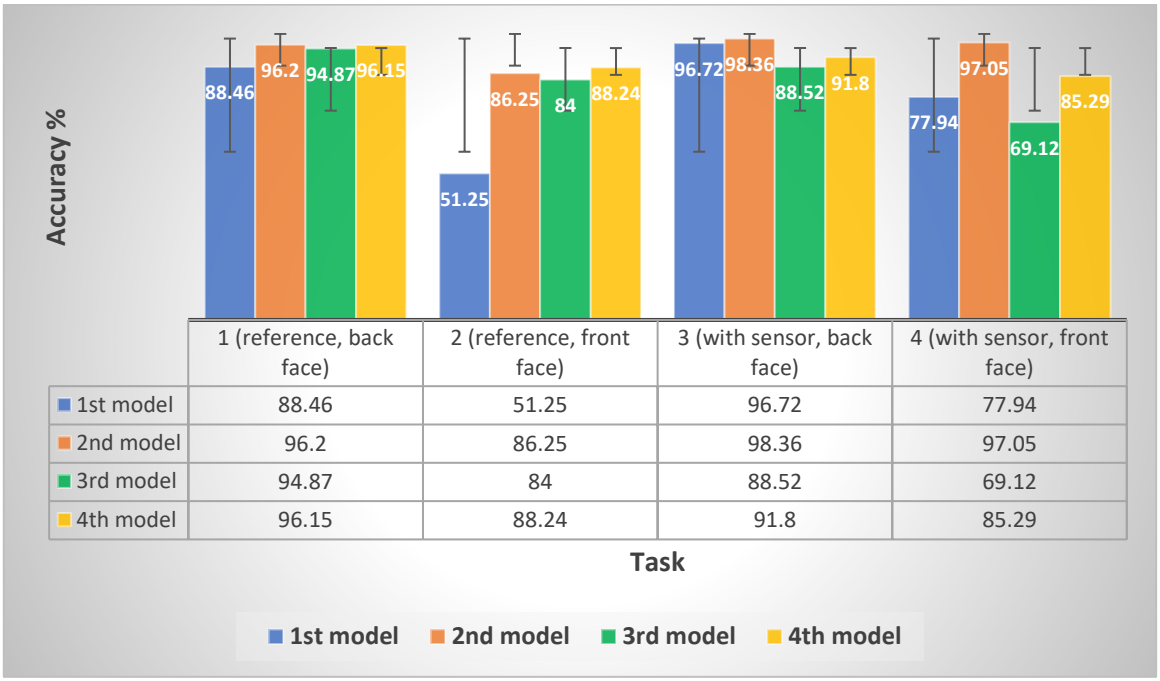

Fig. 5-10: Comparison of the accuracy for different tasks in all four models

Table 5-15: Comparison of the training time for different tasks in all four models

Model \ Task Number	1 (reference, back face)	2 (reference, front face)	3 (with sensor, back face)	4 (with sensor, front face)
1st model	54m 12s	40m 55s	16m 56s	13m 18s
2nd model	62m 2s	42m 7s	17m 10s	13m 5s
3rd model	53m 32s	36m 20s	20m 54s	16m 3s
4th model	55m 33s	37m 59s	23m 2s	39m 35s

Overall, all models perform quite well on the third and fourth datasets. This is due to adding a hybrid glass/carbon sensor on the back face and front face, achieving images with higher contrast between the damaged and undamaged areas (the damaged area is brighter, and the

background is darker) (see Fig. 5-11). The damage recognition accuracy of the first model on the back face and front face increases by 8.26% and 26.74% when using a hybrid glass/carbon sensor. Similarly, adding a sensor improves the accuracy of the second model by 10.8% and 2.16% on the front face and back face, respectively. In both cases, the front face benefits more from adding a sensor. A more complex nature of Prototypical networks in the third and fourth models may capture very detailed features of damage patterns on each side of the sensor-integrated samples, which explains a slightly lower accuracy of these two models on the third and fourth datasets (see Fig. 5-12). Regarding the training time, it is almost the same for all models. If the training time is significantly higher for a model while not improving the performance, it can also be an important factor when selecting the model. Given that ResNet has more layers, it is expected to have a longer training time in models with this network. This has proved to be the case here, but the difference is not big. The results show a faster training time in the third and fourth tasks, confirming the beneficial effect of the hybrid glass/carbon sensing technology in the autonomous detection of BVID using a CNN model.

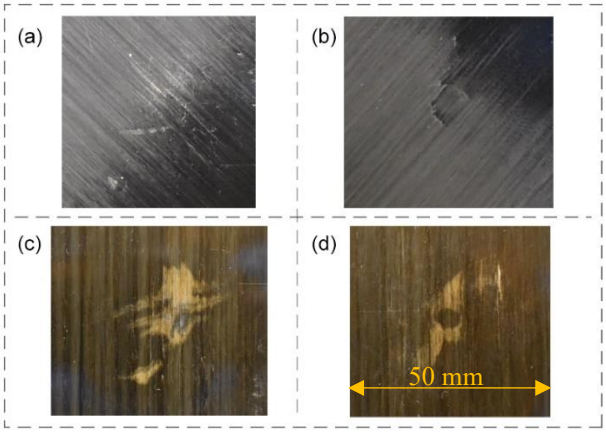

Fig. 5-11: Damage patterns on different datasets (tasks): a) back-face of reference samples (task 1), b) front-face of reference samples (task 2), c) back-face of sensor-integrated samples (task 3), d) front-face of sensor-integrated samples (task 4)

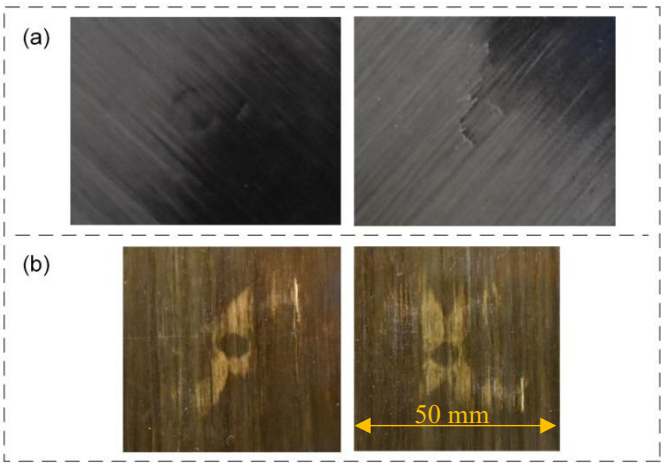

Fig. 5-12: Graphical explanation of a lower accuracy in the third and fourth models (Prototypical networks) when adding a sensor. Impact damage on (a) front-face of reference samples impacted at 36J (left) and 64J (right), and (b) front-face of sensor-integrated samples impacted at 18J (left) and 27J (right). The visual difference between the damage pattern of reference samples impacted at two different energies is significantly less identical than that of sensor-integrated samples. This is true, even though a bigger energy gap exists in (a) than in (b). Given the strong pattern recognition of Prototypical networks, more different damage patterns in sensor-integrated samples impacted at various energies (within the BVID range) may adversely influence the network's performance.

Finally, some points to note: first, when it comes to an understanding of false positives (FPs) and false negatives (FNs), there are a few relevant factors. It is noticeable on the FP images that there are prevalent light reflection anomalies. Images with defects also tend to be brighter on average. This can sometimes give the network the impression that there is a correlation between image brightness and the presence of damage. Similarly, most FN images are darker because images without damage tend to be darker. Some examples of this can be seen in Fig. 5-13. For future work, a more in-depth pre-processing can be performed on images to ensure that the influence of brightness is minimised across the entire image dataset. Second, this study focused only on BVID; all results are based on the performance of the different models on the BVID image dataset. Note that due to the small size of dataset (limited number of images), images of all samples damaged at or below BVID energies (12J, 18J, 27J, 36J, 64J) were included. In this case, the results represent the average model performance on a range of impact energies within the BVID range. This can be seen as a good assessment of the CNN model's performance because the impact damage in real-world examples does not always happen at a well-known energy. However, depending on the specific application and damage monitoring

scenario, it might be interesting for future studies to focus on only a particular impact energy, for example, the threshold of BVID and visible impact damage, to achieve a more precise prediction result. It would allow not only damage detection and localisation, but classification and severity estimation as well. Another potential route for future work is exploring different fibre types and architectures in the sensor structure to generate a different damage pattern on composite surfaces. For example, our preliminary investigations show that if using HS40 carbon prepregs as the sensing layer (instead of YS-90 carbon) or woven glass prepregs as the outer layer (instead of unidirectional glass), a better contrast between the damage pattern of a reference and sensor-integrated sample can be achieved, which accordingly improves the DL or ML model's performance (see Fig. 5-14). The proposed SHM method in this chapter can be further automated by adding a Remotely Operated Vehicle (ROE) that takes surface images of large composite structures, including inaccessible parts, in real-life applications.

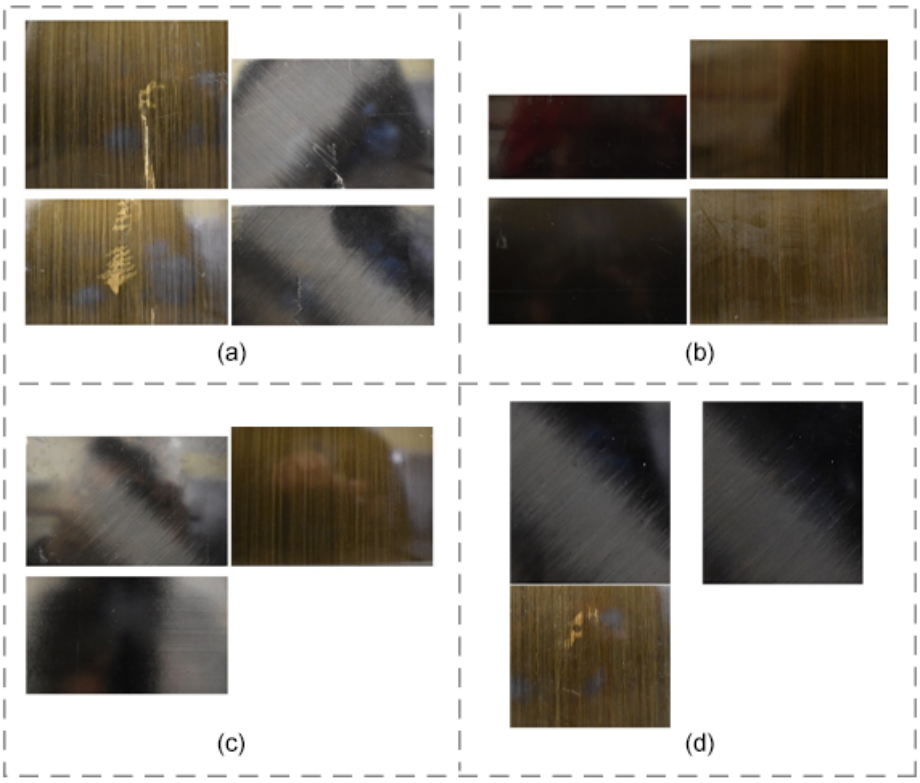

Fig. 5-13: Some examples of the predictions that are most prevalent across networks: a) true positive, b) true negative, c) false positive, d) false negative

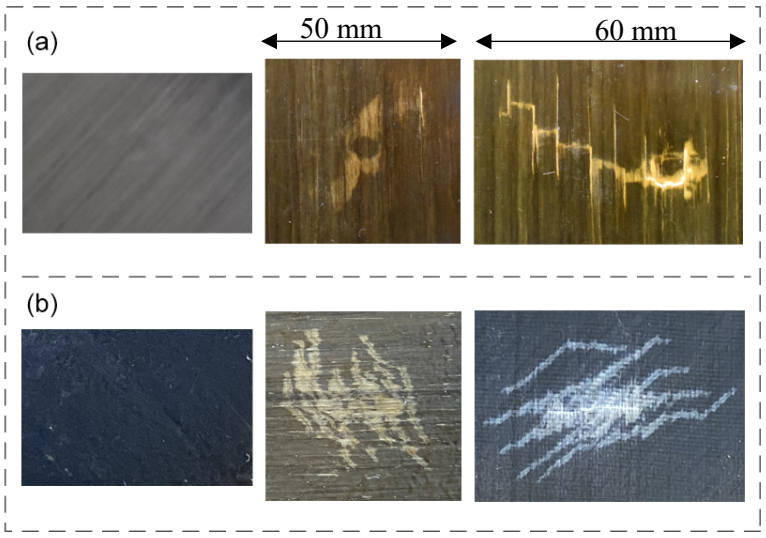

Fig. 5-14: Potential strategies to generate various damage patterns with higher detection possibility: a) using an HS40 carbon layer as the sensing layer (right). The damage pattern is larger and different from a sample without a sensor (left), or with a sensor composed of a YS-90 carbon layer (middle) (these images were taken after the impact test), b) using a woven glass layer as the outer layer (right). The white colour and bi-directional fibres of this glass layer may generate a more recognisable and larger pattern than a sample without a sensor (left), or with a sensor composed of a unidirectional S-glass layer (middle) (these images were taken after the indentation test).

5.5. Summary

This chapter successfully applied four DL models to detect BVID on both impacted and non-impacted surfaces of composite panels with and without a hybrid glass/carbon sensor. The input in all DL models was simple surface images; thus, this study proposed an autonomous BVID recognition system in composite materials using DL models, then improved the DL model's performance by introducing hybrid glass/carbon sensors. The following conclusions can be drawn from the results:

Depending on the dataset, different CNNs can be trained to detect BVID using simple images of the composite structure's surface. The results of all four CNNs in both reference and sensor-integrated composites of this study confirmed that the AI-based BVID detection accuracy is higher on the back-face than the front-face. This is due to a more recognisable damage pattern on the back-face of these thin-walled composite structures. Therefore, where the non-impacted side is accessible, using back-face images as input to machine learning network is preferred.

All four DL models could learn and identify BVID quite well. ResNet outperformed other models in most of the tasks. This is because of the flexible and robust architecture and using residual connections. Also, a Prototypical network can offer higher accuracy than a simple CNN, especially for small datasets, but it may require a higher computational time.

The hybrid glass/carbon sensing technology provides a higher contrast between the damaged and undamaged areas, thus, improving the AI model's performance to a great extent, especially on the front-face. The results of the first and second models showed an improvement of 26.74% and 10.8% in damage detection accuracy when adding a sensor on the front-face. It should be noted that a very complex network, such as a Prototypical network, may capture very detailed features of damage patterns. In this case, as the sensor may add to the variance of the damage pattern, it can slightly decrease the model's accuracy. Nevertheless, the training time of models confirmed that the glass/carbon sensing system could significantly reduce the training time, enhancing the computational efficiency of AI-based damage detection systems.

In future work, the following research directions could be considered:

A more in-depth pre-processing could be performed on input data to refine the design and further optimise the AI model's performance. For example, the BVID range can be narrowed, closer to the threshold of visible impact damage and BVID. Also, more efforts can be made to ensure that the influence of the brightness is minimised in the image dataset.

Exploration of the potential of AI-based damage detection methods in a real-world setting, including scalability and reliability testing. For example, the proposed SHM method can be further automated by adding an ROE that takes surface images of large composite structures, including inaccessible parts.

Design of sensors to create more recognisable damage patterns, achieving a higher contrast between the damaged and undamaged areas. Further analysis of different DL models with input data, including images of composites surface with various sensors, can help find a better relationship between the network performance and damage pattern caused by the sensor.

Chapter 6

Application Case Study

6.1. Introduction

This chapter investigates the feasibility of using hybrid sensors to visualise BVID in curved composite panels. Firstly, a set of curved composite panels are designed and manufactured and, their mechanical response under quasi-static indentation is characterised, followed by a comparison of the results with those of flat panels. After that, hybrid composite sensors are applied on the outer surfaces to investigate their capabilities in BVID visualisation of curved composite structures under both static indentation and low-velocity impact loadings. To represent a real-life application case study, similar dimensions to composite hydrogen storage tanks are considered when designing curved panels. A Nikon camera is also used during the indentation test, allowing for capturing the sensor activation time, and activation area at different stages of the test. This information is connected to data obtained from the load-displacement graphs, enabling a thorough analysis of sensor performance in visualising different stages of BVID.

6.2. Curved Composite Structures

In today's advanced manufacturing world, curved composite structures play a key role in different industries, from aircraft fuselages and wings in aerospace and the car body panel in automotive sectors to curved roofs and bridges in construction and wind turbine blade and solar panels in renewable energy sectors [209,210]. Notably, curved composites also feature prominently in hydrogen storage tanks as they offer several advantages, including a lightweight, high strength-to-weight ratio, high corrosion resistance, and high safety and durability. These are particularly of great interest in sectors embracing hydrogen as a clean energy carrier, including the automotive and aerospace industries [211].

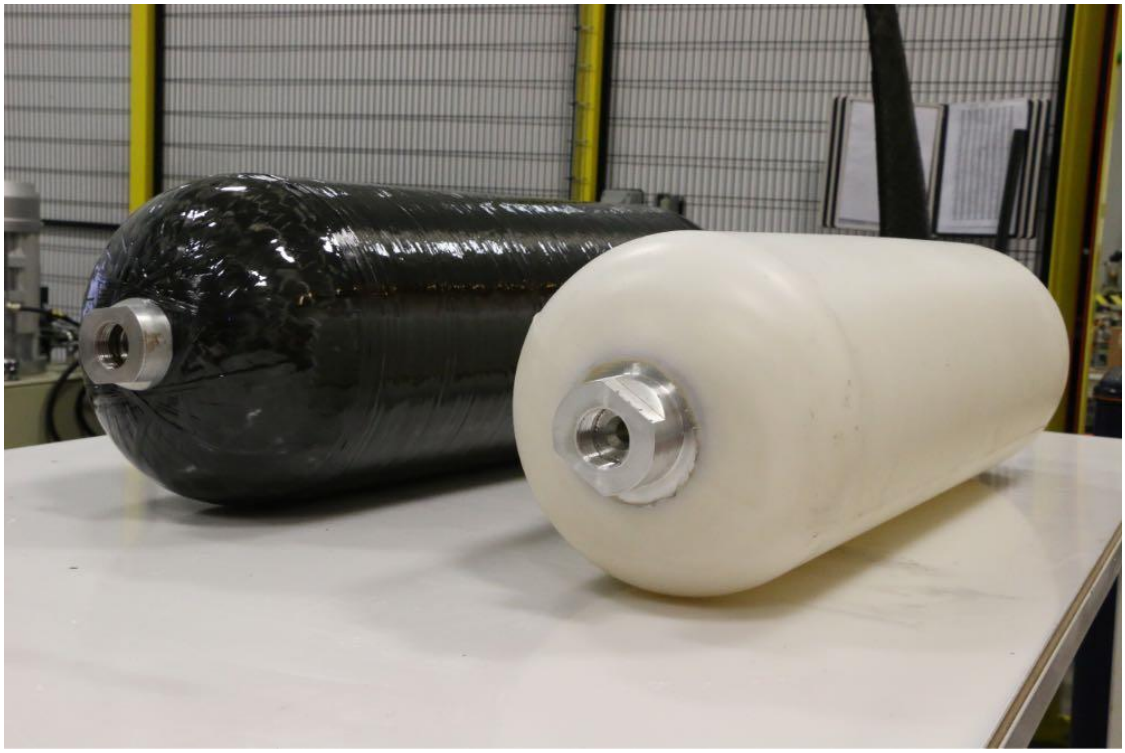

Fig. 6-1: An example of a Type 4 cylindrical hydrogen pressure vessel, made from filament wound carbon fibre over a thermoplastic liner. The tank has been designed for use in the automotive sector and can hold 40 litres of hydrogen at a 350-bar pressure [212]

Two primary types of damage to the composite hydrogen storage tanks reported in the literature are internal damage caused by the cycles of charge and discharge and external damage caused by impact [213]. The latter may happen due to a drop impact and foreign object impact during transportation, dismount, and service, resulting in multiple damage modes such as matrix cracking, dents, fibre breakage, and delamination [214,215]. The research on curved composite structures under out-of-plane loading has mainly focused on the influence of different structural and impactor geometrical parameters on the impact response [209,210,216–226] and very limited studies have explored the health monitoring of curved composite structures under low-velocity impact [215]. For instance, Choi studied the impact response with respect to the "stiffness change" induced by cylinder stress from internal pressure [219], Saghafi et al. [222] investigated the influence of the pre-load and boundary conditions, Yang et al. [210] analysed the influence of impact energy and impact position, Gemi et al. [221] studied the effect of the impact velocity and the pipe diameter, Wan et al. [226] scrutinised the influence of the curvature diameter, and Seifoori et al. [220] investigated the effect of the shape of the projectile nose on the impact response. Moreover, the influence of the geometrical parameters on the impact behaviour of curved composite structures was studied in [216–218]. Rocha et al. [215] applied

fibre Bragg grating sensors on a composite overwrapped pressure vessel for hydrogen storage to monitor the impact damage. The sensing array strategy allowed to detect and locate BVID resulting from drop-weight impact tests. However, there were errors as small as 17 mm and up to 56 mm between the predicted and 'real' impact locations.

This chapter aims to investigate the potential application of the hybrid composite sensors for impact damage monitoring in curved composite structures. This sensing technology is much simpler than other NDE methods and has shown promising performance in improving the visual inspection in flat composite panels, but it has not been applied to curved composites to inspect BVID. This necessitates testing and analysing curved composite panels equipped with the hybrid sensor to understand its effect on mechanical properties such as stiffness, indentation, and impact behaviour. Harris et al. [216] reported that the impact behaviour of curved plates was found to be largely representative of impact testing on a complete cylindrical pipe section, broadly producing a similar delamination threshold load value. Hence, in this research, with a focus on hydrogen storage tanks as a case study, curved composite panels resembling the dimensional features of composite pressure vessels for hydrogen storage are fabricated. These panels are outfitted with hybrid sensors and subjected to static indentation and low-velocity impact tests to evaluate the effectiveness of the hybrid sensor in detecting BVID. Furthermore, while the substitution of static indentation and low-velocity impact tests has been extensively explored in the literature for flat samples, there is currently a lack of information regarding its validity in the context of curved structures. The outcomes of this chapter can provide a valuable reference regarding the relationship between these two tests in the context of curved structures.

6.3. Manufacturing and Test Methods

Two sets of curved composite samples, including *Reference* and *Sensor* samples, were manufactured for this chapter. The former features 32 plies of unidirectional IM7 carbon/8552 epoxy prepregs with quasi-isotropic lay-up of $[45/0/90/-45]_{4s}$. In the latter, a hybrid composite sensor composed of a layer of unidirectional YS-90A carbon prepreg and a layer of unidirectional S-glass/913 epoxy prepreg, both with a 90° orientation, was also applied on both the front face (impacted face) and back face (non-impacted face) of the *Reference* samples. The *Reference* samples were cured at 110 °C for 60 minutes, followed by 180 °C for 120 minutes under a constant 0.7 MPa pressure, as recommended by the manufacturer for IM7/8552 prepregs. The manufacture of the *Sensor* samples followed a two-step process, where the substrate was cured first, and the next day, the sensor was applied on either side, and the entire

structure was cured at 125 °C for 60 minutes under a constant 0.7 MPa pressure, as recommended by the manufacturer for S-glass/913 prepregs [7,125]. A curved metal mould with a radius of 130mm was utilised, and a conventional hand lay-up method was used to stack layers onto it. The mould dimensions were designed to match those of composite hydrogen storage tanks, serving as a practical case study application. Subsequently, a standard vacuum bagging method was applied to the curved aluminium plate, with additional silicone sheets placed over the laminates to ensure a smooth surface and uniform pressure distribution within the autoclave (see Fig. 6-2). Due to limited data on out-of-plane testing of curved composite structures, two samples were manufactured for every single indentation and impact test in this chapter, repeating each test twice to ensure repeatability and reliability.

Fig. 6-2: Different manufacturing stages of the curved composite panels: a) a flat metal sheet transformed into a curved mould with desired curvature radius (13cm) to stack the layers that were cut into standard dimensions, b) the autoclave was set up according to the curing cycle of the prepregs, c) the edges of the cured samples was trimmed using a cutting machine to achieve precise dimensions and smooth edge finish

Following the completion of sample manufacturing, quasi-static indentation tests were initially conducted and analysed, followed by low-velocity impact tests at various impact energies. The

setup for both indentation and impact tests was similar to that of flat samples (as detailed in Chapter Three). However, due to the curved shape of the samples, a custom-designed supporting window and clamping fixture system was created using SolidWorks software and subsequently manufactured and assembled. The design drawings and drafts for this window are provided in Appendix C.

The custom-designed window was made to closely match the one used for flat samples. It includes six points where screws are used to fix the sample from the top side, along with a central empty rectangular area measuring 75mm*125mm, where the sample (100mm*150mm) is placed, ensuring consistent boundary conditions for testing. Note that the sample is secured along its entire length on the shorter side (see Fig. 6-3). This design establishes a reliable platform for comparing the results of both flat and curved sample tests. Moreover, the custom-designed window was utilised for both indentation and impact tests, allowing for a meaningful comparison between the static indentation and low-velocity impact test results on curved composite samples. Visual inspection was performed after completing impact tests to analyse the surface damage. All tests (indentation, impact, visual inspection) were performed at room temperature, and all other test parameters (such as indentation rate, setup of a Nikon camera for capturing images of the back face during indentation test, calculation of displacement and energy in impact tests etc.) were similar to those of testing the flat panels (Chapter Three).

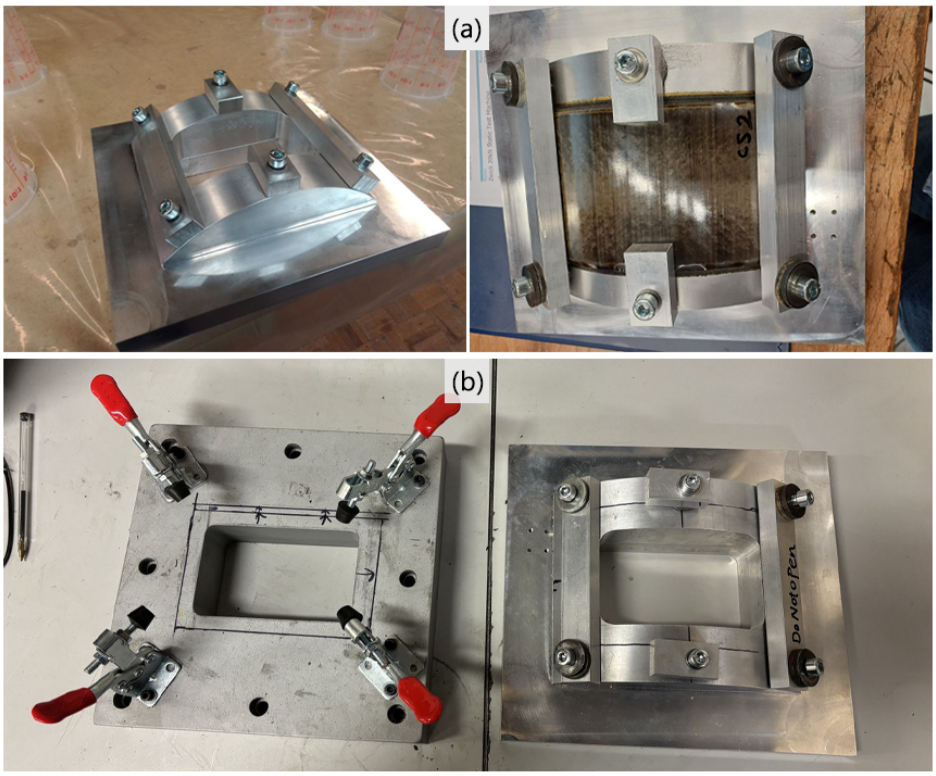

Fig. 6-3: a) The custom-designed supporting window and clamping fixture, b) top view of the supporting windows used for testing of flat and curved samples

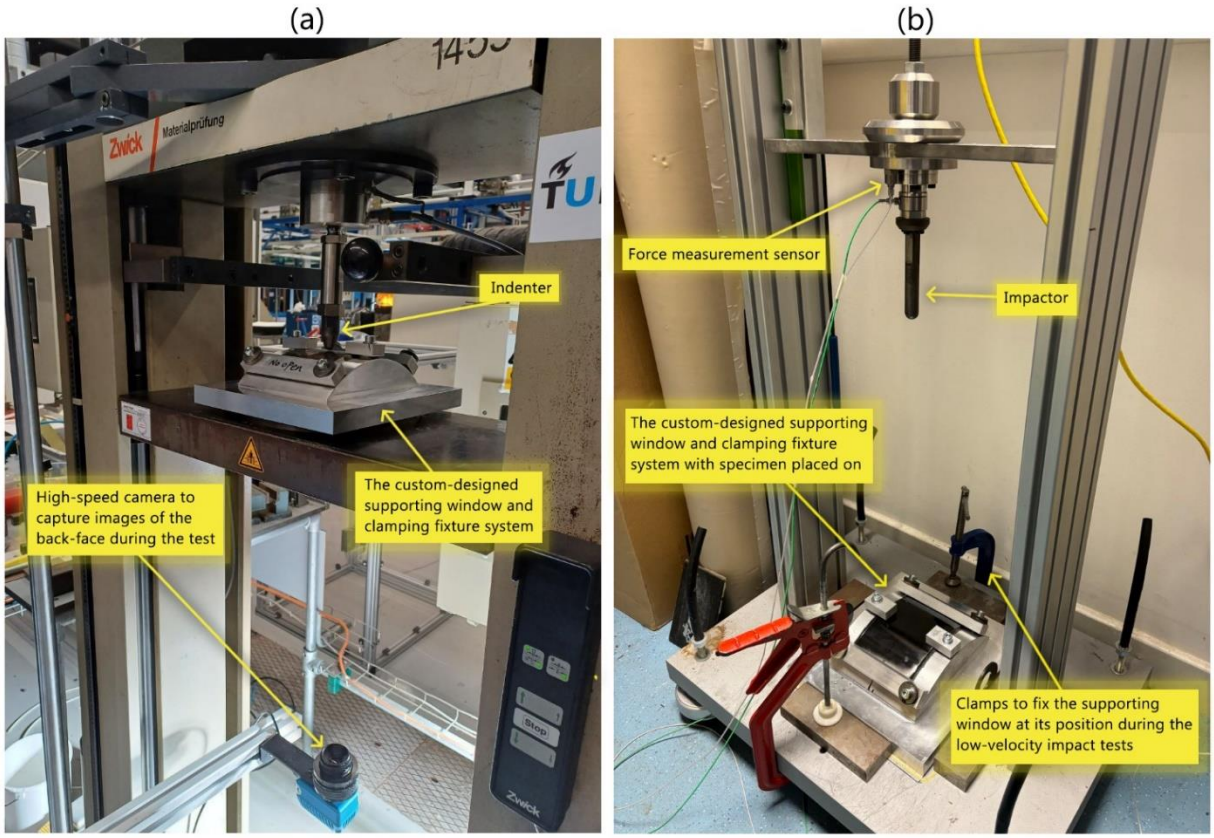

Fig. 6-4: The test setup: a) quasi-static indentation, b) low-velocity impact

To assess internal damage, such as delamination and matrix cracks, the impacted samples were cross-sectioned using a Dremel equipped with a cutting disk designed for carbon fibre composites. The cross-sections were then examined under a microscope with 5x magnification. This process is shown in Fig. 6-5. Additionally, an attempt was made to analyse the internal damage using ultrasonic C-scan, similar to the method used for the flat panels. However, due to the curved shape of the panels manufactured for this chapter, the ultrasonic probe could not be properly applied to the surface, which prevented the capture of the entire damaged area.

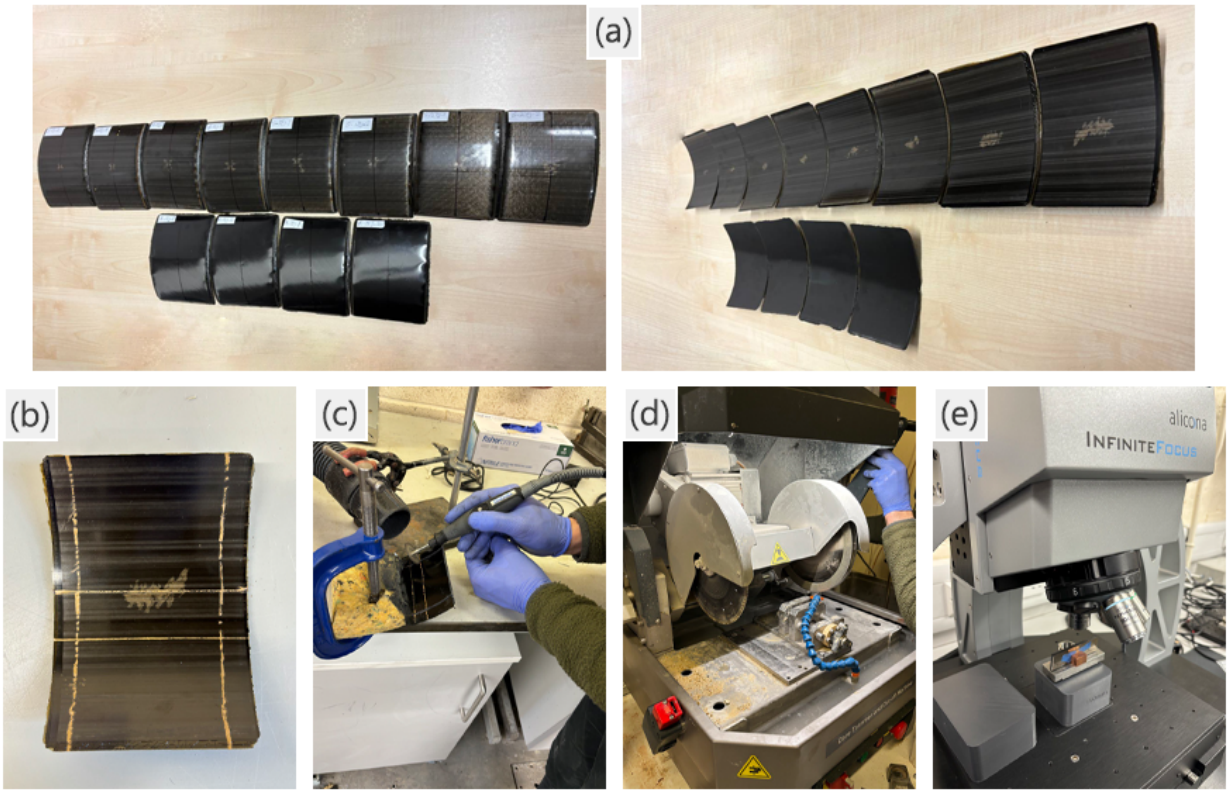

Fig. 6-5: Sample preparation process for internal damage analysis under microscope: a) post-impact test samples, b) marking the sample for targeted sectioning, b) utilising a Dremel with a cutting disk optimised for carbon fibre composites, c) polishing the cross-section to enhance surface quality, using both machine and papers with wet/dry process, d) capturing microscopy images of the prepared cross-section

6.4. Results and Discussion

6.4.1. Quasi-Static Indentation

6.4.1.1. Global Behaviour and Influence of Adding Sensors on Indentation Properties

Fig. 6-6 shows the indentation test results of *Reference* and *Sensor* samples, where for each sample group, the test was conducted two times to ensure repeatability. All samples follow a similar pattern, where a near-linear behaviour is seen until a notable load drop at force and displacement of approximately 5500N and 1.5mm, implying the delamination onset. Then, the graph continues non-linearly up until a second significant drop, which occurs at slightly different forces for different samples, indicating the fibre failure damage. After that, the load does not rise significantly while displacement (deformation) increases. This is highlighted by multiple small load drops, demonstrating that the structure cannot undergo further damage

through deformation, and perforation may happen at any time. The graphs indicate a high level of repeatability across the samples of each group, where there is a notable overlap between the curves before the first load drop, and they gradually differ with an increase in force. A comparison of *Reference* and *Sensor* graphs shows a slightly higher structural stiffness in both Sensor-1 and Sensor-2 specimens than in Reference-1 and Reference-2, suggesting that adding sensors can marginally increase the rigidity, and as the force increases, this becomes more pronounced. It can also be mentioned that adding sensors can increase the fibre failure load threshold to a small extent. To better represent a comparison of the *Reference* and *Sensor* samples, Fig. 6-7 depicts the graphs associated with Reference-1 and Sensor-1 samples. Note that in the rest of this chapter, the *Reference* and *Sensor* refers to Reference-1 and Sensor-1 samples, respectively.

The values of force, displacement, load drop rate, and absorbed energies at the first and second significant load drops are summarised in Table 6-1. The change in energy absorption due to adding sensors at the first load drop is only about 5%, suggesting that delamination in *Reference* and *Sensor* samples occurs at nearly the same force/displacement thresholds. Note that all these results were obtained from *Sensor* samples equipped with two sensors, one on the impacted face and one on the non-impacted face. However, for specific applications, a single sensor may suffice, potentially resulting in even less noticeable changes associated with sensor integration.

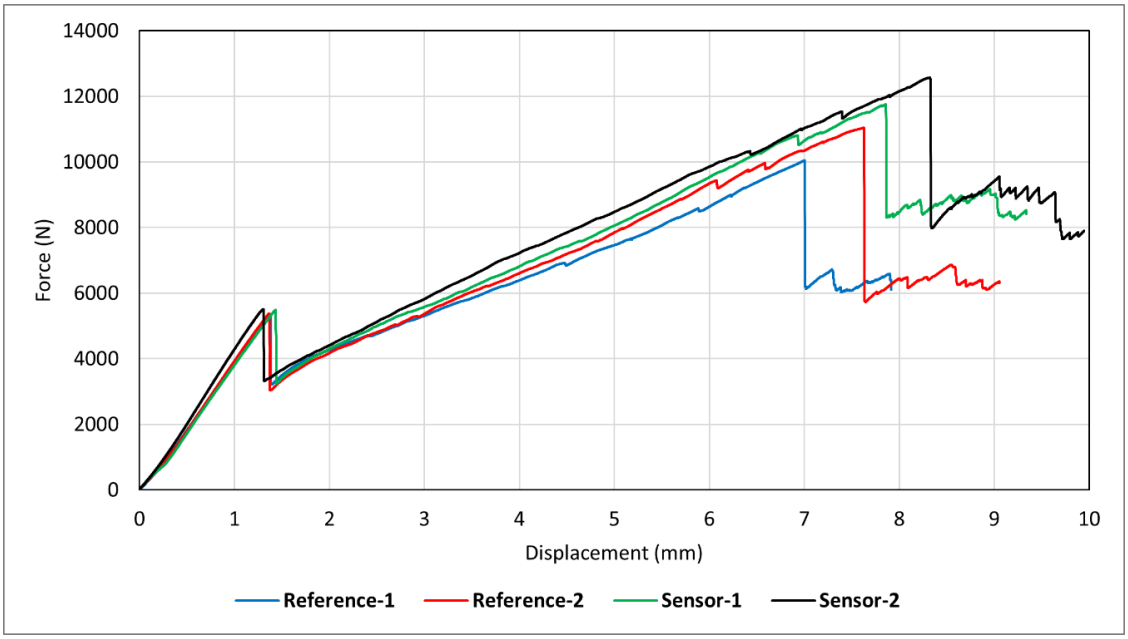

Fig. 6-6: Static indentation test results of all curved samples

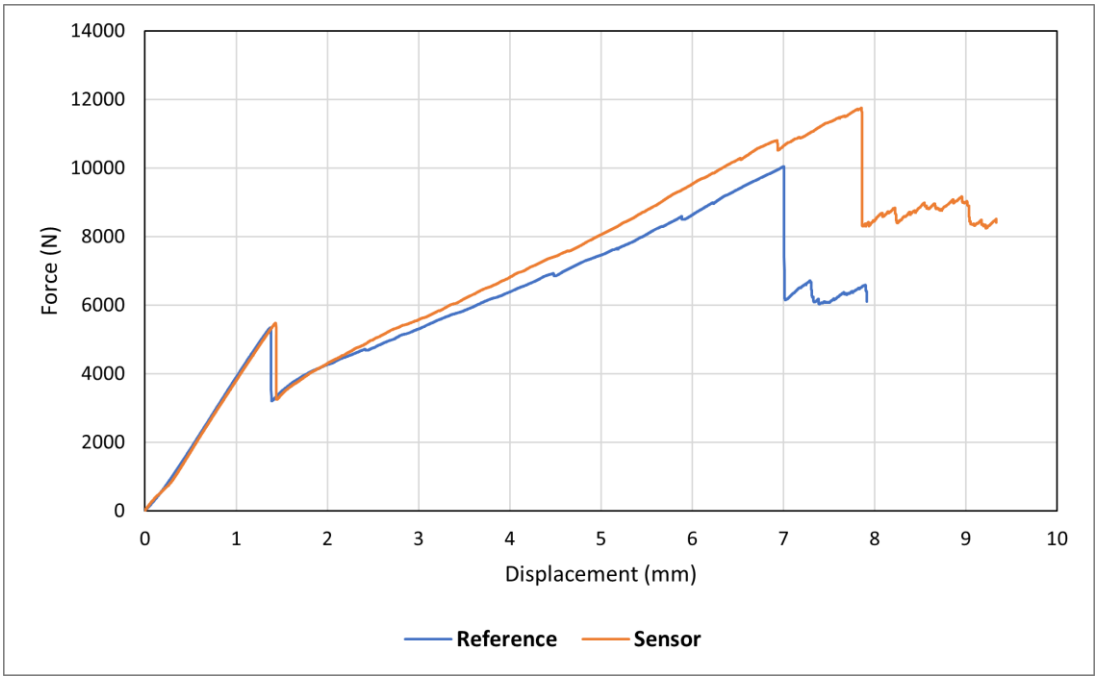

Fig. 6-7: Comparison of indentation response in *Reference* and *Sensor* samples

Table 6-1: Summary of important information obtained from indentation tests

Sample	First load drop (delamination)				Second load drop (fibre failure)			
	Force (N)	Displacement (mm)	Energy absorbed (J)	Load drop ratio (%)	Force (N)	Displacement (mm)	Energy absorbed (J)	Load drop ratio (%)
Reference	5351.47	1.37	3.62	40.02	10047.15	7.00	41.05	38.31
Sensor	5488.29	1.43	3.82	40.76	11751.46	7.85	53.21	29.30

6.4.1.2. Sensor Activation and Visual Inspection

Fig. 6-8 shows force-time graphs of *Reference* and *Sensor* samples during the indentation test, along with selective images of the back face taken at different stages of the test. Fig. 6-8(a) demonstrates that the damage on the back face is not visible both before and after the first load drop, meaning that delamination remains undetected upon visual inspection. Notably, one cannot visually detect the damage long after the delamination onset, extending up to the second load drop, meaning that damage is not detectable even at the onset of fibre failure. It could only become visible shortly after the second load drop. This suggests that the damage could be visualised through visual inspection of the surface only after the structural failure. When

comparing Fig. 6-8(b), illustrating the visual inspection results of *Sensor* samples, with Fig. 6-8(a), interesting observations become apparent. Fig. 6-8(b) shows that damage in *Sensor* samples could be visually detected at a force level as low as nearly 4000N. This is a few seconds before the onset of delamination, making the sensor an excellent tool for detecting and preventing delamination in curved composite structures. The visual damage pattern on the surface becomes larger as the force increases, and, particularly, there is a noticeable change in the shape and size of the activated area at force thresholds for delamination and fibre failure. Note that the images showcased here were captured using a black-and-white camera available at the time of testing. For a more comprehensive interpretation of the images and to observe the colour changes induced by the sensor, please refer to the post-indentation images depicted in Fig. 6-9. A more detailed collection of images captured during the indentation test of curved samples is included in Appendix D.

Table 6-2 presents the minimum energy required for sensor activation, demonstrating a good performance of the sensor, which detects damage at just around 2J. In contrast, the threshold energy for the *Reference* sample was nearly 43J. Fig. 6-9 illustrates the post-experiment visual inspection images of the front face and back face of both samples. Looking at the front face in the *Reference* sample, we can see a discernible dent that is surrounded by a few cracks parallel to the fibre direction (45°). The depth of the permanent indentation left on the top face implies significant damage. In the *Sensor* sample, this is relatively less visible due to sensor activation around the area that has been in contact with the indenter. This is highlighted by yellow patches parallel to the sensor fibre direction (90°). At farther distances from the contact area, some discontinuous, faint stripes parallel to the sensor fibre direction are also visible, which shows the propagation of the damage inside the structure. It is important to highlight that the initial damage mechanism on the front face involves matrix cracking due to compressive loads, followed by a permanent indentation, which marks the point where damage becomes visible. This stage indicates significant structural damage. However, the sensor's utility lies in its ability to detect damage mechanisms occurring before the formation of a permanent indentation, much earlier than the emergence of significant but barely visible damage modes such as delamination. On the back face, in the *Reference* sample, the failure damage mechanism is reflected by a significant fibre pull out at 45° beneath the indented area. This suggests that the applied force has surpassed the bond strength between the fibre and matrix. The back face of the *Sensor* sample clearly demonstrates the damage through a large activated area with a yellow colour. Overall, both in *Reference* and *Sensor* samples, the damage on the back face is more visible

than on the front face. This can be attributed to damage mechanisms on either side, where the top face is under contact force and compression, and the back face undergoes tension.

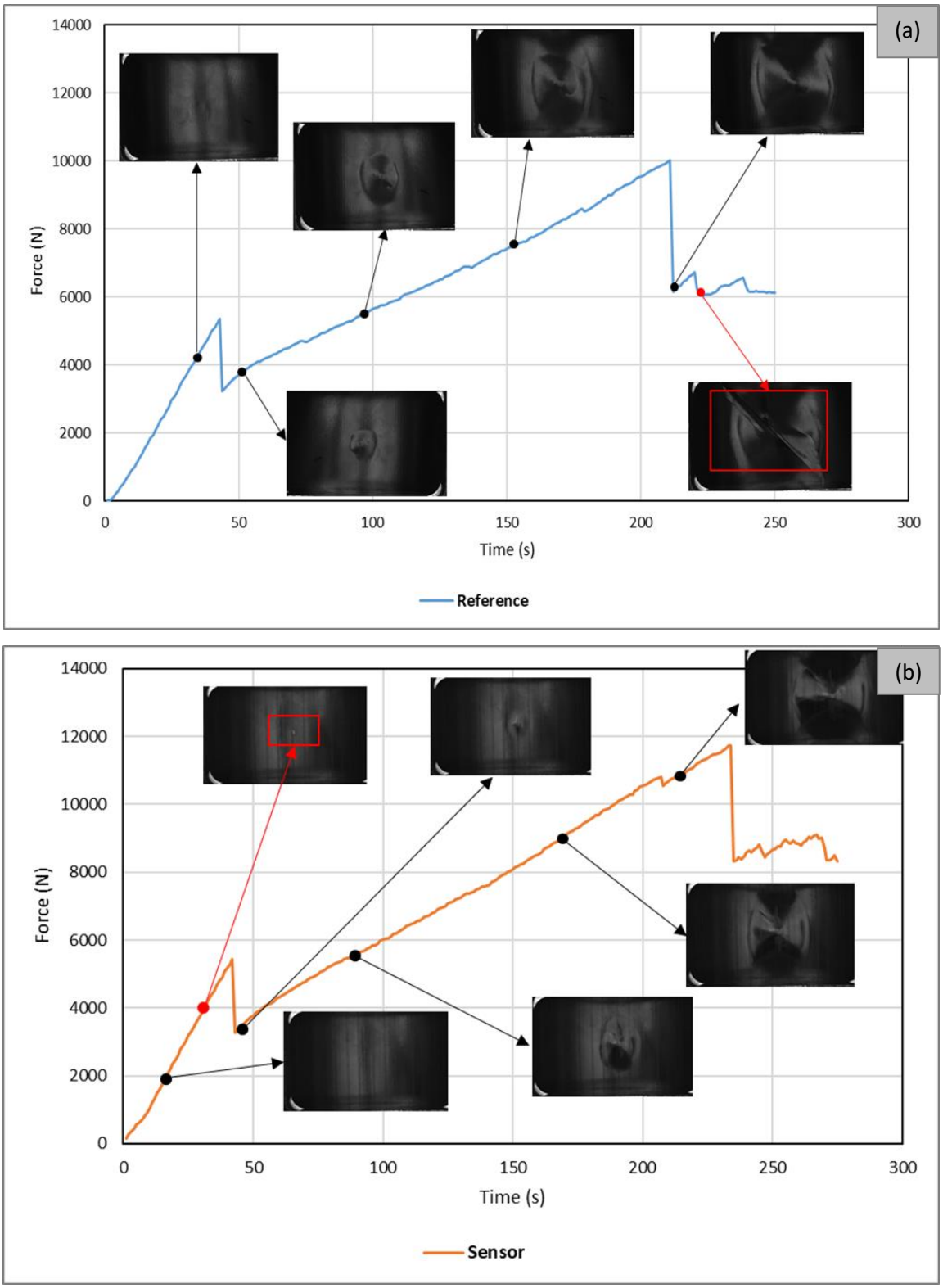

Fig. 6-8: Visual inspection and sensor activation during static indentation experiment: a) *Reference*, b) *Sensor*

Table 6-2: Threshold energies for visually detectable damage (on the back-face)

Sample	Energy (J)
Reference	43.23
Sensor	1.88

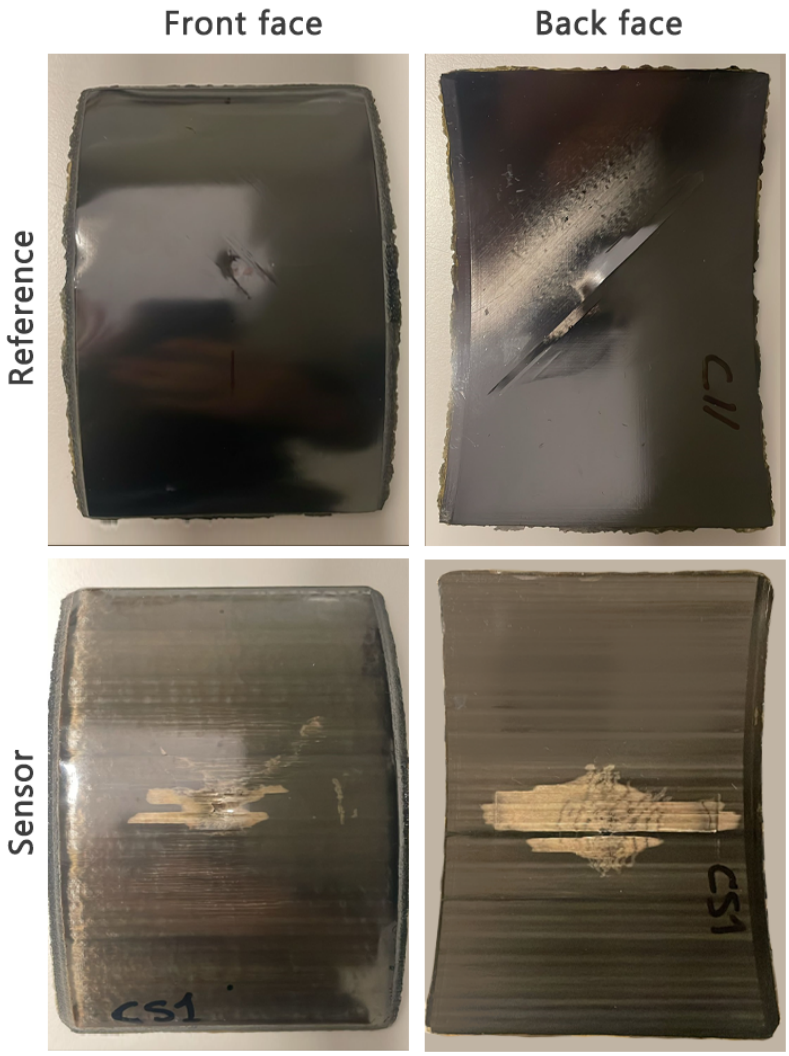

Fig. 6-9: Post-experiment visual inspection: a) *Reference*, b) *Sensor*

6.4.1.3. Comparison of Indentation Behaviour in Curved and Flat Composite Structures

Comparing flat and curved structures offers valuable insights into their respective performances under out-of-plane loading, thereby facilitating the estimation or prediction of the response of curved structures potentially based on the testing of flat structures. This comparative analysis proves especially beneficial considering the potential cost and complexity associated with assessing curved structures. This section outlines a comparison of indentation

response, with a subsequent section providing insight into a comparison of impact behaviour. As shown in Fig. 6-10, both graphs indicate two noticeable load drops, where a linear response is seen before the first load drop. After that, the flat sample continues a linear response, while the curved sample demonstrates a non-linear response and multiple small drops. Interestingly, while the force level at both the first and second load drops is very close in the two graphs, the displacement differs notably. Before the first load drop, the curved sample illustrates a more rigid response as its deformation is considerably lower than that of the flat sample under the same force level. This is mainly due to the curvature of the laminate that can enhance bending stiffness [216]. After the first load drop, however, the curved sample shows a less rigid response than the flat sample, reaching the critical fibre failure load at a higher deformation level. In other words, for the flat structure, the slope of the curve after the first load drop changes slightly, while for the curved sample, the slope after the first load drop decreases significantly. Damage localisation and subsequent large deformation support the delamination propagation along the circumference in the curved sample [209]. Important information obtained from this figure is summarised in Table 6-3. This table highlights two notable differences between the flat and curved samples. The first one is the rate of the first load drop, which is considerably higher for the curved sample, suggesting a larger delamination damage area in the latter. The second notable difference is the absorbed energy associated with the fibre failure damage (at the second drop), which is much higher for the curve panel. Based on these results, the flat and curved structures appear to sustain relatively similar energy levels before undergoing delamination. However, in terms of fibre damage, the curved structure seems to tolerate higher energy levels (approximately 47% higher than the flat sample). In terms of the influence of adding sensors on indentation response, both flat and curved structures show a slightly higher structural stiffness when equipped with the sensor. However, the difference between the *Reference* and *Sensor* samples for both flat and curved structures is not significant.

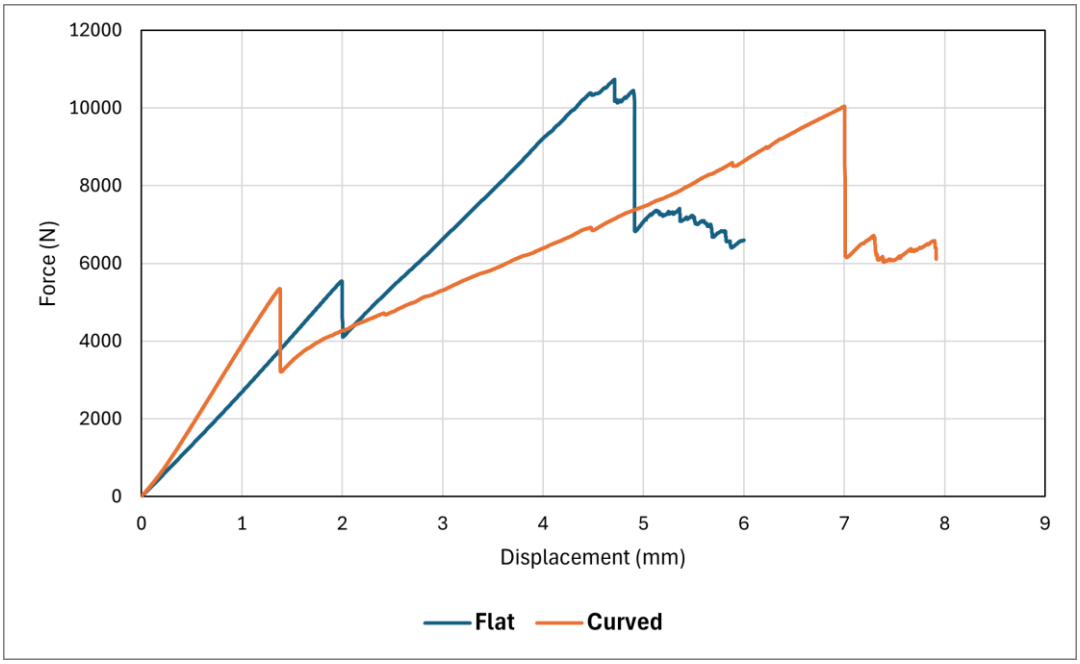

Fig. 6-10: Comparison of static indentation response in curved and flat *Reference* composite samples

Table 6-3: Summary of important information obtained from the comparison of indentation tests in flat and curved samples

Sample	First load drop (delamination)				Second load drop (fibre failure)			
	Force (N)	Displacement (mm)	Energy absorbed (J)	Load drop rate (%)	Force (N)	Displacement (mm)	Energy absorbed (J)	Load drop rate (%)
Flat	5542.28	1.99	5.43	25.85	10445.30	4.89	27.81	34.63
Curved	5351.47	1.37	3.62	40.02	10047.15	7.00	41.05	38.31

6.4.2. Low-Velocity Impact

6.4.2.1. Global Behaviour and Influence of Adding Sensors on Impact Properties

The results presented in the previous section suggested a delamination threshold energy of 3.82J under indentation. As indicated in [7], and discussed in Chapter Three, the impact energy required to induce BVID in quasi-isotropic composite panels was estimated to be 40% higher than the critical energy level derived from the indentation test. Therefore, for the *Sensor* samples, a minimum impact energy of 6J is considered as the lowest impact energy here.

Moreover, three higher energies, including 12J, 18J, and 27J, are considered. For the *Reference* samples, only 12J and 18J are tested. Fig. 6-11 presents the force-displacement graphs of all impact tests conducted on curved samples.

As observed in the graphs, each energy measurement demonstrates excellent repeatability, thereby confirming the accuracy of the impact test results. All graphs demonstrate a near-linear response from the beginning of the test until the force level of approximately 6000N, then show a load drop, followed by a non-linear response until the curve reaches its maximum force and displacement. The load drop confirms the occurrence of delamination. The graphs and visual inspection demonstrated that no penetration, perforation, or fibre failure happened at any of these energies. To better analyse the impact test results, Fig. 6-12 presents a comparison of *Reference* and *Sensor* samples at two impact energies, and important information obtained from all tests is summarised in Table 6-4. The results signify that in both the *Reference* and *Sensor* groups, the absorbed energy and maximum displacement increase with an increase in impact energy. However, a different trend is observed for peak force (maximum force). At 6J and 12J energies, the peak force corresponds to the point where the initial near-linear behaviour ceases, marking the onset of the first load drop. In contrast, for 18J and 27J energies, the maximum force aligns with the maximum displacement, signalling the beginning of the decline in both force and displacement towards zero. Another interesting observation is that in both groups, with an increase in impact energy, the force threshold for the first load drop decreases. This was also reported for curved panels under low-velocity impact in [226].

Fig. 6-12 shows that adding sensors slightly increases the initial structural stiffness, the maximum displacement, and the force level at the maximum displacement. The force-time, force-displacement, and energy-time graphs for all tested samples are provided in Appendix E.

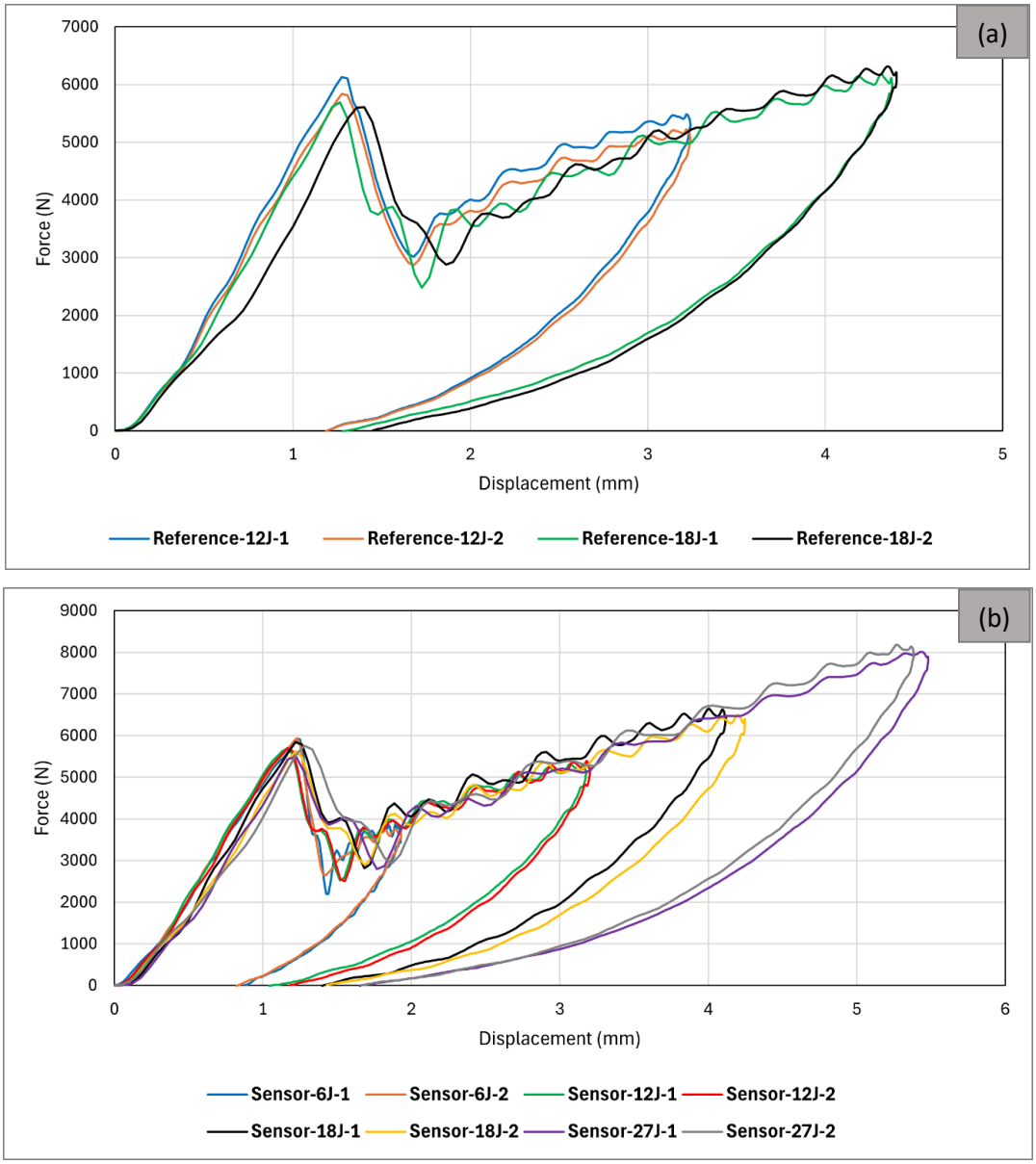

Fig. 6-11: Low-velocity impact test results of all curved samples: a) *Reference*, b) *Sensor*

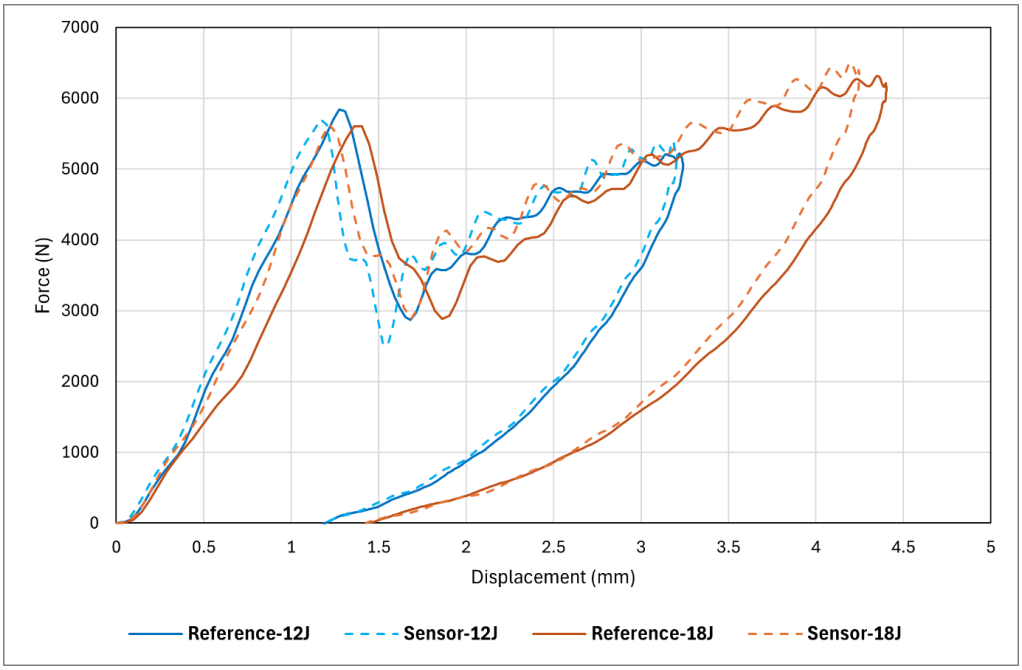

Fig. 6-12: Comparison of impact response in *Reference* and *Sensor* samples

Table 6-4: Summary of important information obtained from impact tests

Sample	Maximum force (N)	Maximum displacement (mm)	Total energy (J)	Elastic energy (J)	Absorbed energy (J)
Reference-12J	5839.53	3.24	12	3.55	8.45
Reference-18J	6314.41	4.40	18	6.05	11.95
Sensor-6J	5934.47	1.92	6	1.51	4.49
Sensor-12J	5702.42	3.20	12	3.57	8.43
Sensor-18J	6500.24	4.24	18	5.69	12.31
Sensor-27J	8181.43	5.38	27	9.12	17.88

6.4.2.2. Visual Inspection and Microscopy Images

This section evaluates internal and surface damage using microscopy and visual inspection images, respectively. The microscopy images reveal internal damage, including matrix cracks and delamination within the plies, across all impact energies ranging from 6J to 27J, observed in both *Reference* and *Sensor* samples. The severity of damage increases with increasing energy levels, evident in the 27J image displaying more pronounced delaminations compared to the 6J image. Additionally, the microscopy images of *Sensor* samples exhibit comparatively lesser

damage than *Reference* samples. This is attributed to the energy absorption by the fracturing of the sensor, thereby reducing the damage experienced by the substrate. This highlights the load-bearing capabilities of the sensor for applications requiring impact resistance (see Fig. 6-13). However, the results of visual inspection reveal that damage at both 12J and 18J is not visibly apparent in *Reference* samples. In contrast, for *Sensor* samples, damage becomes visible even at lower energies, such as 6J. A clear correlation emerges between the area activated by the sensor and the impact energy, with the surface damage pattern increasing alongside energy increases. Comparing flat and curved samples, the damage pattern on the front face appears similar. Yet, on the back face, in curved panels, the damage pattern tends to extend horizontally with increasing impact energy, unlike flat samples where it spreads in both directions. This may be attributed to the curved shape of the former. Overall, the findings of this section suggest that hybrid sensors are capable of detecting BVID both on front face and back face of curved panels.

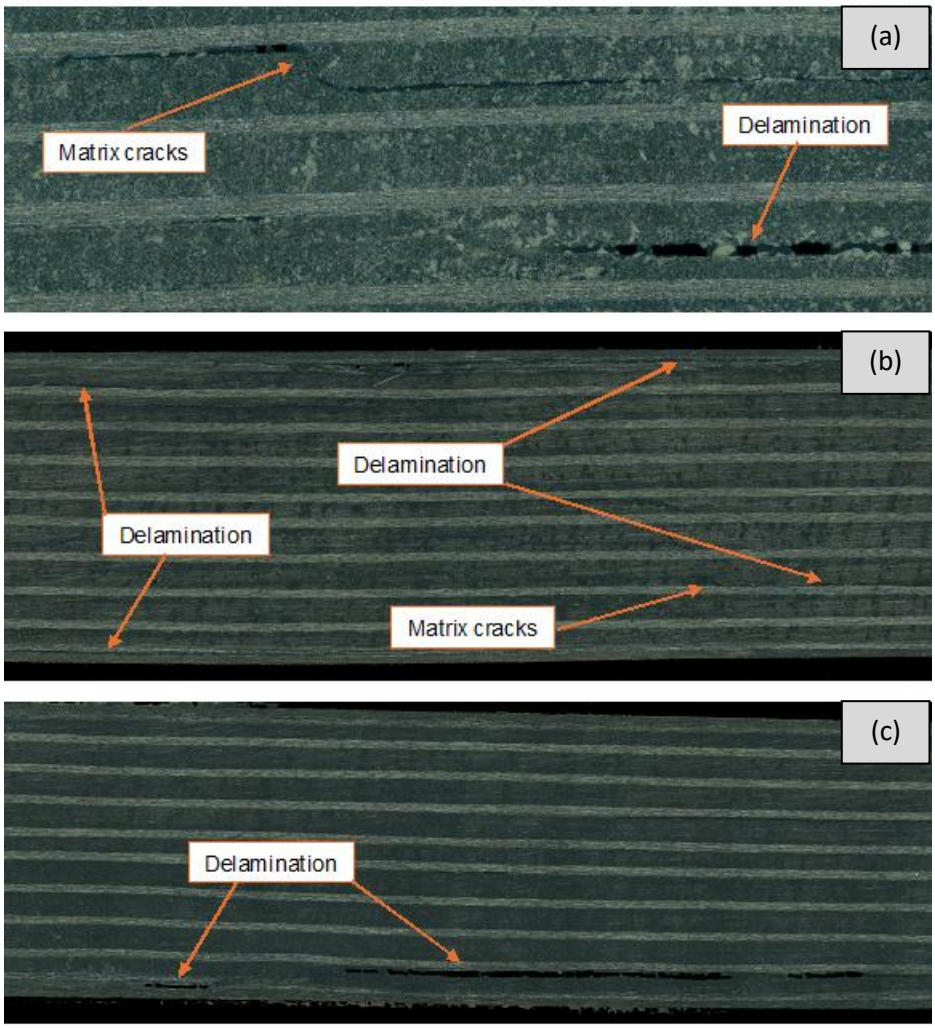

Fig. 6-13: Microscopy images demonstrating different internal damage types, such as shear matrix cracks and delamination at various impact energies: a) *Reference*-18J, b) *Sensor*-6J, c) *Sensor*-27J (all images cover a length of approximately 200mm)

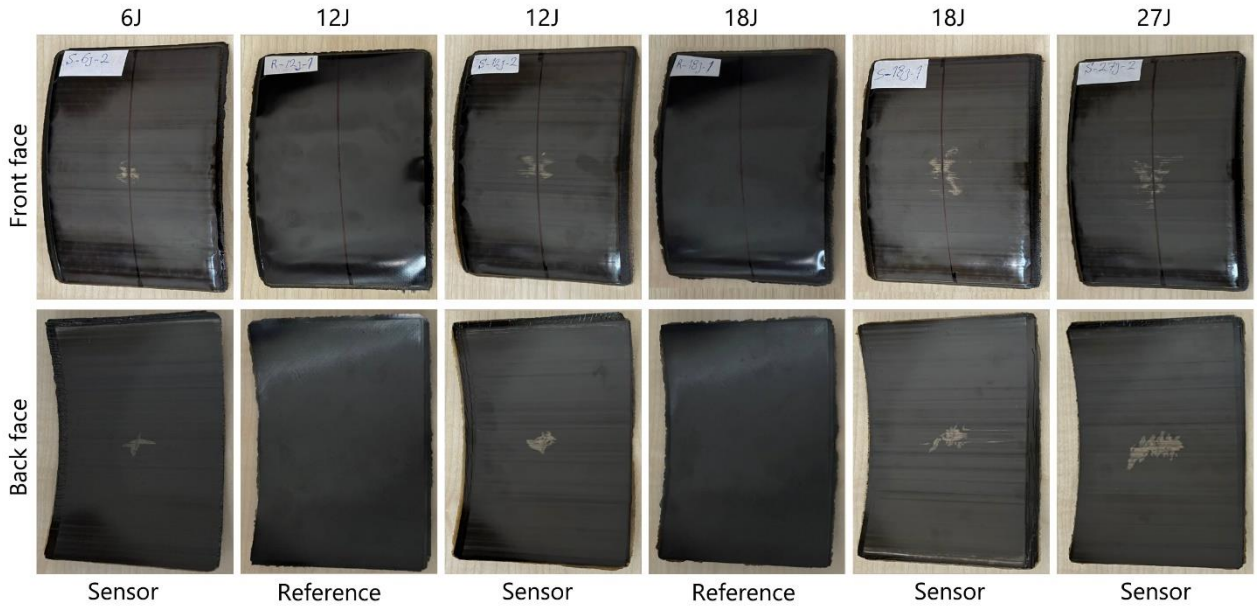

Fig. 6-14: Visual inspection results of impacted *Reference* and *Sensor* samples at various energies

6.4.2.3. Comparison of Impact Behaviour in Curved and Flat Composite Structures

A comparison between the impact response of flat and curved samples for both *Reference* and *Sensor* samples at two different impact energies (12J and 18J) is presented in this section. Fig. 6-15 represents the force-displacement graphs. A comparison of the energy absorption between the flat and curved samples at different energies and across both *Reference* and *Sensor* groups is depicted in Fig. 6-16. It is seen in all graphs of Fig. 6-15 that the initial structural stiffness of the curved samples (the stiffness before the first load drop) is higher than that of the flat samples. Moreover, the level of the load drop is more significant in curved samples than in flat samples in all graphs. This was observed when comparing the indentation test results of flat and curved samples, too. Another interesting point highlighted by the graphs here is that the maximum displacement of the flat and curved samples is always close to each other, while the maximum force of the flat samples is always higher than that of the curved samples, and this difference becomes more significant at a higher impact energy of 18J compared to 12J. Interestingly, however, the absorbed energy calculation results show higher absorbed energy in curved structures than in flat structures across all sample groups and energies (Fig. 6-16). This is because of the more rigid (stiff) nature of the curved samples, specifically before the first load drop, due to their curved shape. Similar results on the comparison of energy absorption in flat and curved composite panels were reported by reference [218].

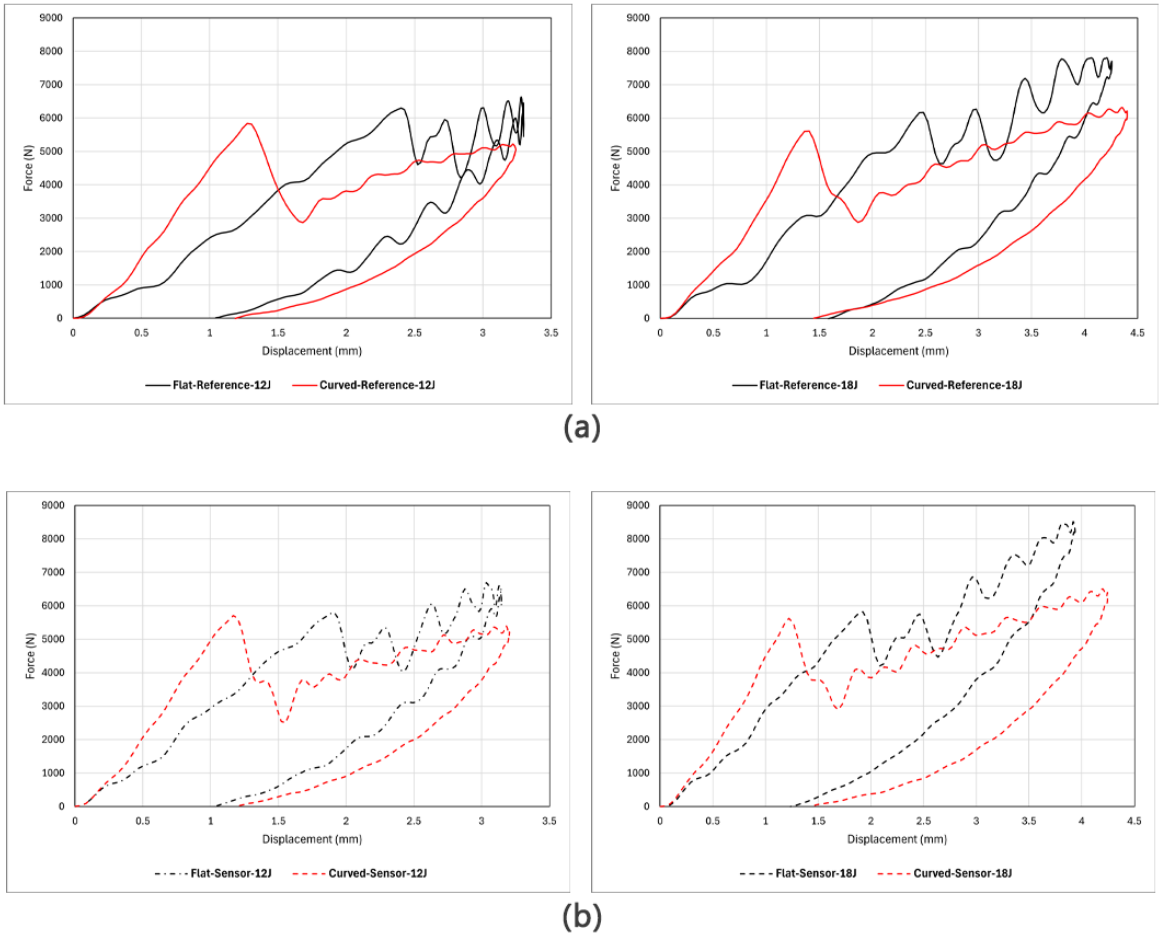

Fig. 6-15: Comparison of impact response in flat and curved samples: a) *Reference* samples, b) *Sensor* samples

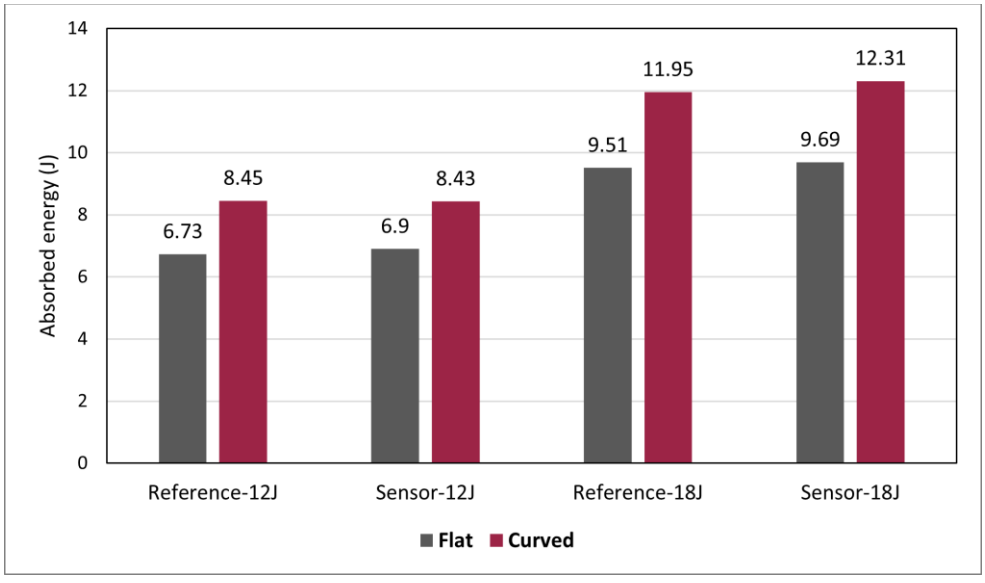

Fig. 6-16: Comparison of absorbed energies during low-velocity impact tests of flat and curved samples

6.5. Comparison of Low-Velocity Impact and Quasi-Static Indentation (in Curved Composite Structures)

A meaningful correlation between the results of the static indentation and low-velocity impact responses of flat composite laminates with quasi-isotropic lay-up was presented in Chapter Three. The findings indicated that the critical delamination load identified through the low-velocity impact test surpasses that determined by the static indentation test by approximately 15% to 30%. Here, two distinct graphs are presented, where one graph compares the two tests within the *Reference* samples (Fig. 6-17(a)), while the other graph does so within the *Sensor* samples (Fig. 6-17(b)). Both graphs show a similar initial structural stiffness for the indentation and impact tests. Similar to the results obtained for the flat samples, the critical delamination load (first load drop) attained through the low-velocity impact test surpasses that of the static indentation test. However, the disparity is minimal. In the case of *Reference* samples, the discrepancy between the critical delamination load of the static indentation test and an average of the low-velocity impact tests at different energies is merely 7%, while in *Sensor* samples, it stands at a mere 5%. The comparison results presented here suggest that estimating the impact critical delamination load based on the indentation tests appears to be a valid approach for curved samples.

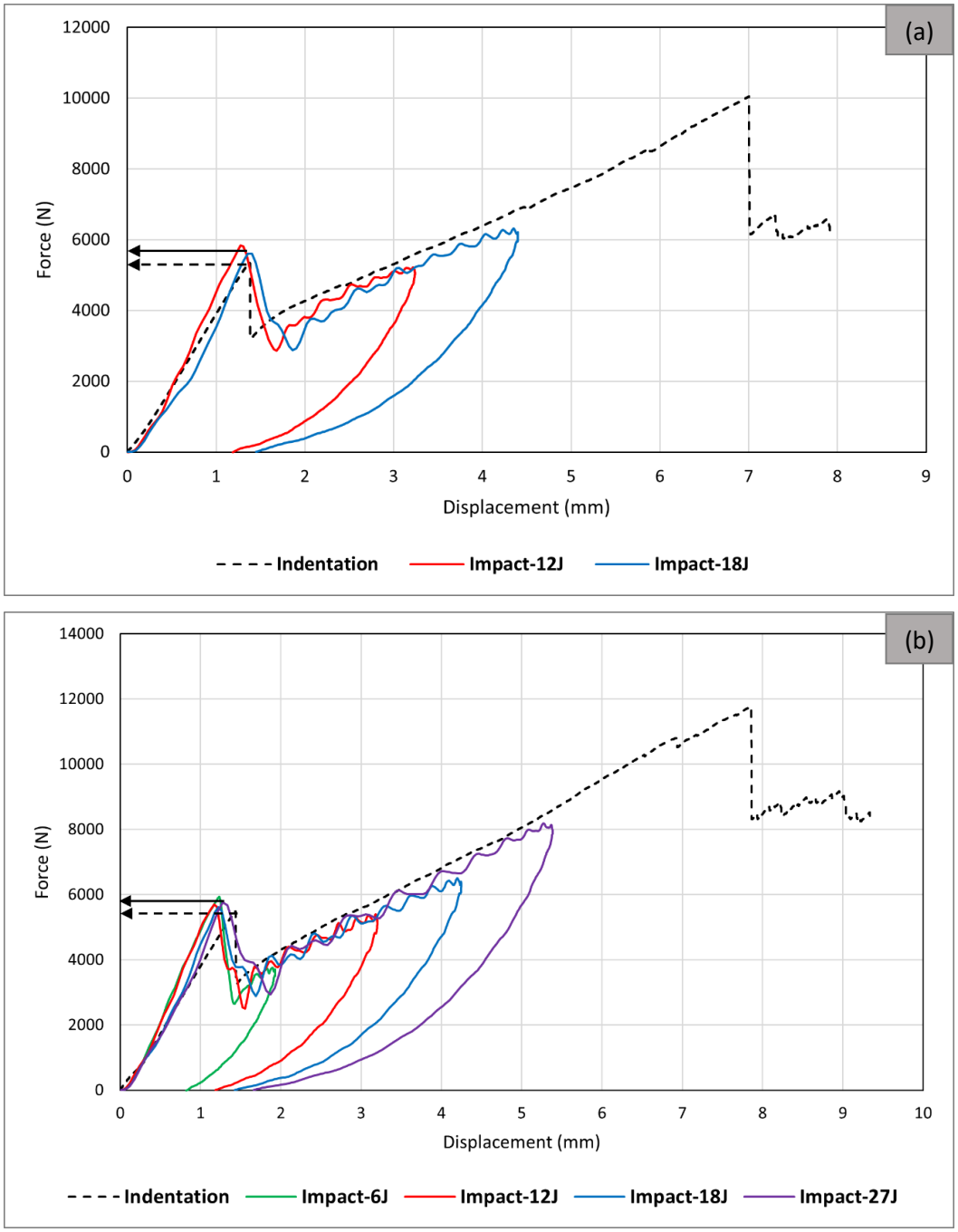

Fig. 6-17: Comparison of quasi-static indentation and low-velocity impact responses in curved composite structures: a) *Reference* samples, b) *Sensor* samples

6.6. Summary

This chapter showcased a practical application of hybrid glass/carbon sensors in detecting BVID within curved composite panels. These panels were manufactured to replicate the dimensions of hydrogen composite storage tanks, providing a real-life case study. A new testing setup suitable for curved panels was developed, facilitating static indentation and low-velocity impact tests at various energy levels on both *Reference* and *Sensor* samples.

Indentation test results indicated a slight increase in energy absorption and structural stiffness as a result of adding two sensors on the two sides of the panels. This change was minimal before the delamination onset and became greater as the test progressed towards the end. Analysis of images taken during the test and visual inspection images showed excellent performance of the sensor in visualising damage caused by indentation. Specifically, the energy threshold for visually detectable damage on the back face of a *Reference* sample decreased significantly from approximately 44J, occurring post-fibre failure, to nearly 2J in a *Sensor* sample, occurring just prior to delamination onset. This underscores the sensor's effectiveness in detecting and monitoring delamination in curved composite profiles.

Furthermore, the impact test outcomes demonstrated sensor activation on both the front and back faces across all tested impact energies. This highlights the sensor's potential as a practical tool for detecting BVID in curved composite laminates. Notably, a correlation between the extent of the activated area and the level of impact energy was observed, implying that the sensor could serve as a means to estimate damage severity as well. Microscopy images of the cross-section revealed a lesser damage extent in *Reference* samples than *Sensor* samples, highlighting the load-bearing capabilities of the hybrid sensors.

A comparison of results between curved and flat panels yielded interesting findings. Four notable differences emerged between the two panel types. In both indentation and impact tests, it was observed that the rate of the initial load drop, linked with delamination, was significantly higher in curved samples. Moreover, impact test results revealed greater energy absorption across various impact energies in both *Reference* and *Sensor* samples within curved panels compared to flat panels. Another interesting difference was related to the correlation between the impact energy and delamination threshold force in force-displacement graphs obtained from impact tests. In flat panels, the delamination threshold force tends to increase with rising impact energy. However, in curved panels, the trend is reversed, indicating that the delamination threshold force decreases as impact energy increases.

Finally, in terms of similarities between static indentation and low-velocity impact tests, a notable observation was made regarding the consistency, particularly in deriving the delamination force threshold, which was markedly higher for curved panels compared to flat panels. The difference between the delamination force thresholds obtained from static indentation and low-velocity impact tests for curved panels was less than 8%, whereas for flat panels, this difference ranged from 15% to 30%.

Chapter 7

Conclusions and Future Work

This thesis presented a substantial body of new work into the application of hybrid composite sensors that can enhance visual inspection of barely visible impact damage. This starts with a comprehensive literature review on different aspects of impact damage visual inspection, including damage metrics, various inspection levels, and their relationship with different types of impact-induced damage, alongside essential parameters for effective inspection. Moreover, recent progress in this field was discussed, including remote visual inspection, AI-based inspection methods, and bio-inspired mechanochromic coatings (sensors) to enhance visual inspection capabilities. This helped identify difficulties and concerns which were consistent with the chapters set out for this thesis. The novelty of the PhD lies in designing and characterising a hybrid composite sensor for visualising barely visible damage caused by out-of-plane loading and assessing its performance by conducting experimental, numerical, and deep learning analyses.

In Chapter Three, a series of quasi-static indentation and low-velocity impact tests were conducted on the composite specimens with and without the attached hybrid sensors, using different impact energy levels. A detailed assessment of damage evolution was carried out through NDE techniques, including ultrasonic C-scan and visual inspection. Comparison between these two types of loading was also presented. This generated a set of detailed experimental results providing a better understanding of the sensor performance. It also served as a reliable resource for developing and validating finite element models. A simple analytical solution, along with two FEA models, were developed to model the out-of-plane loading and response of laminated composites and to facilitate parametric study for better design the sensor. This modelling work served as a complement to the experimental studies. The results of these studies were then presented in Chapter Four. In Chapter Five, four deep learning models with varying levels of complexity were used to detect BVID from images of the impacted and non-impacted surfaces and assess the efficiency of the hybrid sensor in improving the AI-based detection of BVID. In Chapter Six, a new testing setup suitable for curved panels was developed, facilitating static indentation and low-velocity impact tests at various energy levels

on both *Reference* and *Sensor* samples. This chapter showcased a practical application of hybrid glass/carbon sensors in detecting BVID within curved composite panels, which were manufactured to replicate the dimensions of hydrogen composite storage tanks, providing a real-life case study.

The objectives of this research were fully addressed; important findings and new understanding derived from the experimental, numerical, and deep learning studies, as well as some directions for future work, are summarised in the next two sections.

7.1. Conclusions

Chapter 3

The analytical and FEA models serve as efficient and cost-effective tools for sensor design. A simple analytical solution enables the theoretical estimation of delamination onset, considering the effect of elastic and shear modulus, laminate dimensions and indenter diameter. When using FEA for numerical modelling of laminated composites subjected to out-of-plane loading, while both the shell and solid models yielded similar levels of accuracy, the shell model demanded significantly less computational time and effort. Thus, it emerges as the preferable choice for efficient parametric analysis of sensor design. The size of the region of interest, where the laminate is in contact with the indenter, minimally impacts both computational time and accuracy. The influence of boundary conditions outweighs that of ROI size, becoming more pronounced with increased force or energy levels. For low-energy impacts, before the onset of delamination, it remains valid to leave the top side of the laminate unconstrained (without modelling clamps) in numerical simulations.

Chapter 4

The sensors on the two outer surfaces slightly increase the structural stiffness and energy absorption, where the latter can be advantageous for specific impact-resistant applications. Regarding visualising the BVID, however, notable improvements can be achieved when using the sensor. For example, the sensor could decrease the threshold energy for visually detectable damage on the back face from nearly 27J in a *Reference* sample to less than 5J in a *Sensor* sample. On the front face, the threshold energy decreased from nearly 20J in a *Reference* sample to nearly 9J in a *Sensor* sample. The enhancements achieved by using the sensor can be modified by adjusting different sensor design parameters, such as: the fibre direction and ply thickness, the number of the carbon sensing layers, and the introduction of discontinuities in the carbon sensing layer. The latter can modify the shape and size of the visual damage

pattern of the sensor, and it was particularly effective on the back face. Increasing the thickness of the sensing layer and reducing the fibre orientation angle (from 90^{o} towards 0^{o}) results in a higher activation threshold energy for the sensor. The damage patterns on the top and back faces are different, with the back face providing a more recognisable pattern at considerably lower force/energy levels. For low-energy impacts, a correlation between the size of the internal damage and surface visible damage can be estimated. Another conclusion was that static indentation tests can be used to estimate the barely visible damage induced in impact tests on flat quasi-isotropic CFRP laminates.

Chapter 5

All four deep learning models, each with a varying level of complexity, showed proficiency in learning and identifying BVID. ResNet notably outperformed other models across most tasks, owing to its adaptable and resilient architecture, featuring residual connections. Additionally, while a Prototypical network can yield superior accuracy compared to a basic CNN, particularly with small datasets, it may necessitate greater computational time. The accuracy of AI-based BVID detection is higher on the back face compared to the front face. This arises from the more discernible damage patterns typically present on the back face of thin composite structures. Consequently, when the non-impacted side is accessible, using back face images as input to deep learning networks is preferable. The hybrid glass/carbon sensor enhances the performance of deep learning models significantly, particularly on the front face, by providing greater contrast between damaged and undamaged areas. Incorporating a sensor on the front face led to a notable improvement in damage detection accuracy, with the first and second models showing enhancements of 26.74% and 10.8%, respectively. However, the use of a highly intricate network, like a Prototypical network, may capture overly detailed features of damage patterns. In such cases, the addition of a hybrid sensor could introduce variance into the damage pattern, potentially decreasing model accuracy slightly. Nevertheless, including the glass/carbon sensing system was found to substantially reduce training time, thereby enhancing the computational efficiency of AI-based damage detection systems.

Chapter 6

Adding sensors to a curved CFRP panel minimally affected its initial out-of-plane loading response (before delamination initiation), but the sensors showed greater influence as testing progressed. The energy threshold for visually detectable damage on the back face significantly decreased from approximately 44J to nearly 2J, indicating the sensor's efficacy in detecting

delamination onset. A correlation between activated area and impact energy suggests the sensor's potential for estimating damage severity in curved panels. Regarding the comparison of curved and flat panels, curved samples exhibited a higher initial load drop rate and greater energy absorption across different impact energies. Additionally, while delamination threshold force tended to increase with the increase of impact energy in flat panels, it decreases in curved panels. A higher consistency was observed in deriving delamination force thresholds between static indentation and low-velocity impact tests of curved panels than flat panels. The difference between the delamination force thresholds obtained from static indentation and low-velocity impact tests for curved panels was less than 8%, whereas for flat panels, this difference ranged from 15% to 30%. An additional point is that the findings of this chapter have led to a comprehensive understanding of the similarities and differences between the out-of-plane behaviour of flat and curved composite panels. This provides added value to the existing literature on composite structures and may make it possible to replace the challenging testing of curved samples with the simpler testing of flat samples.

7.2. Future Work

This investigation covered various aspects of hybrid glass/carbon sensors for SHM of BVID. In this section, some key areas will be covered where further investigation is recommended by the author with regard to the specific chapters presented.

Chapters 3 and 4

The hybrid sensors evaluated in this study demonstrated significant potential for detecting and visualising delamination. However, the research primarily focused on sensors attached to the non-impacted, or back face, of the structure. Future investigations could explore damage mechanisms and sensor responses on the impacted or front face, which could broaden the sensors' applicability. This is particularly relevant in situations where inspection of the non-impacted side is not feasible.

Building on the foundation of sensor design and application established here, further studies could expand into other areas. For instance, the sensors might be applied to structures that undergo regular thermal cycling [227], such as hydrogen storage tanks or wind turbine blades. Additionally, the sensors may face extreme temperatures in certain applications, potentially compromising their functionality and integrity. Future research can, therefore, examine how real-world environmental conditions affect the sensors and their sensing performance.

Another practical issue to address is the effect of multiple impacts, a scenario commonly encountered in real-world applications and extensively discussed in the literature [228]. Investigating how the sensors perform under repeated impacts and exploring design improvements, such as integrating self-healing capabilities with microcapsules, could enhance their durability and functionality.

In line with the research objective of focusing on BVID, the analytical solution and FEA models in this study were developed to assess the linear elastic response prior to delamination onset. To extend the utility of the sensor across broader scenarios, future developments could include analytical equations and high-fidelity FEA models capable of capturing a range of damage modes, such as fibre tensile and compressive failures, matrix cracking, and their interactions. This would facilitate comparative studies of different damage modes, help understand the sequence of damage, and potentially allow for control over damage mechanisms through adjustments in materials and lay-up strategies. Such modifications could tune sensor activation to occur at a specified damage level.

Chapter 5

A promising direction for future research emerging from this chapter involves experimenting with different fibre types and architectural configurations within the sensor structure to induce unique damage patterns on composite surfaces. A preliminary investigation indicates that using HS40 carbon prepregs for the sensing layer, instead of YS-90 carbon, or employing woven glass prepregs for the outer layer, rather than unidirectional glass, enhances the contrast in damage patterns between *Reference* and *Sensor* samples. It was also observed that introducing discontinuities can notably improve the size and shape of visual damage patterns. This, in turn, could enhance the performance of deep learning models by establishing a clearer correlation between network output and the damage patterns created by the sensor.

Further refinement in pre-processing input data could also enhance the deep learning model's performance. This could involve narrowing the range within which BVID is identified, tightening it around the threshold between visible impact damage and BVID. Additional efforts could also be made to minimise the influence of image brightness variability within the dataset.

Additionally, the practical application of deep learning-based damage detection techniques in real-world scenarios warrants exploration, particularly in terms of scalability and reliability. For instance, the SHM method proposed in this study could be advanced through automation, using remotely operated vehicles equipped to capture surface images of large and possibly

inaccessible composite structures. This would significantly extend the method's applicability and efficiency in operational environments.

Chapter 6

In many practical applications, such as aerospace, wind turbine, and automotive industries, CFRP structures are designed with complex curves to meet both performance and style requirements. Therefore, developing and testing the hybrid sensors for doubly curved structures can be a topic of future research. Moreover, numerical models can enable thorough analysis of the sensor design and performance for curved composite panels. Also, there needs to be further work on cost modelling for this technology on curved composite panels. For example, how much would this save economically in terms of early identification of damage for curved panels.

References

[1] M.R. Wisnom, S. Pimenta, M.S.P. Shaffer, P. Robinson, K.D. Potter, I. Hamerton, G. Czél, M. Jalalvand, M. Fotouhi, D.B. Anthony, H. Yu, M.L. Longana, X. Wu, A. Bismarck, High performance ductile and pseudo-ductile polymer matrix composites: A review, Compos. Part A Appl. Sci. Manuf. 181 (2024) 108029. https://doi.org/10.1016/J.COMPOSITESA.2024.108029.

[2] A.P. Mouritz, Introduction to Aerospace Materials, Woodhead Publishing, 2012. https://doi.org/10.2514/4.869198.

[3] J. Bachmann, C. Hidalgo, S. Bricout, Environmental analysis of innovative sustainable composites with potential use in aviation sector—A life cycle assessment review, Sci. China Technol. Sci. 60 (2017) 1301–1317. https://doi.org/10.1007/S11431-016-9094-Y/METRICS.

[4] E. Abisset, F. Daghia, X.C. Sun, M.R. Wisnom, S.R. Hallett, Interaction of inter- and intralaminar damage in scaled quasi-static indentation tests: Part 1 - Experiments, Compos. Struct. 136 (2016) 712–726. https://doi.org/10.1016/j.compstruct.2015.09.061.

[5] A. Tabatabaeian, S. Liu, P. Harrison, E. Schlangen, M. Fotouhi, A review on self-reporting mechanochromic composites: An emerging technology for structural health monitoring, Compos. Part A Appl. Sci. Manuf. 163 (2022) 107236. https://doi.org/10.1016/J.COMPOSITESA.2022.107236.

[6] M. Saeedifar, D. Zarouchas, Damage characterization of laminated composites using acoustic emission: A review, Compos. Part B Eng. 195 (2020) 108039. https://doi.org/10.1016/J.COMPOSITESB.2020.108039.

[7] S. Fotouhi, M. Jalalvand, M.R. Wisnom, M. Fotouhi, Smart hybrid composite sensor technology to enhance the detection of low energy impact damage in composite structures, Compos. Part A Appl. Sci. Manuf. 172 (2023) 107595. https://doi.org/10.1016/J.COMPOSITESA.2023.107595.

[8] Joint Airworthiness Requirements 25 (JAR 25), part 1 requirements, part 2 acceptable means of compliance and interpretations , For composite structures: JAR25, 25.603 and ACJ 25.603., (n.d.).

[9] C. Bouvet, S. Rivallant, Damage tolerance of composite structures under low-velocity impact, in: V. V. Silberschmidt (Ed.), Dyn. Deform. Damage Fract. Compos. Mater. Struct., 2016: pp. 7–33. https://doi.org/10.1016/b978-0-08-100080-9.00002-6.

[10] Y.D.V. Yasuda, F.A.M. Cappabianco, L.E.G. Martins, J.A.B. Gripp, Aircraft visual inspection: A systematic literature review, Comput. Ind. 141 (2022) 103695. https://doi.org/10.1016/J.COMPIND.2022.103695.

[11] S. Zhong, W. Nsengiyumva, Visual Testing for Fiber-Reinforced Composite Materials, in: Nondestruct. Test. Eval. Fiber-Reinforced Compos. Struct., Springer, Singapore, 2022: pp. 97–132. https://doi.org/10.1007/978-981-19-0848-4_3.

[12] A. Tabatabaeian, S. Fotouhi, M. Fotouhi, Visual inspection of impact damage in composite materials, in: Non-Destructive Test. Impact Damage Fiber-Reinforced Polym. Compos., Elsevier, 2024: pp. 43–67. https://doi.org/10.1016/B978-0-443-

14120-1.00002-9.

[13] https://www.industrial-ndt.com/.

[14] T. Duffy, Aviation Pros, June 2004. (2004). https://www.aviationpros.com/home/article/10386292/common-use-ramp-equipment-supplier-relates-how-technology-is-going-to-improve-ramp-safety-operations.

[15] https://aerocorner.com/.

[16] X.C. Sun, S.R. Hallett, Barely visible impact damage in scaled composite laminates: Experiments and numerical simulations, Int. J. Impact Eng. 109 (2017) 178–195. https://doi.org/10.1016/j.ijimpeng.2017.06.008.

[17] X.C. Sun, S.R. Hallett, Failure mechanisms and damage evolution of laminated composites under compression after impact (CAI): Experimental and numerical study, Compos. Part A Appl. Sci. Manuf. 104 (2018) 41–59. https://doi.org/10.1016/j.compositesa.2017.10.026.

[18] E.A. Abdallah, C. Bouvet, S. Rivallant, B. Broll, J.J. Barrau, Experimental analysis of damage creation and permanent indentation on highly oriented plates, Compos. Sci. Technol. 69 (2009). https://doi.org/10.1016/j.compscitech.2009.02.029.

[19] A.R. Kristnama, X. Xu, M.R. Wisnom, S.R. Hallett, Numerical analysis of high velocity, oblique impacts and residual tensile strength of carbon/epoxy laminates, Compos. Struct. 259 (2021) 113476. https://doi.org/10.1016/J.COMPSTRUCT.2020.113476.

[20] N. Dubary, C. Bouvet, S. Rivallant, L. Ratsifandrihana, Damage tolerance of an impacted composite laminate, Compos. Struct. 206 (2018). https://doi.org/10.1016/j.compstruct.2018.08.045.

[21] C. Bouvet, S. Rivallant, J.J. Barrau, Low velocity impact modeling in composite laminates capturing permanent indentation, Compos. Sci. Technol. 72 (2012) 1977–1988. https://doi.org/10.1016/j.compscitech.2012.08.019.

[22] C. Fualdes, Composites @ Airbus - Damage tolerance methodology Presentation at the Composite Damage Tolerance and Maintenance Workshop, Chicago, 2006.

[23] A.J. Fawcett, G.D. Oakes, Boeing Composite Airframe Damage Tolerance and Service Experience. Presentation at the Composite Damage Tolerance and Maintenance Workshop, Chicago, (2006).

[24] J. Rouchon, Certification of large airplane composite structures, recent progress and new trends in compliance philosophy, in: 17th ICAS Congr., Stockholm, 1990.

[25] M. Thomas, Study of the evolution of the dent depth due to impact on carbon/epoxy laminates, consequences on impact damage visibility and on in service inspection requirements for civil aircraft composite structures, in: Proc. MIL-HDBK, 1994.

[26] X. Chen, H. Ren, C. Bil, Inspection intervals optimization for aircraft composite structures considering dent damage, J. Aircr. 51 (2014) 303–309. https://doi.org/10.2514/1.C032377.

[27] M. Alhammad, N.P. Avdelidis, C. Ibarra-Castanedo, M.E. Torbali, M. Genest, H. Zhang, A. Zolotas, X.P.V. Maldgue, Automated Impact Damage Detection Technique

for Composites Based on Thermographic Image Processing and Machine Learning Classification, Sensors. 22 (2022). https://doi.org/10.3390/s22239031.

[28] S. Hasebe, R. Higuchi, T. Yokozeki, S. ichi Takeda, Internal low-velocity impact damage prediction in CFRP laminates using surface profiles and machine learning, Compos. Part B Eng. 237 (2022) 109844. https://doi.org/10.1016/j.compositesb.2022.109844.

[29] Visual inspection for aircraft. FAA AC 43-204, 1997., 20 (n.d.). https://doi.org/10.1177/1475921720976986.

[30] Visual Inspection of Composite Structures, in: Eur. Union Aviat. Saf. Agency, 2009.

[31] E.D. Megaw, Factors affecting visual inspection accuracy, Appl. Ergon. 10 (1979) 27–32. https://doi.org/10.1016/0003-6870(79)90006-1.

[32] D. Erhart, L.T. Ostrom, C.A. Wilhelmsen, Visual detectibility of dents on a composite aircraft inspection specimen: An initial study, Int. J. Appl. Aviat. Stud. 4 (2004) 111–122.

[33] I. Dafydd, Z. Sharif Khodaei, Analysis of barely visible impact damage severity with ultrasonic guided Lamb waves, Struct. Heal. Monit. 19 (2020) 1104–1122. https://doi.org/10.1177/1475921719878850.

[34] R.H. Bossi, G.E. Georgeson, Nondestructive testing of aerospace composites, Polym. Compos. Aerosp. Ind. (2020) 461–489. https://doi.org/10.1016/B978-0-08-102679-3.00016-2.

[35] M. Siegel, P. Gunatilake, Enhanced remote visual inspection of aircraft skin, 3029 (1997) 10–11.

[36] The International Air Transport Association (IATA) Safety Report, AERO_Q207_article3.pdf (boeing.com), (n.d.).

[37] https://www.mainblades.com/Your guide to general visual inspection of aircraft.

[38] W. Ostachowicz, M. Malcolm, J.-U. SchrRoder-Hinrichs, M. Luczak, MARE-WINT: new materials and reliability in offshore wind turbine technology, Springer, 2016. https://doi.org/10.1007/978-3-319-39095-6_1.

[39] D. Forsyth, J. Komorowski, R. Gould, A. Marincak, Automation of Enhanced Visual NDT Techniques, NDT.Net. 4 (1999).

[40] R. Patel, D. Patel, D. Meshram, A Review on Non-Destructive Testing (NDT) Techniques : Advances , Researches and Applicability, Int. J. Curr. Sci. Res. Rev. 05 (2022) 1342–1355. https://doi.org/10.47191/ijcsrr/V5-i4-59.

[41] W. Guo, L. Soibelman, J.H. Garrett, Imagery Enhancement and Interpretation for Remote Visual Inspection of Aging Civil Infrastructure, Tsinghua Sci. Technol. 13 (2008) 375–380. https://doi.org/https://doi.org/10.1016/S1007-0214(08)70177-9.

[42] S. Wang, A. Zargar, F.-G. Yuan, Augmented reality for enhanced visual inspection through knowledge-based deep learning, Struct. Heal. Monit. 20 (2021) 426–442. https://doi.org/10.1177/1475921720976986.

[43] M. Rice, L. Li, G. Ying, M. Wan, E.T. Lim, G. Feng, V.S. Babu, Automating the visual inspection of aircraft, in: Proc. Singapore Aerosp. Technol. Eng. Conf., 2018.

[44] https://www.mainblades.com/.

[45] U. Papa, S. Ponte, Preliminary Design of an Unmanned Aircraft System for Aircraft General Visual Inspection, Electronics. (2018). https://doi.org/10.3390/electronics7120435.

[46] J. Yang, S. Li, Z. Wang, H. Dong, J. Wang, S. Tang, Using Deep Learning to Detect Defects in Manufacturing: A Comprehensive Survey and Current Challenges, Mater. (Basel, Switzerland). 13 (2020). https://doi.org/10.3390/ma13245755.

[47] J. Miranda, S. Larnier, A. Herbulot, M. Devy, UAV-based Inspection of Airplane Exterior Screws with Computer Vision UAV-based Inspection of Airplane Exterior Screws with Computer Vision, in: 14h Int. Jt. Conf. Comput. Vision, Imaging Comput. Graph. Theory Appl., 2019. https://doi.org/10.5220/0007571304210427.

[48] A.G. Anisimov, R. Beukema, J. Hwang, R. Nijssen, R.M. Groves, AIRTuB: towards automated inspection of leading-edge erosion of wind turbine blades by shape analysis, in: SPIE 11785, Multimodal Sens. Artif. Intell. Technol. Appl. II, 2021. https://doi.org/10.1117/12.2592291.

[49] X. Qing, Y. Liao, Y. Wang, B. Chen, F. Zhang, Y. Wang, Machine Learning Based Quantitative Damage Monitoring of Composite Structure, Int. J. Smart Nano Mater. . 13 (2022) 167–202. https://doi.org/10.1080/19475411.2022.2054878.

[50] I. Tabian, H. Fu, Z.S. Khodaei, Impact Detection on Composite Plates Based on Convolution Neural Network, Key Eng. Mater. 827 (2020) 476–481. https://doi.org/10.4028/WWW.SCIENTIFIC.NET/KEM.827.476.

[51] N. Saeed, N. King, Z. Said, M.A. Omar, Automatic defects detection in CFRP thermograms, using convolutional neural networks and transfer learning, Infrared Phys. Technol. 102 (2019) 103048. https://doi.org/10.1016/J.INFRARED.2019.103048.

[52] M. Azimi, A.D. Eslamlou, G. Pekcan, Data-Driven Structural Health Monitoring and Damage Detection through Deep Learning: State-of-the-Art Review, Sensors 2020, Vol. 20, Page 2778. 20 (2020) 2778. https://doi.org/10.3390/S20102778.

[53] F.-G. Yuan, S.A. Zargar, Q. Chen, S. Wang, Machine learning for structural health monitoring: challenges and opportunities, in: SPIE Smart Struct. + Nondestruct. Eval., SPIE, 2020: p. 2. https://doi.org/10.1117/12.2561610.

[54] C. Nelon, O. Myers, A. Hall, The intersection of damage evaluation of fiber-reinforced composite materials with machine learning: A review, J. Compos. Mater. 56 (2022) 1417–1452. https://doi.org/10.1177/00219983211037048/ASSET/IMAGES/LARGE/10.1177_00219983211037048-FIG19.JPEG.

[55] J. Gu, Z. Wang, J. Kuen, L. Ma, A. Shahroudy, B. Shuai, T. Liu, X. Wang, G. Wang, J. Cai, T. Chen, Recent advances in convolutional neural networks, Pattern Recognit. 77 (2018) 354–377. https://doi.org/10.1016/J.PATCOG.2017.10.013.

[56] H.T. Bang, S. Park, H. Jeon, Defect identification in composite materials via thermography and deep learning techniques, Compos. Struct. 246 (2020) 112405. https://doi.org/10.1016/J.COMPSTRUCT.2020.112405.

[57] S. Sony, K. Dunphy, A. Sadhu, M. Capretz, A systematic review of convolutional

neural network-based structural condition assessment techniques, Eng. Struct. 226 (2021) 111347. https://doi.org/10.1016/J.ENGSTRUCT.2020.111347.

[58] S. Fotouhi, F. Pashmforoush, M. Bodaghi, M. Fotouhi, Autonomous damage recognition in visual inspection of laminated composite structures using deep learning, Compos. Struct. 268 (2021) 113960. https://doi.org/10.1016/J.COMPSTRUCT.2021.113960.

[59] S. Hasebe, R. Higuchi, T. Yokozeki, S. Takeda, Multi-task learning application for predicting impact damage-related information using surface profiles of CFRP laminates, Compos. Sci. Technol. 231 (2022) 109820. https://doi.org/10.1016/j.compscitech.2022.109820.

[60] Q. Guo, X. Zhang, A review of mechanochromic polymers and composites: From material design strategy to advanced electronics application, Compos. Part B Eng. 227 (2021) 109434. https://doi.org/10.1016/J.COMPOSITESB.2021.109434.

[61] C. Calvino, C. Calvino, Polymer-Based Mechanochromic Composite Material Using Encapsulated Systems, Macromol. Rapid Commun. 42 (2021) 2000549. https://doi.org/10.1002/MARC.202000549.

[62] C. Calvino, L. Neumann, C. Weder, S. Schrettl, Approaches to polymeric mechanochromic materials, J. Polym. Sci. Part A Polym. Chem. 55 (2017) 640–652. https://doi.org/10.1002/POLA.28445.

[63] A.R. Studart, A.R. Studart, Towards High-Performance Bioinspired Composites, Adv. Mater. 24 (2012) 5024–5044. https://doi.org/10.1002/ADMA.201201471.

[64] J. Plocher, L. Mencattelli, F. Narducci, S. Pinho, Learning from nature: Bio-inspiration for damage-tolerant high-performance fibre-reinforced composites, Compos. Sci. Technol. 208 (2021). https://doi.org/10.1016/j.compscitech.2021.108669.

[65] N.K. Simha, F.D. Fischer, O. Kolednik, J. Predan, G.X. Shan, Crack tip shielding or anti-shielding due to smooth and discontinuous material inhomogeneities, Int. J. Fract. 135 (2005) 73–93. https://doi.org/10.1007/S10704-005-3944-5/METRICS.

[66] N.K. Simha, F.D. Fischer, O. Kolednik, C.R. Chen, Inhomogeneity effects on the crack driving force in elastic and elastic–plastic materials, J. Mech. Phys. Solids. 51 (2003) 209–240. https://doi.org/10.1016/S0022-5096(02)00025-X.

[67] J.C. Weaver, G.W. Milliron, P. Allen, A. Miserez, A. Rawal, J. Garay, P.J. Thurner, J. Seto, B. Mayzel, L.J. Friesen, B.F. Chmelka, P. Fratzl, J. Aizenberg, Y. Dauphin, D. Kisailus, D.E. Morse, Unifying Design Strategies in Demosponge and Hexactinellid Skeletal Systems, J. Adhes. 86 (2010) 72–95. https://doi.org/10.1080/00218460903417917.

[68] A. Miserez, J.C. Weaver, P.J. Thurner, J. Aizenberg, Y. Dauphin, P. Fratzl, D.E. Morse, F.W. Zok, Effects of Laminate Architecture on Fracture Resistance of Sponge Biosilica: Lessons from Nature, Adv. Funct. Mater. 18 (2008) 1241–1248. https://doi.org/10.1002/ADFM.200701135.

[69] F.D. Fischer, O. Kolednik, J. Predan, H. Razi, P. Fratzl, Crack driving force in twisted plywood structures, Acta Biomater. 55 (2017) 349–359. https://doi.org/10.1016/J.ACTBIO.2017.04.007.

[70] B. Peter Fratzl, H.S. Gupta, F. Dieter Fischer, O. Kolednik, P. Fratzl, H.S. Gupta, F.D.

Fischer, O. Koldnik Erich Schmid, O. Kolednik, Hindered Crack Propagation in Materials with Periodically Varying Young's Modulus—Lessons from Biological Materials, Adv. Mater. 19 (2007) 2657–2661. https://doi.org/10.1002/ADMA.200602394.

[71] G. Czél, M.R. Wisnom, Demonstration of pseudo-ductility in high performance glass/epoxy composites by hybridisation with thin-ply carbon prepreg, Compos. Part A Appl. Sci. Manuf. 52 (2013) 23–30. https://doi.org/10.1016/j.compositesa.2013.04.006.

[72] G. Czél, S. Pimenta, M.R. Wisnom, P. Robinson, Demonstration of pseudo-ductility in unidirectional discontinuous carbon fibre/epoxy prepreg composites, Compos. Sci. Technol. 106 (2015) 110–119. https://doi.org/10.1016/J.COMPSCITECH.2014.10.022.

[73] J. Henry, S. Pimenta, Modelling hybrid effects on the stiffness of aligned discontinuous composites with hybrid fibre-types, Compos. Sci. Technol. 152 (2017) 275–289. https://doi.org/10.1016/J.COMPSCITECH.2017.08.017.

[74] R. Malkin, M. Yasaee, R.S. Trask, I.P. Bond, Bio-inspired laminate design exhibiting pseudo-ductile (graceful) failure during flexural loading, Compos. Part A Appl. Sci. Manuf. 54 (2013) 107–116. https://doi.org/10.1016/J.COMPOSITESA.2013.07.008.

[75] J. Tang, Y. Swolfs, M. Yang, K. Michielsen, J. Ivens, S. V. Lomov, L. Gorbatikh, Discontinuities as a way to influence the failure mechanisms and tensile performance of hybrid carbon fiber/self-reinforced polypropylene composites, Compos. Part A Appl. Sci. Manuf. 107 (2018) 354–365. https://doi.org/10.1016/J.COMPOSITESA.2018.01.020.

[76] J. Tang, A. Aslani, Y. Swolfs, G. Bullegas, S.T. Pinho, S. V. Lomov, L. Gorbatikh, Staggered ply discontinuities for tailoring the tensile behavior of hybrid carbon fiber/self-reinforced polypropylene composites: A study of pattern parameters, Compos. Part A Appl. Sci. Manuf. 125 (2019) 105551. https://doi.org/10.1016/J.COMPOSITESA.2019.105551.

[77] J. Tang, Y. Swolfs, A. Aslani, L. Mencattelli, G. Bullegas, S.T. Pinho, S. V. Lomov, L. Gorbatikh, Engineering tensile behavior of hybrid carbon fiber/self-reinforced polypropylene composites by bio-inspired fiber discontinuities, Compos. Part B Eng. 178 (2019) 107502. https://doi.org/10.1016/j.compositesb.2019.107502.

[78] L. Mencattelli, J. Tang, Y. Swolfs, L. Gorbatikh, S.T. Pinho, Bio-inspired design for enhanced damage tolerance of self-reinforced polypropylene/carbon fibre polypropylene hybrid composites, Compos. Part A Appl. Sci. Manuf. 121 (2019) 341–352. https://doi.org/10.1016/j.compositesa.2019.03.028.

[79] B.D. Wilts, H.M. Whitney, B.J. Glover, U. Steiner, S. Vignolini, Natural Helicoidal Structures: Morphology, Self-assembly and Optical Properties, Mater. Today Proc. 1 (2014) 177–185. https://doi.org/10.1016/J.MATPR.2014.09.021.

[80] B. Chen, X. Peng, C. Cai, H. Niu, X. Wu, Helicoidal microstructure of Scarabaei cuticle and biomimetic research, Mater. Sci. Eng. A. 423 (2006) 237–242. https://doi.org/10.1016/J.MSEA.2005.11.069.

[81] L. Cheng, A. Thomas, J.L. Glancey, A.M. Karlsson, Mechanical behavior of bio-inspired laminated composites, Compos. Part A Appl. Sci. Manuf. 42 (2011) 211–220.

https://doi.org/10.1016/J.COMPOSITESA.2010.11.009.

[82] L.K. Grunenfelder, N. Suksangpanya, C. Salinas, G. Milliron, N. Yaraghi, S. Herrera, K. Evans-Lutterodt, S.R. Nutt, P. Zavattieri, D. Kisailus, Bio-inspired impact-resistant composites, Acta Biomater. 10 (2014) 3997–4008. https://doi.org/10.1016/j.actbio.2014.03.022.

[83] J.S. Shang, N.H.H. Ngern, V.B.C. Tan, Crustacean-inspired helicoidal laminates, Compos. Sci. Technol. 128 (2016) 222–232. https://doi.org/10.1016/J.COMPSCITECH.2016.04.007.

[84] J.L. Liu, H.P. Lee, V.B.C. Tan, Failure mechanisms in bioinspired helicoidal laminates, Compos. Sci. Technol. 157 (2018) 99–106. https://doi.org/10.1016/J.COMPSCITECH.2018.01.033.

[85] C. Calvino, E. Henriet, L.F. Muff, S. Schrettl, C. Weder, C. Calvino, E. Henriet, L.F. Muff, S. Schrettl, C. Weder, Mechanochromic Polymers Based on Microencapsulated Solvatochromic Dyes, Macromol. Rapid Commun. 41 (2020) 1900654. https://doi.org/10.1002/MARC.201900654.

[86] C.J. Norris, G.J. Meadway, M.J. O'Sullivan, I.P. Bond, R.S. Trask, Self-Healing Fibre Reinforced Composites via a Bioinspired Vasculature, Adv. Funct. Mater. 21 (2011) 3624–3633. https://doi.org/10.1002/ADFM.201101100.

[87] C.J. Norris, I.P. Bond, R.S. Trask, The role of embedded bioinspired vasculature on damage formation in self-healing carbon fibre reinforced composites, Compos. Part A Appl. Sci. Manuf. 42 (2011) 639–648. https://doi.org/10.1016/J.COMPOSITESA.2011.02.003.

[88] J.W.C. Pang, I.P. Bond, A hollow fibre reinforced polymer composite encompassing self-healing and enhanced damage visibility, Compos. Sci. Technol. 65 (2005) 1791–1799. https://doi.org/10.1016/J.COMPSCITECH.2005.03.008.

[89] G.J. Williams, I.P. Bond, R.S. Trask, Compression after impact assessment of self-healing CFRP, Compos. Part A Appl. Sci. Manuf. 40 (2009) 1399–1406. https://doi.org/10.1016/J.COMPOSITESA.2008.05.021.

[90] J.W.C. Pang, I.P. Bond, 'Bleeding composites'—damage detection and self-repair using a biomimetic approach, Compos. Part A Appl. Sci. Manuf. 36 (2005) 183–188. https://doi.org/10.1016/J.COMPOSITESA.2004.06.016.

[91] S. Kling, T. Czigány, Damage detection and self-repair in hollow glass fiber fabric-reinforced epoxy composites via fiber filling, Compos. Sci. Technol. 99 (2014) 82–88. https://doi.org/10.1016/J.COMPSCITECH.2014.05.020.

[92] C.J. Hansen, W. Wu, K.S. Toohey, N.R. Sottos, S.R. White, J.A. Lewis, Self-Healing Materials with Interpenetrating Microvascular Networks, Adv. Mater. 21 (2009) 4143–4147. https://doi.org/10.1002/ADMA.200900588.

[93] K.S. Toohey, N.R. Sottos, J.A. Lewis, J.S. Moore, S.R. White, Self-healing materials with microvascular networks, Nat. Mater. 2007 68. 6 (2007) 581–585. https://doi.org/10.1038/nmat1934.

[94] S. Lörcher, T. Winkler, K. Makyła, C. Ouellet-Plamondon, I. Burgert, N. Bruns, Mechanical unfolding of a fluorescent protein enables self-reporting of damage in carbon-fibre-reinforced composites, J. Mater. Chem. A. 2 (2014) 6231–6237.

https://doi.org/10.1039/C3TA14803C.

[95] Sindu Shree, Mathias Dowds, Alina Kuntze, Y. Kumar Mishra, Anne Staubitz, Rainer Adelung, Self-reporting mechanochromic coating: a glassfiber reinforced polymer composite that predicts impact induced damage, Mater. Horizons. 7 (2020) 598–604. https://doi.org/10.1039/C9MH01400D.

[96] T. Magrini, D. Kiebala, D. Grimm, A. Nelson, S. Schrettl, F. Bouville, C. Weder, A.R. Studart, Tough Bioinspired Composites That Self-Report Damage, ACS Appl. Mater. Interfaces. 13 (2021) 27481–27490. https://doi.org/10.1021/acsami.1c05964.

[97] C.M. Geiselhart, H. Mutlu, C. Barner-Kowollik, Prevent or Cure—The Unprecedented Need for Self-Reporting Materials, Angew. Chemie Int. Ed. 60 (2021) 17290–17313. https://doi.org/10.1002/ANIE.202012592.

[98] M.J. Robb, W. Li, R.C.R. Gergely, C.C. Matthews, S.R. White, N.R. Sottos, J.S. Moore, A robust damage-reporting strategy for polymeric materials enabled by aggregation-induced emission, ACS Cent. Sci. 2 (2016) 598–603. https://doi.org/10.1021/acscentsci.6b00198.

[99] C. Calvino, A. Guha, C. Weder, S. Schrettl, Self-Calibrating Mechanochromic Fluorescent Polymers Based on Encapsulated Excimer-Forming Dyes, Adv. Mater. 30 (2018) 1–10. https://doi.org/10.1002/adma.201704603.

[100] L. Shang, W. Zhang, K. Xu, Y. Zhao, Bio-inspired intelligent structural color materials, Mater. Horizons. 6 (2019) 945–958. https://doi.org/10.1039/C9MH00101H.

[101] G. von Freymann, V. Kitaev, B. V. Lotsch, G.A. Ozin, Bottom-up assembly of photonic crystals, Chem. Soc. Rev. 42 (2013) 2528–2554. https://doi.org/10.1039/C2CS35309A.

[102] B.M. Boyle, T.A. French, R.M. Pearson, B.G. McCarthy, G.M. Miyake, Structural Color for Additive Manufacturing: 3D-Printed Photonic Crystals from Block Copolymers, ACS Nano. 11 (2017) 3052–3058. https://doi.org/10.1021/acsnano.7b00032.

[103] H. Wang, K.Q. Zhang, Photonic Crystal Structures with Tunable Structure Color as Colorimetric Sensors, Sensors 2013, Vol. 13, Pages 4192-4213. 13 (2013) 4192–4213. https://doi.org/10.3390/S130404192.

[104] P. V. Braun, Colour without colourants, Nat. 2011 4727344. 472 (2011) 423–424. https://doi.org/10.1038/472423a.

[105] I. Jurewicz, A.A.K. King, R. Shanker, M.J. Large, R.J. Smith, R. Maspero, S.P. Ogilvie, J. Scheerder, J. Han, C. Backes, J.M. Razal, M. Florescu, J.L. Keddie, J.N. Coleman, A.B. Dalton, Mechanochromic and Thermochromic Sensors Based on Graphene Infused Polymer Opals, Adv. Funct. Mater. 30 (2020). https://doi.org/10.1002/adfm.202002473.

[106] R. Zhang, Q. Wang, X. Zheng, Flexible mechanochromic photonic crystals: routes to visual sensors and their mechanical properties, J. Mater. Chem. C. 6 (2018) 3182–3199. https://doi.org/10.1039/C8TC00202A.

[107] E.P. Chan, J.J. Walish, A.M. Urbas, E.L. Thomas, E.P. Chan, J.J. Walish, A.M. Urbas, E.L. Thomas, Mechanochromic Photonic Gels, Adv. Mater. 25 (2013) 3934–3947. https://doi.org/10.1002/ADMA.201300692.

[108] E.P. Chan, J.J. Walish, E.L. Thomas, C.M. Stafford, Block Copolymer Photonic Gel for Mechanochromic Sensing, Adv. Mater. 23 (2011) 4702–4706. https://doi.org/10.1002/ADMA.201102662.

[109] T.H. Park, S. Yu, S.H. Cho, H.S. Kang, Y. Kim, M.J. Kim, H. Eoh, C. Park, B. Jeong, S.W. Lee, D.Y. Ryu, J. Huh, C. Park, Block copolymer structural color strain sensor, NPG Asia Mater. 2018 104. 10 (2018) 328–339. https://doi.org/10.1038/s41427-018-0036-3.

[110] M. Jalalvand, G. Czél, M.R. Wisnom, Numerical modelling of the damage modes in UD thin carbon/glass hybrid laminates, Compos. Sci. Technol. 94 (2014) 39–47. https://doi.org/10.1016/j.compscitech.2014.01.013.

[111] M. Jalalvand, G. Czél, M.R. Wisnom, Damage analysis of pseudo-ductile thin-ply UD hybrid composites – A new analytical method, Compos. Part A Appl. Sci. Manuf. 69 (2015) 83–93. https://doi.org/10.1016/J.COMPOSITESA.2014.11.006.

[112] T. Yokozeki, Y. Aoki, T. Ogasawara, Experimental characterization of strength and damage resistance properties of thin-ply carbon fiber/toughened epoxy laminates, Compos. Struct. 82 (2008) 382–389. https://doi.org/10.1016/J.COMPSTRUCT.2007.01.015.

[113] S. Sihn, R.Y. Kim, K. Kawabe, S.W. Tsai, Experimental studies of thin-ply laminated composites, Compos. Sci. Technol. 67 (2007) 996–1008. https://doi.org/10.1016/J.COMPSCITECH.2006.06.008.

[114] H. Saito, M. Morita, K. Kawabe, M. Kanesaki, H. Takeuchi, M. Tanaka, I. Kimpara, Effect of ply-thickness on impact damage morphology in CFRP laminates, J. Reinf. Plast. Compos. 30 (2011) 1097–1106. https://doi.org/10.1177/0731684411416532/ASSET/IMAGES/LARGE/10.1177_0731684411416532-FIG16.JPEG.

[115] T. Yokozeki, A. Kuroda, A. Yoshimura, T. Ogasawara, T. Aoki, Damage characterization in thin-ply composite laminates under out-of-plane transverse loadings, Compos. Struct. 93 (2010) 49–57. https://doi.org/10.1016/J.COMPSTRUCT.2010.06.016.

[116] M. Fotouhi, M. Jalalvand, M.R. Wisnom, High performance quasi-isotropic thin-ply carbon/glass hybrid composites with pseudo-ductile behaviour in all fibre orientations, Compos. Sci. Technol. 152 (2017) 101–110. https://doi.org/10.1016/j.compscitech.2017.08.024.

[117] G. Czél, M. Jalalvand, M.R. Wisnom, Design and characterisation of advanced pseudo-ductile unidirectional thin-ply carbon/epoxy–glass/epoxy hybrid composites, Compos. Struct. 143 (2016) 362–370. https://doi.org/10.1016/J.COMPSTRUCT.2016.02.010.

[118] G. Czél, M. Jalalvand, M.R. Wisnom, Hybrid specimens eliminating stress concentrations in tensile and compressive testing of unidirectional composites, Compos. Part A Appl. Sci. Manuf. 91 (2016) 436–447. https://doi.org/10.1016/J.COMPOSITESA.2016.07.021.

[119] M. Fotouhi, M. Jalalvand, M.R. Wisnom, Notch insensitive orientation-dispersed pseudo-ductile thin-ply carbon/glass hybrid laminates, Compos. Part A Appl. Sci. Manuf. 110 (2018) 29–44. https://doi.org/10.1016/J.COMPOSITESA.2018.04.012.

[120] T. Rev, M. Jalalvand, J. Fuller, M.R. Wisnom, G. Czél, A simple and robust approach for visual overload indication - UD thin-ply hybrid composite sensors, Compos. Part A Appl. Sci. Manuf. 121 (2019) 376–385. https://doi.org/10.1016/J.COMPOSITESA.2019.03.005.

[121] M. Jalalvand, H. Wu, F. Sheibanian, M. Fotouhi, M. Wisnom, M. Jalalvand, H. Wing, M.L. Wu, F. Sheibanian, M. Fotouhi, M.R. Wisnom, SELF-WARNING HYBRID COMPOSITE PATCHES FOR REPAIRING CRACKED ALUMINIUM PANELS, in: ECCM18 - 18 Th Eur. Conf. Compos. Mater., 2018: pp. 24–28.

[122] M. Böyük, R. Duvar, O. Urhan, A Review of Image Processing based Visual Inspection Methods in Aircraft Maintenance, J. Aeronaut. Sp. Technol. 14 (2021) 185–192.

[123] L. Cook, Visual inspection reliability for composite aircraft structures, Cranfield University, 2009.

[124] G.A.O. Davies, X. Zhang, Impact damage prediction in carbon composite structures, Int. J. Impact Eng. 16 (1995) 149–170. https://doi.org/10.1016/0734-743X(94)00039-Y.

[125] M. Fotouhi, M. Damghani, M.C. Leong, S. Fotouhi, M. Jalalvand, M.R. Wisnom, A comparative study on glass and carbon fibre reinforced laminated composites in scaled quasi-static indentation tests, Compos. Struct. 245 (2020) 112327. https://doi.org/10.1016/J.COMPSTRUCT.2020.112327.

[126] M. Ubago Torres, M. Jalalvand, Additive binding layers to suppress free edge delamination in composite laminates under tension, Compos. Part A Appl. Sci. Manuf. 156 (2022) 106902. https://doi.org/10.1016/J.COMPOSITESA.2022.106902.

[127] S.G. Marino, G. Czél, Improving the performance of pseudo-ductile hybrid composites by film-interleaving, Compos. Part A Appl. Sci. Manuf. 142 (2021) 106233. https://doi.org/10.1016/J.COMPOSITESA.2020.106233.

[128] L.S. Sutherland, C. Guedes Soares, The use of quasi-static testing to obtain the low-velocity impact damage resistance of marine GRP laminates, Compos. Part B Eng. 43 (2012) 1459–1467. https://doi.org/10.1016/j.compositesb.2012.01.002.

[129] H. Kaczmarek, S. Maison, Comparative ultrasonic analysis of damage in CFRP under static indentation and low-velocity impact, Compos. Sci. Technol. 51 (1994) 11–26. https://doi.org/10.1016/0266-3538(94)90152-X.

[130] A.T. Nettles, M.J. Douglas, A comparison of quasi-static indentation to low-velocity impact, NASA Tech. Rep. NASA/TP-20 (2000).

[131] M. Santos, J. Santos, P. Reis, A. Amaro, Ultrasonic C-scan techniques for the evaluation of impact damage in CFRP, Mater. Test. 63 (2021) 131–137. https://doi.org/10.1515/MT-2020-0020/MACHINEREADABLECITATION/RIS.

[132] industrial-ndt, (n.d.). https://www.industrial-ndt.com/dolphitech-dolphicam-2 (accessed March 5, 2024).

[133] S. Abrate, Impact on Laminated Composite Materials, Appl. Mech. Rev. 44 (1991) 155–190. https://doi.org/10.1115/1.3119500.

[134] W. Tan, B.G. Falzon, L.N.S. Chiu, M. Price, Predicting low velocity impact damage

and Compression-After-Impact (CAI) behaviour of composite laminates, Compos. Part A Appl. Sci. Manuf. 71 (2015) 212–226. https://doi.org/10.1016/J.COMPOSITESA.2015.01.025.

[135] E. V. González, P. Maimí, P.P. Camanho, A. Turon, J.A. Mayugo, Simulation of drop-weight impact and compression after impact tests on composite laminates, Compos. Struct. 94 (2012) 3364–3378. https://doi.org/10.1016/J.COMPSTRUCT.2012.05.015.

[136] P. Shabani, L. Li, J. Laliberte, G. Qi, D. Rapking, D. Mollenhauer, High-fidelity simulation of low-velocity impact damage in fiber-reinforced composite laminates using integrated discrete and continuum damage models, Compos. Struct. 313 (2023) 111053. https://doi.org/10.1016/j.compstruct.2023.116910.

[137] R. Olsson, Analytical model for delamination growth during small mass impact on plates, Int. J. Solids Struct. 47 (2010) 2884–2892. https://doi.org/10.1016/J.IJSOLSTR.2010.06.015.

[138] H. Singh, P. Mahajan, Analytical modeling of low velocity large mass impact on composite plate including damage evolution, Compos. Struct. 149 (2016) 79–92. https://doi.org/10.1016/J.COMPSTRUCT.2016.04.009.

[139] A.L. Dobyns, Analysis of Simply-Supported Orthotropic Plates Subject to Static and Dynamic Loads, AIAA J. 19 (1981) 642–650. https://doi.org/10.2514/3.50984.

[140] S.R. Swanson, Contact deformation and stress in orthotropic plates, Compos. Part A Appl. Sci. Manuf. 36 (2005) 1421–1429. https://doi.org/10.1016/J.COMPOSITESA.2004.11.011.

[141] F. Najafi, M.H. Shojaeefard, H. Saeidi Googarchin, Low-velocity impact response of functionally graded doubly curved panels with Winkler–Pasternak elastic foundation: An analytical approach, Compos. Struct. 162 (2017) 351–364. https://doi.org/10.1016/J.COMPSTRUCT.2016.11.094.

[142] G.A. Schoeppner, S. Abrate, Delamination threshold loads for low velocity impact on composite laminates, Compos. Part A Appl. Sci. Manuf. 31 (2000) 903–915. https://doi.org/10.1016/S1359-835X(00)00061-0.

[143] R. Bogenfeld, J. Kreikemeier, T. Wille, Review and benchmark study on the analysis of low-velocity impact on composite laminates, Eng. Fail. Anal. 86 (2018) 72–99. https://doi.org/10.1016/J.ENGFAILANAL.2017.12.019.

[144] L. Kärger, J. Baaran, A. Gunnion, R. Thomson, Evaluation of impact assessment methodologies. Part I: Applied methods, Compos. Part B Eng. 40 (2009) 65–70. https://doi.org/10.1016/J.COMPOSITESB.2008.06.003.

[145] J. Baaran, L. Kärger, A. Wetzel, Efficient prediction of damage resistance and tolerance of composite aerospace structures, Proc. Inst. Mech. Eng. Part G J. Aerosp. Eng. 222 (2008) 179–188. https://doi.org/10.1243/09544100JAERO278.

[146] L. Kärger, J. Baaran, J. Teßmer, Efficient simulation of low-velocity impacts on composite sandwich panels, Comput. Struct. 86 (2008) 988–996. https://doi.org/10.1016/J.COMPSTRUC.2007.04.029.

[147] M. Saeedifar, Impact damage assessment in laminated composites using acoustic emission and finite element methods, Polym. Compos. 45 (2024) 1036–1053. https://doi.org/10.1002/PC.27834.

[148] C.S. Lopes, S. Sádaba, C. González, J. Llorca, P.P. Camanho, Physically-sound simulation of low-velocity impact on fiber reinforced laminates, Int. J. Impact Eng. 92 (2016) 3–17. https://doi.org/10.1016/J.IJIMPENG.2015.05.014.

[149] L. Huang, Y. Tao, J. Sun, D. Zhang, J. Zhao, Assessment of numerical modeling approaches for thin composite laminates under low-velocity impact, Thin-Walled Struct. 191 (2023) 111053. https://doi.org/10.1016/j.tws.2023.111053.

[150] N. Hongkarnjanakul, C. Bouvet, S. Rivallant, Validation of low velocity impact modelling on different stacking sequences of CFRP laminates and influence of fibre failure, Compos. Struct. 106 (2013) 549–559. https://doi.org/10.1016/J.COMPSTRUCT.2013.07.008.

[151] M.R.W. Sakineh Fotouhi, Mohammad Mahdi Ashrafian, Meysam Jalalvand, Amin Farrokhabadi, Mohammad Fotouhi, Modelling of Self-Sensing Hybrid Composites for Detection of Barely Visible Impact Damage, in: 10th Eur. Work. Struct. Heal. Monit. (10th EWSHM), 2022.

[152] H. Suemasu, O. Majima, Multiple delaminations and their severity in nonlinear circular plates subjected to concentrated loading, J. Compos. Mater. 32 (1998) 123–140. https://doi.org/10.1177/002199839803200202.

[153] G.A.O. Davies, P. Robinson, J. Robson, D. Eady, Shear driven delamination propagation in two dimensions, Compos. Part A Appl. Sci. Manuf. 28 (1997) 757–765. https://doi.org/10.1016/S1359-835X(97)00015-8.

[154] R. Olsson, M. V. Donadon, B.G. Falzon, Delamination threshold load for dynamic impact on plates, Int. J. Solids Struct. 43 (2006) 3124–3141. https://doi.org/10.1016/j.ijsolstr.2005.05.005.

[155] S.A. Lukasiewicz, INTRODUCTION OF CONCENTRATED LOADS IN PLATES AND SHELLS, Prog. Aerosp. Sci. 17 (1976) 109–146.

[156] A. Wagih, P. Maimí, N. Blanco, E. V. González, Scaling effects of composite laminates under out-of-plane loading, Compos. Part A Appl. Sci. Manuf. 116 (2019) 1–12. https://doi.org/10.1016/J.COMPOSITESA.2018.10.001.

[157] K.N. Shivakumar, W. Elber, W. Illg, Prediction of Impact Force and Duration Due to Low-Velocity Impact on Circular Composite Laminates, J. Appl. Mech. 52 (1985) 674–680. https://doi.org/10.1115/1.3169120.

[158] A. Laulusa, O.A. Bauchau, J.Y. Choi, V.B.C. Tan, L. Li, Evaluation of some shear deformable shell elements, Int. J. Solids Struct. 43 (2006) 5033–5054. https://doi.org/10.1016/J.IJSOLSTR.2005.08.006.

[159] X.C. Sun, M.R. Wisnom, S.R. Hallett, Interaction of inter- and intralaminar damage in scaled quasi-static indentation tests: Part 2 – Numerical simulation, Compos. Struct. 136 (2016) 727–742. https://doi.org/10.1016/J.COMPSTRUCT.2015.09.062.

[160] Nippon Graphite FIber / High Performace Pitched Based Carbon Fiber, (n.d.). https://www.ngfworld.com (accessed October 5, 2023).

[161] F. Ahmad, F. Abbassi, M.K. Park, J.W. Hong, Numerical investigation to evaluate effect of fiber orientation on penetration-resistance of an aircraft composite material, Mech. Adv. Mater. Struct. 26 (2019) 1613–1621. https://doi.org/10.1080/15376494.2018.1444226.

[162] H. Cui, D. Thomson, S. Eskandari, N. Petrinic, A critical study on impact damage simulation of IM7/8552 composite laminate plate, Int. J. Impact Eng. 127 (2019) 100–109. https://doi.org/10.1016/j.ijimpeng.2019.01.009.

[163] J. Zhou, P. Wen, S. Wang, Numerical investigation on the repeated low-velocity impact behavior of composite laminates, Compos. Part B Eng. 185 (2020) 107771. https://doi.org/10.1016/J.COMPOSITESB.2020.107771.

[164] J. Zou, Z. Lei, R. Bai, D. Liu, H. Jiang, J. Liu, C. Yan, Damage and failure analysis of composite stiffened panels under low-velocity impact and compression after impact, Compos. Struct. 262 (2021) 113333. https://doi.org/10.1016/J.COMPSTRUCT.2020.113333.

[165] M. Saeedifar, H. Hosseini Toudeshky, The Effect of Interlaminar and Intralaminar Damage Mechanisms on the Quasi-Static Indentation Strength of Composite Laminates, Appl. Compos. Mater. 30 (2023) 871–886. https://doi.org/10.1007/S10443-023-10123-X/FIGURES/13.

[166] S. Sádaba, F. Martínez-Hergueta, C.S. Lopes, C. Gonzalez, J. LLorca, Virtual testing of impact in fiber reinforced laminates, Struct. Integr. Durab. Adv. Compos. Innov. Model. Methods Intell. Des. (2015) 247–270. https://doi.org/10.1016/B978-0-08-100137-0.00010-9.

[167] J. Reiner, N. Zobeiry, R. Vaziri, A stacked sublaminate-based damage-plasticity model for simulating progressive damage in composite laminates under impact loading, Thin-Walled Struct. 156 (2020) 107009. https://doi.org/10.1016/J.TWS.2020.107009.

[168] M. Saeedifar, M.A. Najafabadi, D. Zarouchas, H.H. Toudeshky, M. Jalalvand, Clustering of interlaminar and intralaminar damages in laminated composites under indentation loading using Acoustic Emission, Compos. Part B Eng. 144 (2018) 206–219. https://doi.org/10.1016/J.COMPOSITESB.2018.02.028.

[169] T. Rev, G. Czél, M. Jalalvand, M.R. Wisnom, Unidirectional hybrid composite overload sensors, in: 21st Int. Conf. Compos. Mater., ICCM21, China, 2017.

[170] A. Tabatabaeian, S. Fotouhi, P. Harrison, M. Fotouhi, On the Optimal Design of Smart Composite Sensors for Impact Damage Detection, in: 20th Eur. Conf. Compos. Mater., Lausanne, 2022. https://eprints.gla.ac.uk/269885/ (accessed March 7, 2024).

[171] A. Tabatabaeian, B. Campbell, P. Harrison, M. Fotouhi, Low velocity impact behaviour of mechanochromic sandwich composites, in: 17th Int. Conf. Adv. Exp. Mech., Glasgow, 2023.

[172] A. Tabatabaeian, R. Mohammadi, P. Harrison, M. Fotouhi, Characterisation and Application of Bio-Inspired Hybrid Composite Sensors for Detecting Barely Visible Damage under Out-of-Plane Loadings, Sensors 2024, Vol. 24, Page 5170. 24 (2024) 5170. https://doi.org/10.3390/S24165170.

[173] S.Z.H. Shah, S. Karuppanan, P.S.M. Megat-Yusoff, Z. Sajid, Impact resistance and damage tolerance of fiber reinforced composites: A review, Compos. Struct. 217 (2019) 100–121. https://doi.org/10.1016/J.COMPSTRUCT.2019.03.021.

[174] M. Saeedifar, M.A. Najafabadi, D. Zarouchas, H.H. Toudeshky, M. Jalalvand, Barely visible impact damage assessment in laminated composites using acoustic emission, Compos. Part B Eng. 152 (2018) 180–192.

https://doi.org/10.1016/J.COMPOSITESB.2018.07.016.

[175] A. Leroy, D. Scida, É. Roux, F. Toussaint, R. Ayad, Are there similarities between quasi-static indentation and low velocity impact tests for flax-fibre composites?, Ind. Crops Prod. 171 (2021). https://doi.org/10.1016/j.indcrop.2021.113840.

[176] B. Hachemane, R. Zitoune, B. Bezzazi, C. Bouvet, Sandwich composites impact and indentation behaviour study, Compos. Part B Eng. 51 (2013) 1–10. https://doi.org/10.1016/j.compositesb.2013.02.014.

[177] T. Allen, S. Ahmed, W. Hepples, P.A. Reed, I. Sinclair, M. Spearing, A comparison of quasi-static indentation and low-velocity impact on composite overwrapped pressure vessels, J. Compos. Mater. 52 (2018) 4051–4060. https://doi.org/10.1177/0021998318774401.

[178] C. De Marco Muscat-Fenech, J. Cortis, C. Cassar, Impact damage testing on composite marine sandwich panels. Part 2: Instrumented drop weight, J. Sandw. Struct. Mater. 16 (2014) 443–480. https://doi.org/10.1177/1099636214535167.

[179] Y. Aoki, H. Suemasu, T. Ishikawa, Damage propagation in CFRP laminates subjected to low velocity impact and static indentation, Adv. Compos. Mater. Off. J. Japan Soc. Compos. Mater. 16 (2007) 45–61. https://doi.org/10.1163/156855107779755318.

[180] A. Tabatabaeian, B. Jerkovic, P. Harrison, E. Marchiori, M. Fotouhi, Barely visible impact damage detection in composite structures using deep learning networks with varying complexities, Compos. Part B Eng. 264 (2023) 110907. https://doi.org/10.1016/J.COMPOSITESB.2023.110907.

[181] A. Wang, X. Liu, Q. Yue, G. Xian, Comparative study on the low-velocity impact properties of unidirectional flax and carbon fiber reinforced epoxy plates, Mech. Adv. Mater. Struct. 0 (2023) 1–12. https://doi.org/10.1080/15376494.2023.2179705.

[182] G. Czél, M. Jalalvand, M.R. Wisnom, Demonstration of pseudo-ductility in unidirectional hybrid composites made of discontinuous carbon/epoxy and continuous glass/epoxy plies, Compos. Part A Appl. Sci. Manuf. 72 (2015) 75–84. https://doi.org/10.1016/J.COMPOSITESA.2015.01.019.

[183] B. Campbell, A. Tabatabaeian, P. Harrison, M. Fotouhi, Improving visual inspection of barely visible impact damage in carbon/flax micro-sandwich structures, in: 26th Int. Conf. Compos. Struct., Porto, 2023.

[184] K. Deng, H. Liu, L. Yang, S. Addepalli, Y. Zhao, Classification of barely visible impact damage in composite laminates using deep learning and pulsed thermographic inspection, Neural Comput. Appl. (2023) 1–15. https://doi.org/10.1007/s00521-023-08293-7.

[185] S.A. Zargar, F.G. Yuan, Impact diagnosis in stiffened structural panels using a deep learning approach, Struct. Heal. Monit. 20 (2021) 681–691. https://doi.org/10.1177/1475921720925044.

[186] Z. Wei, H. Fernandes, H.G. Herrmann, J.R. Tarpani, A. Osman, A Deep Learning Method for the Impact Damage Segmentation of Curve-Shaped CFRP Specimens Inspected by Infrared Thermography, Sensors 2021, Vol. 21, Page 395. 21 (2021) 395. https://doi.org/10.3390/S21020395.

[187] K.C. Jung, S.H. Chang, Advanced deep learning model-based impact characterization

method for composite laminates, Compos. Sci. Technol. 207 (2021) 108713. https://doi.org/10.1016/j.compscitech.2021.108713.

[188] O. Ahmed, X. Wang, M.V. Tran, M.Z. Ismadi, Advancements in fiber-reinforced polymer composite materials damage detection methods: Towards achieving energy-efficient SHM systems, Compos. Part B Eng. 223 (2021) 109136. https://doi.org/10.1016/J.COMPOSITESB.2021.109136.

[189] M.P. Delaney, S.Y.K. Fung, H. Kim, Dent depth visibility versus delamination damage for impact of composite panels by tips of varying radius, J. Compos. Mater. 52 (2018) 2691–2705. https://doi.org/10.1177/0021998317752502.

[190] How Does Emissivity Affect Thermal Imaging?(2021), https://www.flir.co.uk/.

[191] K. Choudhary, B. DeCost, C. Chen, A. Jain, F. Tavazza, R. Cohn, C.W. Park, A. Choudhary, A. Agrawal, S.J.L. Billinge, E. Holm, S.P. Ong, C. Wolverton, Recent Advances and Applications of Deep Learning Methods in Materials Science, Npj Comput. Mater. 8 (2022) 1–26. https://doi.org/10.1038/s41524-022-00734-6.

[192] A. Semenov, V. Boginski, E.L. Pasiliao, Neural networks with multidimensional cross-entropy loss functions, Comput. Data Soc. Networks. CSoNet 2019. Lect. Notes Comput. Sci. 11917 LNCS (2019) 57–62. https://doi.org/10.1007/978-3-030-34980-6_5/TABLES/1.

[193] C.H. Chen, P.H. Lin, J.G. Hsieh, S.L. Cheng, J.H. Jeng, Robust multi-class classification using linearly scored categorical cross-entropy, Proc. 3rd IEEE Int. Conf. Knowl. Innov. Invent. 2020, ICKII 2020. (2020) 200–203. https://doi.org/10.1109/ICKII50300.2020.9318835.

[194] J. Singh, R. Banerjee, A study on single and multi-layer perceptron neural network, Proc. 3rd Int. Conf. Comput. Methodol. Commun. ICCMC 2019. (2019) 35–40. https://doi.org/10.1109/ICCMC.2019.8819775.

[195] M. Rautela, J. Senthilnath, E. Monaco, S. Gopalakrishnan, Delamination prediction in composite panels using unsupervised-feature learning methods with wavelet-enhanced guided wave representations, Compos. Struct. 291 (2022) 115579. https://doi.org/10.1016/J.COMPSTRUCT.2022.115579.

[196] N. Elyasi, M. Hosseini moghadam, Classification Of Skin Lesions By Topological Data Analysis Alongside With Neural Network, (2020).

[197] A. Giusti, D.C. Cireşan, J. Masci, L.M. Gambardella, J. Schmidhuber, Fast image scanning with deep max-pooling convolutional neural networks, 2013 IEEE Int. Conf. Image Process. ICIP 2013 - Proc. (2013) 4034–4038. https://doi.org/10.1109/ICIP.2013.6738831.

[198] D. Yu, H. Wang, P. Chen, Z. Wei, Mixed pooling for convolutional neural networks, Lect. Notes Comput. Sci. (Including Subser. Lect. Notes Artif. Intell. Lect. Notes Bioinformatics). 8818 (2014) 364–375. https://doi.org/10.1007/978-3-319-11740-9_34/COVER.

[199] K. He, X. Zhang, S. Ren, J. Sun, Deep Residual Learning for Image Recognition, in: Proc. IEEE Conf. Comput. Vis. Pattern Recognit., 2016: pp. 770–778.

[200] J. Deng, W. Dong, R. Socher, L.-J. Li, Kai Li, Li Fei-Fei, ImageNet: A large-scale hierarchical image database, in: IEEE Conf. Comput. Vis. Pattern Recognit., Institute

of Electrical and Electronics Engineers (IEEE), 2009: pp. 248–255. https://doi.org/10.1109/cvpr.2009.5206848.

[201] K. Weiss, T.M. Khoshgoftaar, D.D. Wang, A survey of transfer learning, J. Big Data. 3 (2016) 1–40. https://doi.org/10.1186/S40537-016-0043-6/TABLES/6.

[202] Y. Wang, Q. Yao, J.T. Kwok, L.M. Ni, Generalizing from a Few Examples: A Survey on Few-shot Learning, ACM Comput. Surv. 53 (2020). https://doi.org/10.1145/3386252.

[203] B. Kulis, Metric Learning: A Survey, Found. Trends® Mach. Learn. 5 (2013) 287–364. https://doi.org/10.1561/2200000019.

[204] J. Snell, K. Swersky, T.R. Zemel, Prototypical Networks for Few-shot Learning, Adv. Neural Inf. Process. Syst. 30 (2017).

[205] H. Li, J. Li, X. Guan, B. Liang, Y. Lai, X. Luo, Research on Overfitting of Deep Learning, Proc. - 2019 15th Int. Conf. Comput. Intell. Secur. CIS 2019. (2019) 78–81. https://doi.org/10.1109/CIS.2019.00025.

[206] D.P. Kingma, J.L. Ba, Adam: A Method for Stochastic Optimization, 3rd Int. Conf. Learn. Represent. ICLR 2015 - Conf. Track Proc. (2014).

[207] A. Paszke, S. Gross, F. Massa, A. Lerer, J. Bradbury, G. Chanan, T. Killeen, Z. Lin, N. Gimelshein, L. Antiga, A. Desmaison, A. Köpf, E. Yang, Z. DeVito, M. Raison, A. Tejani, S. Chilamkurthy, B. Steiner, L. Fang, J. Bai, S. Chintala, PyTorch: An imperative style, high-performance deep learning library, in: Adv. Neural Inf. Process. Syst., 2019.

[208] A. Entezami, H. Shariatmadar, C. De Michele, Non-parametric empirical machine learning for short-term and long-term structural health monitoring, Struct. Heal. Monit. 21 (2022) 2700–2718. https://doi.org/10.1177/14759217211069842.

[209] J. Gebhardt, M. Schlamp, I. Ehrlich, S. Hiermaier, Low-velocity impact behavior of elliptic curved composite structures, Compos. Struct. 193 (2023) 108026. https://doi.org/10.1016/B978-0-12-823979-7.00006-5.

[210] J.S. Yang, W.M. Zhang, F. Yang, S.Y. Chen, R. Schmidt, K.U. Schröder, L. Ma, L.Z. Wu, Low velocity impact behavior of carbon fibre composite curved corrugated sandwich shells, Compos. Struct. 238 (2020) 1–16. https://doi.org/10.1016/j.compstruct.2020.112027.

[211] C. He, R. Yu, H. Sun, Z. Chen, Lightweight multilayer composite structure for hydrogen storage tank, Int. J. Hydrogen Energy. 41 (2016) 15812–15816. https://doi.org/10.1016/J.IJHYDENE.2016.04.184.

[212] hydrogen-innovation.co.uk, (n.d.). https://hydrogen-innovation.co.uk/composite-hydrogen-tank-aims-to-decarbonise-road-transportation/ (accessed March 19, 2024).

[213] M. Zhang, H. Lv, H. Kang, W. Zhou, C. Zhang, A literature review of failure prediction and analysis methods for composite high-pressure hydrogen storage tanks, Int. J. Hydrogen Energy. 44 (2019) 25777–25799. https://doi.org/10.1016/J.IJHYDENE.2019.08.001.

[214] W. Zhou, J. Wang, Z. bo Pan, J. Liu, L. hua Ma, J. yi Zhou, Y. fan Su, Review on optimization design, failure analysis and non-destructive testing of composite

hydrogen storage vessel, Int. J. Hydrogen Energy. 47 (2022) 38862–38883. https://doi.org/10.1016/J.IJHYDENE.2022.09.028.

[215] H. Rocha, P. Antunes, U. Lafont, J.P. Nunes, Processing and structural health monitoring of a composite overwrapped pressure vessel for hydrogen storage, Struct. Heal. Monit. (2023). https://doi.org/10.1177/14759217231204242/ASSET/IMAGES/LARGE/10.1177_14759217231204242-FIG17.JPEG.

[216] W. Harris, C. Soutis, C. Atkin, Impact Response of Curved Composite Laminates: Effect of Radius and Thickness, Appl. Compos. Mater. 27 (2020) 555–573. https://doi.org/10.1007/s10443-020-09826-2.

[217] M. Albayrak, M.O. Kaman, I. Bozkurt, Experimental and Numerical Investigation of the Geometrical Effect on Low Velocity Impact Behavior for Curved Composites with a Rubber Interlayer, Springer Netherlands, 2023. https://doi.org/10.1007/s10443-022-10094-5.

[218] E. Avazpoor, A.H. Kazemian, H. Rahmani, Numerical and Experimental Investigations on the Low Velocity Impact Properties of Glass Fiber Reinforced Epoxy Composites: Effects of Radius of Curvature, Fibers Polym. 24 (2023) 3289–3298. https://doi.org/10.1007/s12221-023-00291-9.

[219] I.H. Choi, Low-velocity impact response analysis of composite pressure vessel considering stiffness change due to cylinder stress, Compos. Struct. 160 (2017) 491–502. https://doi.org/10.1016/j.compstruct.2016.10.023.

[220] S. Seifoori, A. Mahdian Parrany, S. Mirzarahmani, Impact damage detection in CFRP and GFRP curved composite laminates subjected to low-velocity impacts, Compos. Struct. 261 (2021) 113278. https://doi.org/10.1016/j.compstruct.2020.113278.

[221] D.S. Gemi, Ö.S. Şahin, L. Gemi, Experimental investigation of the effect of diameter upon low velocity impact response of glass fiber reinforced composite pipes, Compos. Struct. 275 (2021). https://doi.org/10.1016/j.compstruct.2021.114428.

[222] H. Saghafi, G. Minak, A. Zucchelli, Effect of preload on the impact response of curved composite panels, Compos. Part B Eng. 60 (2014) 74–81. https://doi.org/10.1016/j.compositesb.2013.12.026.

[223] C. Zhang, K.T. Tan, Low-velocity impact response and compression after impact behavior of tubular composite sandwich structures, Compos. Part B Eng. 193 (2020) 108026. https://doi.org/10.1016/j.compositesb.2020.108026.

[224] R. Panciroli, M. Ahmadi, M. Fotouhi, G. Minak, Low-velocity impact on preloaded and curved laminates, 2nd ed., Elsevier Ltd., 2022. https://doi.org/10.1016/B978-0-12-823979-7.00006-5.

[225] W. Liu, C. Sang, K. Jin, J. Hou, M. Yin, Experimental investigations into damage mechanism in the low-velocity impact and tension-after-impact testing of z-pin reinforced curved CFRP composite, Polym. Compos. (2024) 1–17. https://doi.org/10.1002/pc.28109.

[226] Y. Wan, Y. Liu, C. Hu, J. Yao, F. Wang, B. Yang, The failure mechanism of curved composite laminates subjected to low-velocity impact, Acta Mech. Sin. Xuebao. 39 (2023). https://doi.org/10.1007/s10409-023-23113-x.

[227] A. Tabatabaeian, A.R. Ghasemi, B. Asghari, Specification of non-uniform residual stresses and tensile characteristic in laminated composite materials exposed to simulated space environment, Polym. Test. 80 (2019) 106147. https://doi.org/10.1016/J.POLYMERTESTING.2019.106147.

[228] M. Sadighi, R. Alderliesten, Impact fatigue, multiple and repeated low-velocity impacts on FRP composites: A review, Compos. Struct. 297 (2022) 115962. https://doi.org/10.1016/J.COMPSTRUCT.2022.115962.

Appendix

<u>Appendix A:</u> Visual inspection results, including images and videos, taken during the static indentation tests of flat panels

IM7/8552-Reference sample

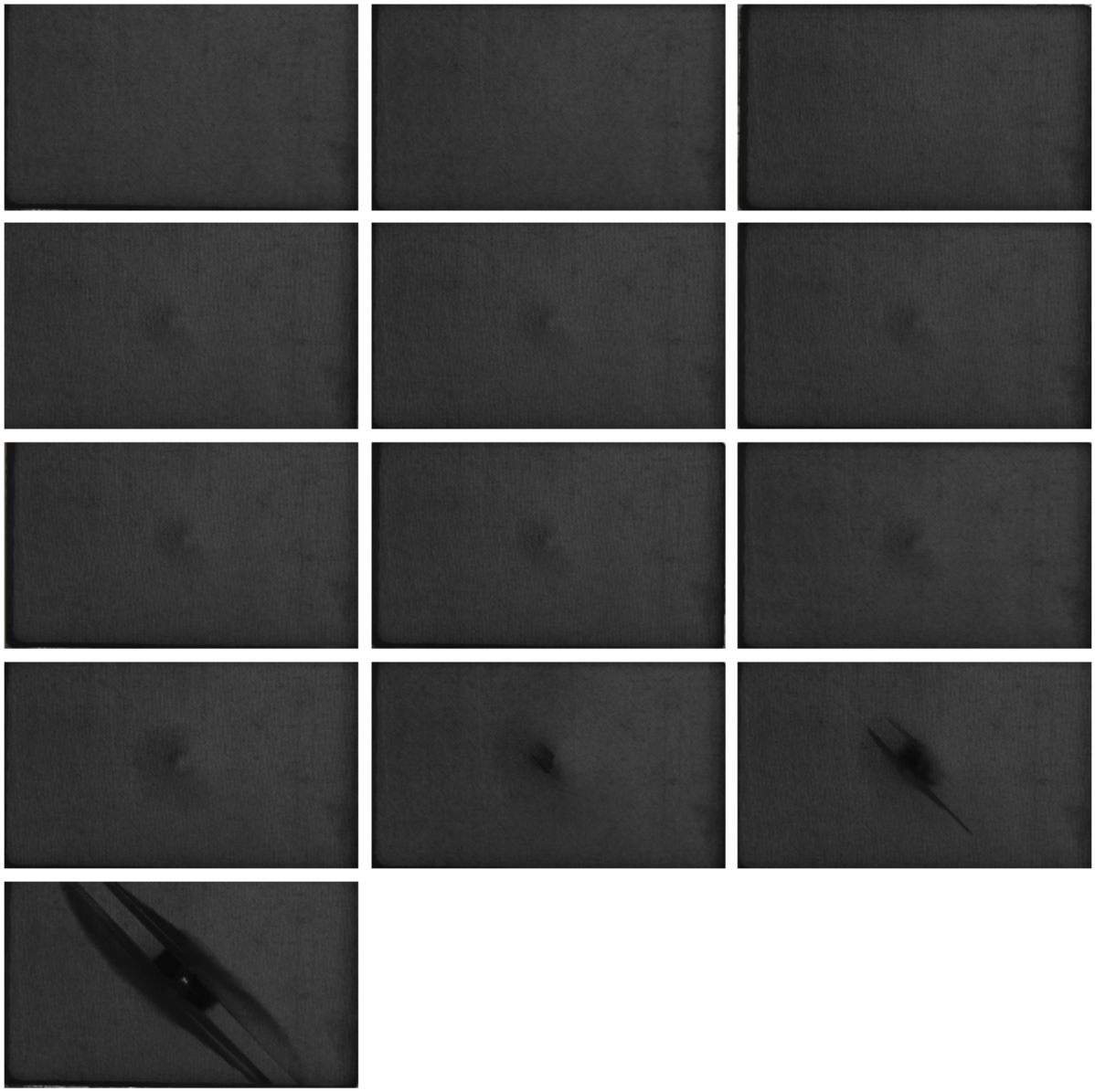

IM7/8552-Sensor (0) sample

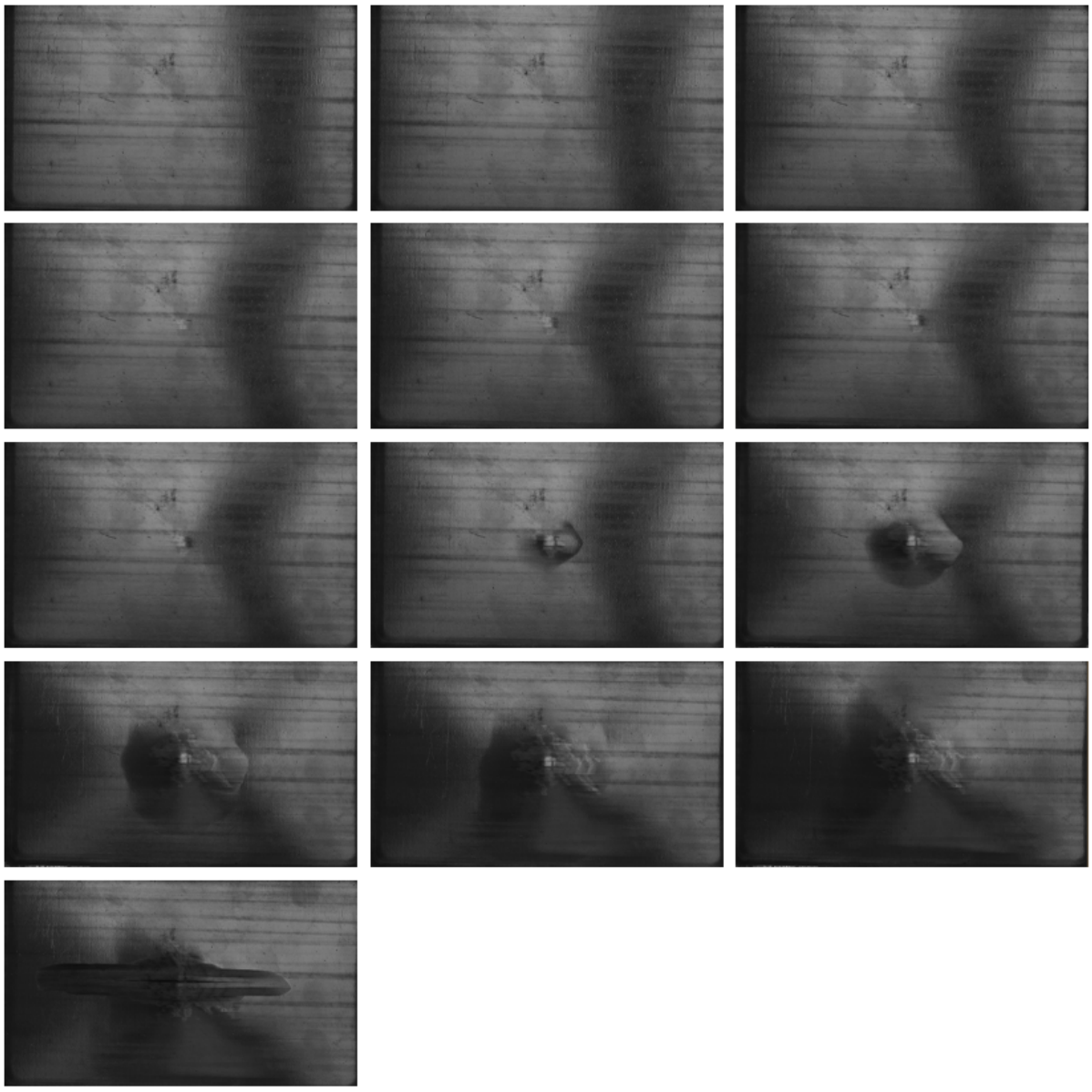

IM7/8552-Sensor (45) sample

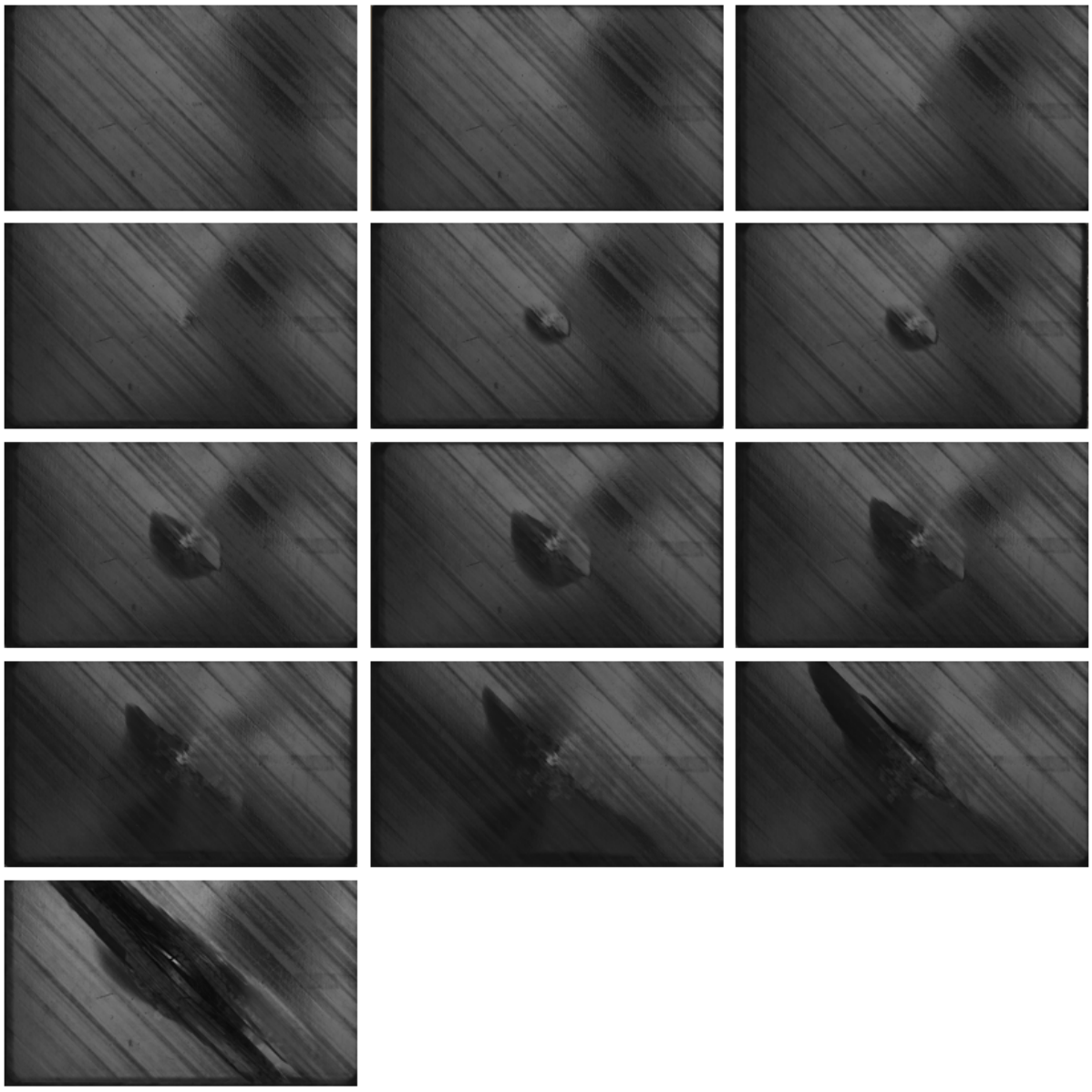

Hybrid flax/carbon: Reference sample

https://youtu.be/4HzeaKb3G2E

Hybrid flax/carbon: Sensor sample

https://youtu.be/HWBf6GO2Fls

Hybrid flax/carbon: Sensor with cuts sample

https://youtu.be/ySRDX4cj924

<u>Appendix B:</u> Impact test results for flat Reference (R) and Sensor (S) samples at 12J, 18J and 27J energies

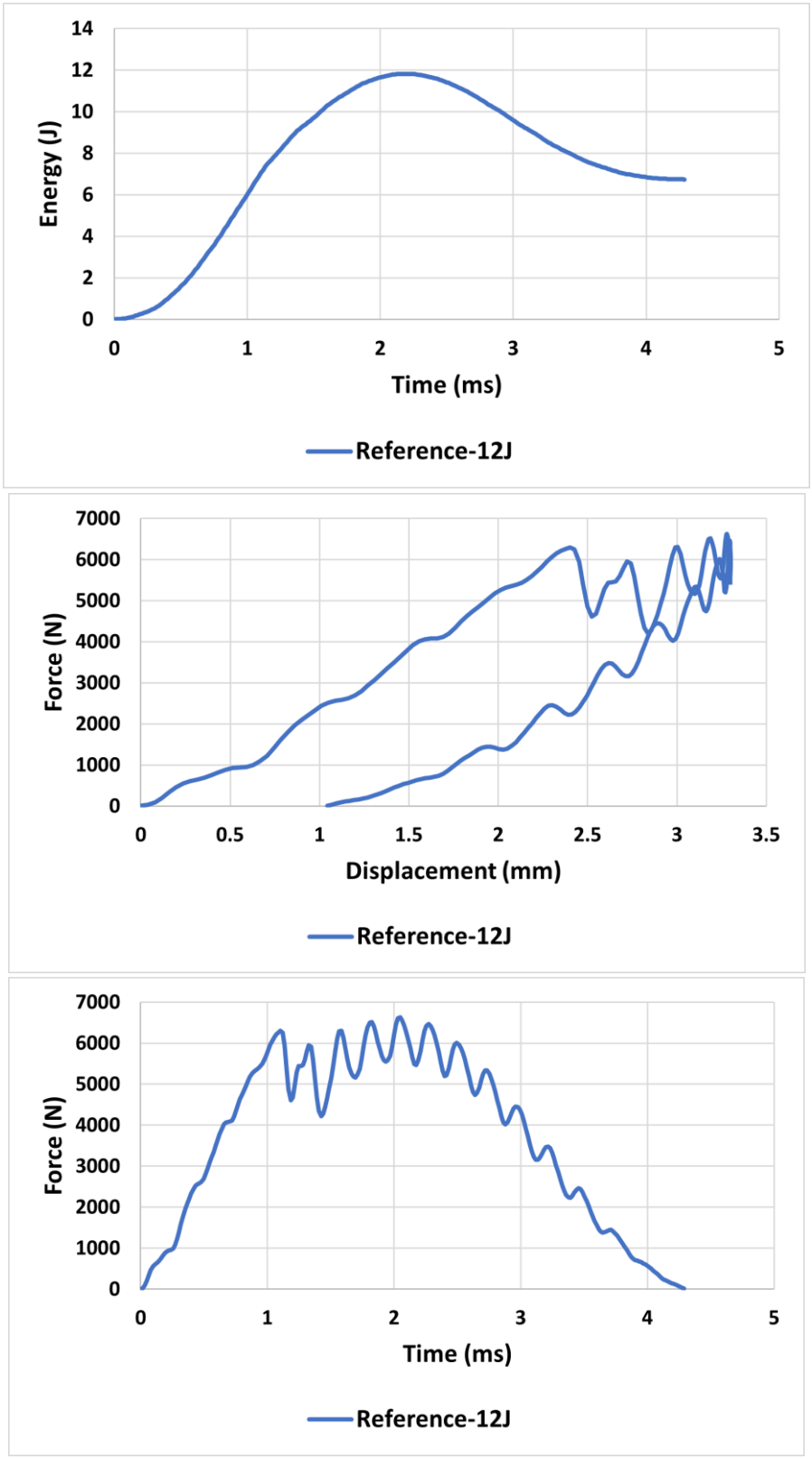

Fig. 1: 12J, R1

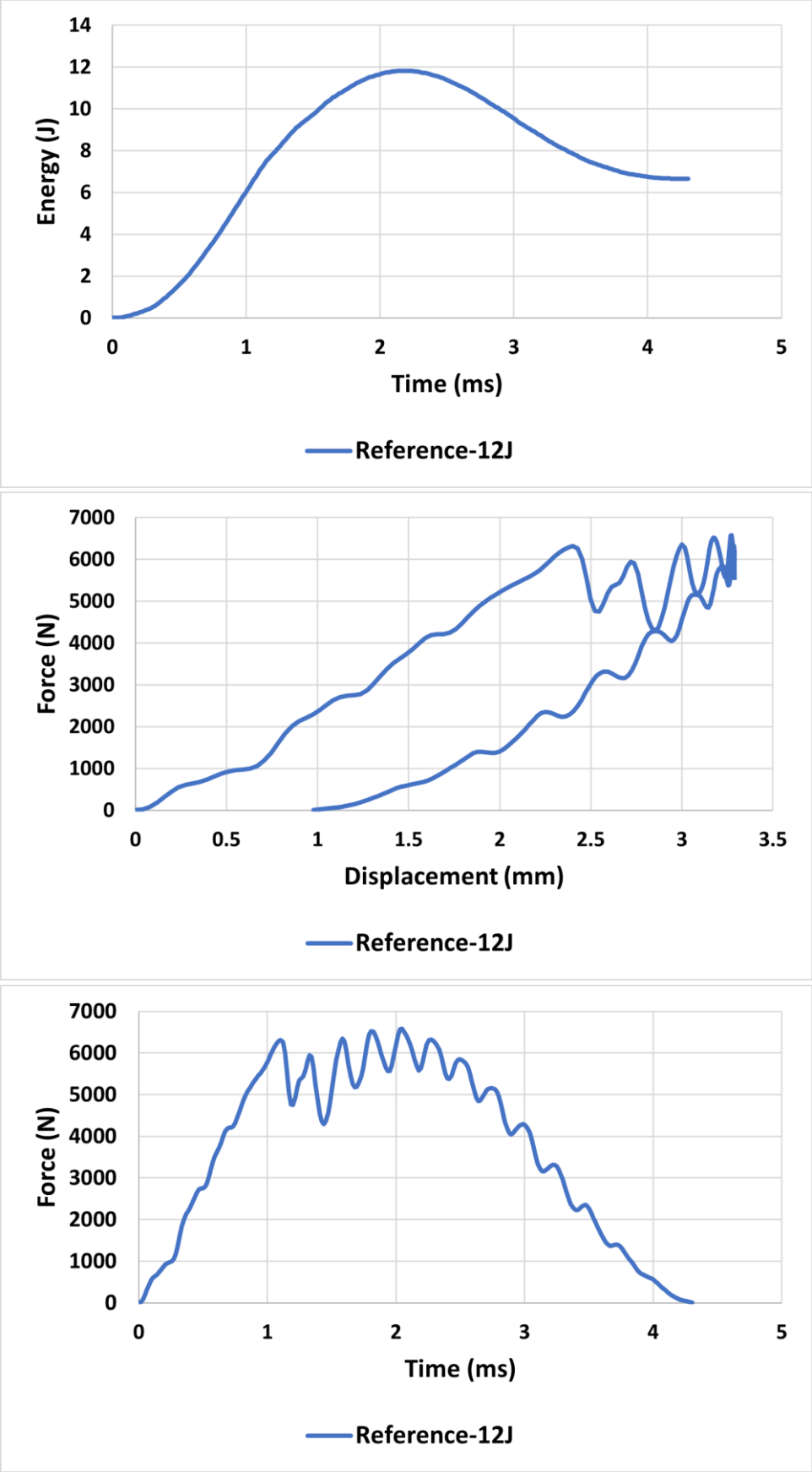
Energy (J)
14
12
10
8
6
4
2
0
0
1
2
3
4
5
Time (ms)
Reference-12J
Force (N)
7000
6000
5000
4000
3000
2000
1000
0
0
0.5
1
1.5
2
2.5
3
3.5
Displacement (mm)
Reference-12J
Force (N)
7000
6000
5000
4000
3000
2000
1000
0
0
1
2
3
4
5
Time (ms)
Reference-12J

Fig. 2: 12J, R2

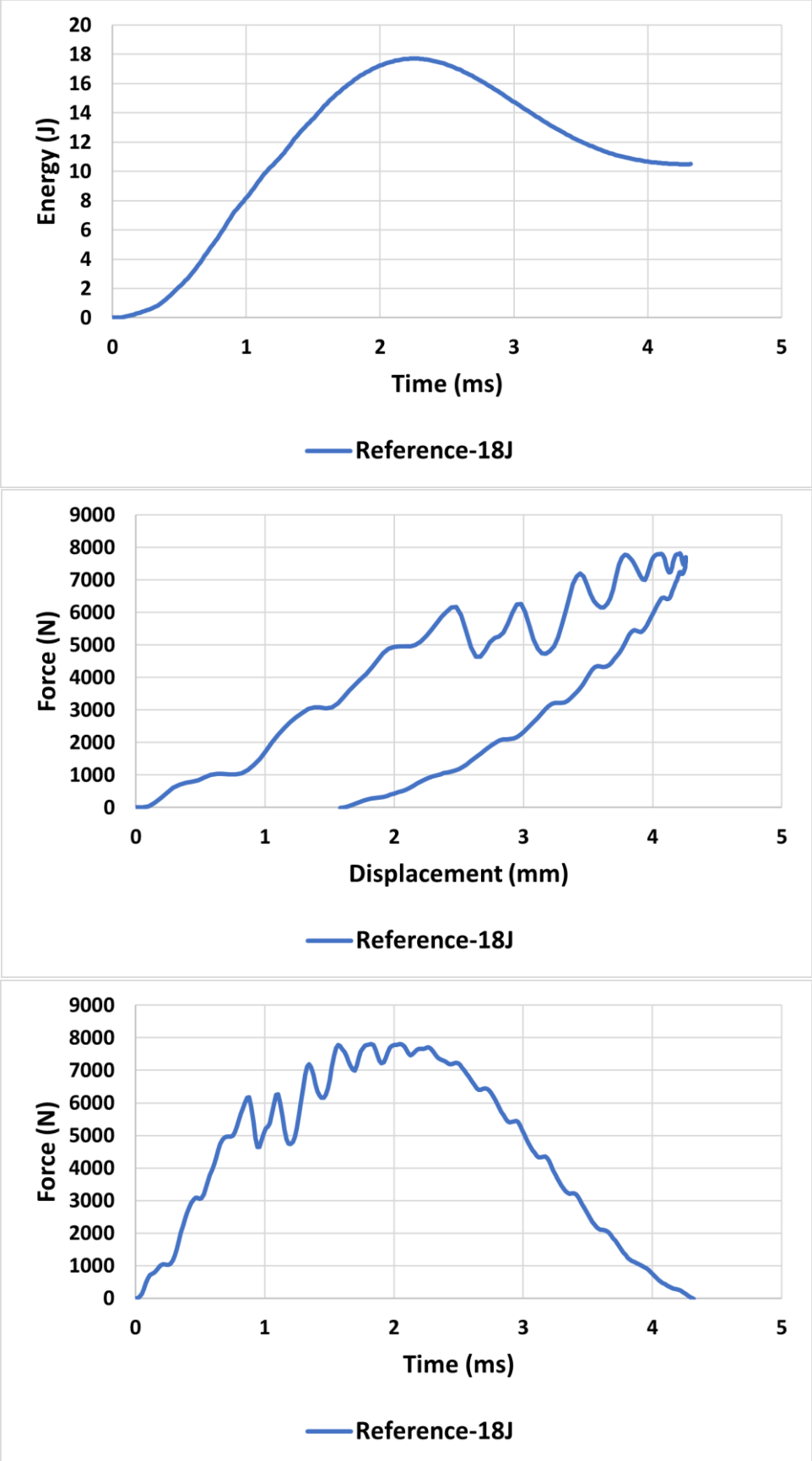
Energy (J)
20
18
16
14
12
10
8
6
4
2
0
0
1
2
3
4
5
Time (ms)
Reference-18J
Force (N)
9000
8000
7000
6000
5000
4000
3000
2000
1000
0
0
1
2
3
4
5
Displacement (mm)
Reference-18J
Force (N)
9000
8000
7000
6000
5000
4000
3000
2000
1000
0
0
1
2
3
4
5
Time (ms)
Reference-18J

Fig. 3: 18J, R1

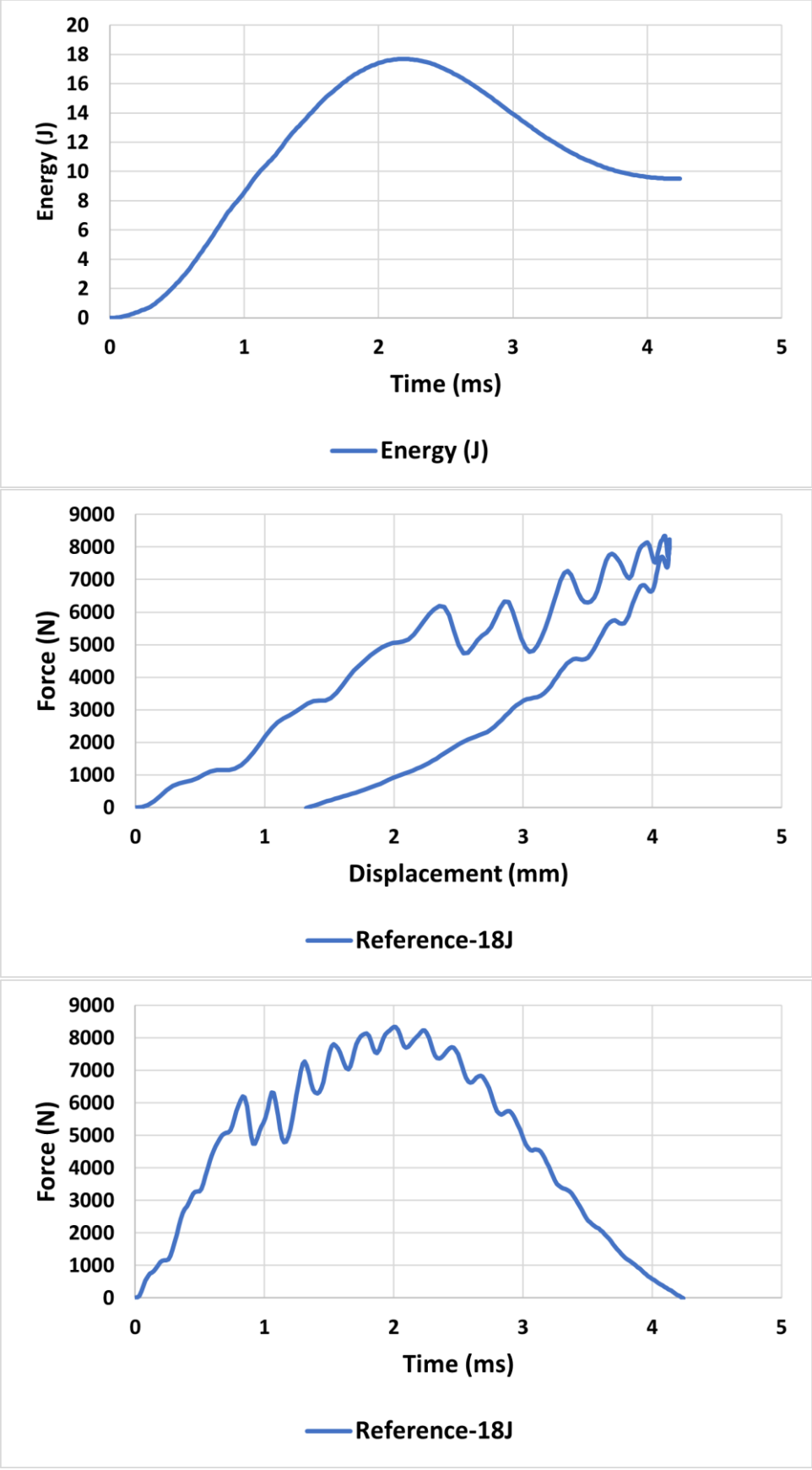
Energy (J)
Time (ms)
Energy (J)
Force (N)
Displacement (mm)
Reference-18J
Force (N)
Time (ms)
Reference-18J

Fig. 4: 18J, R2

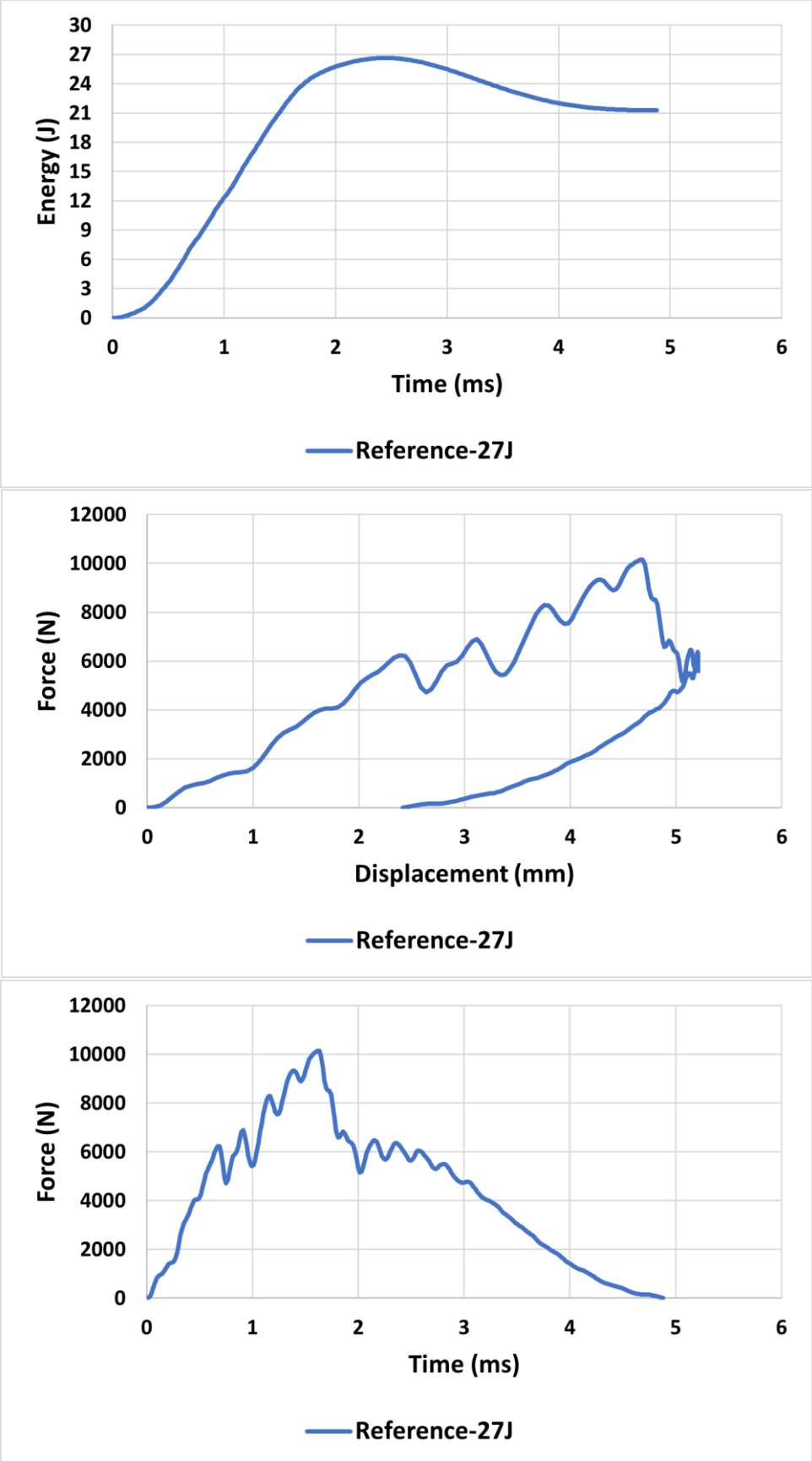
Energy (J)
30
27
24
21
18
15
12
9
6
3
0
0
1
2
3
4
5
6
Time (ms)
Reference-27J
Force (N)
12000
10000
8000
6000
4000
2000
0
0
1
2
3
4
5
6
Displacement (mm)
Reference-27J
Force (N)
12000
10000
8000
6000
4000
2000
0
0
1
2
3
4
5
6
Time (ms)
Reference-27J

Fig. 5: 27J, R1

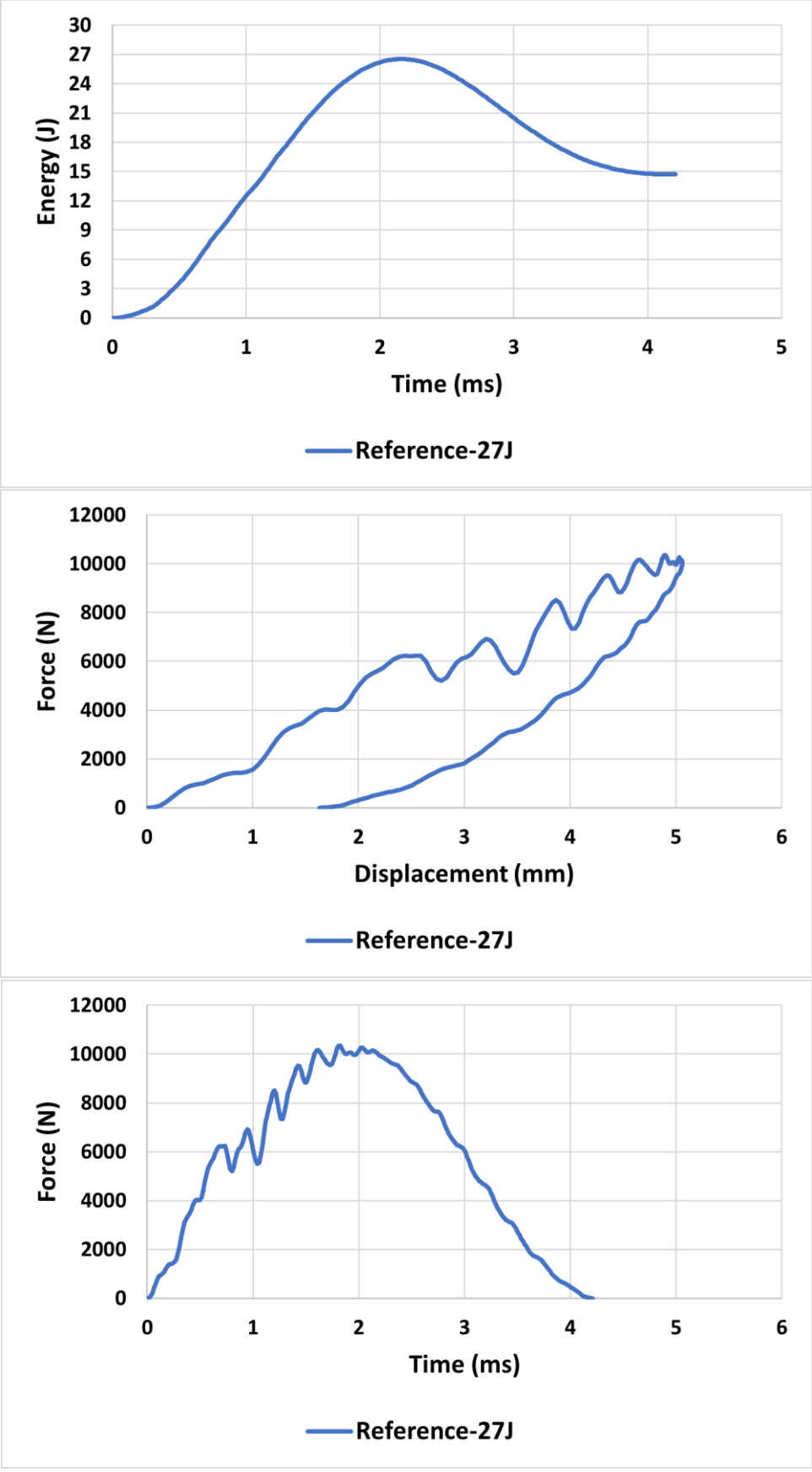
Energy (J)
30
27
24
21
18
15
12
9
6
3
0
0
1
2
3
4
5
Time (ms)
Reference-27J
Force (N)
12000
10000
8000
6000
4000
2000
0
0
1
2
3
4
5
6
Displacement (mm)
Reference-27J
Force (N)
12000
10000
8000
6000
4000
2000
0
0
1
2
3
4
5
6
Time (ms)
Reference-27J

Fig. 6: 27J, R2

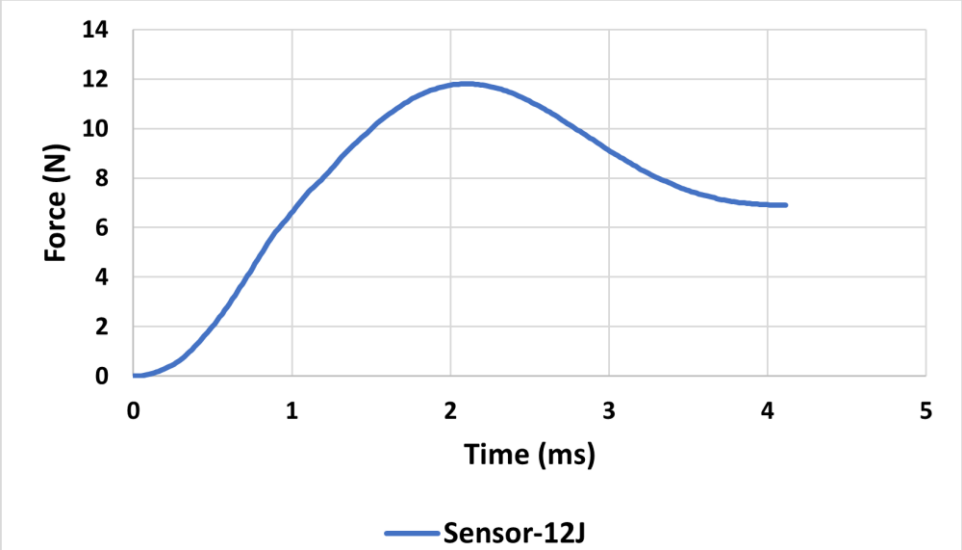
14
12
10
8
6
4
2
0
Force (N)
0
1
2
3
4
5
Time (ms)
Sensor-12J

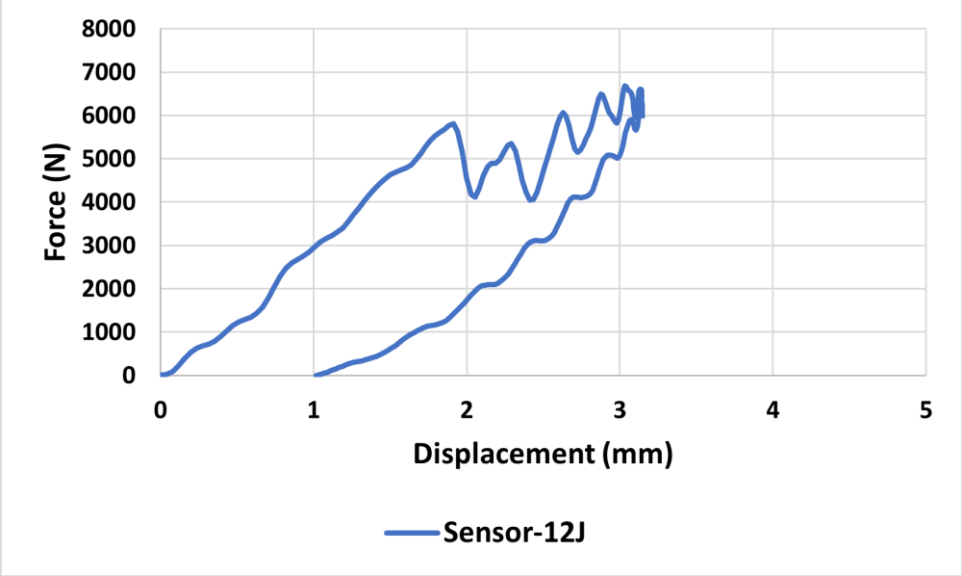
8000
7000
6000
5000
4000
3000
2000
1000
0
Force (N)
0
1
2
3
4
5
Displacement (mm)
Sensor-12J

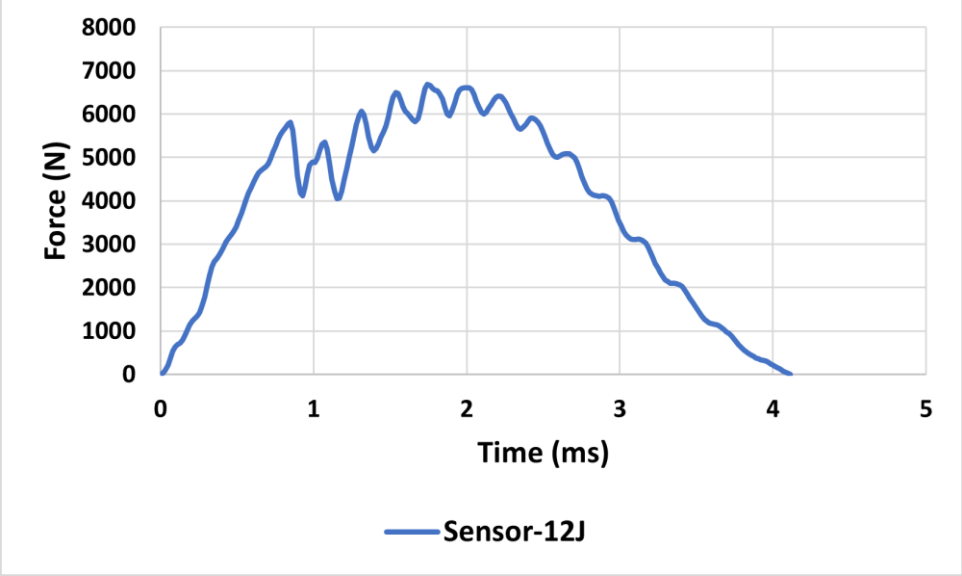
8000
7000
6000
5000
4000
3000
2000
1000
0
Force (N)
0
1
2
3
4
5
Time (ms)
Sensor-12J

Fig. 7: 12J, S1

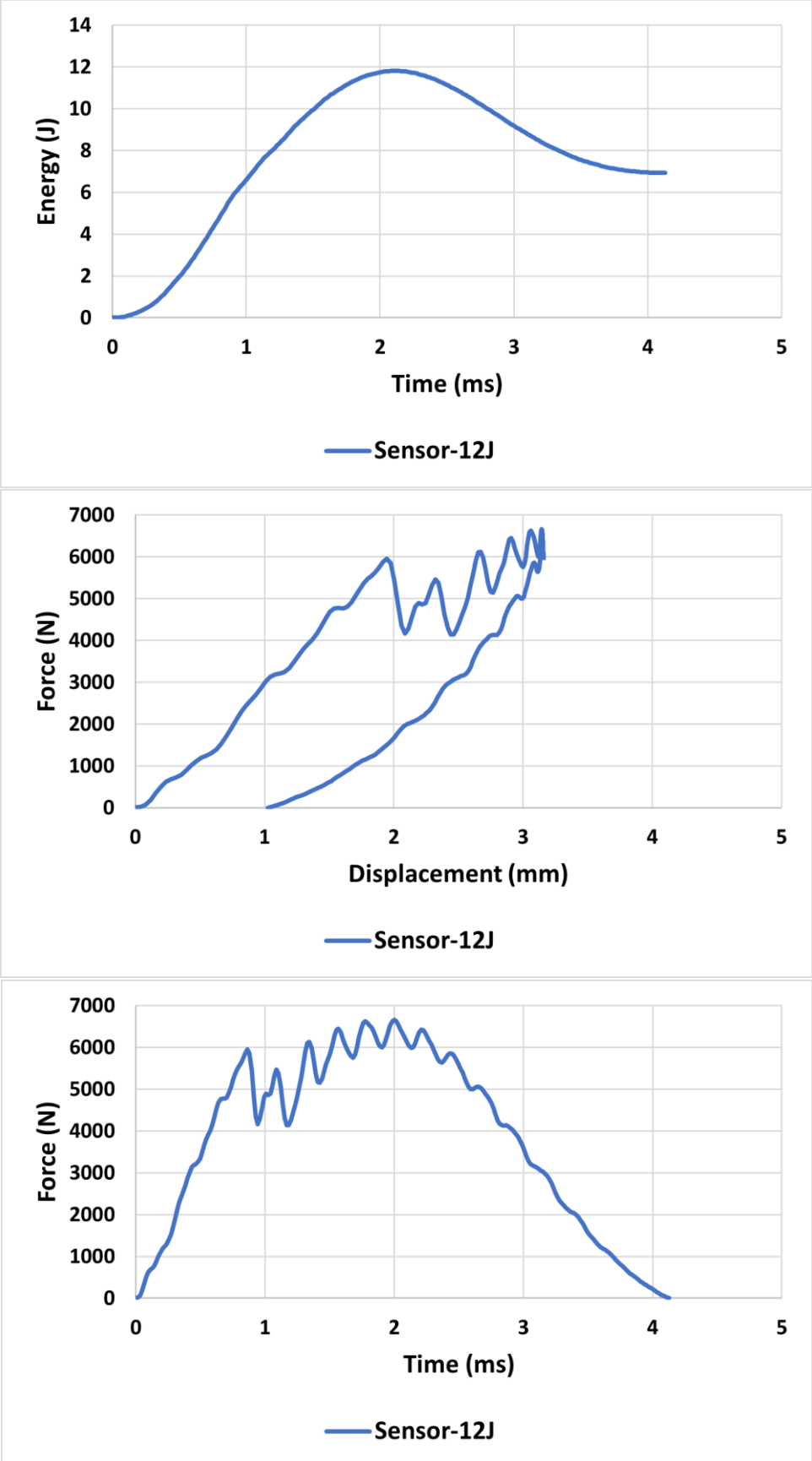
Energy (J)
14
12
10
8
6
4
2
0
0
1
2
3
4
5
Time (ms)
Sensor-12J
Force (N)
7000
6000
5000
4000
3000
2000
1000
0
0
1
2
3
4
5
Displacement (mm)
Sensor-12J
Force (N)
7000
6000
5000
4000
3000
2000
1000
0
0
1
2
3
4
5
Time (ms)
Sensor-12J

Fig. 8: 12J, S2

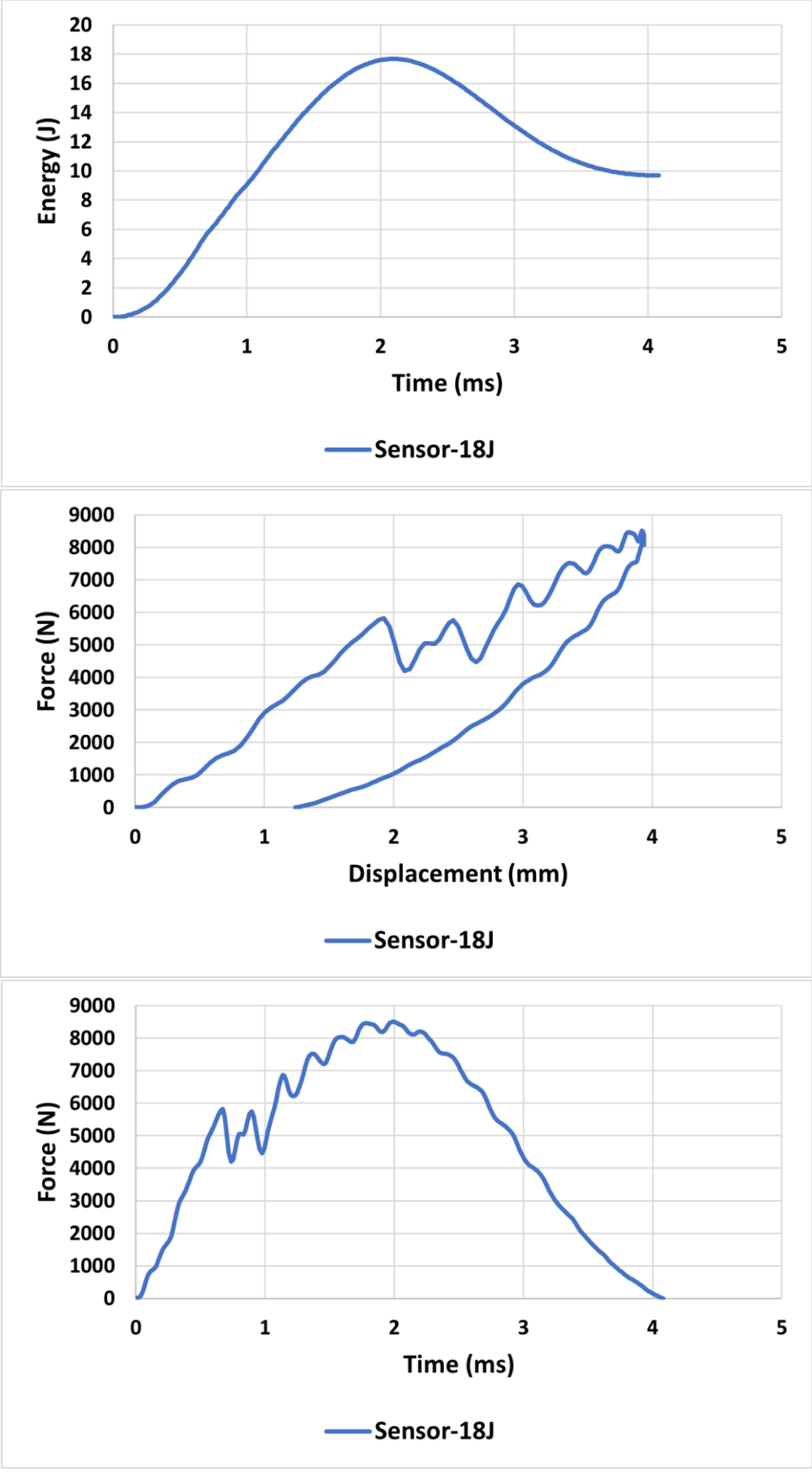
Energy (J)
Time (ms)
Sensor-18J
Force (N)
Displacement (mm)
Sensor-18J
Force (N)
Time (ms)
Sensor-18J

Fig. 9: 18J, S1

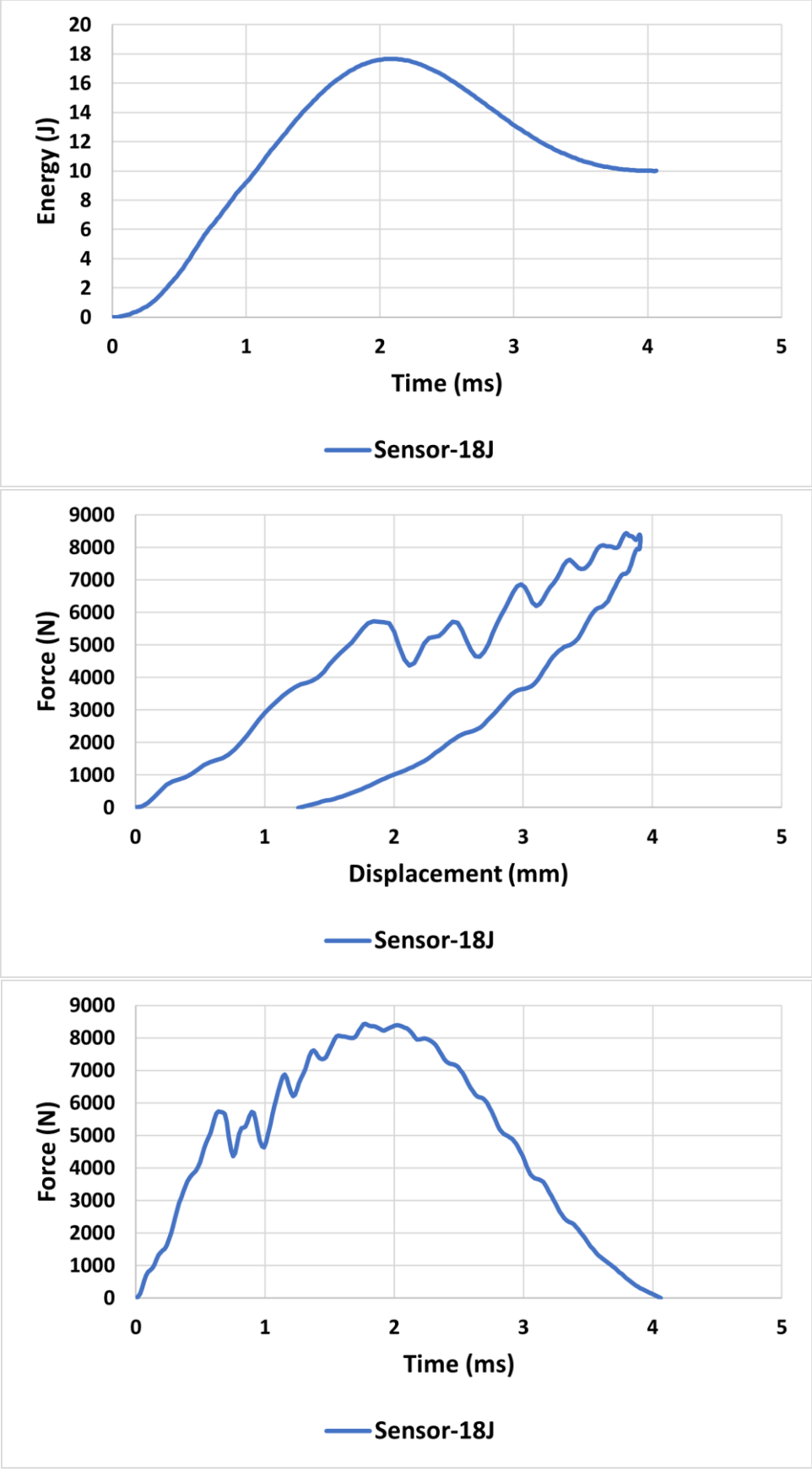
Energy (J)
20
18
16
14
12
10
8
6
4
2
0
0
1
2
3
4
5
Time (ms)
Sensor-18J
Force (N)
9000
8000
7000
6000
5000
4000
3000
2000
1000
0
0
1
2
3
4
5
Displacement (mm)
Sensor-18J
Force (N)
9000
8000
7000
6000
5000
4000
3000
2000
1000
0
0
1
2
3
4
5
Time (ms)
Sensor-18J

Fig. 10: 18J, S2

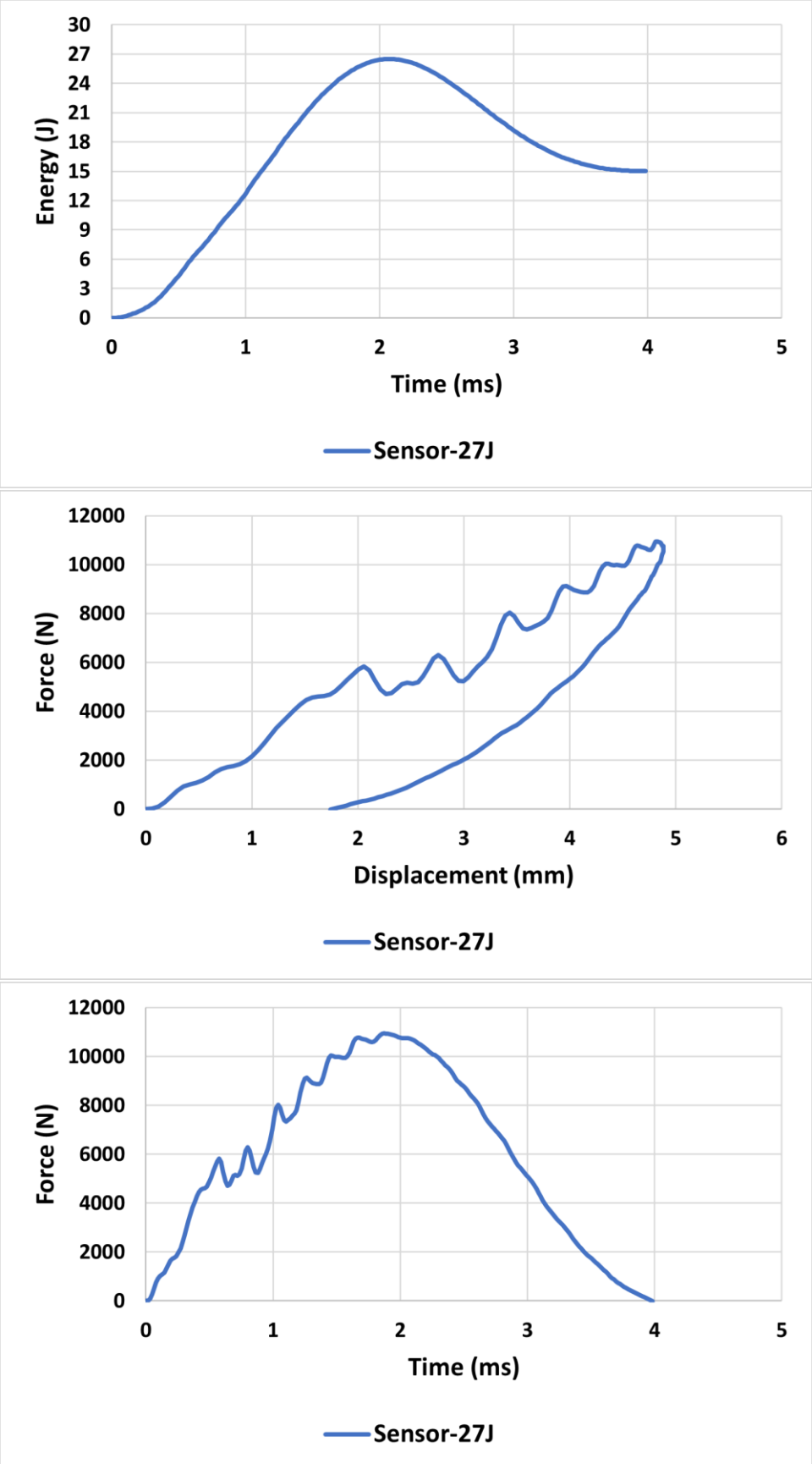
Energy (J)
30
27
24
21
18
15
12
9
6
3
0
0
1
2
3
4
5
Time (ms)
Sensor-27J
Force (N)
12000
10000
8000
6000
4000
2000
0
0
1
2
3
4
5
6
Displacement (mm)
Sensor-27J
Force (N)
12000
10000
8000
6000
4000
2000
0
0
1
2
3
4
5
Time (ms)
Sensor-27J

Fig. 11: 27J, S1

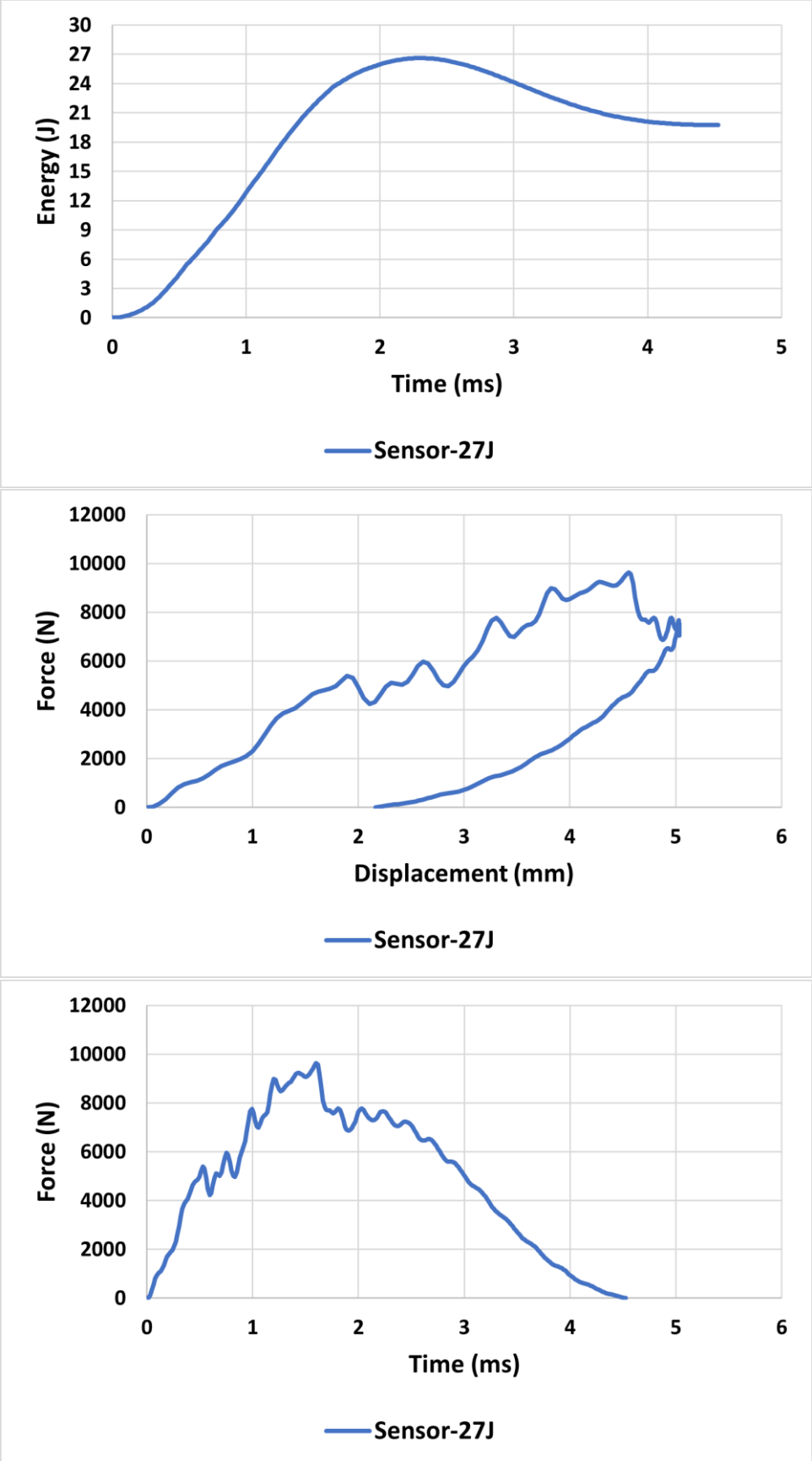
Energy (J)
30
27
24
21
18
15
12
9
6
3
0
0
1
2
3
4
5
Time (ms)
Sensor-27J
Force (N)
12000
10000
8000
6000
4000
2000
0
0
1
2
3
4
5
6
Displacement (mm)
Sensor-27J
Force (N)
12000
10000
8000
6000
4000
2000
0
0
1
2
3
4
5
6
Time (ms)
Sensor-27J

Fig. 12: 27J, S2

<u>Appendix C:</u> Engineering drawings of the custom-designed supporting window and clamping fixture for testing curved panels

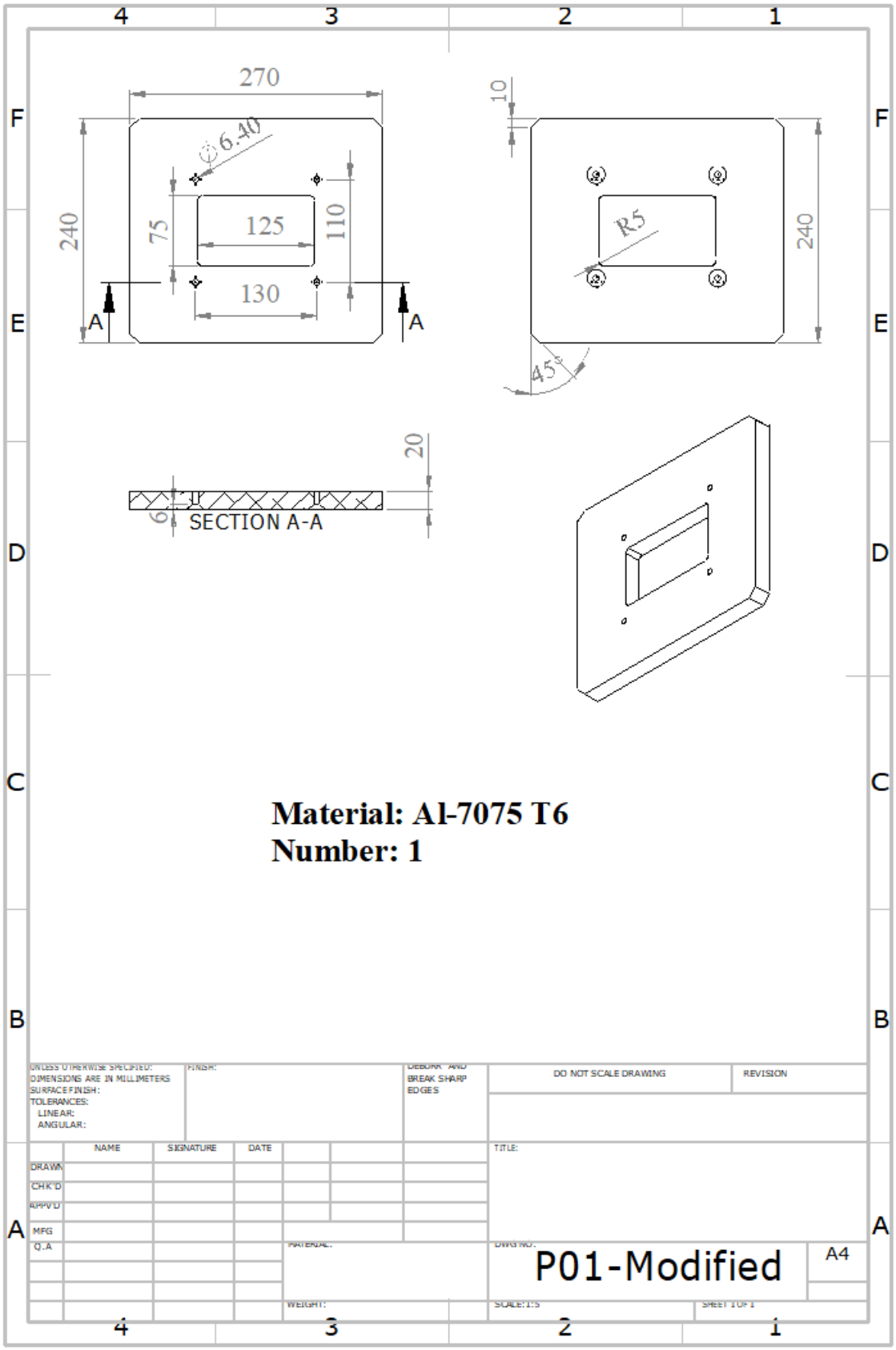

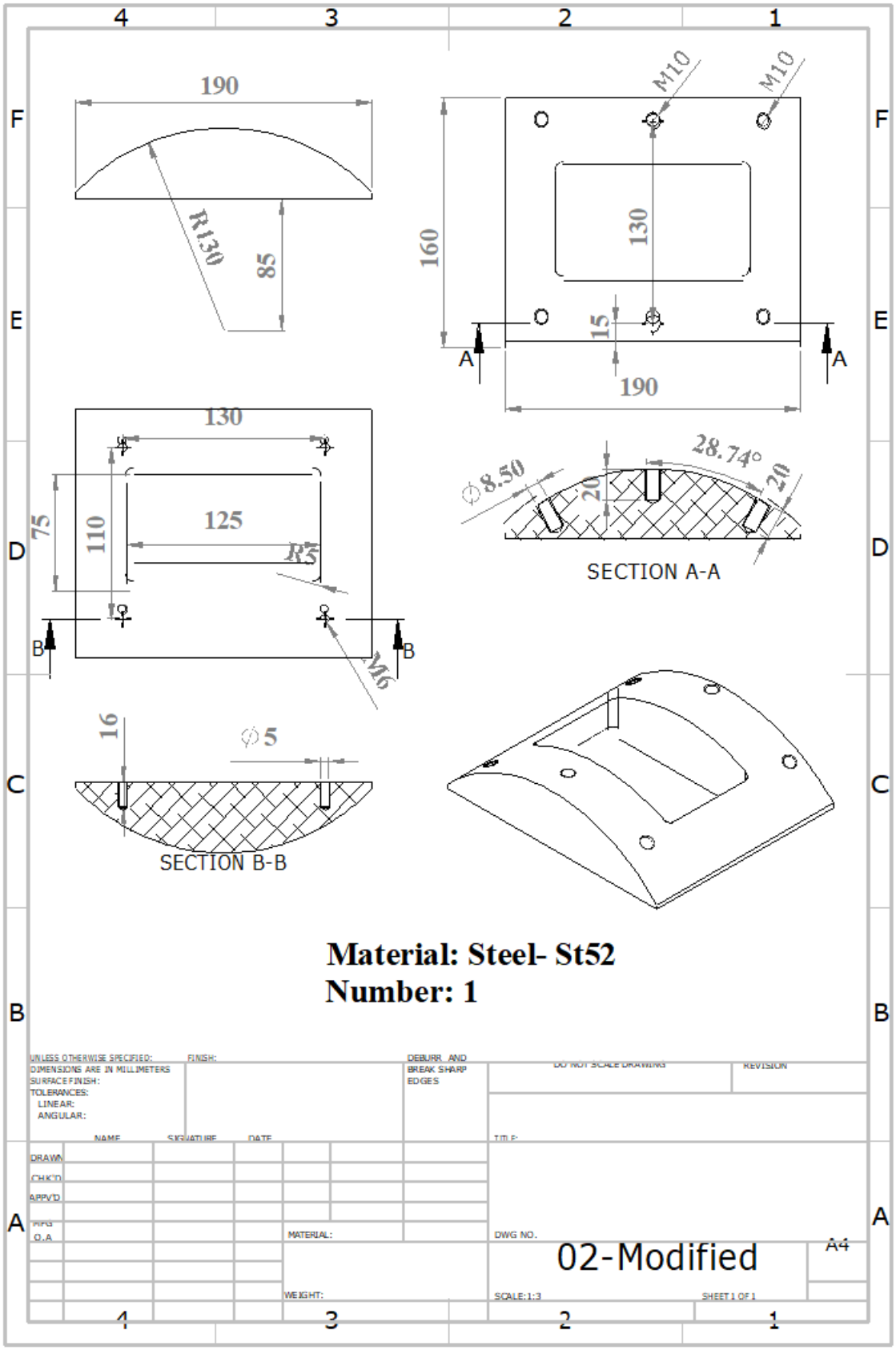
190
R130
85
M10
M10
160
130
15
190
A
A
130
75
110
125
R5
B
B
M6
28.74°
Ø8.50
20
20
SECTION A-A
16
Ø5
SECTION B-B
Material: Steel- St52
Number: 1
UNLESS OTHERWISE SPECIFIED:
DIMENSIONS ARE IN MILLIMETERS
SURFACE FINISH:
TOLERANCES:
LINEAR:
ANGULAR:
FINISH:
DEBURR AND
BREAK SHARP
EDGES
DO NOT SCALE DRAWING
REVISION
NAME
SIGNATURE
DATE
TITLE:
DRAWN
CHK'D
APPV'D
MFG
Q.A
MATERIAL:
DWG NO.
02-Modified
A4
WEIGHT:
SCALE:1:3
SHEET 1 OF 1

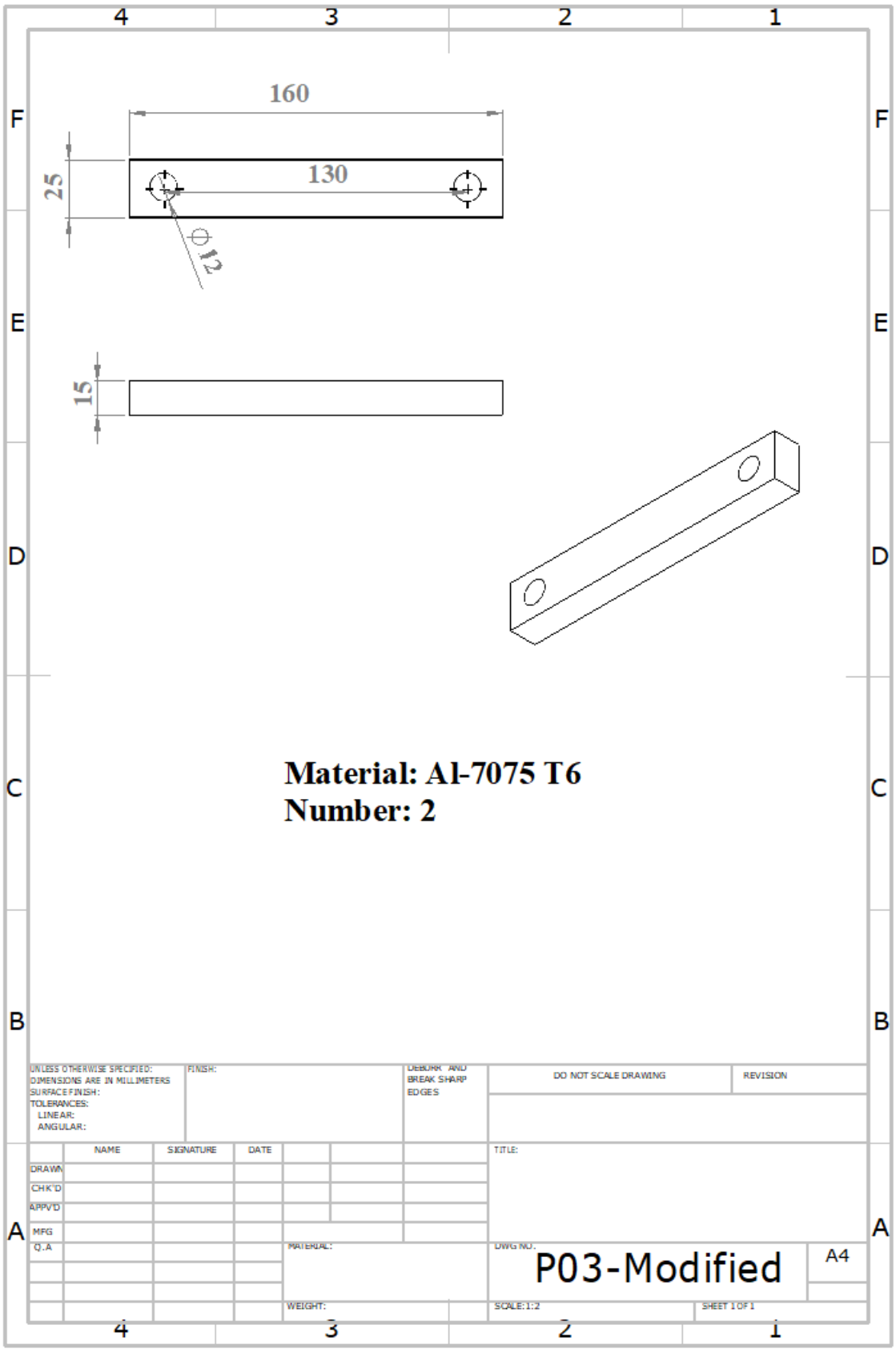
160
130
25
Φ12
15
Material: Al-7075 T6
Number: 2
UNLESS OTHERWISE SPECIFIED:
DIMENSIONS ARE IN MILLIMETERS
SURFACE FINISH:
TOLERANCES:
LINEAR:
ANGULAR:
FINISH:
DEBURR AND BREAK SHARP EDGES
DO NOT SCALE DRAWING
REVISION
NAME
SIGNATURE
DATE
DRAWN
CHK'D
APPV'D
MFG
Q.A
TITLE:
MATERIAL:
DWG NO.
P03-Modified
A4
WEIGHT:
SCALE:1:2
SHEET 1 OF 1

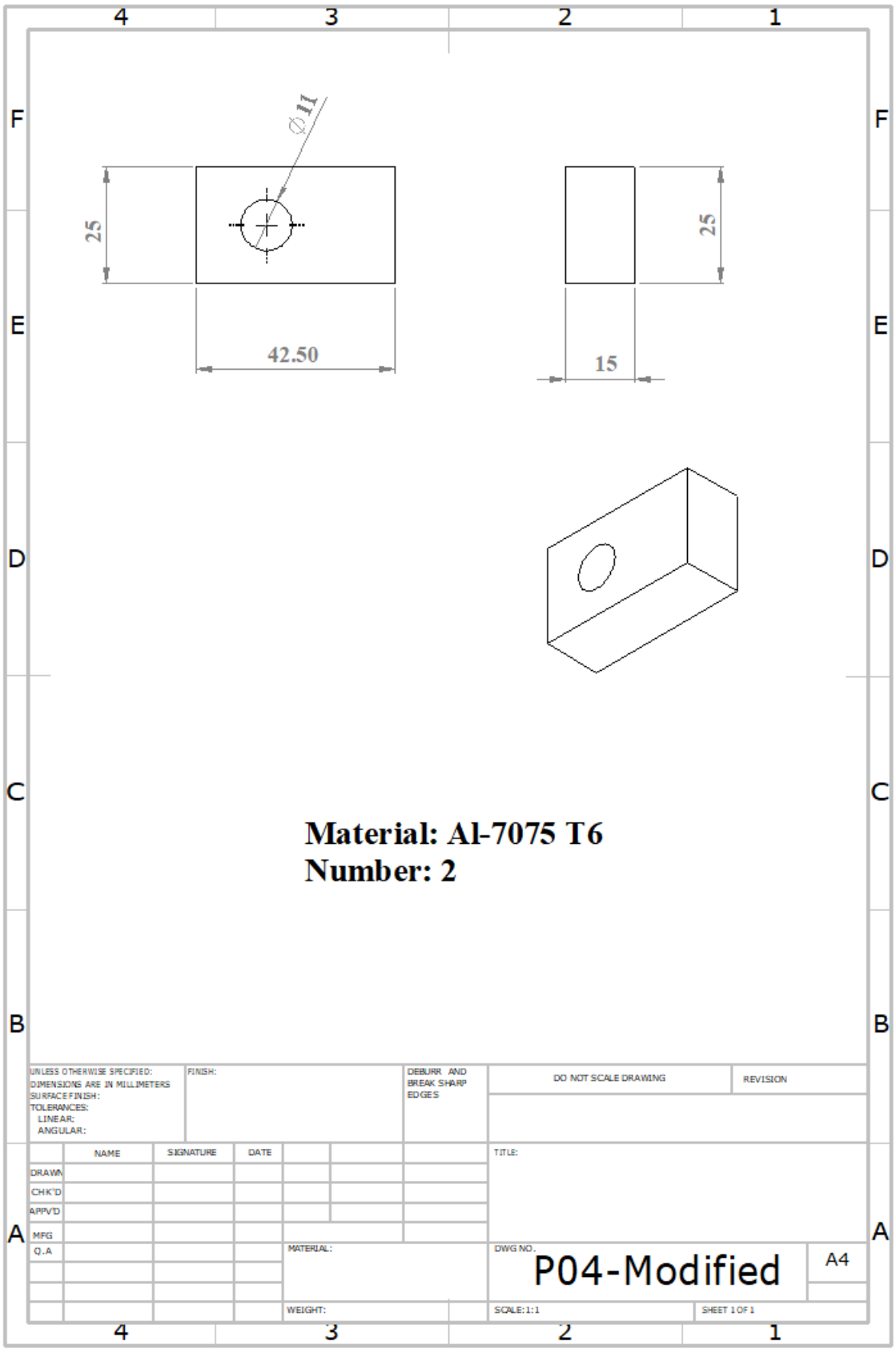
4
3
2
1
F
E
D
C
B
A
∅11
25
42.50
25
15
Material: Al-7075 T6
Number: 2
UNLESS OTHERWISE SPECIFIED:
DIMENSIONS ARE IN MILLIMETERS
SURFACE FINISH:
TOLERANCES:
LINEAR:
ANGULAR:
FINISH:
DEBURR AND BREAK SHARP EDGES
DO NOT SCALE DRAWING
REVISION
NAME
SIGNATURE
DATE
TITLE:
DRAWN
CHK'D
APPV'D
MFG
Q.A
MATERIAL:
DWG NO.
P04-Modified
A4
WEIGHT:
SCALE:1:1
SHEET 1 OF 1

<u>Appendix D:</u> Visual inspection results (images) taken during the static indentation tests of curved panels

Reference sample

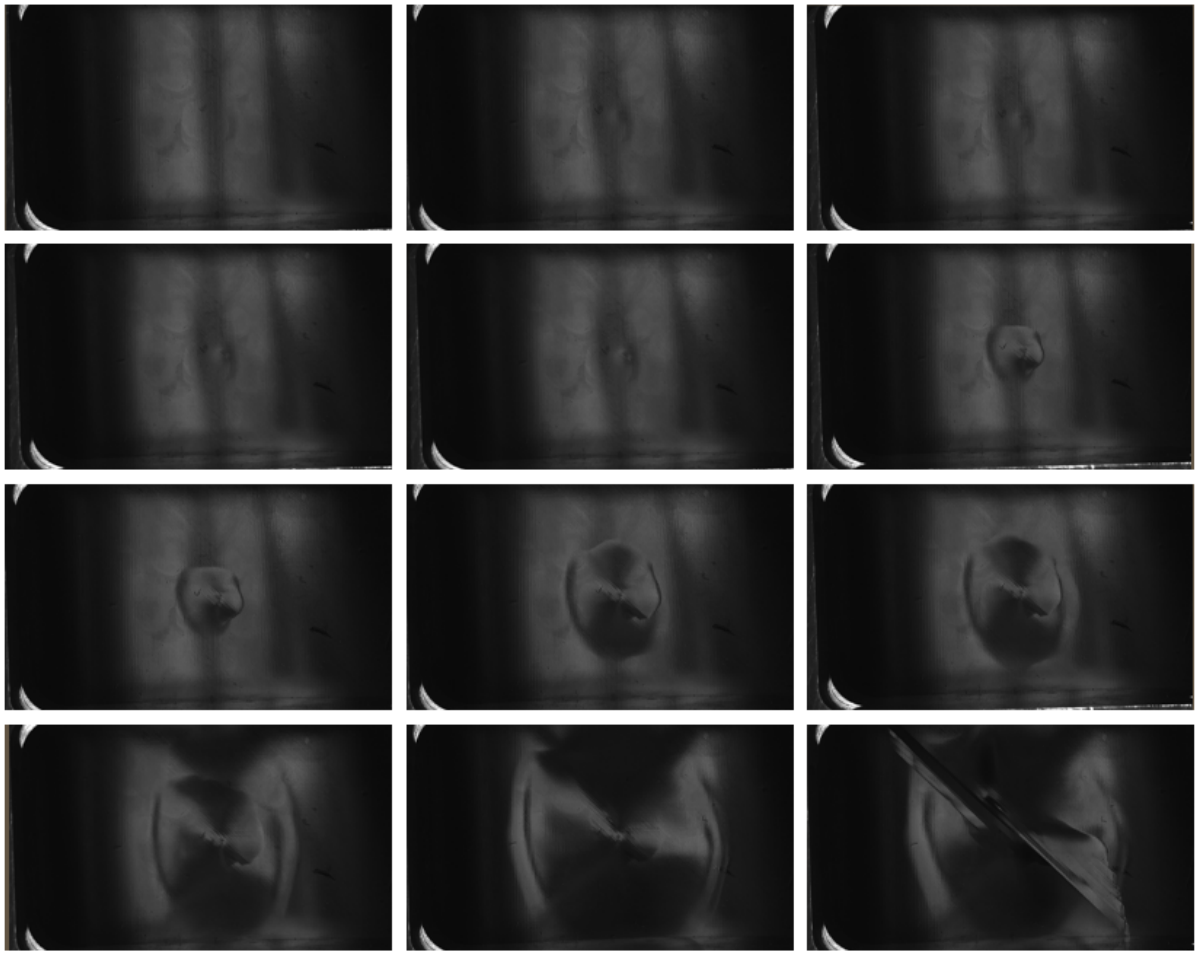

Sensor sample

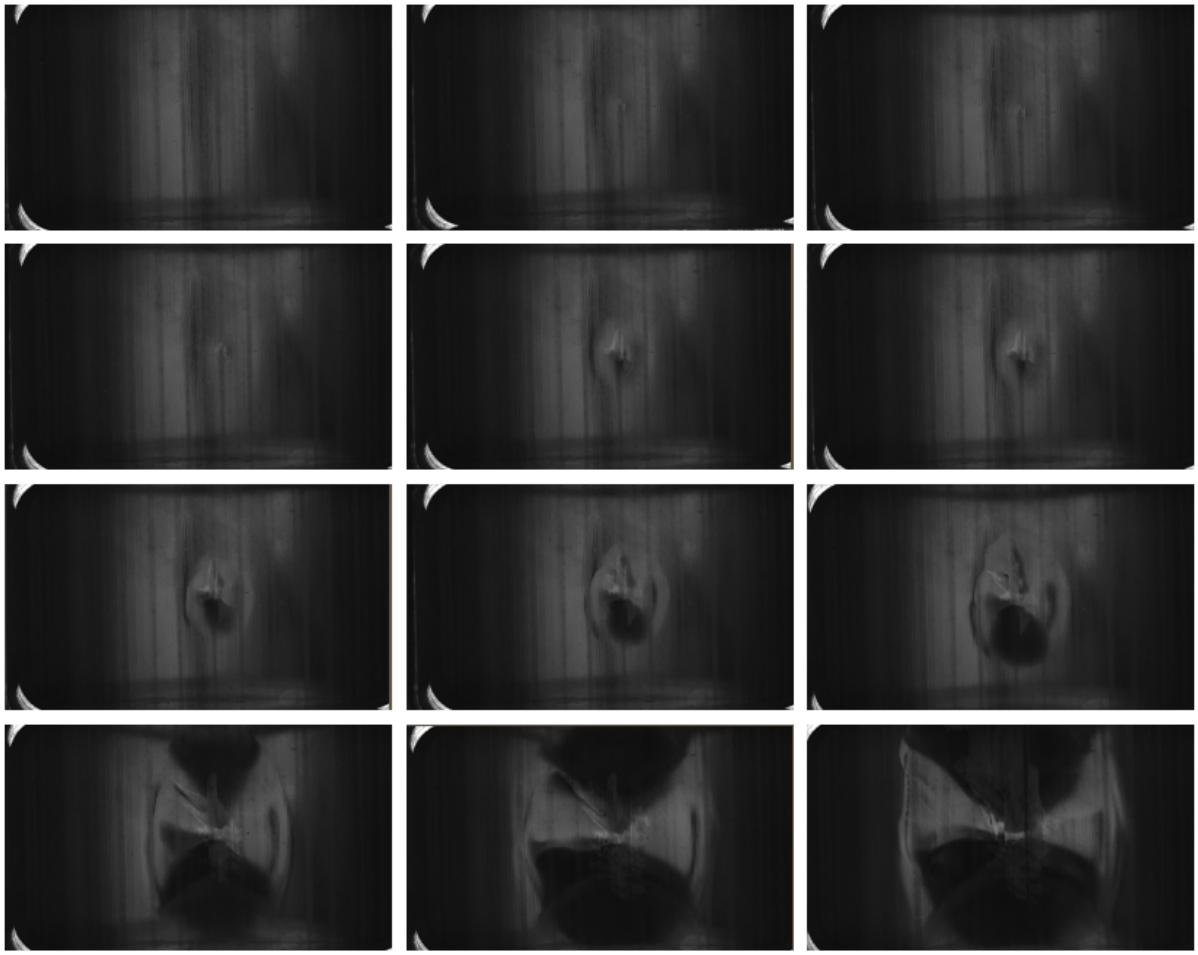

<u>Appendix E:</u> Impact test results for curved Reference (R) and Sensor (S) samples at 6J, 12J, 18J and 27J energies

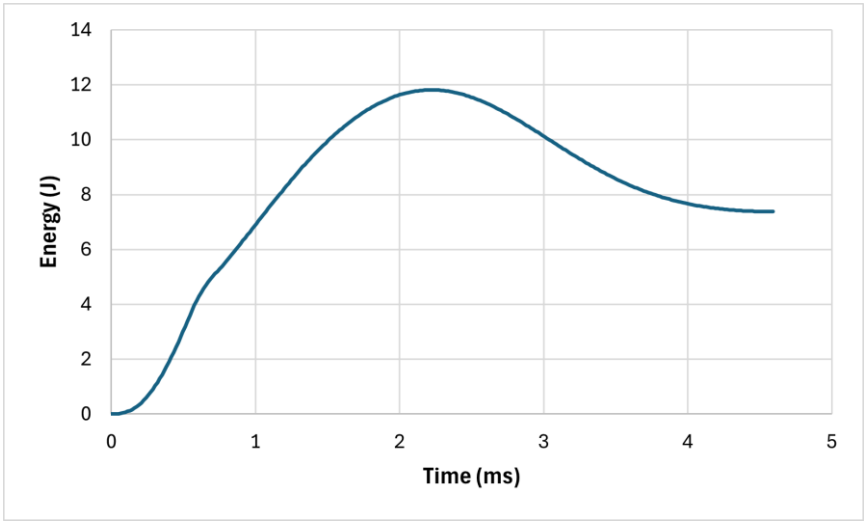

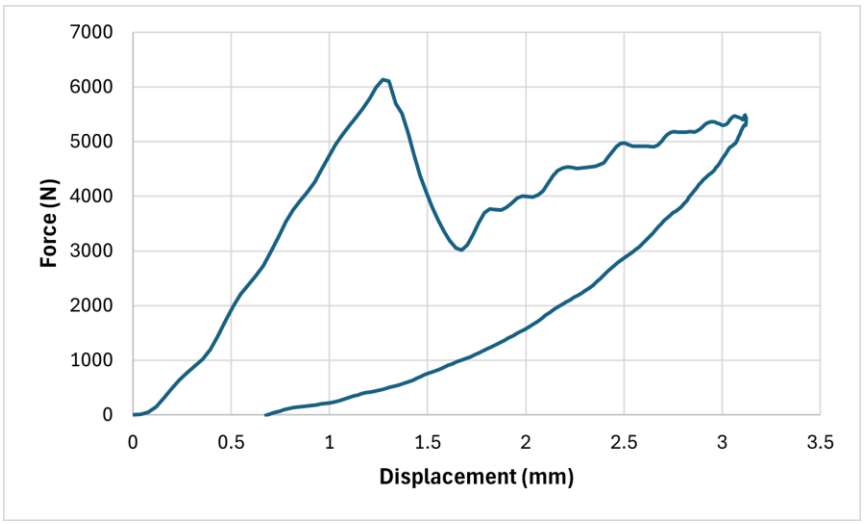

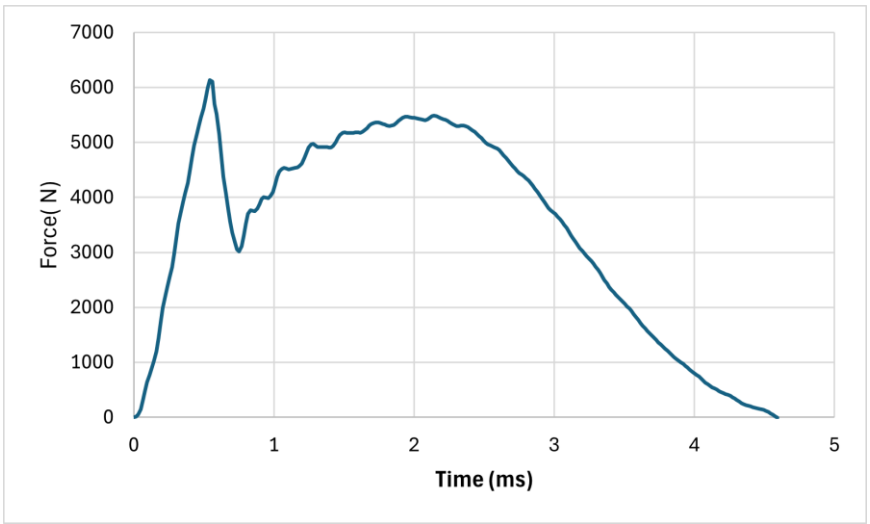

Fig. 1: 12J, R1

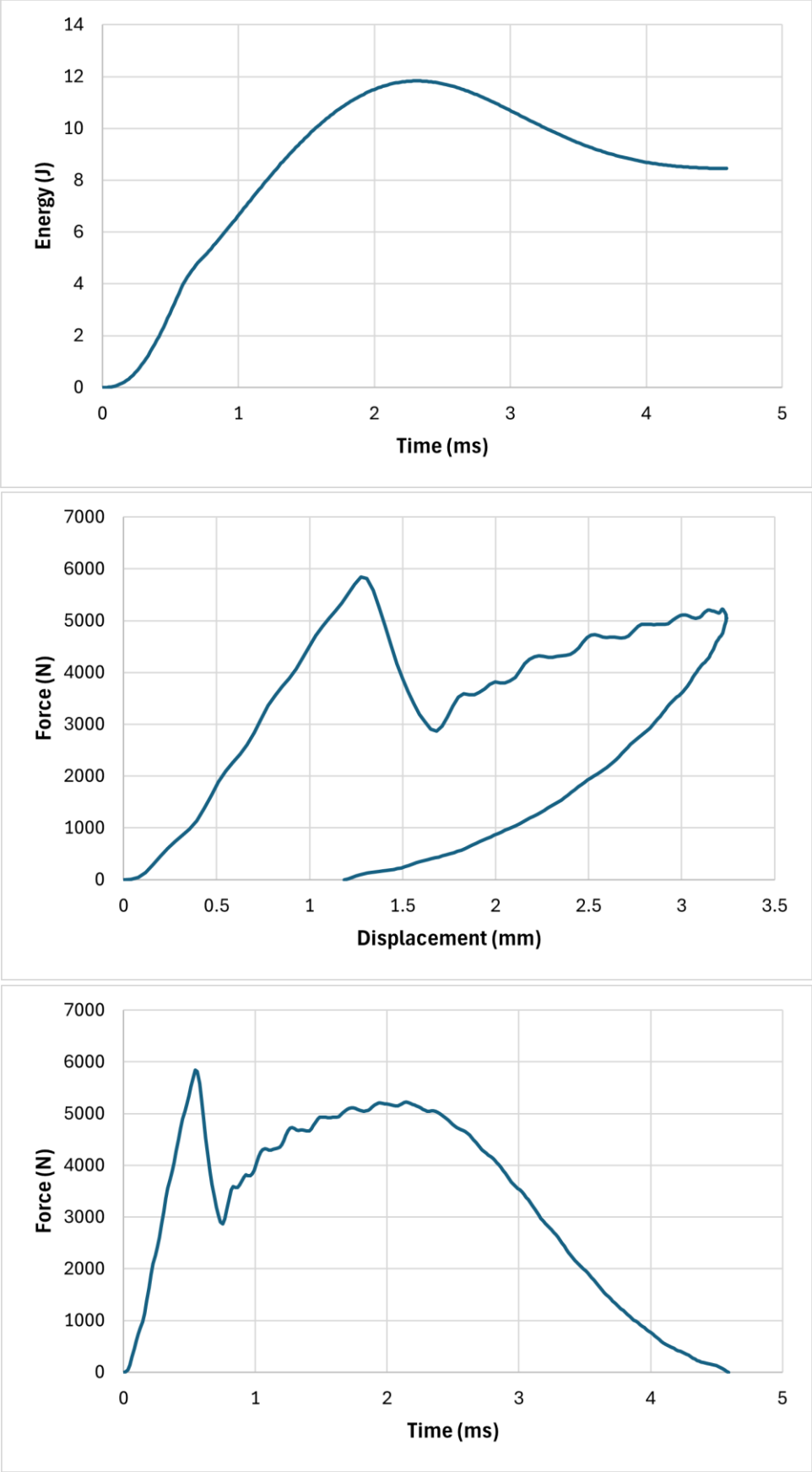
Energy (J)
14
12
10
8
6
4
2
0
0
1
2
3
4
5
Time (ms)
Force (N)
7000
6000
5000
4000
3000
2000
1000
0
0
0.5
1
1.5
2
2.5
3
3.5
Displacement (mm)
Force (N)
7000
6000
5000
4000
3000
2000
1000
0
0
1
2
3
4
5
Time (ms)

Fig. 2: 12J, R2

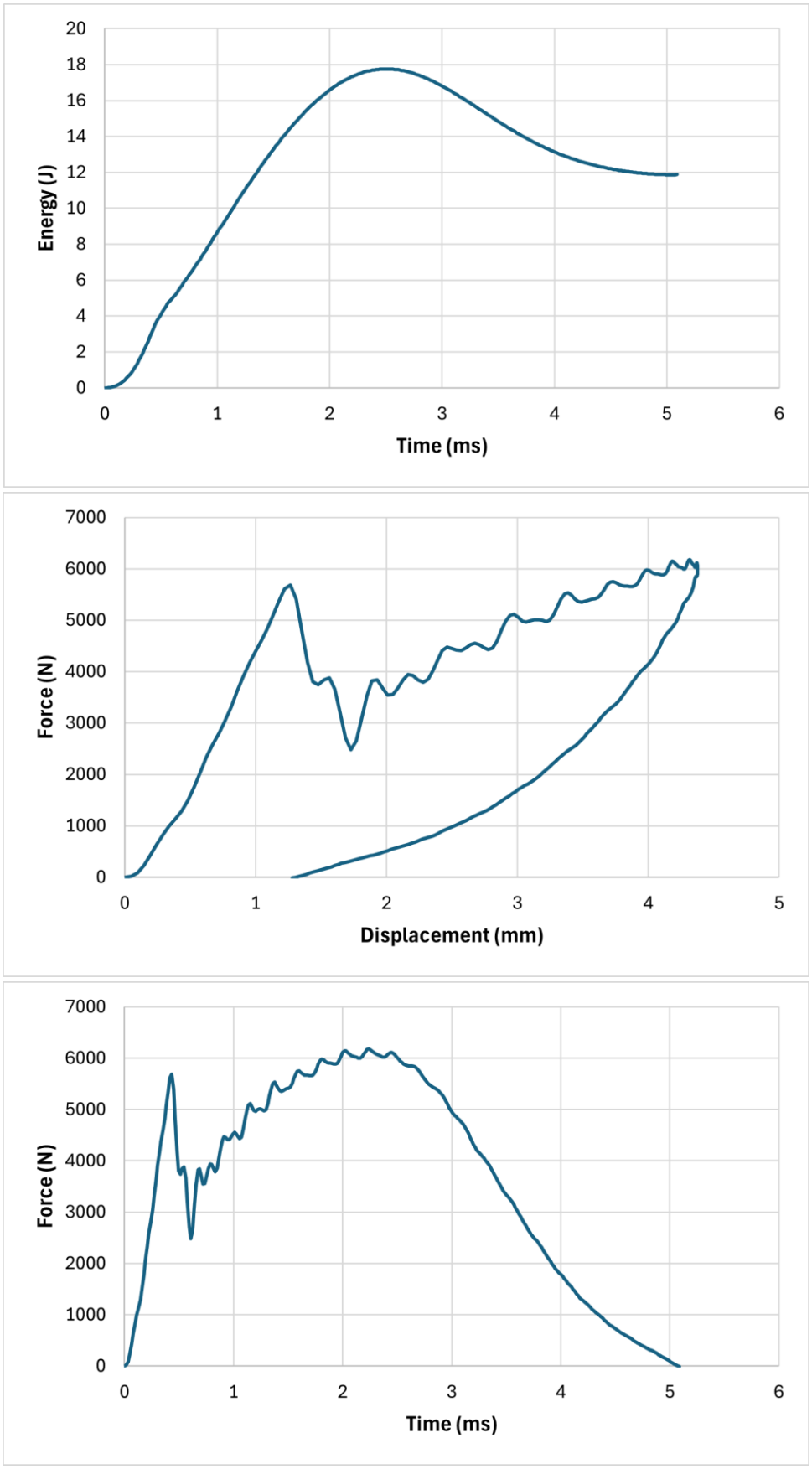

Fig. 3: 18J, R1

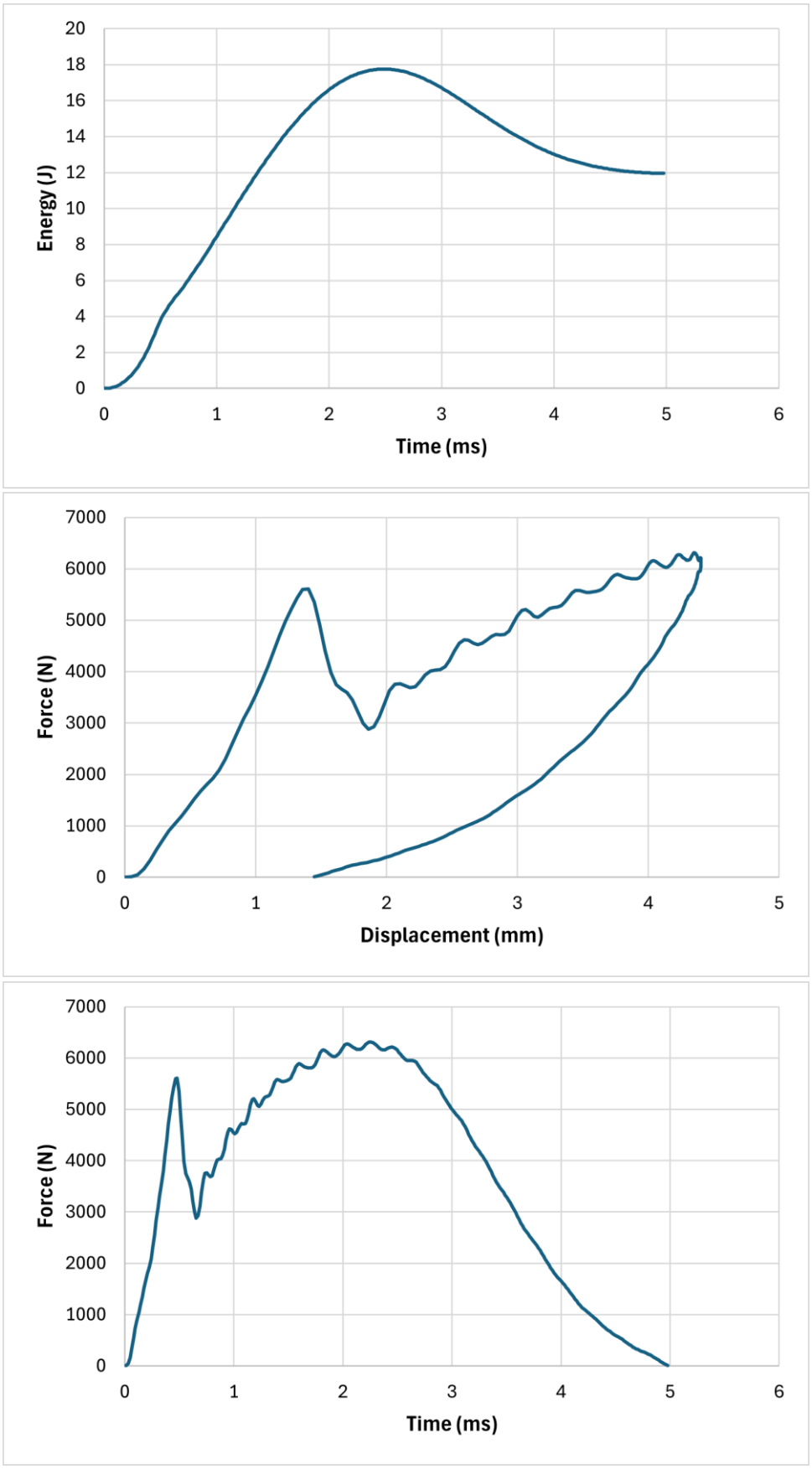

Fig. 4: 18J, R2

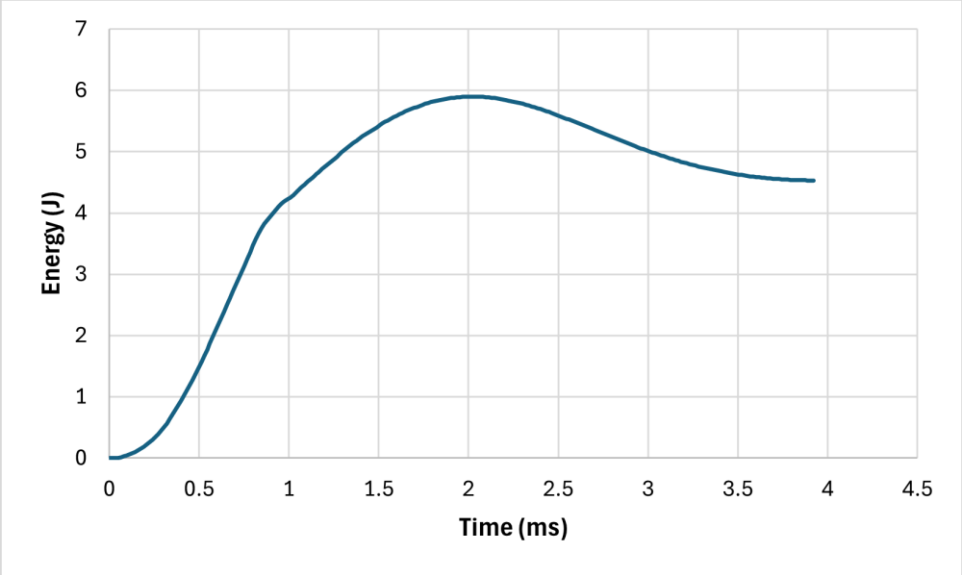
Energy (J)
Time (ms)
0
1
2
3
4
5
6
7
0
0.5
1
1.5
2
2.5
3
3.5
4
4.5

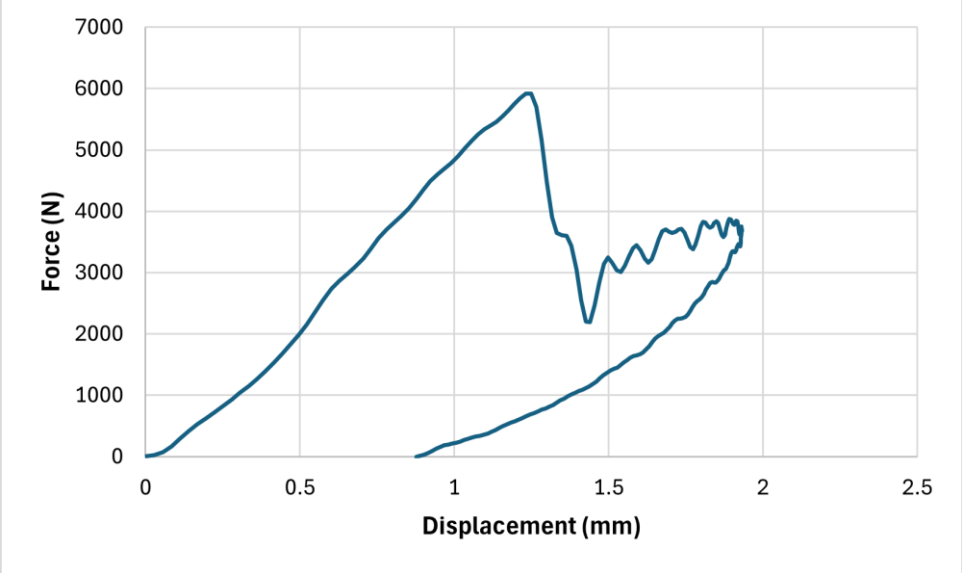
Force (N)
Displacement (mm)
0
1000
2000
3000
4000
5000
6000
7000
0
0.5
1
1.5
2
2.5

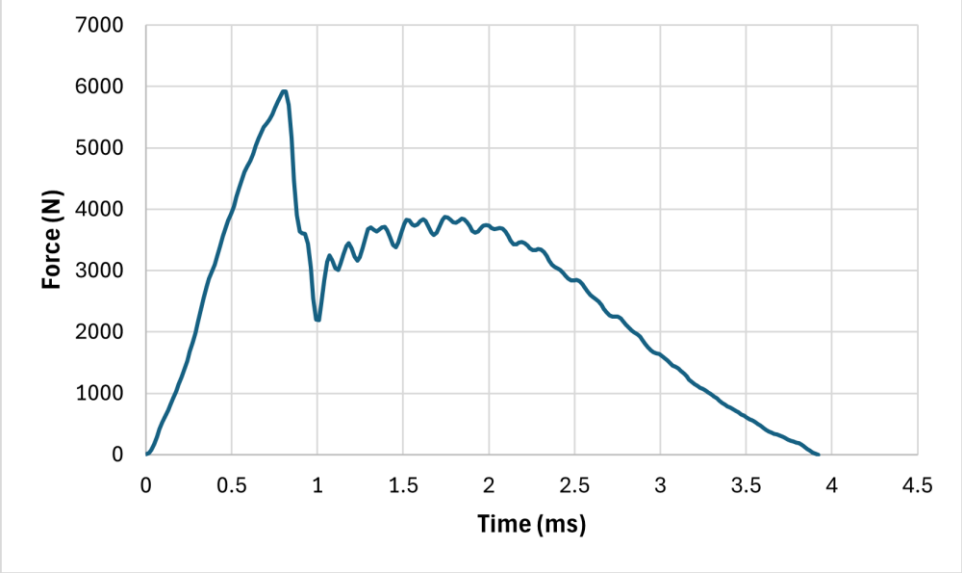
Force (N)
Time (ms)
0
1000
2000
3000
4000
5000
6000
7000
0
0.5
1
1.5
2
2.5
3
3.5
4
4.5

Fig. 5: 6J, S1

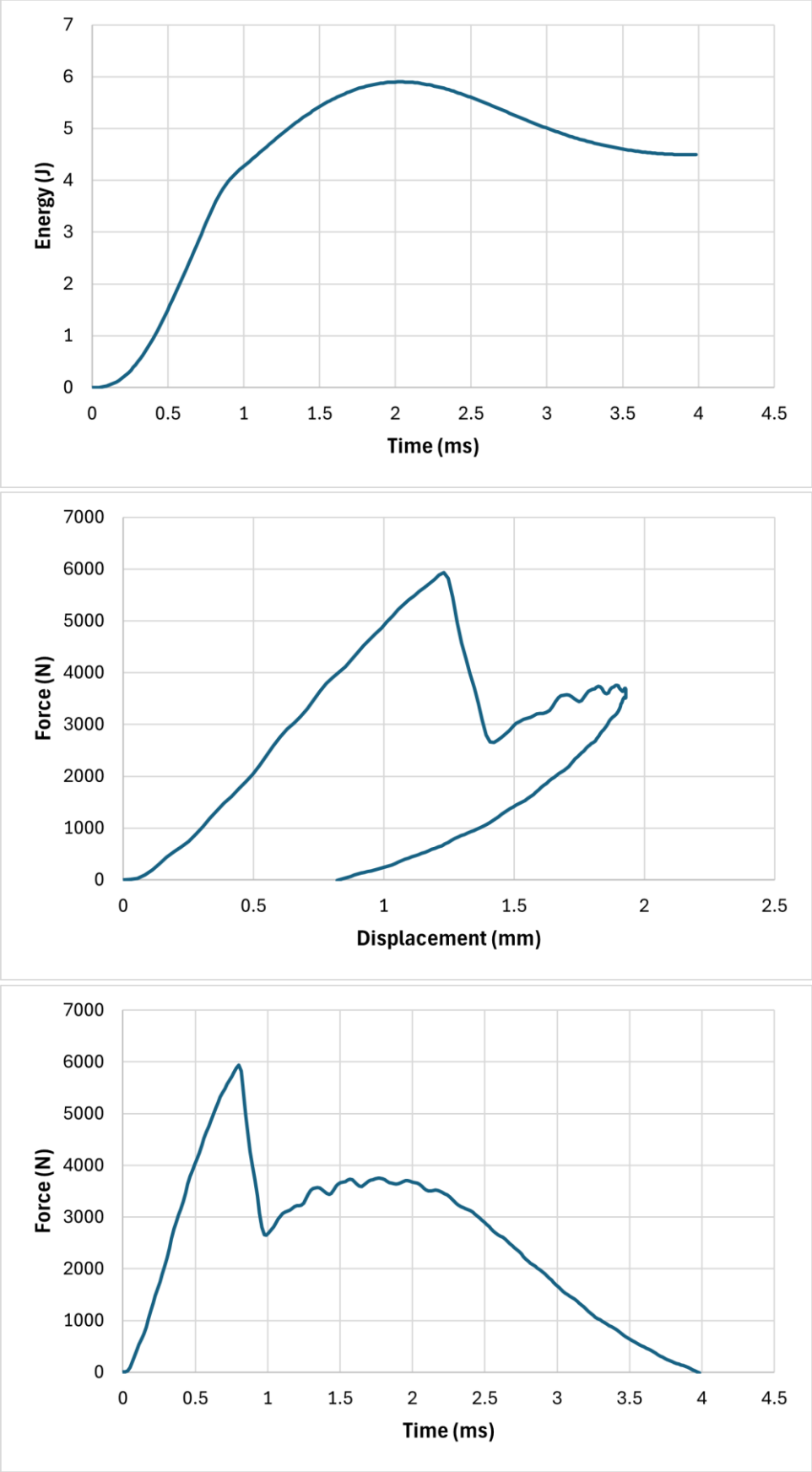

Fig. 6: 6J, S2

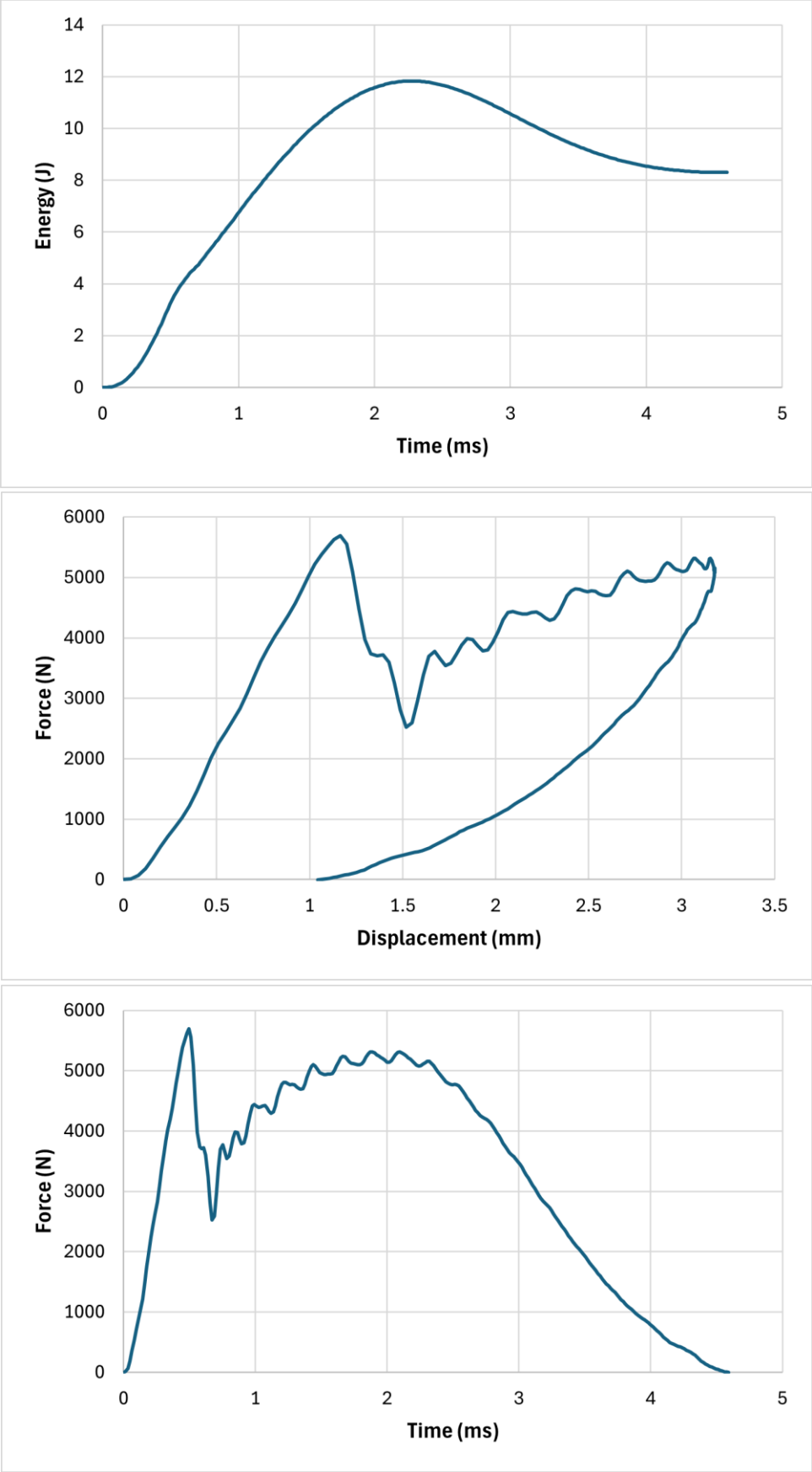
Energy (J)
14
12
10
8
6
4
2
0
0
1
2
3
4
5
Time (ms)
Force (N)
6000
5000
4000
3000
2000
1000
0
0
0.5
1
1.5
2
2.5
3
3.5
Displacement (mm)
Force (N)
6000
5000
4000
3000
2000
1000
0
0
1
2
3
4
5
Time (ms)

Fig. 7: 12J, S1

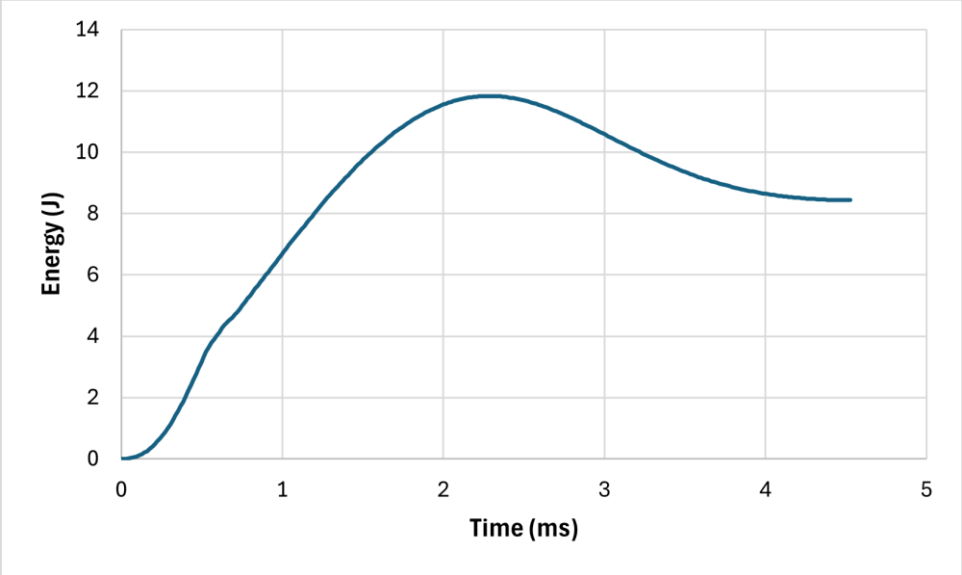
Energy (J)
14
12
10
8
6
4
2
0
0
1
2
3
4
5
Time (ms)

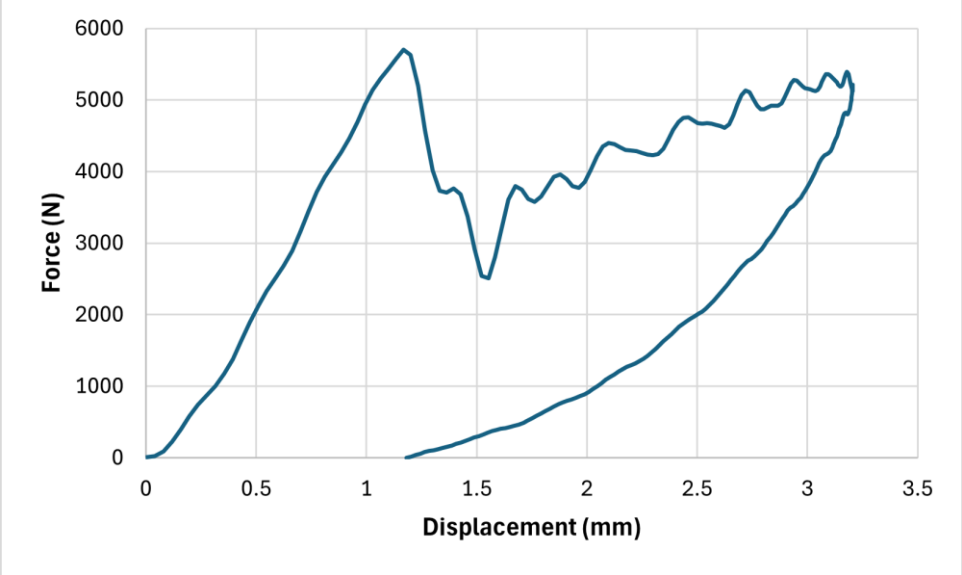
Force (N)
6000
5000
4000
3000
2000
1000
0
0
0.5
1
1.5
2
2.5
3
3.5
Displacement (mm)

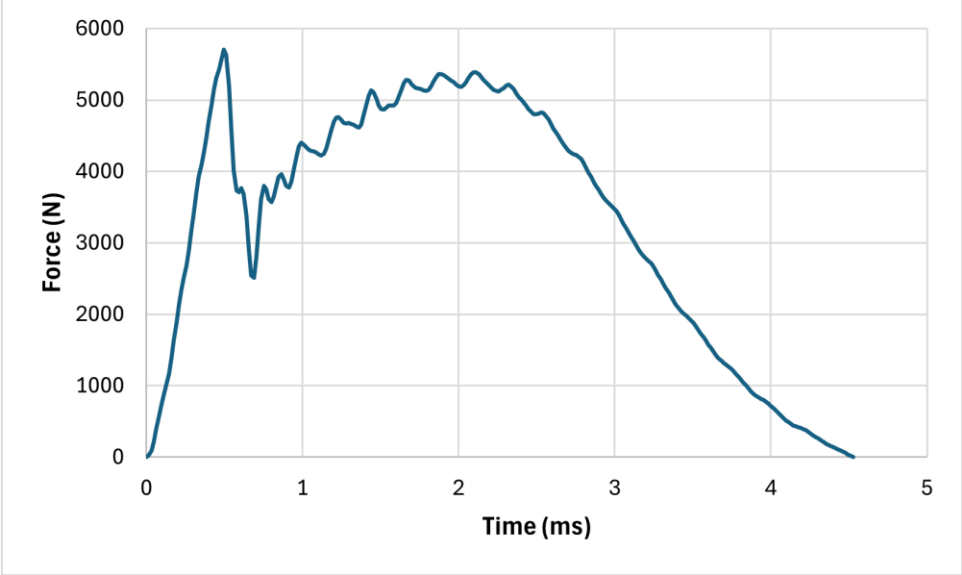
Force (N)
6000
5000
4000
3000
2000
1000
0
0
1
2
3
4
5
Time (ms)

Fig. 8: 12J, S2

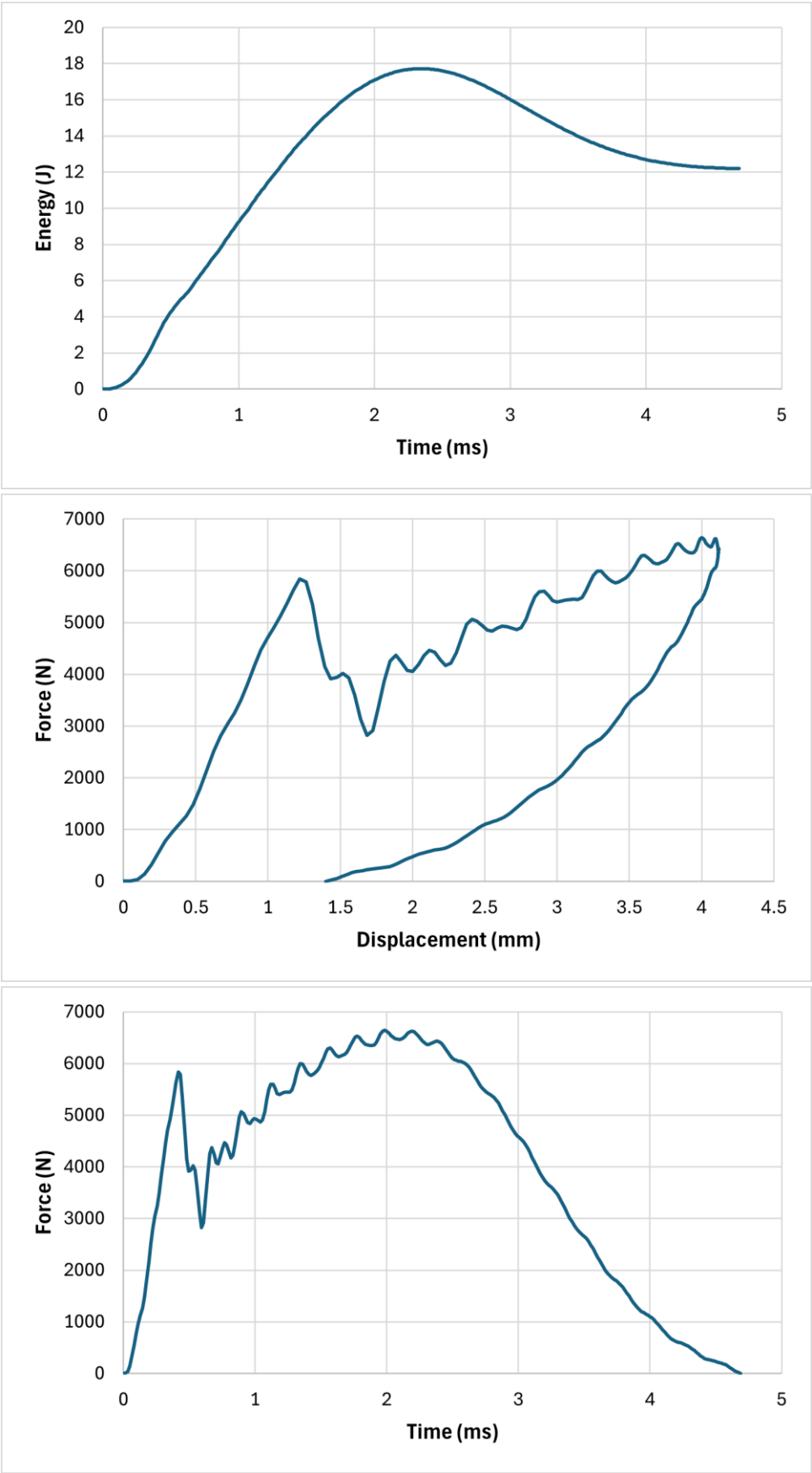

Fig. 9: 18J, S1

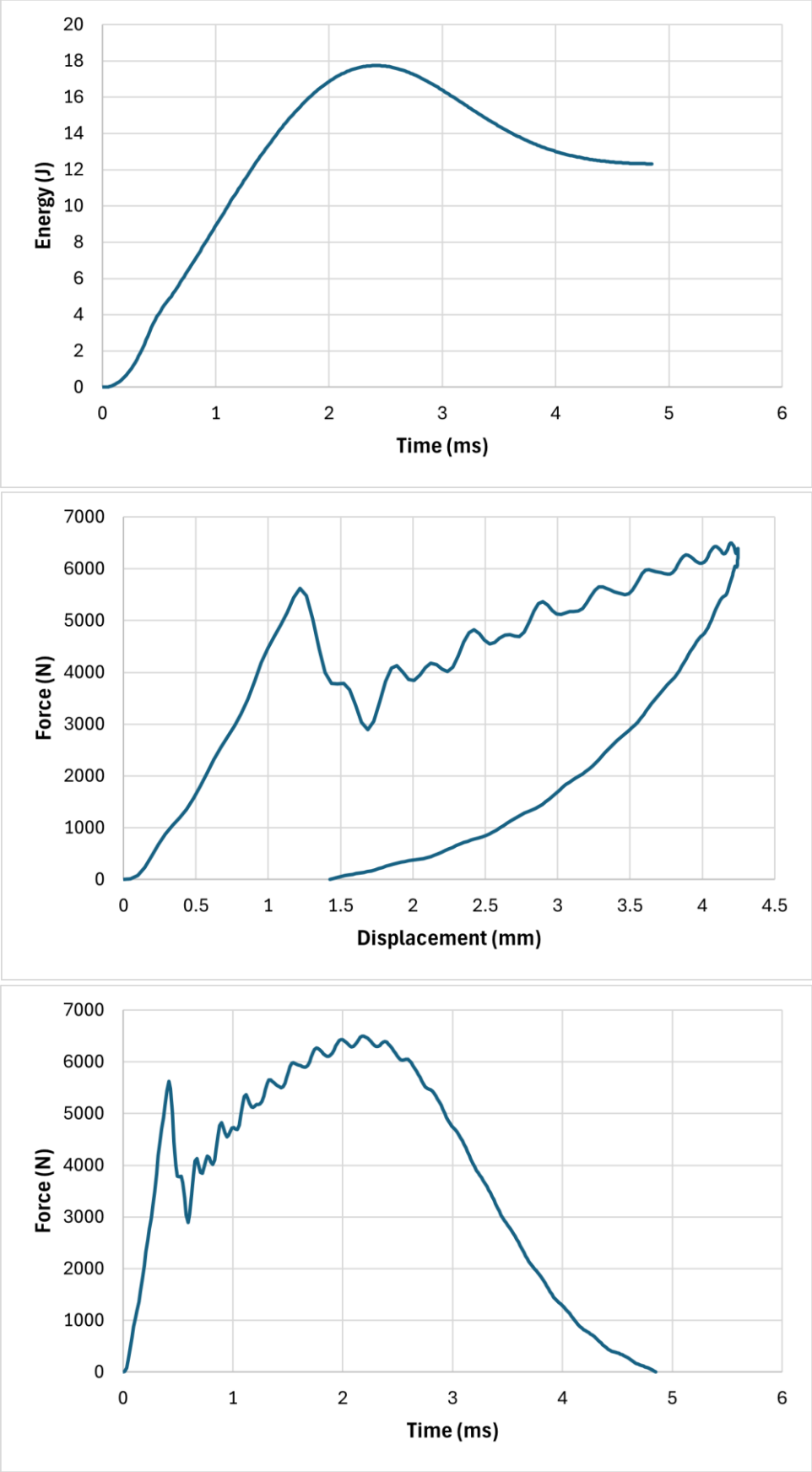

Fig. 10: 18J, S2

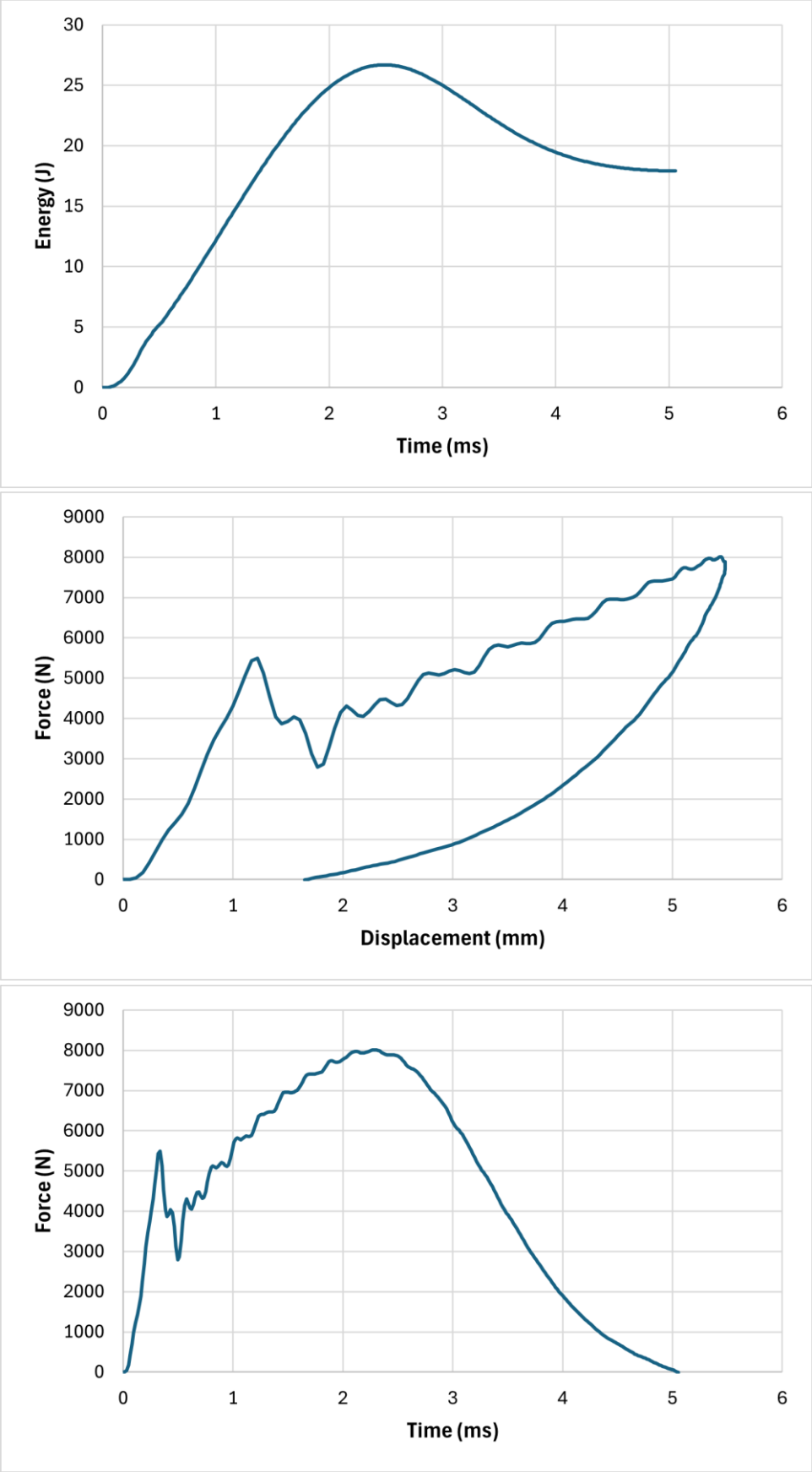
Energy (J)
30
25
20
15
10
5
0
0
1
2
3
4
5
6
Time (ms)
Force (N)
9000
8000
7000
6000
5000
4000
3000
2000
1000
0
0
1
2
3
4
5
6
Displacement (mm)
Force (N)
9000
8000
7000
6000
5000
4000
3000
2000
1000
0
0
1
2
3
4
5
6
Time (ms)

Fig. 11: 27J, S1

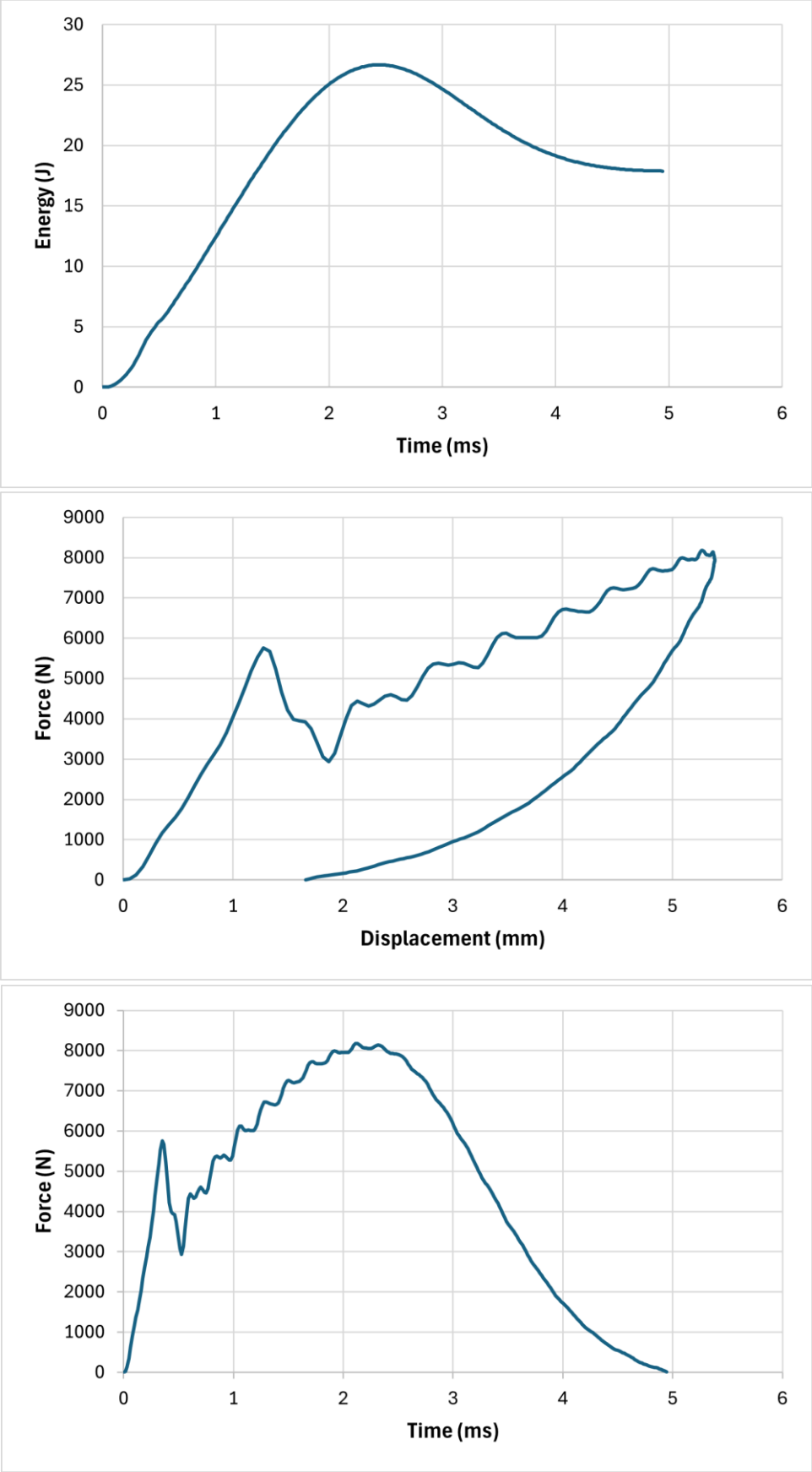
Energy (J)
30
25
20
15
10
5
0
0
1
2
3
4
5
6
Time (ms)
Force (N)
9000
8000
7000
6000
5000
4000
3000
2000
1000
0
0
1
2
3
4
5
6
Displacement (mm)
Force (N)
9000
8000
7000
6000
5000
4000
3000
2000
1000
0
0
1
2
3
4
5
6
Time (ms)

Fig. 12: 27J, S2